Design of Food-Inks for 3D printing of food images

A thesis presented in partial fulfilment of the requirements for the degree of

PhD in Food Technology

at Massey University, Manawatū, New Zealand.

Teresa Francis Wegrzyn

Jan 2016

Abstract

Food Layered Manufacture (FLM) is a novel food structuring which uses the Additive Manufacturing process (commonly termed 3D printing) to shape solid or gelled foods. Material is deposited layer-by-layer by a robotics system controlled from a digital template. FLM requires greater control of structure formation than in conventional food manufacturing. This thesis examines formulation design for a prototype Food-Inks 3D printer which extrudes a fluid thread of food material (Food-Ink) to produce a 3D colour image embedded in a food item. The first Food-Ink design target is a bread-or cake-like food with an elastomeric foam structure (sponge product, SP).

Chapter 1 introduces FLM technologies, product concepts and formulation design strategies, identifies design tasks for Food-Ink formulation, and surveys current understanding of SP structure development. Chapter 2 examines flow behaviour requirements for Food-Inks on piping, colour-mixing and deposition of image voxels, and characterises the flow behaviour of model SP Food-Inks. The critical design parameters are the Food-Ink shear-thinning and viscoelastic properties, the relaxation times for stop-start-stop flow, the viscosity ratio between Food-Ink base and added colour, and the pipe diameters on pumping and voxel deposition. Chapters 4 & 5 apply a suite of test methods developed in Chapter 3 & Appendix D to examine structure development in a non-wheat SP formulation. Substitution with different flours produces variants in SP cooked structure. A blackgram bean-buttermilk soluble fraction stabilises the batter foam interface and contributes to the elastomeric protein-non-starch polysaccharide domain of the cooked SP. Flour particulates control cooked SP void organisation by modulating batter bubble size and number distributions and the liquid phase volume, while soluble flour biopolymers control bubble expansion by modulating the flow properties of the liquid phase.

The Food-Inks 3D printer applies a new technology with little supporting information in the public domain. The study concludes that SP formulations are unsuited for this application. The overall study outcomes are 1) a comprehensive identification of constraints on Food-Ink and equipment design for the Food-Inks 3D printing application, and 2) a system-level design summary for SP formulation that includes novel structuring functions identified for non-wheat flours.

Acknowledgements

I am very grateful to the Riddet Institute (a New Zealand Centre of Research Excellence funded by the New Zealand Tertiary Education Commission), which contributed a PhD studentship and travel awards for this study. Thank you to my supervisors, Richard H. Archer and Matt Golding, for your patient support, and to Charles Brennan for your supervision at the project start. I also thank the TI Food and Nutrition group (Zeist, The Netherlands) for hosting me on a working visit funded by an Education New Zealand Postgraduate Study Abroad Award. For practical help, thanks to Andrew McNaughton (Otago Centre for Confocal Microscopy, University of Otago) for microtomography setup, and Elaine Booker (Massey Veterinary school) for carrying out cryo-sectioning. Thanks also for helpful discussions and generous sharing of information to Kjeld van Bommel at TNO, The Netherlands and Jeff Lipton at Cornell University (3D printing of food materials), to M. Doube, T. Shea and J.D Russ (structure analysis), and to Tuoc Trinh for introducing me to rheology. The Massey Food Technology support staff also deserve a big thank-you for their practical and cheerful support.

This work is dedicated to my parents, Maria and Jan Wegrzyn, who provided financial support for thinking and writing.

Table of Contents

Additionally, bound into this thesis is a copy of Wegrzyn, T. F., Golding, M., & Archer, R. H. (2012). Food Layered Manufacture: A new process for constructing solid foods (Trends in Food Science and Technology, 27, 66-72), which was produced as part of this study. Video files of batters prepared in the study are accessible on the CD in the pocket attached to the back cover, as are permissions for images in the text sourced from other publications.

List of Tables

List of Illustrations

Chapter One. Introduction

1.1 The study context: the Food-Inks 3D Printer project

The research for this PhD is part of a 'Food-Inks 3D printer' project. The project aim is to develop a prototype product for a consumer-customised food item produced by a new structuring process for solid and gelled foods. The new process applies Additive Manufacturing (commonly known as 3D printing) to fabricate food items, using a point-of-sale extrusion-based 3D printer to embed a recognisable image chosen by the customer within the food item. The project plan encompasses the design of equipment hardware, colour-metering software, base material formulation, and colour-matching of the source image to the food material. The combination of base material formulation with the colouring process is the Food-Inks part of the project. The base structuring material, in the form of a fluid or paste (*Food-Ink*), is mixed with food dyes to produce colour-matched *voxels* (3D image pixels). The first prototype product for design is a bread- or cake-like food (termed *sponge product* in this study) for point-of-sale fabrication. The deposited sponge product Food-Ink, formed of multiple layers of deposited voxels, expands and sets during an independent (non-printer) microwave cooking step.

This chapter describes the Additive Manufacturing process as it applies to food materials, introduces structure development in sponge products, and discusses product design in relation to Food-Inks formulation, which is the topic of this study.

1.2 Additive manufacturing and its application to food fabrication

1.2.1 Nomenclature

In this thesis, Additive Manufacturing (AM) is the generic *process*, various manufacturing methods used to implement the process are *technologies,* and the use of a particular technology to fabricate an end product is an *application*. Particular applications of the process targeted at specific market segments are *product concepts*, and may only exist at the conceptual stage. Mass-customisation refers to the fabrication of personalised items (individualised fabrication) (Kaplan & Haenlein, 2006). The use of AM (sometimes called Layered Manufacture) to produce food items is termed *Food Layered Manufacture* (FLM) (Wegrzyn, Golding, & Archer, 2012) to remove any confusion with the manufacture of food additives.

1.2.2 Use of the Additive Manufacturing process for fabrication of food items

Based on initial research carried out as part of this study, Wegrzyn, Golding & Archer (2012) published the first review of FLM concepts, technologies and example applications. A copy of the review is bound in at the end of the thesis. The review content remains topical, and is briefly summarised and updated in this section. More recent FLM examples not described in the review are marked by an asterisk (*).

The formal definition of the AM process is "joining materials to make objects from 3D model data, layer by layer" (ASTM International, 2012). Commonly-used non-technical terms for AM include *rapid prototyping* and *3D printing*. The desired 3D object form is sliced digitally into a template made of thin sequential layers. This slice template controls robotic deposition of material layers along the XYZ-axis,

from the bottom up. Deposited layers must maintain their form until the structure is set into a continuous solid or gelled object. Fusion of the deposited material with previous layers may occur layer by layer during deposition, or in a separate post-deposition step that fuses the whole object. AM enables fabrication of novel structures unachievable by conventional non-food manufacturing processes. These include variable material composition within an object (e.g. metal alloys, composites), production of internal cavities within a solid object, and the control of object structure at multiple scales.

The AM process is applicable to a broad range of manufacturing technologies and materials. AM technologies most suited to FLM are described with examples. 1) Heat-sintering of the surface layer of a sinterable powder is followed by deposition of a subsequent powder layer. It was applied to sinter complex shapes from table sugar crystals or sugar-rich powders (e.g. Gray, 2010; The CandyFab Project, 2008). 2) Photo-curing at the surface of a liquid is followed by covering the shaped surface with another layer of liquid. It was applied to form solid writing at micrometre scale within a transparent solution of uncooked egg white, using highly-directed laser heating to set the egg protein to an opaque white aggregate (TNO Food Processing group, The Netherlands, K. van Bommel, pers. comm.*). 3) Powder layers are bound together by an overprinted layer of liquid binder that may vary spatially in composition (*3DP™*). This technology is applied commercially to produce small and large customised shapes by overprinting sugar crystals with water and coloured dyes, with fusion of the printed structure on drying, and excess powder removed after fusion (The Sugar Lab, 2013*). 4) Low-pressure extrusion uses a syringe pump (or inkjet print head) to deliver a continuous thread (or separate drops) of a liquid or paste. The printed material is melted for deposition, then resets at room temperature once deposited (*hot-melt extrusion*). This technology was used in the design of FLM equipment and formulations for customised shaping of chocolate melt in the 'ChocALM' project (Causer, 2009). 5) Low-pressure extrusion technologies as in 4) are applied to extrude a fluid or biopolymer solution at room temperature, with post-deposition setting dependent on chemical reactions, biopolymer crosslinking, or phase transformations which take place on cooking or refrigeration (*extrusion-based AM*). Lipton et al. (2010) applied this technology to shape protein pastes stabilised by transglutaminase into complex structures, and to embed a two-colour image into cookie dough, before setting the formed items by cooking. 6) In *Layered Object Manufacture* pre-cast material sheets cut individually to form the object layers are then fused into a cohesive solid by laminating the stacked layers with a binder solution.

These potential FLM technologies may be used together or in combination with non-AM technologies. As a non-food example in *biofabrication* (the formation of artificial cell tissues by the AM process), electro-spinning of supporting fibres was combined with cell inkjet printing in the same build to strengthen the formed tissue (Malda et al., 2013*). Additionally, the deposition of a fluid thread may be stabilised by the use of moulds to contain spread of the deposited material.

FLM has the potential to utilise novel food materials. For example, the 'Insect au gratin' design project formed complex lacework objects by extrusion-based AM of high-protein insect powders added to icing or soft cheese (Soares et al., 2011); while Cohen et al. (2009) formed gelatin and xanthan

solutions together using a twin-head extrusion-based AM system, to produce mixed gels that ranged in sensory texture from smooth and uncohesive to granular and strongly cohesive. FLM enables consumer-controlled design of colour, flavour and structure in food items. With the appropriate nutritional *materials sets*, FLM could be used to fabricate food items designed to meet the dietary needs of a particular individual (*personalised nutrition*).

In AM, object build time increases with increasing resolution of the food structure. Co-development of suitable materials sets is an essential part of FLM equipment design. FLM formulations must provide greater control of structure development than formulations for conventional manufacture of solid and gelled foods. FLM is best suited to consumer-customisation of novel high-value low-volume food items that include individualised design input from the consumer. Section 1.4.1 discusses formulation design for FLM in more detail.

1.3 Process conditions

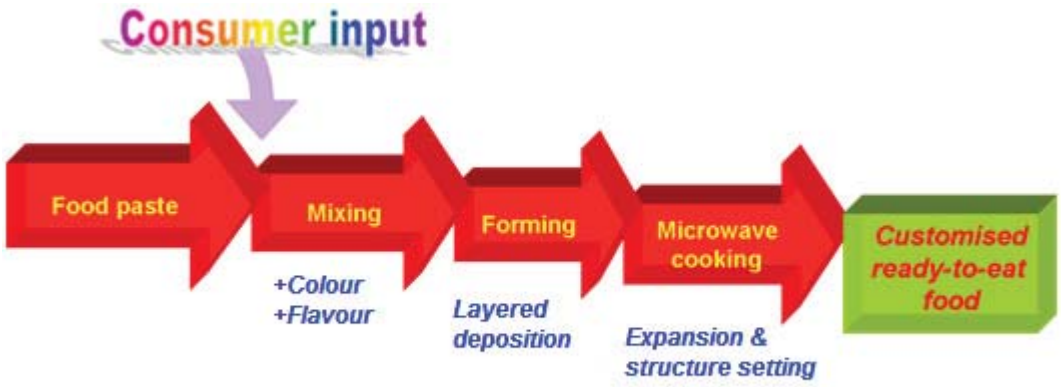

Figure 1.1 Steps in Food-Inks 3D printing to produce a point-of-sale food item containing an embedded 3D image. Consumer input is in the form of uploaded image (+ texture, + flavour in later design iterations).

1.3.1 The Food-Inks 3D printer project

The project aim is to develop a prototype product for a consumer-customised food item carrying an embedded full-colour image. After deposition of colour-matched image voxels in a thread of structure-forming fluid using extrusion-based AM, the food item form is set or cooked, to deliver a ready-to-eat food within a time period compatible with point-of-sale fabrication, e.g. a pizza parlour item. The first prototype product is 'a bread-or cake-like non-sweet food, formed from a pipeable starch-based paste and cooked to an expanded structure in a post deposition rapid cooking step'. The preliminary process design outline developed for this study is presented in Appendix B. Fig. 1.1 outlines the steps in printing using the Food-Inks 3D printer, including a post-deposition microwave cooking step to set structure in the bread- or cake-like food (sponge product, SP).

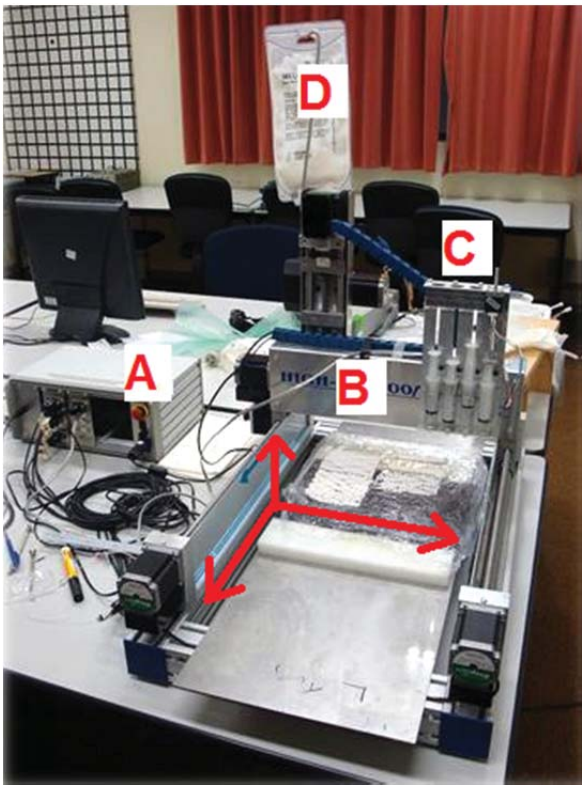

Figure 1.2 The first prototype equipment setup for the Food-Inks 3D printer. A) Digital control system for the XYZ-robot and 4-colour dye-dosing. B) Moveable robotic arm holding C) dye dispenser system with syringes controlled by low-volume stepper motors. B) is able to move along the direction of the arrows. Attached to a post is D), a sterile pouch containing uncoloured Food-Ink. Below the pouch, but not visible, is a fixed peristaltic pump that controls the flow of Food-Ink along a tubing line from the pouch to the robotic arm at B).

According to Ulrich & Eppinger (2011b) the Food-Inks 3D printer project is a *technology-push* design project for which the driver is commercialisation of a new technology. Hadiyanto considers the situation when both technology and product are innovative as the most challenging for process design (Hadiyanto, 2007). In many food products, small alterations to ingredient proportions or to physical manipulation of a formulation can markedly affect product quality (Ubbink, Burbidge, & Mezzenga, 2008). Food product design is a *process-intensive* product design task: that is, the product and process must be developed in tandem (Earle & Earle, 2009b; Ulrich & Eppinger, 2011b).

1.3.1.1 Food-Inks 3D Printer setup

The first prototype of the Food-Inks 3D printer equipment (Fig. 1.2) had an XYZ-robotic arm for fluid delivery, with 18 mm i.d. silicon tubing attached to a controllable peristaltic pump. The formation of coloured voxels was envisaged as using a static mixer to mix small doses of dye from a four-colour dye dispenser directly into a continuous thread of uncoloured food fluid. Pumping trials were carried out with a model Food-Ink fluid of xanthan-rice flour (Fig. 1.3). Note the waviness in of the deposited thread, which is due to random fluid oscillation during deposition of viscous fluid threads under piping flow, as described by Lipton, Boban, Hiller & Lipson (2010).

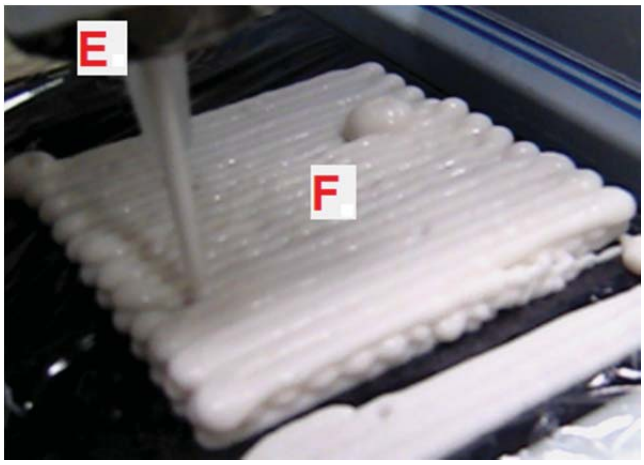

Figure 1.3 Deposition of a model xanthan-rice flour paste as a continuous thread, using the first iteration of the Food-Inks 3D printer equipment set-up. Mixing of dyes with the paste is planned to take place in a Kenics static mixerat E) (shown here with internal mixing elements removed). The thread is being deposited layer by layer (F), but in the absence of dye addition and mixing.

1.3.1.2 Food-Ink colour-matching to image pixels

The aim of the Food-Inks 3D printer application is to deposit discrete voxels within a continuous fluid thread in a way that forms an embedded image after deposition of consecutive layers. Crucial to successful printing is 1) effective micro-mixing of high-viscosity structured Food-Ink fluids with dye and flavour, and 2) delivery of an ordered set of voxels in stable layers (upper voxel volume initially set at 0.27 mL; Appendix B). The mixing system chosen for the first conceptual configuration of the Food-Inks 3D printer was a static mixer, which mixes two (or more) fluid streams by slicing and recombining the fluid flow in a fixed geometry placed along the flow path.

Figure 1.4 Dye addition to a standard cake batter to evaluate the effect of cooking on product colour (image courtesy of S. Kim).

The project included a study on colour-matching between image and food image. Fig. 1.4 shows cooked samples of a sponge cake formulation to which dyes were added before cooking to examine the

effect of cooking on colour-matching to the source image (Kim, 2015; Kim, Golding, & Archer, 2012). A joint study outline (Appendix C) was developed with the aim of modelling the influence of base material, dye type, fluid mass ratios and fluid viscosity ratios on mixing Food-Inks with colour. Only an initial investigation was carried out on methods to quantify mixing in coloured flows, as the test mixing rig designed for this study was ineffective at delivering reproducible pumping rates.

1.3.2 Microwave cooking

The microwave cooking step to set SP Food-Ink structure is independent of the technology used in the Food-Inks 3D printer. This section reviews fundamentals of the microwave cooking process. Heat transfer in microwave cooking of SPs differs to that under steaming or baking, in which energy is transferred to the dough/batter by infrared irradiation and by heat transfer from heated air surrounding the item. Microwave cooking uses electromagnetic energy at a frequency which modulates the polarity of dielectric materials. The most common frequency for domestic microwave ovens is 2450 Hz, while commercial units generally use 1450 Hz (Mudgett, 1986). The rate of microwave heating within a food is determined by (Mudgett, 1986; Sakiyan, Şumnu, Sahin, & Meda, 2007; Shukla & Anantheswaran, 2001):

- Bulk dielectric properties of the food item
- Microwave penetration depth
- Oven geometry
- Food item geometry.

The amount of microwave energy absorbed by a substance is related to material bulk density by:

$$P_V = \frac{\rho C_P \, \Delta T}{\Delta t}$$

where P_V is power absorbed per unit volume, ρ is density, C_{P} is specific heat capacity, ΔT is temperature rise and Δt is cooking time, under conditions of no heat exchange with the surroundings, and assuming the substance has a constant specific heat capacity (Schiffmann (2005), quoted in Megahey, McMinn, & Magee (2005)).

During cooking, microwave energy penetrates directly into the food interior (Zhang & Datta, 2006) causing agitation in dipolar and ionisable molecules. Agitated molecules transfer some of the absorbed energy to adjacent molecules through kinetic action (Mudgett, 1986; Ryynänen, 1995). The bulk response of a material to microwave heating can be quantified using three parameters: *dielectric constant* (ε'), the capacity of the material to store electromagnetic radiation; *dielectric loss factor* (ε''), the capacity to release stored energy as heat; and *penetration depth*, a measure of the distance into the material that electromagnetic energy penetrates before reduction to $1/e$ of initial intensity (Ndife, Şumnu, & Bayindirli, 1998). Water is a dipolar molecule, and salts and organic acids dissociate into ionic molecules that migrate within an electromagnetic field. The moisture and salt content and the pH-driven dissociation of ionic molecules all markedly influence heating rate under microwave cooking (Chin, Campbell, & Thompson, 2005). The expansion of SP foams during cooking will also influence heating rate, as penetration depth increases with decreasing material density.

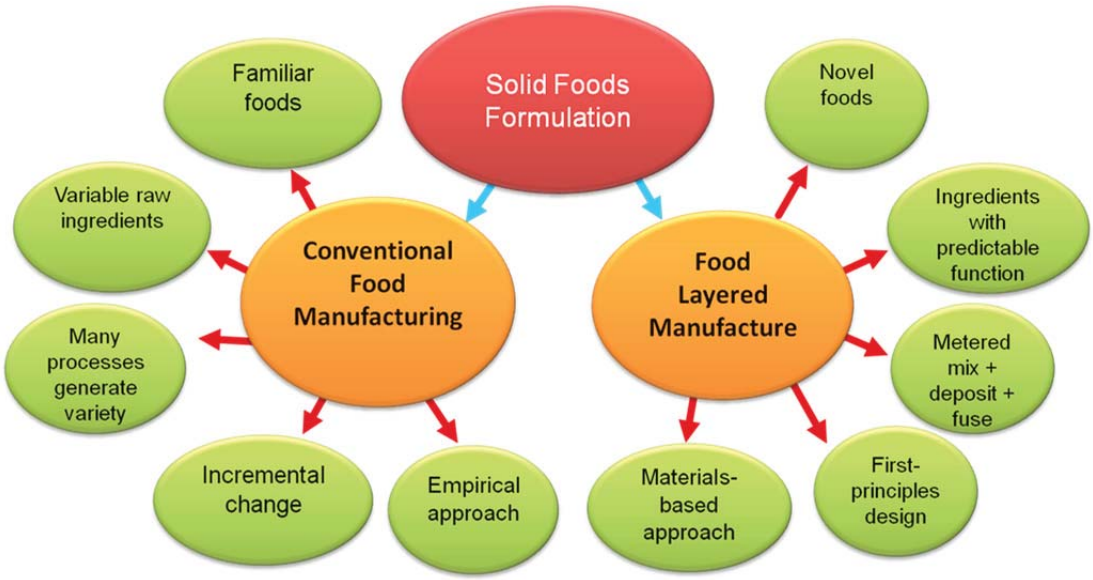

Figure 1.5 Comparison of formulation design of solid foods for conventional food manufacturing and for Food Layered Manufacture.

1.4 The food product development process

In this study several product design tools were useful in framing the Food-Inks formulation design task: the generic design process outlined by Ulrich & Eppinger (2008); and chemical engineering process design tools used by Hadiyanto (2007) to identify design needs for small-bakery process optimisation. Other sources on the design process for food formulation were Earle & Earle (2009a), and Mascitelli (2011). Expositions on structure-function relationships of food ingredients also helped to direct the study (Aguilera & Lillford, 2008; Tolstoguzov, 2003, 2006).

This section describes stages in the design process: the creation of a design process roadmap (end-user needs, specifications for product quality factors, design task prioritisation); how the parts of the product function together (*product architecture*); development of tools to evaluate the design process (design specifications, test systems, competitor product benchmarking); and prototype development with cycles of product optimisation. The design process is not necessarily linear. As more information about the product system becomes available steps in the design process may be carried out concurrently or go through multiple cycles of modification.

1.4.1 Formulation design for Food Layered Manufacture

It is useful to examine formulation design for FLM of solid foods and for conventional food manufacturing. Fig. 1.5 compares the key features of each formulation approach as discussed in Wegrzyn et al. (2012). In conventional food manufacturing, the primary aims in formulation design are to optimise traditional food processes at an industrial scale, to modify formulations to meet new nutritional requirements (e.g. develop gluten-free products) and to reduce costs by substituting cheaper, functionally-equivalent ingredients. Rather than recreatinhg existing products manufactured at lower cost by conventional means (and inviting unfavourable comparisons), FLM products, especially first generation products, benefit from introducing novel food items to the consumer.

Taking breadmaking as an example, formulation design for conventional manufacturing is primarily a translation of production methods for manually-produced, local bread specialties to industrial scale. Many flavours and textures of wheat breads can be produced using only wheat flour, water, leaven and salt. Structural variety is generated by manipulating processing parameters, such as the degree of kneading or fermentation conditions. Milled wheat kernel (wheat flour) remains the primary multifunctional ingredient. Much of quality control in breadmaking, in the form of strategies to manage flour variability, occurs before the flour reaches industrial formulators. Strategies include wheat flour production, selective breeding, grain conditioning and flour blending: such management of ingredient variability is a significant cost in conventional food manufacturing (Morgan & Depp, 2008, p. 419).

As FLM limits food structuring operations to ingredient metering, mixing, deposition and fusion of deposited layers, process flows and formulation designs in conventional solid food manufacturing may require extensive redesign for FLM applications (Wegrzyn et al., 2012). FLM materials sets must also be highly-standardised and perform consistently in a particular FLM application (Wegrzyn et al., 2012). The complexity and variability of plant- and animal-derived food materials make this development of standardised materials sets for FLM challenging. In biofabrication, between-batch variability of *hydrogels* (biopolymers such as alginate and gelatin used as gel-forming carrier solutions for extrusion-based biofabrication) requires frequent recalibration of print conditions (Tessmar, Brandl, & Gopferich, 2009), while there are no standardised testing protocols or flow models to determine hydrogel functionality on extrusion and structure setting (Malda et al., 2013). These technical hurdles need to be addressed in the design of materials sets for extrusion-based FLM applications such as the Food-Inks 3D printer.

1.4.2 The product design process

This section describes the steps in Food-Inks formulation design approach, based primarily on components of the generic product design process outlined by Ulrich & Eppinger (U&E) (Ulrich & Eppinger, 2011b); and the chemical engineering-based approach used in the thesis of Hadiyanto (HD), who applied the Delft Design Matrix process approach to optimise decision-making models for multi-item baking in a small-scale bakery (Hadiyanto, 2007).

1.4.2.1 Components of voxel printing in the Food-Inks 3D printing application

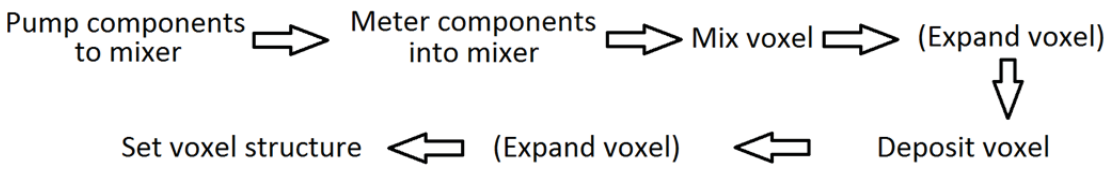

Figure 1.6 Schematic for Food-Ink voxel production in the Food-Inks 3D printer application. Steps in brackets may be optional.

Fig. 1.6 is a schematic of the stages in voxel formation for the Food-Inks 3D printing application. The flow properties of the Food-Ink must enable controllable piping, mixing, deposition and structure formation before setting. The voxel is coloured by metered dye addition in the mixer, and delivered on

deposition to the correct position without voxel distortion or between-voxel mixing. The relative placement of voxels must be maintained during any post-deposition events (e.g. slumping, post-deposition voxel expansion). For this study, the Food-Inks design target is a SP formulation for a point-of-sale, bread- or cake-like food carrying an embedded image: voxels will therefore undergo an additional expansion step between deposition and structure setting.

1.4.2.2 Initial boundary setting for the SP Food-Inks design task

The first steps in the HD design approach are to identify relevant existing information, establish boundaries to the design task, and set appropriate *design criteria* (HD thesis, Chap. 2). The equivalent step in the U&E process is to identify *end-user/process needs*. A preliminary food product development outline created at the start of the study (see Appendix B) forms the basis of a comprehensive list of end-user/process needs for the design of a SP Food-Ink (Table 1.1 column 1, over page). These are broken down in column 2 into *quality factors* (HD), discrete design components that contribute to individual needs (Wibowo & Ng Ka, 2001, quoted in Chap. 2 of HD). Quality factors can be aligned with steps along the process flow (Table 1.2, over page). Flexibility is retained in the design process by not specifying processing operations at this stage (HD thesis, Chap. 2).

1.4.2.3 Design task prioritisation

Not all quality factors may be targeted in the development of a prototype product, while some tasks may be too complex to execute in a single development cycle. To prioritise individual design tasks for the overall project, U&E rank the end-user/process needs (Ulrich & Eppinger, 2008), while HD gives priority to steps aligned with the greatest number of quality factors (HD thesis, Chap. 2). The importance of controlling voxel shape and position from the mixing step onwards is evident on examining the quality factors in Table 1.1. For a SP Food-Ink, the expansion and phase transformation on cooking must not compromise voxel positioning. In Table 1.2 the process steps associated with the most quality factors are 'Fractionate standardised materials sets' and 'Microwave cooking'. As the first refers to optimisation of a finalised SP Food-Ink formulation choice, the step 'Microwave cooking' becomes the primary design task, in line with Hadiyanto's evaluation of the baking process as the main control point for bakery process design (HD thesis, Chap. 2).

1.4.2.1 Design specifications: measures of prototype success

In U&E, design specifications are developed which "spell out in precise, measureable detail what the product has to do". The specification should be concrete and measurable (Ulrich & Eppinger, 2011b), and may define limits of acceptability (Earle & Earle, 2009b). These specifications are termed product *quality standards* in the food industry (Earle & Earle, 2009b).

The key metric for the Food-Inks 3D printer project is how closely the printed, set food product matches the source image. Preliminary metrics were assigned in column 3 of Table 1.1 to listed quality factors. Metrics with an asterisk (*) require interaction with the Food-Inks 3D printer (or suitable test equivalent) to assign specification values. Some formulation metrics are self-evident, and some readily

Table 1.1 Preliminary design requirements for Food-Ink formulations used to produce a point-of-sale bread- or cake-like food carrying an embedded colour image (first Food-Ink prototype). *Metrics that require Food-Inks 3D printer equipment for testing.

End-user/process need	Quality factor	Preliminary metric/specification
Deposit and maintain voxels in multiple layers on printing, to deliver embedded image	Correct voxel shape	*0.27 mL voxel size target
		Image analysis of product slices
	Structure forms rapidly	Appreciable structure within 5 s?
	Structural strength for additional layers	Slumping tests?
		*Printed and set within 8 min
Maintain voxel shape and position on microwave cooking	Controllable expansion	
	Predictable structure setting	
	Bread- or cake-like product	Standard mechanical tests for SP texture?
Pipeable at low pressure with rapid delivery	Controllable flow	*
	Acceptable print time	*Prints 200-600 mL/min for A5 size
Mixable with dyes, flavours, and other pastes	Micro-metered mixing with colour and flavour in liquid, paste or solid form	*0.27 mL voxel size target
	Uncoloured and with neutral flavor	Colour quantified by suitable measuring equipment, flavor by sensory testing
Meets consumer needs	Correct voxel shape and position	Image analysis of product slices
	Bread- or cake-like product	Standard consumer sensory tests for SPs?
	Acceptable print time	*Printed and set within 8 min
	Meets food safety standards	Appropriate industry microbiological tests
	Affordable	Food industry costing models
Ingredient pastes and powders storable for up to 6 months	Meets food safety standards	Appropriate industry microbiological tests
	Retains ingredient function	Test piping and cooking
Suitable for point-of-sale production	Acceptable print time	*Printed and set within 8 min
	Surface area 210 x 148 mm (A5)	
	Meets food safety standards	Appropriate industry microbiological tests
	Affordable	Food industry costing models

Table 1.2 Alignment of stages along the process flow of the Food-Inks 3D printing application with formulation quality factors listed in Table 1.1. [Events in square brackets are optional]. [a]Water may be added to rehydrate an ingredient; and sponge product formulations may be aerated during voxel formation and deposition.

	Raw materials	**Fractionate standardised materials sets**	**Store materials sets**	**Start printer flow**	**Mix in colour, flavour, [water, gas][a]**	**Form embedded image**	**Microwave cooking**	**Cool**	**Pack-age**	**Point-of-sale**
Actor space	Ingredient suppliers			User interaction on printing			User interaction on structure setting	User interaction post-cooking		Consumers
Formulation quality factor		Controllable flow Bread- or cake-like texture Controllable structure setting Meets food safety standards	Meets food safety standards Retains ingredient function	Controllable flow	Controllable flow Acceptable print time Micro-metered mixing	Correct voxel position Rapid structure reformation after deposition Able to support additional layers	Controlled expansion Controlled structure setting Correct voxel position Bread- or cake-like texture			Correct voxel position Bread- or cake-like product Acceptable print time Meets food safety standards Affordable
Time period		< 1 month	3-6 months	5 min	8 min					
Temperature range			-20 °C to ambient	4 °C to ambient			Ambient to < 120 °C	100 °C to 20-50 °C	20-50 °C	20-40 °C
Phases and transformations		Liquid, solid-liquid dispersion, powder Liquid → powder			Liquid-solid dispersion [→ liquid-solid-gas foam] [Powder→ liquid-solid dispersion]		Liquid-solid-gas foam → Solid-air foam	Solid-air foam		

measured by existing industrial tests (e.g. food microbiological testing protocols). Others must be tailored to the printer requirements, but can be tested independently of printer hardware (e.g. capacity to support subsequent layers). Specifications and suitable tests for Food-Ink formulations are examined further in Chaps. 2 & 3 and Appendix D.

1.4.3 Product architecture: a scheme of design element interactions

Once a process analysis has defined end-product specifications, the formulation design elements must be identified. U&E state that a product design can be split into *physical elements*, the "…parts, components, and subassemblies that ultimately implement the product's function", and *functional elements*, "…individual operations and transformations that contribute to the overall performance of the product" (Ulrich & Eppinger, 2011a). The *product architecture* describes how functional and physical elements are organised into *chunks* that interact to carry out the overall product function. Chunks optimally "…implement one or a few functions in their entirety", and interactions between chunks are "generally fundamental to the primary functions of the product" (U&E, pp. 184-185). An *integral architecture* bundles many product operations in a few chunks; in a *modular architecture*, one chunk generally performs one operation/transformation (Ulrich & Eppinger, 2011a). Products with an integral design may suffer from poorly thought-out interactions between chunks, necessitating extensive redesign in product iterations. Modular designs with carefully considered interactions enable greater design flexibility during the product development cycle (Stoll, 1999).

If we evaluate food product formulations in these design terms (i.e. the formulation is the product under design) the ingredient components form the "parts, components and sub-assemblies" (physical elements). Structuring operations/transformations to produce the food item generated by ingredient interactions represent the functional elements of the formulation design. For example, a cake batter begins expansion when CO_2 dissolved in the liquid phase transfers into the gas phase in existing bubbles; therefore, the interaction between leavening agents and other batter components to produce CO_2 gas for transfer into bubbles can be classed as a functional element of the formulation design. It could be described by 'Activate volatile expansion agent'; and be linked to more than one stage in baking e.g. 'Activate before cooking' and 'Activate on heating', as occurs in double-acting baking powder. In comparison, structuring operations performed mechanically by an external agent (such as mixing and heating) can be classed as a type of 'user interaction' with the design target (formulation) to produce the end-product (= food item), in the same way that a person using a standard paper printer loads paper into the paper tray.

The functionality of a multi-component formulation is highly dependent on interactions between the molecular components of ingredients (Tolstoguzov, 2003), with structure development in conventional solid food formulations often determined by a few multi-functional ingredients. The components of an integral ingredient chunk can have many interactions with each other or with the components of other ingredients. Wheat flour in breadmaking (composed primarily of starch granules, protein, lipids and non-starch polysaccharides) is a good example. Specific components contribute to dough viscoelastic properties, bubble interface properties, the rate of product expansion, etc. The chunk components may have competing effects. For example, non-polar lipids (surface-active molecules that

destabilise the gas-liquid interface of bread dough bubbles) appear in the same flour sample as polar lipid fractions with interface-stabilising properties (Sroan & MacRitchie, 2009). A useful strategy to meet the requirement for highly-standardised FLM materials sets may be to deconstruct SP formulations to generate (novel) modular architectures in place of the integral architecture of wheat-flour based SP formulations.

1.4.4 Predictive modelling of prototype effectiveness

An important part of the design process is to identify appropriate tests to predict prototype effectiveness where there are no suitable existing metrics to evaluate the quality factor(s) to be tested. During cycles of product development, prototypes are tested to see if performance falls within the constraints defined by design specifications.

1.4.4.1 Test systems for competitor products and design prototypes

A design prototype or a competitor product may be evaluated in tests and models that apply to only part of the product. Formulation prototypes can then be assessed indirectly by applying flow behaviour tests and comparing performance to specifications of the appropriate flow model. This removes the need to test each formulation in the Food-Inks 3D printer (which may itself be under cycles of development). Development and validation of such models is part of the product development process, and they remain useful over multiple cycles of product development.

According to Hadiyanto, in food process design "…ready-to-use first-principle relationships on food quality and their transformations are scarce. The major part of the available information is data driven and translated into expert knowledge based on rules or translated into (statistical) correlations… An integral prediction of all phenomena in food products requires a systems approach investigating how a multitude of external variables affect a single phenomenon, and subsequently predicting quality by connecting all relevant variables and phenomena in mathematical (quantitative or semi quantitative) models" (Hadiyanto, 2007, p. 14). The chemical engineering term *first-principle* refers to events at the molecular level and to fundamental properties of the system such as heat capacity (Hill, 2009); while *transformation* refers to phase change (e.g. from liquid to solid) or a change in chemical composition. Most food process models are semi-empirical, or tailored to specific applications, rather than based on fundamental physical properties and phase changes.

The solution space for FLM sits closer to this chemical engineering design approach than to conventional food formulation. The need for highly predictable (and therefore controllable) printing and setting properties for Food-Ink formulations means that formulation behaviour must be tailored to a higher standard than generally found in the food industry. The complexity of interactions contributing to SP structure development suggests that a *systems approach* to evaluate critical attributes across the whole system under examination is essential. This approach was taken in this study in choosing appropriate functional tests for flow and setting behaviour of SP-based Food-Inks and in deconstructing SP formulations for modular redesign.

1.4.5 Competitor product benchmarking

Information gathering in the early stages of product design provides knowledge about patents,

published literature and existing (competitor) products (Hadiyanto, 2007, Chap. 2,; Ulrich & Eppinger, 2011c). Competitor benchmarking evaluates existing products by ranking the attributes of an existing product against the design specifications. After function and component analysis to deconstruct the design features of the benchmarked product, design solutions may be *reverse engineered* (functionally reconstructed without necessarily duplicating the source product).

In this study the deconstruction of SP structure development included a comprehensive analysis of the relevant scientific information (excluding patents). Some bounds on the system were set by envisioning how existing SP formulations might interact with the Food-Inks 3D printer system. The rheological requirements of the Food-Inks 3D printer system excluded firm doughs, uncooked SP formulations which were sensitive to handling history, and formulations with a time-dependent requirement for structure development outside of the printing application time constraints. Examples of excluded formulations are viscoelastic bread dough, wheat flour–based formulations that develop gluten networks on pumping and standing, and foam-based formulations that change rapidly with time. Non-yeasted unsweetened non-wheat batter bread formulations which remain stable over extended period of standing, and which have the capacity to form a thread represent the best potential solution space for a SP Food-Ink.

The analysis also identified gaps in existing knowledge. Fundamental understanding in the scientific literature for structure development in SPs is based almost exclusively on wheat-based, Western-style baked products. A growing number of publications explore structuring alternatives in gluten-free bread and cake formulations and in Asian SPs. However, the information on structure development for non-wheat flour and non-baked SPs is very limited, and the process as described for wheat-based SPs remains the primary conceptual model. Bloksma (1990a; Bloksma) provides the best succinct model for events during structure development in baked wheat bread; while e.g. the baking technology publications of Cauvain & Young (2000a, 2006a, 2007b) detail extensive information for food technologists on ingredient component function and interactions in a range of baked wheat-flour SPs.

1.4.6 Methods for prototype optimisation

Once prototype development of the chosen product design begins, optimisation studies can fine-tune interactions between design chunks. Large numbers of formulation variations for testing in formulation development can be reduced to reasonable levels by choosing a valid sub-sampling strategy (Arteaga, Li-Chan, Vazquez-Arteaga, & Nakai, 1994). Preliminary experiments must identify the correct parameter limits for the various ingredients or processes before the full trial. The output data can be used to derive response surfaces as a way of visualising ingredient interactions (*response surface methodology*). A good example of this approach is the comprehensive study of Gan et al. (2007) to optimise sugar and coconut milk levels in a cassava cake formulation. Response surface analysis can also be applied to more fundamental research, e.g. to interpret ingredient interactions in a calorimetry study of cake formulation on heating (Kobylanski, Perez, & Pilosof, 2004).

Another type of formulation development (perhaps best described as ‘shotgun plus cycles of refinement, relying on formulator expertise’) does not apply formal experimental design. Instead, formulation variants, using best-guess ingredients, are evaluated in rounds of exhaustive testing for

functionality. Many ingredients are trialled together in early development, and selectively removed in later formulations to confirm those truly necessary for functionality. A good example of this approach is the academic study of Rakkar (2007) for gluten-free bread formulation design, which was supported by a commercial bakery and presumably incorporated expert knowledge in decision-making. This approach (which best represents industrial approaches to SP formulation) was surprisingly successful, finding a suitable formulation to meet all production and consumer requirements within 200 test bakes.

1.4.7 Design requirements for Food-Ink voxel formation

The Food-Inks 3D printer system has a limited range of mechanical structuring operations and needs standardised, predictable behaviour of Food-Inks during voxel formation and structure setting. Control of Food-Ink formulation flow properties before structure setting is essential for correct assembly and deposition of voxels, while control of expansion and setting of SP Food-Inks under microwave cooking is essential to retain the fidelity of the embedded image in the end-product. For highly-standardised behaviours in FLM formulations, ingredients in conventional SP formulations may be inappropriate, or may need to be fractionated for standardisation. Food-Ink flow properties and structure development before and after cooking in SPs must be re-evaluated for Food-Ink design.

Trying for a modular architecture in the design approach for FLM formulations may be more effective over time than empirical testing in the development of highly-standardised materials sets for FLM. Analysis of target Food-Ink formulations in terms of the U&E physical/functional element scheme provides a template for more flexible formulation design. It incorporates existing knowledge of ingredient function and molecular mechanisms in SP production, but is not limited by existing preconceptions. It is evident that the chunk 'wheat flour ingredient functions' needs to be deconstructed into smaller functional units to produce an effective SP Food-Ink formulation for the Food-Inks 3D printer application. Deconstruction of SP formulation behaviour also benefits from taking a systems-based approach in defining the key functional elements in structure development, as ingredient component interactions are very complex.

1.5 Transitions and transformations in sponge products

As part of the deconstruction process, the next section examines existing knowledge on structure formation in SP food systems to identify potential design elements for SP formulations. Relationships between formulation composition and SP structure development need to be identified at the *macro* scale (item shape and size), the *meso* scale (foam organisation), and the *micro* scale (organisation of the composite non-gas phase). In this study, the term *baking* is limited to the description of conventional thermal cooking in a radiant energy oven, and the term *crumb* applies to the internal structure of baked and microwave-cooked SPs. The gas phase in SPs is present as *bubbles* in doughs/batters, and as interconnected *voids* continuous with the atmosphere in cooked SP foams.

1.5.1 Overview of structure development in sponge products

In structural terms SPs begin as bubble-containing, liquid-particulate-gas *closed-cell* foams (dough/batter) that expand on heating to produce an elastomeric *cellular solid* with an *open-cell* foam structure (Gibson & Ashby, 1997c; Scanlon & Zghal, 2001). Bubble populations in doughs and batters are

introduced by several different mechanisms (discussed in detail in section 4.3). Bubble expansion in the dough or batter is driven by primarily by degassing of CO_2 and water vapour into bubbles. Cellular organisation in many expanding foam systems has a self-similar (*self-scaling*) relation between components at differing scales (Gibson & Ashby, 1997c) (see Fig. 1.7), although each foam system has a minimum size below which bubbles become energetically unstable.

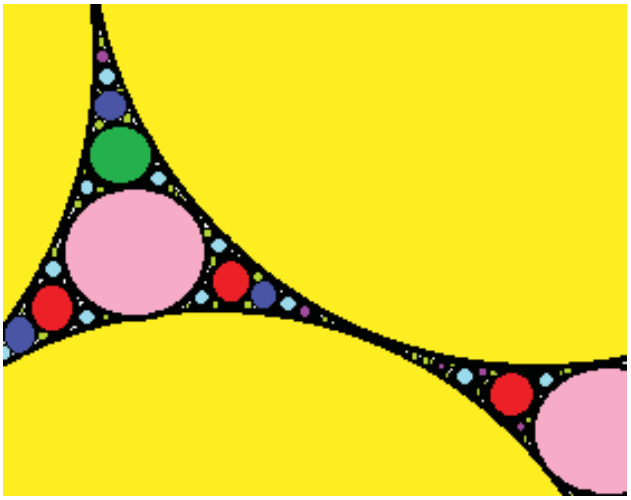

Figure 1.7 Schematic showing the self-scaling nature of bubble packing in a generic foam under continuous expansion.

Expansion stops when the dough/batter reaches a critical temperature at which the liquid-particulate fraction transitions to a solid material. Individual bubbles in the foam rupture during setting, forming an interconnected porous network and releasing heated gases and water vapour. The solid phase is a composite elastomeric gel, with separate starch and protein-rich domains. Bubble shapes formed at the time of solidification may be retained in the cooked products. For example, highly expanded polyhedral foam voids (typical of a foam in which the gas phase volume is great enough to induce bubble distortion) can be observed in wheat bread (Falcone et al., 2005; Shimiya & Nakamura, 1997), while Jaffa Cake structure is more typical of a foam in which bubbles retain a mostly spherical shape (Gibson & Ashby, 1997c). The dynamics of bubble disproportionation, coalescence and collapse are fundamental events in droplet systems, with similarity to events commonly described in food liquid-liquid emulsions.

1.5.2 Hierarchy of structure in sponge products

Specific features of SP structure (e.g. size and shape of cooked product; organisation of bubbles in dough/batter; domain organisation in the cooked solid) can be placed along a scale continuum ranging in size from the whole product down to the molecular scale. Structural features along the scale continuum can be organised into different *levels* to produce a *hierarchy* defined by observation (Allen, 2013). Fig. 1.8 (over page) illustrates a *hierarchy of structur*e for SPs as defined for this study. A complex transformation on cooking alters the attributes of these structural features.

At the first hierarchy level, *macrostructure* refers to the bulk physical features of the uncooked

dough/batter and the finished product. Measures of macrostructure include cooked product shape, size, porosity, bulk density, and bulk rheological measurements of the dough/batter or the cooked product. Mesostructure refers to the gas phase organisation within the liquid-particulate phase in doughs/batters, and within the open-cell solid phase in cooked products. Liu & Scanlon (2003) previously suggested a hierarchy of scale for wheat bread which partitioned voids arbitrarily into three sub-levels of large, medium and small size, based on visual perception of product mesostructure. However, as a consequence of the self-similar nature of foamed systems SPs may display continuously increasing distributions for many physical attributes. In this study SP mesostructure (i.e. bubble/void organisation) is considered to form a single hierarchy level covering a broad length scale range that overlaps the length scale of the next level.

The next hierarchy level of *microstructure* refers to the organisation of the composite structure in the sponge product solid phase, which contains distinct biopolymer *domains.* Tolstoguzov (2006) considers that the low co-miscibility of biopolymers is primary to structure and texture development in foods. Poor miscibility may drive the partitioning of biopolymer mixtures into separate, more concentrated domains, leaving a low-concentration mixture behind. Observation of an apparently homogenous composite food solid or the liquid phase of a complex formulation by differential staining and/or at magnification is needed to characterise the next hierarchy level of domain *sub-structures.*

Sub-structures may help define the structural and functional properties of a domain. Taking the starch granule in SP formulations as an example of a biopolymer domain, granule sub-structures that formed during granule development in the plant include a coating which controls water uptake until a critical temperature is reached, an amylose region at the granule centre which is readily soluble during granule gelatinisation, and a less soluble amylopectin region closer to the granule exterior which helps to maintain the granule envelope structure during gelatinisation. The gelatinised granule forms an important physical component of the composite solid in cooked SP microstructure.

The final hierarchy level, *molecular organisation*, refers to molecules and molecular assemblies within a sub-structure that contribute to structure determination, e.g. interactions between wheat gluten proteins that stabilise the gluten network in dough. Note that dough/batter systems are much more dynamic and unstable at all hierarchy levels than cooked SPs, in which structure has been stabilised by transformation of the continuous liquid phase into an elastomeric biopolymer gel containing gelatinised granules. However, changes occurring at the molecular level after cooking may still alter the physical properties of the cooked product, for example, firming of SP texture on staling.

Mack & Becker (2013) described a hierarchy of time scale to characterise changes from the molecular level to the macrostructure level for structure formation events in breadmaking which sits alongside the hierarchy of structure described in this study.

1.5.3 Qualitative description of sponge product structure

Techniques commonly used to visualise SP microstructure include bright field and polarised light microscopy, electron microscopy (EM), confocal scanning laser microscopy, and computed x-ray tomography at meso- and micro-scale. SPs have fragile structures readily disrupted during sample preparation for microscopic analysis. In a high-resolution study of bread by light microscopy (Hug-Iten et

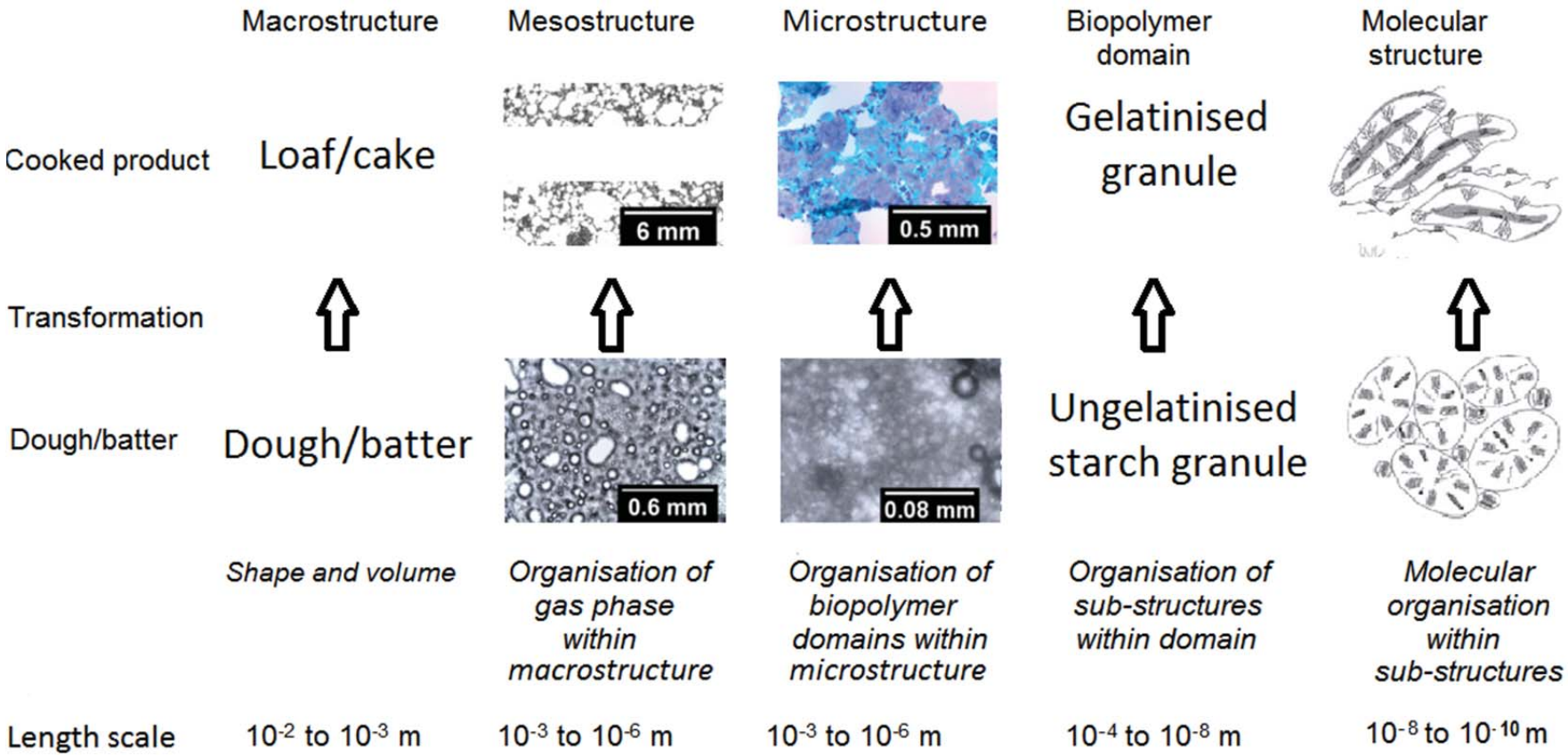

Figure 1.8 **Hierarchy of structure for sponge products, defining structural terms used in this study. Molecular structure images were sourced from Delcour et al. (2010). Other images were collected in this study.**

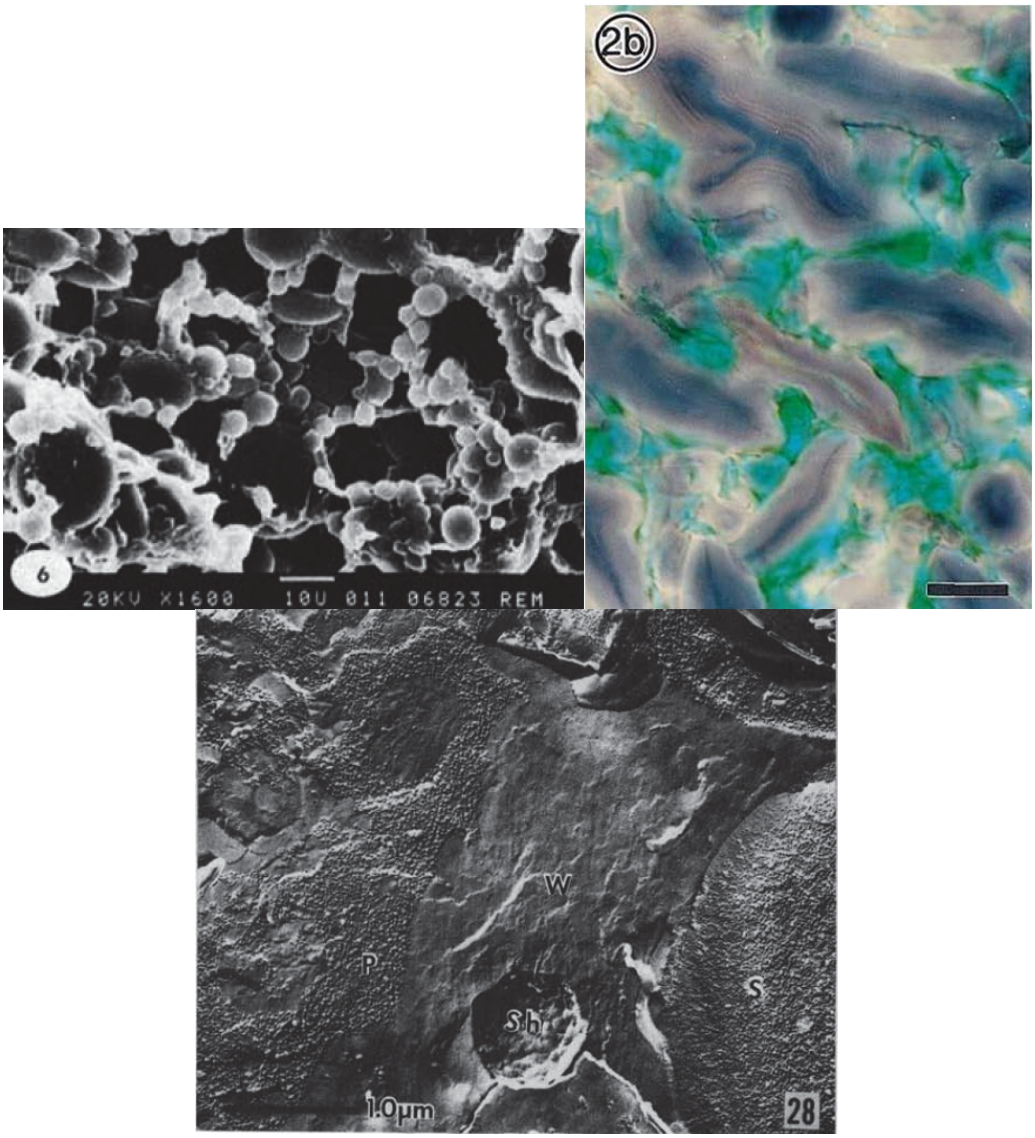

Figure 1.9 Microscopy analysis of sponge product structure. Top left: electron micrograph of wheat bread dough showing the positioning of wheat starch granules aligned in the thin layer between bubbles (image width, 200 µm). Reprinted from Pomeranz, Meyer & Seibel (1984). Top right: cryotome section of wheat bread crumb, stained for starch with iodide and counterstained with FastS Green (image width, 57 µm). Reprinted with permission from Hug-Iten et al. (1999), © 1999 Academic Press. Bottom: high-resolution freeze-fracture electron micrograph of bread crumb. S= starch granule, W= water, P= protein, Sb= solid fat body, (image width, 5 µm). Reprinted from Fretzdorff et al. (1982).

al., 1999), cryo-sectioning minimised structure breakdown, while minimal fixing and staining protocols avoided extensive leaching of soluble material such as amylose polymers from the sample (e.g. Fig. 1.9 top right). Starch granule images from this study can be compared with the empty centres of starch granules visualised in heavily-fixed material, as reported in Parkkonen, Heinonen, & Autio (1997). Although scanning electron microscopy is commonly applied to visualise SPs, sample structure often collapses during sample dehydration. Cryo-scanning EM (e.g. Fig. 1.9 top left; Gonzales Barron & Buteler (2008); Rojas et al., (2000)) and high-resolution freeze-fracture EM reduce artefacts of EM preparation

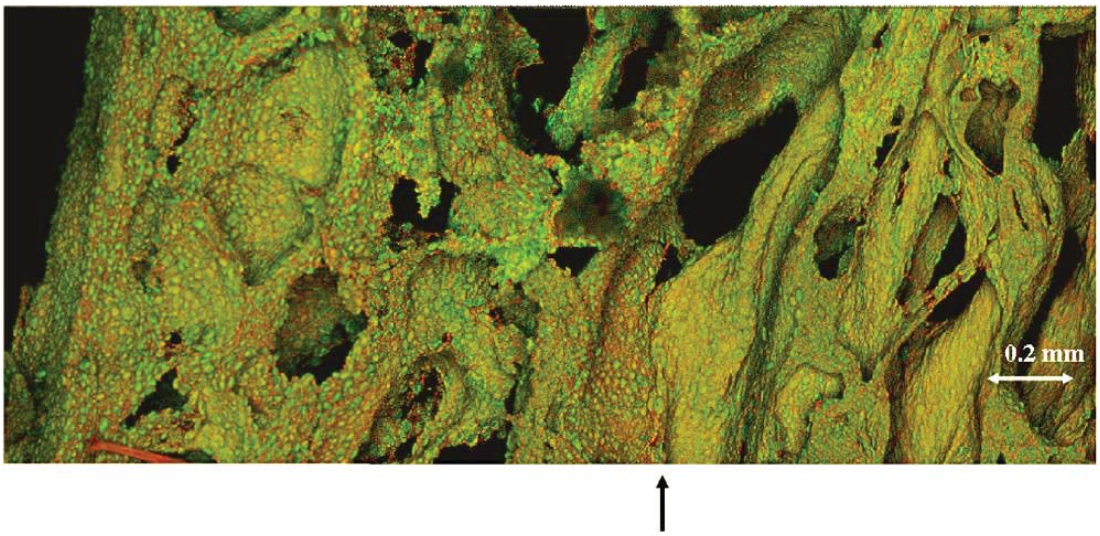

Figure 1.10 Mesostructure and microstructure of wheat bread, visualised by confocal scanning laser microscopy of dough baked with fluorescent dyes (starch is coloured green, and protein red). The arrow marks the transition from poorly hydrated crust at the left to more hydrated crumb at the right (image width 2.8 mm). Reprinted with permission from Primo-Martin, van Neuwenhuijzen, Hamer, & Van Vliet (2007), © 2006 Elsevier Ltd.

in SP samples - Fretzdorff, Bechtel & Pomeranz (1982) could distinguish separate domains of soluble protein, starch, fat and water in bread crumb using freeze-fracture EM (Fig. 1.9 bottom).

Confocal scanning laser microscopy maintains sample integrity better, as fluorescent dyes specific for ingredient fractions can be added into SP formulations before cooking, or diffused into cooked samples without fixation. CSLM generates a 3D image by overlaying images captured at multiple focal planes through a thickly-sectioned sample, disrupting the material less during preparation. Visualisation of both SP mesostructure and microstructure can be carried out on the same sample. Two predominant domains are evident in visualisation studies of SP microstructure (Fig. 1.9 top right & Fig. 1.10). A starch domain that fills much of the crumb microstructure is contained mostly within intact starch granule envelopes, with a portion of starch material evident outside granules. The starch domain is surrounded by an amorphous protein-rich biopolymer domain, which also contains non-starch polysaccharides (primarily arabinoxylans) which modulate wheat dough viscosity (e.g. Döring et al., 2015).

In the CSLM image of bread in Fig. 1.10, the crust (which undergoes setting earlier and at lower water concentration than the crumb) is more clearly separated into individual granules embedded in the protein-rich domain (Primo-Martin et al., 2007). Limiting water content in the crust limits granule gelatinisation (Pomeranz et al., 1984). Granules in the crumb are less evident, due to masking of the protein stain by extruded starch polymers. In the cryosectioned image of wheat-bread crumb in Fig. 1.9 right, extruded starch material (stained dark blue) can be seen fusing two granules together. The iodide stain differentiates between amylopectin polymers (stained brown/violet) that form the starch granule envelope and amylose polymers (stained blue) localised predominantly at the granule centre. Amylose and amylopectin biopolymers are considered mutually insoluble, despite amylopectin being a branched form of amylose (Kalichevsky & Ring, 1987). In Fig. 1.9 right, regions not stained with iodine are counter-

stained with a non-specific dye. This light blue counterstain does not differentiate between biopolymers or yeast cell fragments in the protein-rich domain. Thin green fibrils seen against a light blue background may be insoluble strands of gluten that contribute to wheat-bread crumb integrity.

This SP microstructure was first described as resembling *bricks and mortar* by Sandstedt, Schaumberg, & Fleming, (1954), quoted in Willhoft (1973) and was described as have separate, but bicontinuous, starch and protein polymer phases by Eliasson & Larsson (1993). While visualisation of meso- and microstructure using these methods provides insights into transformation events during structure development in SPs, the information is generally qualitative in nature.

1.5.4 Quantitative description of SP products

Crumb structure is most often reported qualitatively in studies of SPs, but may also be reported quantitatively. A qualitative evaluation may be enough when sensory quality for consumers is the target attribute for control. SP mesostructure can be recorded by capturing the cut product surface as a 2D image (photograph, digital scanned image or ink print of the product surface). Structural features in the images are quantified by manual or digital image analysis. Analysis of structural features apparent in the SP cut surface has been used to predict consumer rating of crumb structure (e.g.Angiolini & Collar, 2009; Gonzales-Barron & Butler, 2008; Lassoued, Delarue, Launay, & Michon, 2008), but the value for void size quantification is limited. Image resolution constrains the information content in a scanned image or photograph: Datta, Sahin, Şumnu, & Keskin (2007) report that scanner resolution of 300 dpi cannot resolve objects < 85 μm in size, while digital camera imaging is not useful for voids < 67 μm (Gonzales Barron & Buteler, 2008). Additionally, interpretation of a 3D structure from a 2D image of the cut surface generates errors and omissions (Gonzalez-Barron & Butler, 2006). Finally, there is no standardised methodology for image analysis, apart from the C-Cell system used in the baking industry (C-Cell, Warrington, UK) (Cauvain & Young, 2006f). As many studies do not have access to C-Cell equipment, optimisation of conditions for image acquisition and analysis must be developed independently for each study.

1.5.4.1 Methods to quantify SP mesostructure and microstructure

1.5.4.1.1 Microscopy analysis by sectioning

The traditional method to quantify features in a 3D object is to slice the object into thin sections for microscopic analysis, following a rigorous, statistically-valid sectioning and measurement process. This sectioning approach is termed stereology (Howard & Reed, 2005d; Russ, 2005b). In this study, the term object refers to the whole item under examination, while the term particle, in reference to digital image analysis only, refers to smaller structures embedded within the item. Point and grid counting of various structures within a thin section of the object can provide robust estimates of bulk properties such as particle volumes and interface surface areas (Howard & Reed, 2005a). Automated digital image analysis is often used, but is not as simple as it seems to apply. Human vision is much more adept at edge detection than machine vision and therefore better suited to segmentation of the section into discrete features (Russ, 2005b). A statistically-robust manual grid count with particle counts in the tens or hundreds may describe the sample more precisely than digital image analysis with counts in the

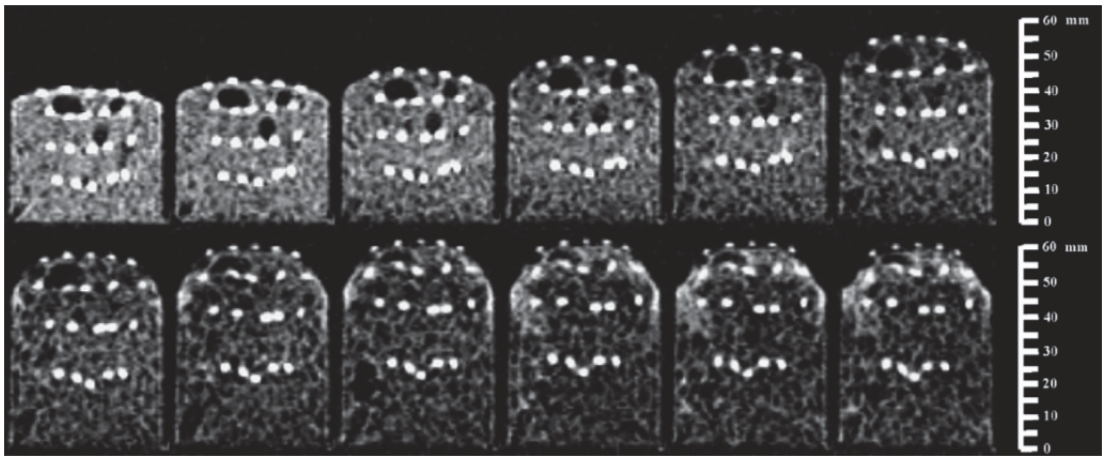

Figure 1.11 Magnetic Resonance Imaging of bread dough during baking, showing internal spatiotemporal movement of markers (bright points) during expansion and setting. Reprinted with permission from Wagner et al. (2008), © 2007 Elsevier Ltd.

thousands (Howard & Reed, 2005c). It is essential in stereological analysis to have uniform random sampling of the object and of consecutive sections, and an unbiased count of particles (Howard & Reed, 2005c). Small particles embedded in an object may be bisected only once or twice in the sectioning process, while large particles are sectioned many times. A procedure that results in an unbiased count must be applied to compensate for the greater proportion of area assigned to large particles.

1.5.4.1.2 3D reconstruction on x-ray computed tomography analysis

Adequate description of structural features in a complex interconnected network may require a more complete model of the system (Kroustrup & Gundersen, 2001). An effective non-destructive method to capture the 3D structure of porous materials is x-ray computed tomography (CT). Up to 1,000 autoradiography images at high resolution are taken of a sample rotating through the Z-axis. Visualisation of the material depends on the relative opacity of the solid phase to x-ray irradiation. The x-ray data is deconvoluted by image processing software to create a series of sections along the sample Z-axis. Together, the output stack of very thin sections can be reconstructed into a 3D image. CT analysis is non-destructive and can be carried out at different scales. At higher resolution, x-ray computed microtomography (μCT) is able to resolve structures as small as 5-20 μm in size.

The use of CT to visualise SP structure was first reported by Lim & Barigou (2004). CT also allows real-time monitoring of internal changes to mesostructure. Babin et al. (2006) examined changes in bubble populations during dough proving, and Falcone et al. (2005) described the anisotropic organisation of voids in cooked wheat bread. In an elegant experiment to identify structural changes during baking, Whitworth (2008) built a forced-air oven inside a CT scanner to follow expansion and setting in cakes, muffins and bread in situ.

Wagner, Quellec, Trystram, & Lucas (2008) also imaged dough in real-time during baking, but using Magnetic Resonance Imaging (Fig. 1.11), to correlate mesostructure development with temperature and pressure measurements at specific positions. Compared with structure acquisition by microscopic methods, the acquisition process by CT and Magnetic Resonance Imaging is more rapid, does not involve

sample treatments that may destroy delicate features, and provides a complete structure without the need to infer 3D structure from sectioned material. However, there are still challenges in quantitative measurement of complex highly-interconnected structures. The limitation for many researchers is lack of access to expensive or in-house software to deconvolute the organisation of complex porous materials. Appendix D discusses image analysis methods for SP structure analysis in detail.

1.5.5 Quantitative description of foamed and porous systems

The structure of SPs shares morphological features with other foamed and porous materials. Methodologies developed to quantify physical attributes in one such system may be applicable to others. Void size distribution in cooked SPs can be considered as self-scaling between 10^{-6} to 10^{-3} m (three orders of magnitude). This is due in part to the composite nature of the solid phase in the cooked products, in which bulky particles such as starch granules and cell wall fragments may expand into the smallest voids during transformation (cooking).

Quantitative descriptions of foamed material structure developed for porous systems include: measurement of solid-gas phase mesostructure in cancellous bone to estimate load-bearing capacity; analysis of channels in porous rocks to model the path of water movement; and quantification of bubbles trapped in lava rocks in order to reconstruct bubble formation and expansion events during lava degassing on depressurisation. This last is of interest to SP structure formation as, by analogy, volcanologists cannot directly study the molten lava (the rock equivalent of dough/batter) but must infer events in lava degassing from structures in the rock (cooked product equivalent). Note that many lava rocks are closed-cell rather than open-cell foams.

To aid in the interpretation of foam structure development during lava depressurisation Shea et al. (2010) derived models of bubble populations under varying conditions of bubble *nucleation* (formation) and expansion. Fig. 1.12 shows plots of bubble volume fraction and number density graphed against size which are diagnostic for dynamic events in bubble populations (Shea et al., 2010). A single stage of nucleation and bubble growth produces a lognormal distribution when volume fraction is plotted against bubble size. Unstable bubble populations develop volume fraction distributions that become skewed towards larger sizes (disproportionation), broaden and flatten (bubble collapse), or develop a bimodal distribution with a truncated larger peak (coalescence). Continuous or accelerating nucleation and growth results in distributions enriched for smaller bubbles, while multiple stages of nucleation and growth produce multimodal distributions. The general shape of plots of bubble number against size is also responsive to changing rates of gas–driven expansion.

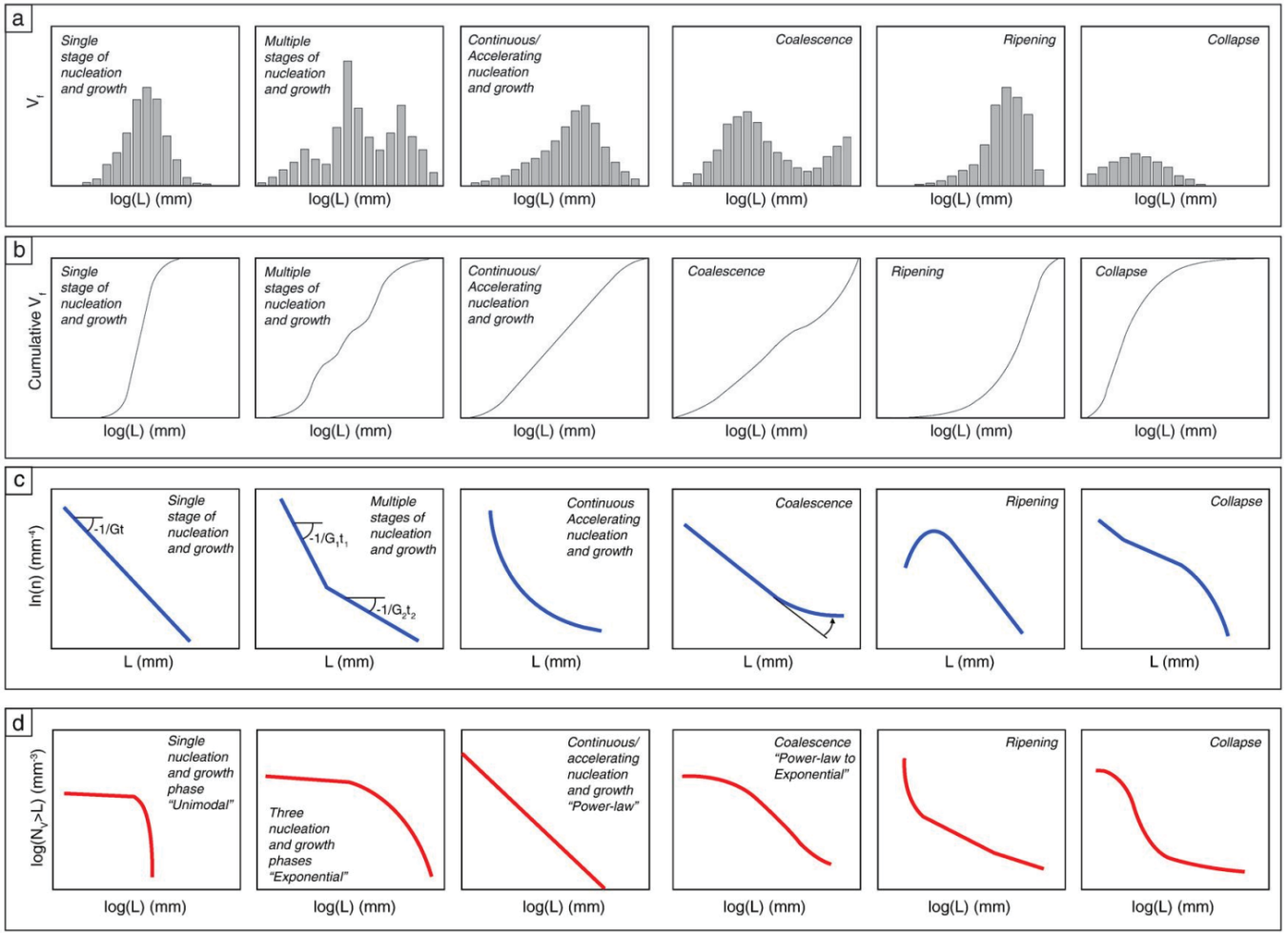

Figure 1.12 **Dynamic changes in bubble size and number density for model bubble populations undergoing nucleation and gas phase expansion under differing bubble stability conditions. a) volume fraction; b), cumulative volume fraction; c) number density; d) cumulative number density. G = growth rate, t = time. Reprinted with permission from Shea et al. (2010), copyright Elsevier, B.V.**

1.5.6 Structure characterisation by mechanical testing

Bourne (2002) differentiates between mechanical tests on foods designed to correlate with the sensory evaluation of product texture and those tests designed to describe rheological attributes of structure. This review deals only with mechanical testing to evaluate product structure. A foundation text on the physical and mechanical properties of cellular solid-gas foams (Gibson & Ashby, 1997c) described SPs as elastomeric open-cell cellular solids: the connection of internal voids with the atmosphere affects the response of SP foams on deformation. The anisotropic nature of SPs means that mechanical properties vary with product orientation (Falcone et al., 2005).

The aim of most material testing of SP formulations and cooked products is to monitor ingredient and process quality for industrial manufacture. These tests are generally empirical; that is, the arbitrary design of testing equipment means that fundamental mechanical parameters such as absolute stress and strain cannot be determined (Dobraszczyk & Morgenstern, 2003). More fundamental parameters are determined in standardised material tests using mathematical models for fluid and solid material deformation.

1.5.6.1 Doughs, batters and cooked sponge products are viscoelastic materials

The multiphase system of dough/batter is a dynamic dispersion composed of a liquid (continuous) phase; a gas phase, in the form of a foam comprising bubbles containing a mixture of air, CO_2, water vapour and volatiles; and a solid particulate phase of starch granules and cell fragments, including endosperm cell walls. The liquid phase contains ionic molecules (salts, organic acids), simple water-binding molecules (sugars, oligosaccharides, peptides) and soluble proteins and polysaccharides. Cooked SPs are compressible, open-cell, elastomeric cellular solids (Gibson & Ashby, 1997c). SP doughs/batters are non-Newtonian viscoelastic fluids, and cooked SPs are viscoelastic solids.

The response of a viscoelastic material under deformation has features of both a viscous fluid and an elastic solid (Trinh & Trinh, 2009b) and lags in deformation response after application or removal of an external force (TA Instruments, 2013). A viscoelastic fluid initially resists flow under an applied force, and also continues to flow for a period after the force is removed; while an elastic solid resists deformation and returns to its original shape after removal of an applied force, as long as the bonds/structures shaping the solid have not been destroyed.

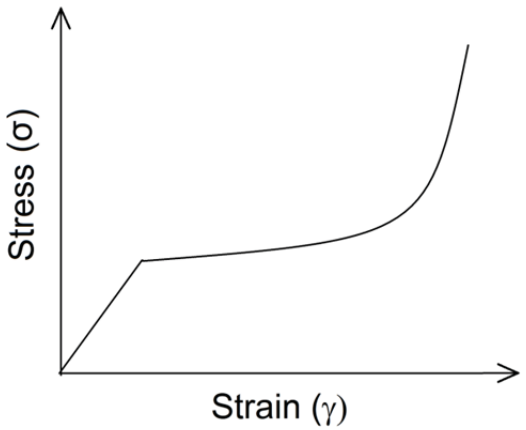

Figure 1.13 Generalised mechanical response of an elastomeric foam under compression.

Compression testing of a SP material to destruction typically produces a three-stage stress-strain curve, as described by Gibson & Ashby (1997b) for a generic open-cell elastomeric solid (Fig. 1.13). At low strain the SP foam initially deforms proportionally with applied deformation as cell walls begin to buckle (first linear component of the stress-strain response curve in Fig. 1.13). With wall collapse and progressive exclusion of the air phase, the curve transitions to a lower stress-strain ratio, at a plateau for a time. Towards the completion of air exclusion from the foam, the stress-strain ratio rises until the foam is compressed to its limit, representing the complete exclusion of the gas phase. Compressed samples may recover on removal of the strain if they are not stressed beyond the point of buckling and wall damage (Gibson & Ashby, 1997b).

Bread under deformation is more elastic than plastic in behaviour, that is, cell wall failure is primarily by buckling in many folds, rather than by bending and breaking at a single point (Liu & Scanlon, 2003). Zghal, Scanlon & Sapirstein (2002) modified a model for elastomeric foam compression developed by Gibson & Ashby to account for the experimental response of wheat-bread crumb. The modified model predicted bread bulk material properties, but was unable to predict localised failure of bread structure due to the irregular mesostructure (*anisotropy*) of bread compared with model cellular solids. While there is no general model for SP deformation under compression testing, comparative measures of SP mechanical properties can be derived from the shape of the curve during testing to destruction (Trinh & Trinh, 2009a).

1.5.7 Closed-cell foam formation and transition to an open-cell sponge

Bubble formation in doughs and batters begins with the incorporation of bubble initiation sites, either on the breakup of air folded into the formulation (e.g. by whisking, kneading, or creaming fat) (Campbell & Mougeot, 1999), or by addition of gas entrained on the surface of particulate ingredients (Hoseney, 1994; Shimiya & Yano, 1987). CO_2 is solubilised in the liquid phase as a result of fermentation or acidification and heating of bicarbonate salts (Cauvain & Young, 2006d). After solubilisation, CO_2 partitions into the gas phase into existing bubbles by concentration-driven diffusion through the liquid phase and transfer across the bubble interface (Scanlon & Zghal, 2001; van Vliet, Janssen, Bloksma, & Walstra, 1992).

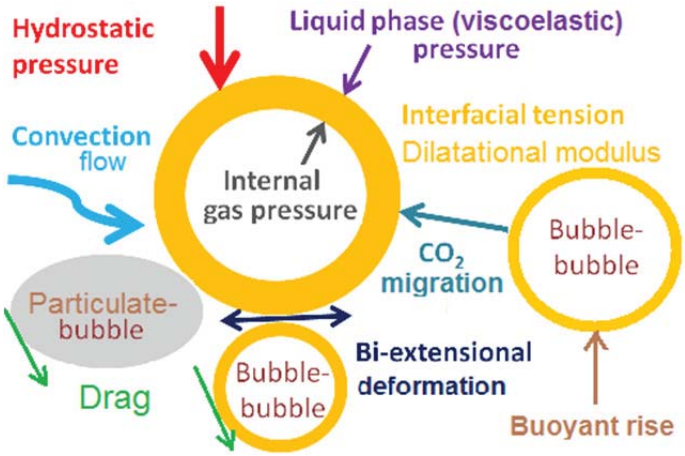

Figure 1.14 Processes and forces acting on individual bubbles and bubble populations in dough/batter.

Bubble formation and expansion is stabilised by the properties of an interfacial film that partitions at the bubble-liquid phase interface, and by the rheological properties of the non-gas fraction (Bloksma, 1990a; Mills, Wilde, Salt, & Skeggs, 2003; Primo-Martin, Hamer, & de Jongh, 2006; Sroan & MacRitchie, 2009). In wheat-bread dough the interface is composed primarily of surface-active wheat proteins (displaced in part by more rigid wheat lipids over time) as well as a minor portion of other surface-active molecules (Primo-Martin et al., 2006). The *surface tension* is a measure of how well this interfacial layer, which is in equilibrium with the dough liquid phase, is able to form and stabilise bubbles. The properties of the interfacial layer also include the capacity to support a rapid increase in interfacial surface area with bubble expansion. This *surface dilatational viscoelastic response* is an important influence on bubble stability on expansion and contraction. Yang & Foegeding (2011) identified the elastic component of dilatational viscoelasticity as the most influential factor in stabilising model protein foams.

Particulates coating or embedded in the interface (e.g. sugar or fat crystals, cell wall fragments) may contribute to bubble stabilisation (Cauvain & Young, 2006d; Pareyt, Finnie, Putseys, & Delcour, 2011), primarily by inhibiting bubble-bubble contact that results in coalescence. In uncooked cake batter with an unemulsified solid fat, those bubbles trapped within the separate fat phase are constrained from expanding (Bell et al., 1975; Sahi & Alava, 2003).

Forces and fluid processes acting on bubbles within the dough/batter (Fig. 1.14) affect the growth rate and movement of the bubble population (e.g. Fan, Mitchell, & Blanshard, 1999; Grenier, Lucas, & Le Ray, 2010; Handleman, Conn, & Lyons, 1961; Kokelaar & Prins, 1995; Mizukoshi, Maeda, & Amano, 1980; van Vliet et al., 1992). Bubble movement is influenced by the volume fraction and the size distribution of the bubble population, hydrostatic pressure (including gravity-driven liquid drainage from between-bubble channels), heat-convection flows generated during cooking, drag arising from the action of local fluid flow on individual bubbles, bubble buoyant rise, and physical containment of bubbles by adjacent particulates and emulsion drops. The growth of an individual bubble is affected by bubble size (and internal gas pressure), the pressure and viscoelasticity of the external medium

(including hydrostatic pressure), net migration of gas in and out of the bubble, and the surface tension and dilatational elasticity of the layer of surface-active molecules partitioned at the gas-liquid interface. Bubble shape is modulated by the yield stress and viscoelastic properties of the liquid phase, by interactions with adjacent bubbles and particulates, and by the drag on the bubble generated during streaming flow or buoyant rise.

Gas diffusion gradients drive the transfer of CO_2, water vapour and volatiles from the liquid phase into bubbles. The air inside bubbles also expands with increasing temperature (Confroti, 2006; Kumagai, Lee, Kumagai, & Yano, 1990). Contacting non-gas particles may crowd expanding bubbles, while collision between bubbles may result in growth by coalescence. Small bubbles also lose gas content to near-neighbour bubbles of larger size, by transfer on contact between bubble interfaces, or by concentration-dependent diffusion of the gas through the liquid phase (disproportionation) driven by the decreasing surface energy requirement for expansion with increasing bubble size (van Vliet et al., 1992).

Extensional shear deformation is the primary form of strain experienced by dough on foam expansion. Separate fractions of the gluten network of bread doughs enable dough stretching around the expanding bubble (*bi-extensional* deformation) and also stabilise the extended film by restricting bubble expansion (*strain hardening*) (Rouille´ et al., 2005; Sliwinski, Kolster, & Van Vliet, 2004). Bubble stability in batters, which are more liquid, is more dependent on the density and viscosity of the liquid phase, the interface stability on expansion (Chesterton et al., 2013), and the resistance of the foam to drainage on standing.

CO_2 solubility decreases markedly on heating, leading to a rapid expansion of bubbles in the early stage of dough/batter cooking (Moore & Hoseney, 1985). With increasing CO_2 release, bubble expansion increases, decreasing the number density of bubbles in the cooked product crumb (Cauvain & Young, 2006d). A decrease in batter or dough stiffness during early heating also increases the expansion capacity of the foam (Bloksma, 1990b; Gaines & Donelson, 1982). Bubble expansion in the later stages of cooking is driven primarily by an increase in water vapour pressure (Bloksma, 1990b; Fan et al., 1999; Matz, 1972). Wheat bread dough expansion on baking into loaf form was attributed as one third to CO_2- and air-driven expansion and two-thirds to expansion of water vapour and fermentation volatiles (Bloksma, 1980; Stauffer, 1998).

Thermosetting of the formulation signals the end of expansion in the gas phase and is associated with breakage of intact foam bubbles to produce an interconnected void network and a solid non-gas phase (*foam-to-sponge* transition) (Singh & Bhattacharya, 2005; Whitworth, 2008). In baked product, the internal structure produced on cooking is related to the spatiotemporal gradient formed on heat transfer during baking. Heat transfer is gradual from the product surface to the interior, and occurs on migration of heated water vapour towards the cooler centre once a surface crust has formed. Bubble expansion and structure setting take place along this gradient sequentially from the product surface to the centre (Baik & Marcotte, 2003; Lostie, Peczalski, & Andrieu, 2004; Mondal & Datta, 2008; Sablani, Marcotte, Baik, & Castaigne, 1998; Zhang & Datta, 2006).

1.5.8 Ingredient function in sponge product formulations

In SPs formulations flours are multifunctional ingredients that contribute many structure-forming functions (both positive and negative) during product formation (Cauvain & Young, 2006d; Edwards, 2007). As seen in the structure studies of cooked SP products, gelatinised starch granules form structural 'bricks' in close proximity, held in place by a continuous 'mortar' of an elastomeric gel comprised of protein and non-starch polysaccharide (NSP). Before gelatinisation wheat starch granules act as solid filler particles in the multiphase dough/batter fluid. The fluid is comprised primarily of soluble biopolymers (proteins and NSPs), ionic salts, organic acids, sugars and small oligosaccharides, and may have a liquid or a gel appearance.

Wheat flour composition has been studied extensively in order to develop predictors for performance and quality. A number of fundamental texts on baking technology from the Campden and Chorleywood Food Research Association (Cauvain, 2003; Cauvain & Young, 2000a, 2006a, 2007a, 2007b) detail the technical and scientific basis for formulation and bakery process trouble-shooting. Amongst many others, Eliasson & Larsson (1993) and Hoseney (1994) reviewed the influence of flour component functionality in wheat-flour baked products. According to Cauvain "…the rules which govern the development of any cake product are both complex and interactive" (Young, Davies, & Cauvain, 1999).

Cauvin & Young (2006b) summarised the influence of ingredients commonly used in industrial manufacture of Western-style baked products. Flours are the predominant structuring component in SPs, and may be the only source of starch and protein for structuring (i.e. they are integral chunks according to the U&E design approach definition). In bread dough after work- and time-dependent manipulation, the wheat gluten proteins form a highly viscoelastic network with structuring function. Non-flour proteins (e.g. from egg) and NSPs (e.g. xanthan, carboxymethylcellulose) provide alternatives for the structuring function of the gluten network in gluten-free (GF) SPs. Emulsifiers are used commercially to improve cooked SP texture, and to stabilise doughs and batters (reviewed in Faergemand & Krog, 2006).

Expansion of product before and during baking is achieved with chemical or live leavening agents. Liquid fats, individual solid fats, and composite baking fats formulated with multiple melting temperatures can improve gas retention and cooked texture in cake batters and decrease bubble coalescence in bread doughs (Pareyt et al., 2011). Sugars act as bulking agents and water activity agents, and also contribute to product texture and taste. The physical properties of flour particulates and associated entrained air also contribute to dough/batter flow behaviour and development of product structure. For example, Cauvain & Young (2000a) recommend a wheat-flour particle size below 90 μm for cake production, while in rye bread, very large particles in rye flour reinforce the cooked product structure (Autio & Salmenkallio-Marttila, 2001).

An ingredient component may play several roles during SP structure development. For example, the high sugar content of cake formulations initially aids foam formation by increasing liquid phase viscosity during whisking. This also stabilises the foam on standing, reducing bubble collapse before cooking. During cooking sugars act as temperature-dependent plasticizing agents which compete for water, modifying the thermosetting properties of starch granules (Chiotelli, Rolee, & Le Meste, 2000).

1.5.8.1 State transitions in sponge product setting

The chemical and physical changes critical to the thermosetting of doughs and batters to form solid-air open-celled sponges are 1) starch granule swelling on heating, which induces rapid dough/batter viscosification and 2) transformation of the liquid phase to a protein-rich elastomeric biopolymer gel. Physical and temporal coordination between the transformations to starch granules and to the continuous liquid phase is needed for successful structure formation (Sroan, Bean, & MacRitchie, 2009). Hadiyanto's work identified the key phase transitions in a range of bakery products from cakes and breads to crackers as: starch gelatinisation, protein denaturation, water evaporation, glass transition and starch crystallisation.

The sensorial experience of texture in a SP depends on position in an item (e.g. crust vs. crumb) and on local moisture content. The crisp surface crust of wheat bread is in a glassy state due to lower moisture content after baking, while the crumb is in the rubbery state (Fig. 1.15 top) (Hadiyanto et al., 2007). Starch gelatinisation and protein denaturation initiate structure setting, and are lumped together in the HD model. Water evaporation occurs mostly in the drying step after the structure becomes an open-cell foam. The degree of starch gelatinisation (which is limited by water availability in the formulation) and the glass transition of the SP solid define whether that part of the SP product has a crisp or soft sensory texture. Sensory texture scores for typical Dutch bakery products segregated into distinct groups (Fig. 1.15 bottom) when mapped on a plot of degree of starch gelatinisation (α) against the difference between glass transition temperature determined calorimetrically (T_g) and room temperature (i.e. T_g - 20 °C) (Hadiyanto et al., 2007). For example, soft bread crumb becomes crisp and crunchy when water is removed from the product on toasting. Cookies and crackers become rubbery as they absorb water from the atmosphere on staling. Cellular solid organisation remains the same, only texture alters. As (SP texture = structure + water content + water partitioning within microstructure) SP texture after cooking can be therefore be controlled by modulating the post-cooking moisture content of the SP.

1.5.8.2 Starch granules: transformation on cooking, and structuring role

When Howard, Hughes & Strobel (1968) substituted extracted starch polymers for ungelatinised starch granules, starch in the form of intact granules, not just in polymer form, was required for well-shaped cakes, confirming a role for the whole granule after gelatinisation in formation of the cooked microstructure. On screening different starch sources for breadmaking, Kusunose, Fujii & Matsumoto (1999) identified that potato starch granules were unable to support structuring processes. They postulated that potato granule gelatinisation occurred at too low a temperature to co-ordinate with the continuous phase transformation from liquid to elastomeric gel required for effective SP structure setting.

Starch granules added to liquid will take up some water on hydration at room temperature, but tightly-packed amylose and amylopectin chains continue to associate with each other in an ordered structure, limiting the degree of glucose residue hydration. Complete starch polymer hydration (gelatinisation) requires heat to disrupt the starch polymer structure and enable water to pack aroundthe glucose residues. Gelatinisation is a multi-stage non-equilibrium process, sensitive to heating

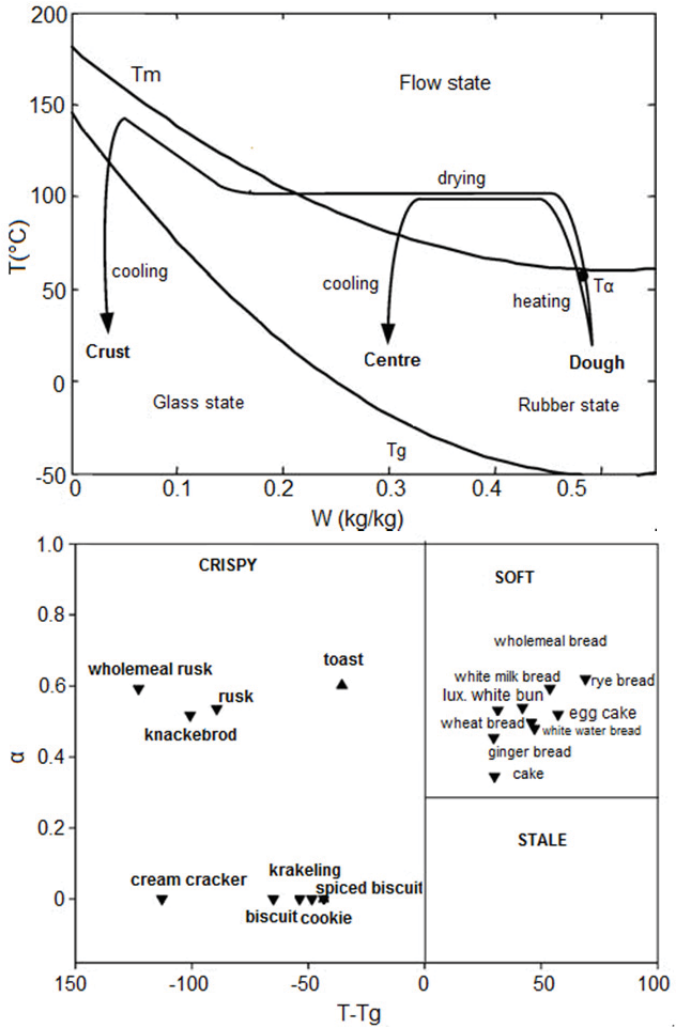

Figure 1.15 State transitions for the baking process. Top: state transition diagram for the bread baking process. T_g refers to the glass transition temperature; T_α to the temperature of starch gelatinisation (and associated transformation reactions during foam-to-sponge transition); and T_m to the temperature of starch polymer melting. Bottom: texture map of typical Dutch baked products, with the degree of starch gelatinisation plotted against the difference between T_g and room temperature (T). Reprinted with permission from Hadiyanto et al. (2007), © 2007 Elsevier Ltd.

rate and the availability of local water. Thomas & Atwell (1999) and Tester & Morrison (1990) identify two stages: initiation of gelatinisation (when semi-crystalline starch polymers first begin to lose their highly-ordered structure on heating), and granule swelling on extensive hydration.

Gelatinisation initiates over a narrow temperature range for an individual granule, although the typical temperature range for a specific starch or flour may be broad across the granule population (Donald, 2001). The critical temperature for each granule is related to the resistance of the granule exterior to water uptake. Proteins and lipids binding to the amylopectin-rich surface of the granule contribute to granule resistance to gelatinisation (Israkarn, Hongsprabhas, & Hongsprabhas, 2007). The initial loss of ordered structure in granule polymers can also be detected calorimetrically as a transient endothermic drop in system enthalpy. As local water availability decreases this endothermic response shifts incrementally to higher temperatures (Ghiasi, Hoseney, & Varriano-Marston, 1983; Zanoni,

Smaldone, & Schiraldi, 1991). Other components such as sugars and NSPs that compete for available water increase the initialisation temperature (e.g. Marcotte, Sablani, et al., 2004; Xue & Ngadi, 2007).

In SP production hydrating granules are not exposed to extensive shear, so that granule structures are retained in the product (Thomas & Atwell, 1999), as observed in the cooked microstructure of SPs. Granules of different sizes may distribute differently within a gelatinised starch gel (Puncha-arnon et al., 2008; Rasper & deMan, 1980) and within the SP cooked product microstructure (e.g. Park, Wilson, Chung, & Seib, 2004) influencing the rheological properties of uncooked and cooked SP formulations. Starch polymers may leach from granules on gelatinisation as heating continues. The degree of leaching depends on the starch source, stress forces on the granule, and the local water availability. More polymer leaches from granules with high amylose content, as amylose, primarily found at the granule centre, is more readily solubilised than amylopectin.

In breads, cakes, and biscuits the variability described in the degree of granule gelatinisation of baked SP on baking (e.g. Hadiyanto et al., 2007; Lineback & Wongsrikasem, 1980) is determined by the local water availability (Derby, Miller, Miller, & Trimbo, 1975; Zanoni et al., 1991). A number of early studies (reviewed in Willhoft, 1973) recognised the importance of granule gelatinisation to the increase in batter or dough viscosity and to structure setting in cake and bread formulations during the later stages of baking. Starch polymer gelatinisation sequesters water from the liquid phase, some of which is released on protein denaturation or on decreasing hydration of sugars with increasing temperatures (Hoseney, 1984; Hoseney, Lineback, & Seib, 1978).

1.5.8.3 Proteins and non-starch polysaccharides contribute an elastomeric gel

The development, physical properties, and functional contribution of gluten network to wheat bread structure have been studied exhaustively. Alternative structuring proteins (e.g. from egg, dairy or legume) may replace the gluten-rich non-starch domain of wheat flour as the 'mortar' in the cooked SP structure; but will have different temperature denaturation profiles and will alter the mechanical properties of the cooked SP. Substitute systems formulated from maize zein protein were used to form a protein network in model gluten-free breads (Schober, Bean, Boyle, & Park, 2008). Enzymatic cross-linking of non-gluten proteins by transglutaminase improved the functionality of some types of flour in GF batters and bread by providing a network analogue for gluten (Renzetti, Dal Bello, & Arendt, 2008). For non-wheat bread formulations, NSPs with structure-stabilising properties may replace proteins as the primary structural component in the formulation of some crumb products (e.g. rye bread structure, see Ashwini, Jyotsna, & Indrani, 2008); and GF formulations. Blackgram beans are used, alone or in combination with other flours, in a number of structured bread-type foods from the Indian sub-continent (e.g. idli, dhosa, vada, bori). Blackgram protein and arabinogalactan-rich pectic polysaccharide provided an effective aggregating matrix to support steamed idli bread structure (Susheelamma & Rao, 1974).

1.5.9 Microwave cooking: influence on sponge product structure

The nature of microwave heating affects internal water vapour heating in SPs, resulting in a moisture loss process that differs in fundamental ways from that on conventional thermal heating (baking) (Şumnu, 2001). Penetration of microwave energy into food increases with decreasing product density: a drop in dough/batter density occurs in cakes and breads on expansion (Datta, 2001). Each component of a multi-component food may have different dielectric properties, potentially resulting in over-heated or under-heated regions. It should be noted that the standing time after microwave heating is considered as part of the cooking process, as the product continues to experience extensive internal movement of heated water vapour and water loss on cooling. Finally, the heating profile may be affected by item volume: the dielectric properties of oil were the predominant influence on heating rate in small food volumes, while in larger volumes the heat capacity of the oil was more influential (Shukla & Anantheswaran, 2001).

Baked, leavened cakes and breads depend on the formation of a surface crust on baking: once it has formed, there is a gradual heat transfer by heated water vapour migration from the product surface to the cooler centre that drives starch gelatinisation and dough/batter solidification (see section 1.5.7). Baked SP formulations often perform poorly on cooking in a microwave oven with forced air circulation, as contact of the product with moving air at ambient temperature encourages water loss from the product and cools the surface, inhibiting the formation of a sealing crust (Şumnu & Sahin, 2005). During microwave cooking of SPs, this process, acting in combination with the direct penetration of microwave energy, may generate heat gradient patterns that are the reverse of those on baking, so that the interior of a cake or bread is hotter than the surface (Baker, Davis, & Gordon, 1990; Megahey et al., 2005; Zhang & Datta, 2006). In some studies, moisture loss from microwave products increases at a constant rate on microwave cooking and continues during cooling (Lambert, Gordon, & Davis, 1992; Megahey et al., 2005; Umbach, Davis, & Gordon, 1990), disrupting the normal slow transition in internal temperature experienced by dough/batter on baking. The wide variation and inconsistency in heating pattern reported for SP formulations on microwave cooking can be explained by the sensitivity of microwave heating to formulation composition and density, and the geometry of both item and oven (see section 1.3.2).

The bulk heating effect of microwave cooking on the dough or batter interior may drive very rapid product expansion, particularly in smaller items. Keskin et al. (2004) reported that wheat-bread rolls expanded to full product volume within 0.5-0.75 seconds of a two min cook cycle. The rapid expansion results in a rapid increase in foam surface area compared with baking, which in turn increases the rate of heated CO_2 and water transfer into the gas phase. Altered patterns of foam expansion and internal convection flows in dough or batter on microwave cooking alter the cooked SP mesostructure (Baker et al., 1990; Martin & Tsen, 1981). Given the compressed time scale for expansion on microwave cooking of chemically leavened SPs, activation of CO_2 production before cooking has been suggested as an effective way to achieve the required product macro- and mesostructure (Dodson, 2001).

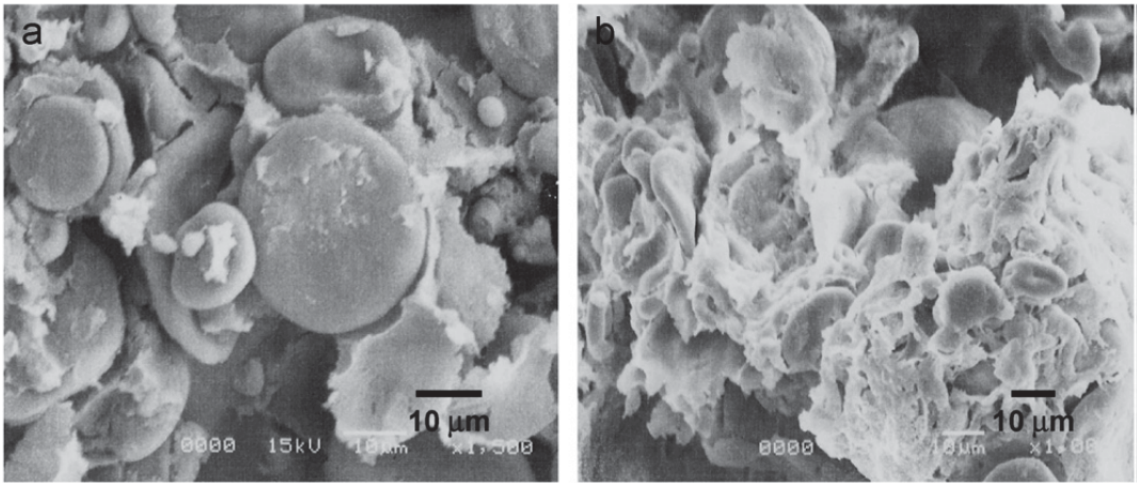

Figure 1.16 Scanning Electron Microscopy of pound cake microstructure after cooking for 5 min using microwave energy (left), or baking for 40 min (right). Note the difference in image scale. Reprinted with permission from Sánchez-Pardo, Ortiz-Moreno, Mora-Escobedo, Chanona-Pérez, & Necoechea-Mondragón (2008), © 2008 Swiss Society of Food Science and Technology.

The shortened cook time and altered heating gradients on microwave cooking disrupt the usual order of chemical interactions and water transfer between starch and protein-rich domains during baking. For example, bagel formulations (Umbach et al., 1990) and cake formulations (Sánchez-Pardo et al., 2008) had a lower degree of starch gelatinisation when cooked by microwave heating than the corresponding formulations when baked (see Fig. 1.16). The rapid rate of microwave heating disrupts the mass-transfer of water required for successful granule gelatinisation (Sakonidou, Karapantsios, & Raphaelides, 2003). In hamburger bun dough, decreasing the gluten content increased cooked product volume on microwave cooking, but decreased it on baking (Ozmutlu, Şumnu, & Sahin, 2001), suggesting that the gluten network resisted expansion at the much more rapid rate of foam expansion under microwave cooking. The disruption of spatiotemporal patterns of heat and water availability affects product quality. Sensory evaluation perceived a low-fat cake formulation as drier on microwave cooking than the corresponding formulation when baked, even though measured product moisture levels were the same (Li & Walker, 1996). Formulation for microwave applications may address structure and texture problems produced by microwave cooking of SPs (Shukla & Anantheswaran, 2001).

Microwave heating is not in general commercial use as the sole heating source for SP manufacture (Şumnu, 2001). It is commonly used for specialist tasks like breadcrumb drying (Şumnu & Sahin, 2005) or as part of an industrial combination-oven system (Hadiyanto et al., 2008; Hoseney, Miller, Bassi, & Maningat, 2001). While the published research identifies that baked products are poorly suited to microwave cooking, SP formulations usually cooked by steaming may be easier to adapt for microwave cooking.

1.6 Food-Inks to make sponge products with an embedded image

Based on the current information on events in SP structure development, a generic design for SP structure development under microwave cooking has three primary functional design elements (structuring operations): 1) aerate the formulation to produce a liquid-particulate-gas foam (foam formation), 2) expand the three-phase foam by bicarbonate addition and by gas expansion on microwave heating (foam expansion), and 3) transform the closed-cell, gas-particulate-liquid foam to an open-cell solid-air sponge (structure setting). For the Food-Inks 3D printer project, SP mesostructure development must be tightly controlled to maintain voxel shape and position, by modulating batter flow behaviour for correct voxel deposition, and by controlling bubble size/number distributions during foam formation and expansion, both before and after cooking.

1.6.1 Study approach and critical factors

The primary research aims of the study are to define the design requirements to control Food-Ink flow during piping, mixing and voxel deposition, and to control structure formation in SPs, within the context of Food-Ink formulation design for the Food-Inks 3D printer.

1.6.2 Sponge product design

- The dynamics of bubble populations in doughs and batters and the bubble stability on expansion, both before and during cooking, contribute to the development of foam mesostructure in SPs.
- Structure setting in dough/batter and the transformation to a solid foam depends on the spatiotemporal co-ordination of starch gelatinisation, protein denaturation and non-starch polysaccharide reconfiguration associated with bulk heating and water loss from the liquid phase.
- Work-sensitive and time-dependent formulations (e.g. wheat SPs containing gluten) are not suitable for extrusion-based FLM applications such as the Food-Inks 3D printer.
- Modelling microwave cooking is outside the study bounds, as too many factors influence the heating profile of a food item.

Steamed SP formulations that do not depend on the formation of a sealing crust during cooking are less likely to undergo the internal convection flows and compression observed in baked products, and should be more suitable to adapt as a SP Food-Ink. There is a significant knowledge gap for SP structure development apart from Western-style, wheat-based SPs cooked by baking. Assumptions about ingredient functionality and critical events in structure formation may not necessarily translate to non-wheat SPs cooked by other means. Therefore, empirical test systems and metrics developed to evaluate wheat SPs may not provide valid information when applied to non-wheat SP formulations.

1.6.3 Flow behaviour requirements for Food-Inks

A Food-Ink must have the following flow properties:

- Compatibility with Food-Inks 3D printer pumping and mixing requirements.
- For voxel deposition, a (multiphase) structure-forming fluid is piped through an outlet to give a colour-matched voxel of appropriate size.
- After deposition, the voxel maintains shape and position until structure is set.

1.6.4 Structure development requirements for a sponge product Food-Ink

Structure development during the 3D Food-Inks printing application must:

- Be highly controllable in post-deposition SP foam expansion and setting on cooking.
- Have rapid enough structure setting to meet time requirements of the Food-Inks 3D printing application.

The next chapter examines Food-Ink flow behaviour requirements to determine design constraints and key material properties for the Food-Inks 3D printing application.

As part of the design task is to identify and develop appropriate test systems to evaluate design prototype effectiveness, the methods used in this study are inserted directly into the relevant section of text, rather than placed in a separate chapter. These method sections are formatted as:

1.6.4.1 Method for…

- *Bulleted text in italics.*

Additional data (timecourse video files of batters) can be found as .avi files on the CD in the pocket attached to the thesis cover.

Chapter 2. Food-Ink flow behaviour

2.1 Printing behaviour of Food-Inks

The Food-Inks 3D printing application assumes an extrusion-based AM technology, with formation of a (continuous) thread of fluid or paste-like material. It can be split into stages which may each have different specifications for the interaction between Food-Ink and equipment. Additionally, the post-print behaviour of the formulation is critical to the retention of voxel structure during structure setting. This chapter identifies fluid flow properties for the Food-Ink for the stages in the Food-Inks 3D printer application. It introduces rheological models for fluid behaviour under pipe flow and on mixing, and examines test methods and systems suitable for defining the relevant material properties for the Food-Inks 3D printer application. Experimental data from a model Food-Ink fluid relevant to SP formulations are interpreted within the Food-Inks 3D printer design specifications. As an important part of the product design process is the development of suitable models to predict prototype suitability to meet end-user specifications, models and testing procedures for multiphase fluid flow behaviour are evaluated to identify appropriate predictive tests of prototype effectiveness.

Food-Ink formulations for 3D printing must be pipeable, mixable and formable: where piping refers to the transfer of the Food-Ink formulation from a reservoir to the final deposition site; mixing to any process of mixing of formulation streams (as in, for example, colour mixing, dye or flavour introduction); and forming to the retention of sample positional information (i.e. coloured voxels, shape) for uncooked material during the entire deposition and setting process.

2.1.1 Material flow in the Food-Inks 3D printing application

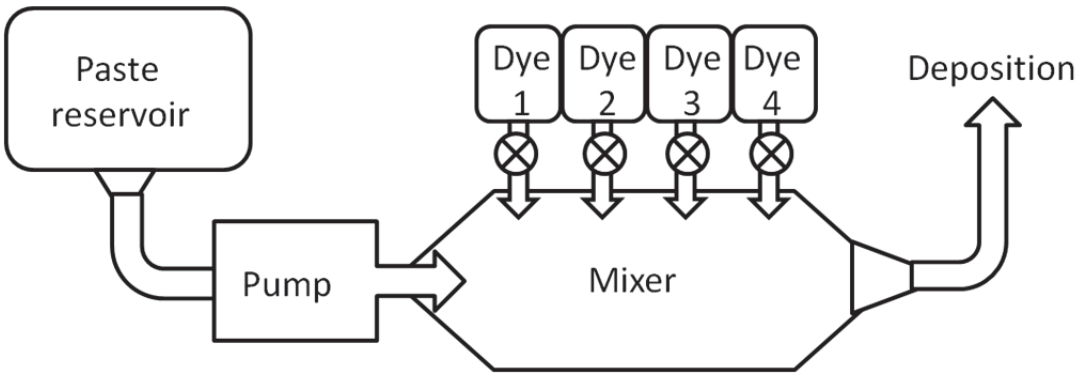

Figure 2.1 Schematic of flow path during the Food-Inks 3D printing application, assuming continuous flow and a 4-dye colour-matching process.

In the work-flow description for the Food-Inks 3D printer application (Fig. 2.1) a structure-forming fluid Food-Ink at rest in a reservoir is pumped to a mixing chamber, in which colour is added via metered flow to match voxel colour requirements. After colour-matching, voxels are deposited through a moveable outlet to produce the 3D object carrying an embedded image. Constrictions in pipe diameter

along the fluid flow path may occur at the paste reservoir, as the Food-Ink moves into the mixer, at the mixer outlet, and at the deposition outlet. The colour is food dye in liquid form. Alternative design configurations include solid dyes in place of liquid, or multiple (at least four) pre-coloured base streams which are then mixed to the desired colour.

The first iteration of the design (see section 1.3.1) assumes continuous pipe flow, in order to minimise the number of stop-start breaks in flow during printing. The most appropriate pump types for continuous flow of viscous fluids are positive displacement plunger pumps and peristaltic pumps. Plunger pumps (e.g. syringe pumps) suit metering operations for fluids with lower viscosity, such as thin liquid dyes (Coulson, Richardson, Backhurst, & Harker, 1999c), while peristaltic pumps and syringe pumps can be used for higher-viscosity fluids, e.g. paste-like Food-Inks (Cole Parmer, 2012). Fluid in a peristaltic pump moves along a deformable tube by being squeezed between the pump outside wall and three (or more) rollers rotating around a central spindle. Peristaltic pumps produce a pulsed flow. According to manufacturer's information, peristaltic pump curves are dependent on the fluid viscosity and must be determined from the manufacturer's data. Pumping effectiveness reduces greatly with increasing viscosity.

Positive displacement pumps are the usual pumping systems used to deliver fluid feed stock to extrusion-based AM systems. The Fab@Home 3D printing system (Cohen et al., 2009) uses syringe pumps with diam. of 1-2 cm, driven by compressed air at 100-1000 psi (680-6800 MPa) (J. Lipton, pers. comm.), a significantly higher delivery pressure than produced by peristaltic pump systems.

The Food-Ink must maintain a stable structure in the reservoir before pumping, without settling of particulates or syneresis of formulation components. To enable pumping and mixing, the Food-Ink must lose structure rapidly and flow readily, while on deposition it must reform rapidly to minimise voxel distortion. This *stop-start-stop* flow requirement for Food-Inks is similar to the flow requirement for toothpaste.

2.1.2 General design considerations for Food-Ink flow behaviour

Factors to be taken into account in the design of the piping, mixing and deposition system in order to deliver a discrete colour voxel at the required position, without slumping before structure setting:

- Minimal reduction of flow resulting from constrictions along the printing system that introduce *extensional* or *elongational* shear (fluid stretching) (Rao, 2007d) (i.e. a need to retain a high deposition rate).
- No cross-contamination of colour between voxels after mixing.
- No deformation of voxel shape between mixing and deposition.
- A minimum void volume between mixing and deposition.
- Rapid development of structure in Food-Ink, to maximise retention of voxel post-deposition.
- Self-supporting behaviour for multiple deposition layers.

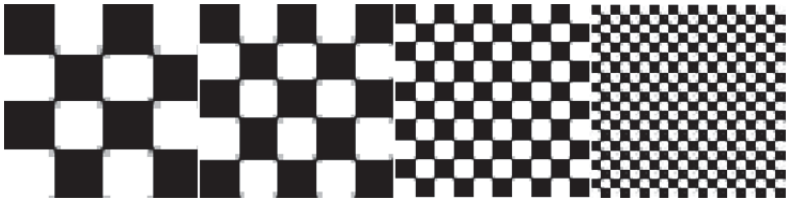

Figure 2.2 **Illustration (left to right) of 3.9 dpi, 5 dpi, 10 dpi and 20 dpi printed at actual size.**

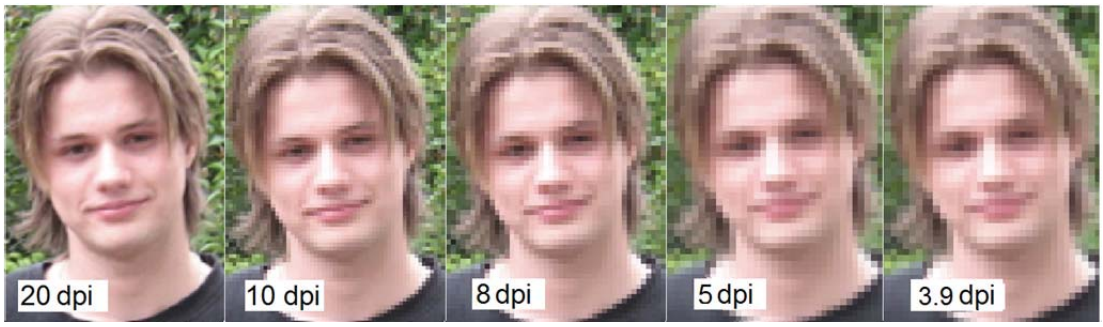

Figure 2.3 **Degradation of an original digital image printed at A5 size (145 x 210 mm) with decreasing resolution. The equivalent cubic voxel widths range from 1.25 mm (20 dpi) to 6.5 mm (3.9 dpi).**

2.1.3 Initial specifications for piping, mixing and deposition of Food-Inks

The target for the Food-Inks 3D printer is to produce an embedded image with voxels colour-matched to a source image. At the time of experimentation a working configuration of the Food Inks 3D printer and mixing system remained undeveloped. Section 1.3.1 described the initial prototype of the 3D Food-Inks printing equipment. A product design outline developed at the start of this study (Appendix B), for Food-Ink formulations to produce a point-of-sale, A5-sized food item with an embedded image in multiple layers, defined the initial boundary conditions for Food-Ink piping, mixing and deposition based on the setup of the initial equipment prototype (Table 2.1, over page). The target print time for a point-of-sale application was set at 8 min (requiring a flow rate of 200-600 mL/min), with a mixing system able to meter and mix sub-microlitre volumes for voxel colour-matching, and a response within seconds for the Food-Ink thread to stop flowing (redevelop structure) after deposition.

An initial voxel size of 0.27 mL (chosen as a realistic volume to enable voxel colour matching by mixing multiple dye streams) corresponded to an image print resolution of 3.9 dpi (Fig. 2.2). Fig. 2.3 reproduces a digital image of a face when printed at A5 size with decreasing image resolution. On adding the probable loss of resolution associated with the printing process, a resolution of 10 dpi appears to be the lowest resolution able to maintain adequate image information for an A5 size printed food item. Therefore, the voxel size range specified in this study was set between 3.9-10 dpi.

Table 2.1 Specification of boundary conditions for piping, mixing and deposition of Food-Inks. [a]Outlet minimum values assume that viscoelastic fluids experience two-fold die-swell on exiting the outlet (the imagine machine, 2013).

Parameter	Equipment description	Range
Pipe flow	Peristaltic pump with 20 mm i.d. tubing	200-600 mL/min
Start flow Stop flow		Within seconds
Mixing	Static mixer Micro-metering	10:1 to 1000:1 volume ratio & 1:1 to 100:1 viscosity ratio Sub-microlitre dye volumes
Post-deposition structure		Self-supporting for > 6 layers
Target voxel size	Mixer outlet between 1-3 mm	3.9-10 dpi
		16-270 µL volume
		2.5-6.5 mm width
Pipe flow	Peristaltic pump with 20 mm i.d. tubing	200-600 mL/min
Outlet	Square or round shape	Square thread 1.25[a]-6.5 mm Round thread 1.4[a]-7.0 mm diam.

Table 2.1 defines the initial boundary conditions for Food-Ink piping, mixing and deposition based on the setup of the first equipment prototype (Appendix B; section 1.3). The target print time for a point-of-sale application was set at 8 min (requiring a flow rate of 200-600 mL/min), with a mixing system able to meter and mix sub-microlitre volumes for voxel colour-matching, and a response within seconds for the Food-Ink thread to stop flowing (redevelop structure) after deposition. Table 2.1 lists the range of image resolutions, and the calculated voxel volumes and outlet diameters for printing a fluid thread using either a square outlet (cubic voxel in a square thread) or a round outlet (cylindrical voxel in a round thread). A voxel with cubic shape has volume of 270 µL at 3.9 dpi, 132 µL at 5 dpi, 16 µL at 10 dpi (2 µL at 20 dpi), with width h of 6.5 mm, 5.0, 2.5 mm and 1.27 mm, respectively. The diameter d of a voxel with the same volume on production as a cylindrical thread can be derived using $d = 1.0855h^{1/3}$.

Die-swell, the expansion of viscoelastic fluids on exiting a pipe (discussed in section 2.3.4), decreases the minimum size of the outlet required to deliver a thread of known thickness by around half (the imagine machine, 2013), and the minimum outlet diameters in Table 2.1 have been adjusted to account for a two-fold increase in diameter on exiting the outlet.

2.2 Properties of fluid flow on piping and deposition

This section introduces fluid flow concepts relevant to Food-Ink behaviour on fluid transfer from reservoir to mixer by piping, and Food-Ink deposition. The three types of fluid flow behaviour relevant to the Food-Inks 3D printing application are fluid *shear deformation* (during pipe flow and colour-mixing), fluid extensional shear deformation (during Food-Ink deposition and post-deposition voxel spread), and the breakdown and development of fluid structures on applying or removing an external force on the fluid (stop-start-stop flow behaviour).

Most food fluids contain multiple components, and may also have multiple phases. Different types of particle-containing fluids (bubbles in foams, *drops* in emulsions and solid *particulates* in *dispersions*) may show some similarity in flow behaviour (Michaelides, 2006), in part because fluid bulk rheology is influenced primarily by interactions at the surface of physical components in the system (e.g. polymer chains, particles) (Aguilera & Stanley, 1999). The particle physical properties, the *volume fraction* of the particle phase and the degree of particle-particle and particle-fluid interaction are important in determining the flow behaviour of multiphase fluids. These interactions can also result in time-dependent development of physical structures within a fluid (e.g. polymer aggregates, particle networks). Fluids with molecular or particulate interactions which generate structures that affect flow behaviour are termed *structured fluids*, (TA Instruments, 2012).

Flow models are mathematical relationships developed from experimental data that provide approximations to predict flow behaviour for complex food fluids (Fischer et al., 2009; Steffe & Daubert, 2006a). The derived rheological parameters may not necessarily correspond directly to observable flow characteristics (i.e. they are mathematical rather than phenomenological constructs) (Mader, Llewellin, & Mueller, 2013). Fundamental equations of state to model fluid flow model 3D flow using tensor field notation, which expresses fluid flow as a vector field with nine directions (Shenoy, 1999b). Fluid flow models are often reduced to fewer dimensions to simplify computation, ignoring the three dimensional nature of fluid response to external forces.

2.2.1 Fluid flow in a pipe

The flow of viscous food fluids through a straight pipe is generally *laminar* and not turbulent, that is, the fluid flows in smooth streamlines without breaking up into eddies. The equipment geometry is important, as constrictions and expansions along a pipe may disrupt streamline flow (Coulson, Richardson, Backhurst, & Harker, 1999a).

2.2.1.1 Factors contributing to bulk flow in a pipe

The Mechanical Balance equation is used to predict fluid flow in a simple pipe system:

$$gZ_1 + \frac{P_1}{\rho} + \frac{v_{z1}^2}{\alpha} - W = gZ_2 + \frac{P_2}{\rho} + \frac{v_{z2}^2}{\alpha} + E_f$$, (Rao, 2007b).

The parameters gZ_1 and gZ_2 are terms for hydrostatic pressure in the system at input and output points with height Z_1 and Z_2, respectively. The fluid average flow velocity in the pipe, v, is calculated from the volumetric flow rate and the pipe diameters at Z_1 and Z_2. Fluid density is ρ, fluid pressure at point x is P_x, α is a kinetic energy correction factor, W the work output of the pump per unit mass, and E the energy loss per unit mass due to friction in the pipe and fittings along the flow path.

Factors that influence the rate of fluid flow in the system are fluid density, hydrostatic pressure due to height differences in the pipe system, friction loss, and pressure drop along the system. Friction loss increases with increasing fluid viscosity (Coulson et al., 1999c). The pressure drop ΔP between inlet and outlet ($\Delta P = P_2 - P_1$) is the pressure force required to overcome friction drag at pipe walls and fittings, height changes along the system, and any changes in fluid kinetic energy, such as those that occur as the fluid flow accelerates on pumping. Pressure drop is proportional to the square of fluid velocity.

Simple pipe flow models are used to predict useful flow parameters, such as pressure drop and

frictional drag on the fluid along the pipe system. The system geometry must be taken into account. Bends and constrictions/expansions in pipe diameter affect the rate of flow and may introduce uneven flow patterns across the pipe (Coulson et al., 1999a). The pump type also influences flow in the system (Rao, 2007b). Rearrangement of the Mechanical Balance equation shows that W, the work required from the pump to move the fluid through the system, is the sum of losses from pressure drop, kinetic energy loss, loss in gravitational potential energy, and friction loss (Steffe & Daubert, 2006a).

On deformation of a fluid or solid, the *strain* (γ) on a material is a measure of the change in dimension caused by an applied stress (σ). Fluid flowing in a pipe experiences a gradient of *shear strain* that develops when friction retards fluid flow at the pipe wall; the strain decreases to zero at the pipe centreline (Rao, 2007e). Rheological tests modelling the effect of shear deformation on a fluid may therefore predict fluid behaviour under pipe flow.

2.2.2 Shear deformation in fluids

2.2.2.1 Rheometric test systems for flow under shear deformation

Testing of flow behaviour under shear deformation is generally carried out on food fluids using geometries with one fixed and one moving surface (rotating or sliding). With rotational tests, the measure of fluid resistance to rotational deformation is quantified by transformation of torque and rotational frequency data into stress and strain values, using mathematical models of the test geometries (Fischer & Windhab, 2011). Common test geometries for rotational shear deformation of fluids are plate-plate, cup-and-bob, and vane-and-cup configurations that rotate around a central spindle. The deformation force increases from the spindle to the edge of the shearing surface due to an increase in rotational velocity with increasing radius. With plate-plate geometries, a correction can be made by using a test geometry in which the gap decreases from the edge of the rotating plate to the centre (cone-and-plate geometry) (Metzger, 2002). Particulate dispersions and foams are generally tested using plate-plate and vane-and-cup geometries, as interactions between particles and the walls of the test geometry can generate anomalous torque measurements, e.g. when a lubricating layer of particle-free liquid forms close to the wall (*wall slip*) (Rao, 2007d).

2.2.2.2 Models for simple and structured fluids under shear deformation

The simplest behaviour for a fluid under a strain with a gradual increase in rotation rate at the shear surface with *shear rate* $\dot{\gamma}$ is that of a *Newtonian* fluid, for which the response of the fluid as shear stress (σ) depends linearly on the shear rate, $\dot{\gamma}$ (Fig. 2.4). Shear stress carries a unit of pressure, the Pascal (Pa; N/m^2). Examples of Newtonian food fluids are honey and sugar syrup. The *viscosity* (η) of a Newtonian fluid is the ratio of shear stress to shear rate:

$$\eta = \sigma / \dot{\gamma},$$

i.e. the slope of the Newtonian curve in Fig. 2.4 gives the fluid viscosity.

However, most food fluid systems have a non-linear relationship between shear rate and shear stress (*non-Newtonian* fluids). A fluid with greater decrease in shear stress with increasing shear rate than shown by Newtonian fluids is described as *shear-thinning* (Fig. 2.4). Non-dilute polysaccharide solutions are examples of shear-thinning food fluids. Other food systems, such as starch granule

dispersions, may be *shear-thickening*, increasing in the rate of viscosity increase with increasing shear rate (Fig 2.4). Fluids with gradual increases in shear-thinning and shear-thickening behaviour generally have a power law relationship between shear rate and shear stress; although in some systems the onset of shear-thickening can be abrupt. The viscosity of non-Newtonian fluids under shear at shear stress σ and shear rate $\dot{\gamma}$ is reported as the *apparent viscosity* (η_A), as the measured viscosity depends on test conditions, i.e. the slope of the curve changes with changing shear rate.

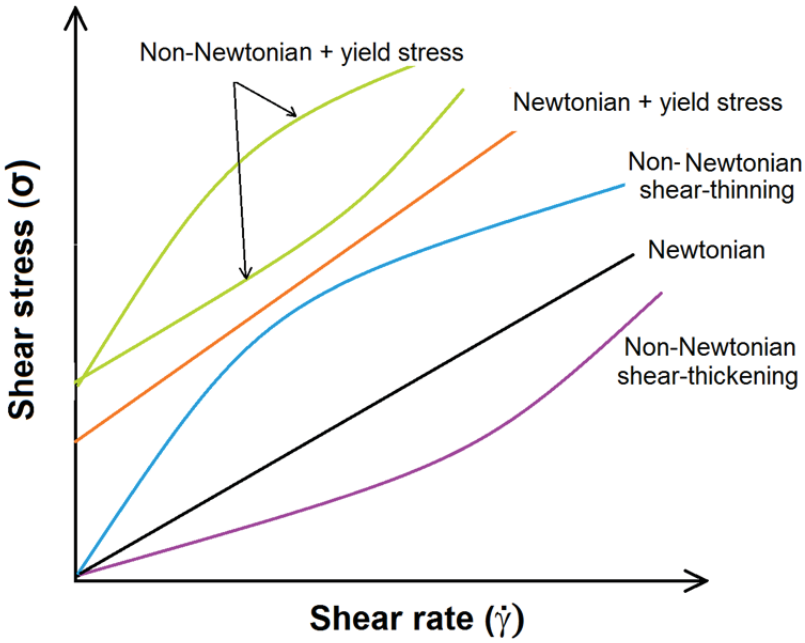

Figure 2.4 Shear-stress deformation curves at increasing shear rate for various types of fluid flow behaviour.

One model for fluid flow is the *power law model* (rearranged to give apparent viscosity):

$$\eta_A = \frac{\sigma}{\dot{\gamma}} = \frac{K\gamma^n}{\dot{\gamma}} = K(\dot{\gamma})^{n-1},$$

where n is the dimensionless flow behaviour index (termed *power index* in this study) and K is the flow consistency index with unit $\mathrm{Pa\,s}^n$ (termed *consistency coefficient* in this study and reported with the unit Pa s). The value of n is 1 for Newtonian fluids, $n < 1$ for shear-thinning fluids, and $n > 1$ for shear-thickening systems (Coulson et al., 1999a). A highly shear-thinning fluid, for example, has n of 0.1-0.2. Values for n and K are determined experimentally.

If a fluid develops some type of network structure at rest, a minimum deformation must be applied to generate fluid flow (*yield stress*, σ_Y). Below the yield stress the fluid has the properties of an elastic solid, as fluid structures are in a jammed state (Ovarlez, Tocquer, Bertrand, & Coussot, 2013). Examples of food structured fluids with yield stress behaviour are biopolymer solutions and particle-containing fluids (gas-liquid foams, solid-liquid dispersions and liquid-liquid emulsions) at concentrations that allow frequent polymer-polymer or particle-particle interactions.

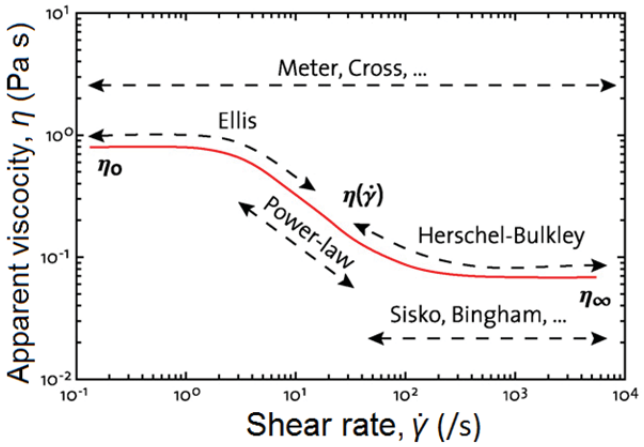

Figure 2.5 Examples of flow models for a simple structured fluid under laminar flow. Reprinted with permission from Fischer et al. (2009) © 2009 Académie des sciences.

Static yield stress is the shear stress needed before flow begins in a yield stress fluid at complete rest, while *dynamic yield stress* is the minimum shear stress below which a moving fluid stops flowing (Malvern Instruments, 2012). These rheological properties are important in quantifying Food-Ink stop-start-stop flow behaviour.

The addition of a yield stress component to a power law fluid gives the *generalised Herschel-Bulkley equation* for shear stress, with yield stress σ_{YHB}:

$$\sigma = \sigma_{\mathrm{YHB}} + B(\dot{\gamma})^{p}.$$

The apparent viscosity η_{HB} of the Herschel-Bulkley fluid is calculated as:

$$\eta_{\mathrm{HB}} = \sigma_{\mathrm{YHB}} + B(\dot{\gamma})^{P+1},$$

with parameter B replacing K as the consistency coefficient and p replacing n as the power index in the simple power law equation (as the two equations are calculated differently).

These examples of fluid models are partial rheological models across the range of flow behaviour. Fig. 2.5 shows a number of partial rheological models fitted across the flow behaviour response of a simple structured fluid. More inclusive and sophisticated flow models have been developed for specific applications and fluid types. Most flow models describe systems once they have reached steady state flow (*fully developed* flow). As flow behaviour in real food systems is often not fully developed, the relevance of steady state models to a particular system must be evaluated by the researcher (Mader et al., 2013) - the flow path for the Food-Inks 3D printer system will not be at fully developed flow during critical steps such as deposition. The choice of rheometer type, test geometry and test conditions limit the characterisation range, particularly for complex fluids. Individual rheological test systems can have a limited capacity to characterise the entire fluid flow response to shear deformation, and the type of fluid flow behaviour to be modelled influences the choice of rheometric test system.

2.2.3 Relaxation times in structured fluids

Complex food fluids generally show time-dependent flow behaviour, e.g. stop-start-stop flow does not occur instantaneously. Fluids with history-dependent flow behaviour may also thin (*thixotropic* fluid) or thicken (*antithixotropic* fluid) with increasing time under constant shear deformation. For example, ketchup, a thixotropic food fluid, flows readily after being stirred but builds up structure on standing, so that yield stress and apparent viscosity increase on aging (Steffe & Daubert, 2006c).

The *relaxation time* of a structured fluid (λ) refers to a characteristic memory time scale for the fluid to transition from one steady state to another under deformation (Hinch, 2013). Description of structured fluids with time-dependent response to flow (such as thixotropic polymer solutions containing particulates or viscoelastic fluids) must include time-dependent flow parameters (Herran & Coutris, 2013). Individual components in a multi-component fluid may each have a different relaxation time, producing a complex relaxation response in the fluid. The relaxation response is more complex for systems which have been perturbed, but have not yet fully recovered their resting structure. To minimise the effects of structure history in time-dependent fluids, it is critical that sample preparation and handling is consistent when measuring the flow behaviour of structured fluids.

Yield stress behaviour relates to the relaxation times of fluid structures (de Souza Mendes, 2013; Kamble, Pandey, Rastogi, & Lele, 2013; Livescu, 2012). de Souza Mendes (2013) differentiates between fluids with an ideal yield stress, which show a consistent yield stress behaviour over months, and fluids that vary in yield stress depending on the measurement timeframe. For history-dependent fluids, the yield stress is often expressed across a range of values (Emady, Caggioni, & Spicer, 2013). The food fluids relevant to this study do not have ideal stress behaviour. Multiphase food fluids such as cake batters are so complex in structure that they inevitably exhibit some yield stress behaviour within the timeframe of interest for food production processes. For Food-Ink stop-start-STOP flow behaviour after deposition of an extruded thread of material, a short relaxation time for reformation of fluid structure is essential if the deposited form is to be retained.

2.2.4 Characterisation of viscoelastic fluids

A viscoelastic fluid displays a combination of elastic (solid-like) and viscous (fluid-like) behaviour on application of an external force, which produces a lag in the fluid response to shear deformation (Trinh & Trinh, 2009b). Elastic effects in fluids can result from stretching and relaxation of polymer chains in solutions to align with the shear direction (Herran & Coutris, 2013) or from flexing of deformable particles dispersed in the liquid phase (e.g. blood cells in blood flow (Wikipedia, 2014), bubbles in foams). Elastic effects may influence the flow behaviour of complex fluids significantly, especially at low shear rate, and will also affect deposition behaviour at an outlet.

To characterise viscoelastic materials, the material is held between two surfaces while one surface oscillates back and forth in relation to the other (*dynamic shear rheometry*). For viscoelastic fluids, the test systems are generally plate-plate, bob-and-cup or vane-and-cup geometries rotated at a central spindle. The tests apply a circular oscillation at frequency ω (with unit /s), and oscillation amplitude is measured as a portion of one full rotation (%strain). For viscoelastic materials the torque data produced

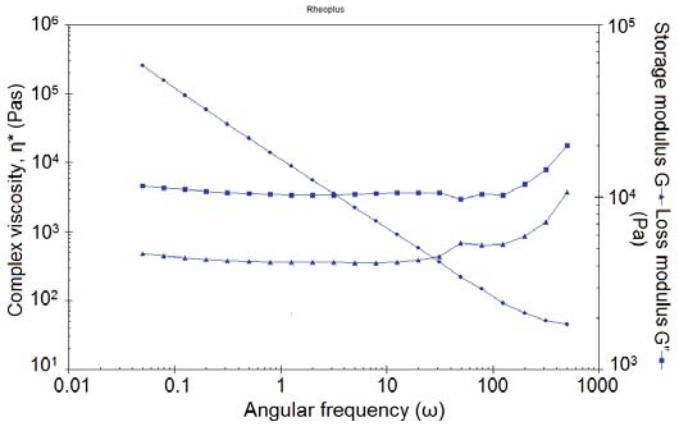

Figure 2.6 Frequency response of 1% xanthan solution (0.5% NaCl, 0.1% K sorbate) at fixed strain, using plate-plate geometry with 1 mm gap: complex viscosity (●), storage modulus (▲), loss modulus (■). Ouput image generated by Rheoplus/32 software.

under the back-and-forth oscillation of the rotating surface has the form of a periodic sinusoidal wave. The wave amplitude and time lag in relation to the applied sinusoidal force provide a measure of fluid viscoelasticity.

At low amplitude oscillating shear within the *linear viscoelastic range* of the material (generally within 0.1-5.0 %strain) the fluid structures contributing to the material viscoelastic properties are not disrupted irreversibly, although localised rearrangements take place (Rao, 2007d). Within this range the sinusoidal torque data can be deconvoluted as the *complex viscosity* (η^*), a complex number calculated from *storage modulus*, G' (a measure of the energy stored by the elastic component) and *loss modulus*, G" (a measure of energy dissipated by the viscous component):

$$\eta^* = G' + iG".$$

G' is derived from the cosine component of the sigmoidal fluid response curve on oscillatory deformation, and $G"$ from the sine component. In dense dispersions and highly viscoelastic fluids $G' > G"$, represents predominantly elastic behaviour (Van Der Vaart et al., 2013).

The deformation range over which a viscoelastic material has a linear response to oscillatory shear deformation can be determined by fixing the test strain and ramping frequency, or by fixing frequency and ramping strain. As an example of a viscoelastic response determined in this study, a frequency sweep was applied to a xanthan-salt solution (Fig. 2.6), using the method described in the following section. The viscosity values under fixed strain and ramped frequency indicated the fluid had a linear viscoelastic response between 0.1 < ω < 10.

2.2.4.1 Method for low-shear oscillatory rheological testing

- *Measurements were made using an Anton Paar Rheometer MCR301 with Rheoplus 32/ Ver. 2.81 software (Anton Paar, Graz, Austria). Fluid was placed with minimal handling between 25 mm diam. roughened plate-plate geometry at 2 mm gap inside a high-humidity chamber to retain moisture, and rested for 30 min before analysis.*
- *To determine the linear viscoelastic range, strain was set at 5% and the frequency of oscillation ramped linearly between 0.05-500 Hz.*

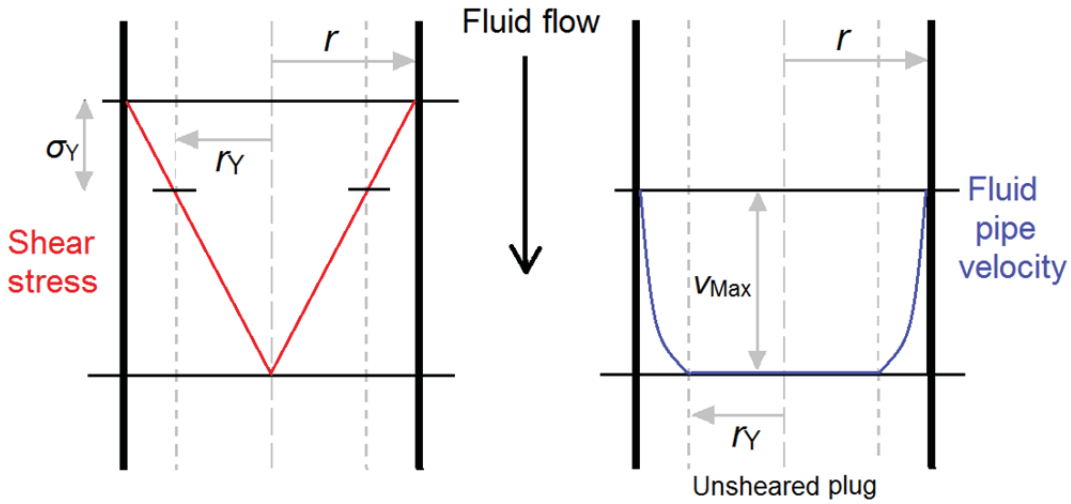

Figure 2.7 Steady state pipe flow of a yield stress fluid showing profiles for: left, shear stress (in red) and right, the corresponding fluid velocity in the pipe (in blue). Pipe radius, *r*; pipe radius at yield stress, r_Y; maximal velocity of flow at the unsheared core, $v_{Max;}$ yield stress, σ_Y. Based on Coulson, Richardson, Backhurst & Parker (1999a).

2.3 Shear deformation in pipe flow

2.3.1 Velocity and shear gradients in pipe flow

As fluid travels along a pipe, the flow velocity decreases from the pipe centre to the wall due to friction on the fluid at the pipe wall (fluid-boundary interaction). The development of frictional drag is a function of pipe roughness and diameter, fluid flow rate and fluid flow behaviour. For continuous laminar flow of fluid in a circular pipe, the shear stress decreases linearly from a maximum value at the wall to zero at the centreline (Fig. 2.7 left), with a corresponding decrease in shear rate from the pipe centreline to the wall.

As a result of the shear stress gradient, slowing of fluid velocity due to friction decreases in a non-linear fashion from the pipe centreline to the wall. The shape of the fluid velocity gradient profile depends on the fluid properties. During flow of a yield stress fluid in a circular pipe (see Fig. 2.7 right) "if the shear stress at the wall is less than the yield stress, no flow occurs. If it is greater than the yield stress, flow will take place in the region between the wall and the point where the shear stress equals the yield stress. Inside this region, the fluid will flow as an unsheared plug" (Coulson et al., 1999a, p. 112). Regions of a fluid with yield stress behaviour are slowed or stopped close to the wall, while the fastest fluid velocity is experienced by a core of fluid at the pipe centre travelling at the same rate. This simplified model is presented to introduce the role of yield stress in pipe flow. Rao (2007a) gives a more extensive 3D model of flow forces generated on pipe flow.

2.3.2 Model application to flow behaviour of food fluids in pipe flow

Models for pipeline flow of power law fluids are well developed. Steffe & Daubert (2006c) consider that power law equations are a reasonable approximation of pipeline behaviour for pourable and

spoonable food fluids and for yield stress fluids which do not form extensive structure on standing. However, the fluid flow behaviour under extrusion-based AM occurs at a different scale to industrial food pumping applications, with rapid flow rates, smaller pipe and outlet diameter, and a requirement for dynamic yield stress behaviour (stop-start-STOP flow).

The pressure drop ΔP for a power law fluid under steady state laminar flow is calculated from:

$$\Delta P = \frac{2KL}{(d/2)}\left[\left(\frac{3n+1}{4n}\right)\left(\frac{4}{n(d/2)^2}\right)\right]^n Q^n$$, (Steffe & Daubert, 2006b).

L and d are pipe length and diameter, K and n, the power law parameters, and Q, the flow rate. For a shear-thinning fluid with $n < 1$, doubling the flow rate Q increases pressure drop by a factor of 2^n. As the flow rate increases the shear imposed on the fluid increases, decreasing the apparent viscosity of shear-thinning fluids (Steffe & Daubert, 2006b). Highly shear-thinning fluids drop by orders of magnitude: the more shear-thinning a Food-Ink is, the broader the change in apparent viscosity with increasing flow velocity. Pipe flow modelling of structured fluids is made more complex by the non-linear degradation of fluid velocity from the centreline to the wall in power law and yield stress fluids.

2.3.3 Flow behaviour on peristaltic pumping

Experimental measurement of flow in flexible tubing (i.d. 20 mm) was made under peristaltic pumping for shear-thinning, non-viscoelastic carboxymethylcelullose solution. The maximal fluid velocity occurred close to the wall in the pinched section, increasing local shear rate thirty-fold and halving apparent viscosity compared with flow in unpinched tubing (Tanner et al., 2012). Peristaltic pumping introduces periodic rapid increases in local shear deformation adding a non-linear, time-dependent term to the modelling of Food-Ink flow on piping, especially if the peristaltic pump is the sole source of flow in the Food-Ink 3D printer.

2.3.4 Fluids exiting a pipe

Under laminar flow conditions a Newtonian fluid exits a pipe of diameter d_{outlet} as a stream with the same diameter (Fig. 2.8), while viscoelastic fluids expand to a diameter greater than d due to the removal of the constraining force of the pipe walls on the fluid structure (Al-Muslimawi, Tamaddon-Jahromi, & Webster, 2013; Rao, 2007d). This die swell behaviour, which can be up to 300% expansion for a highly viscoelastic fluid, will affect the thread diameter of a fluid under extrusion-based AM. Depending on the fluid relaxation time, viscoelastic fluids may continue to flow after the pumping force is removed. This lag in response to the cessation of pumping is a negative factor in controlling intermittent Food-Ink deposition.

Fluid flow models can potentially predict the behaviour of viscoelastic fluids on exiting an outlet: open-source computational fluid dynamics software generated flow patterns corresponded to the experimental observations of the same fluids (Favero, Secchi, Cardozo, & Jasak, 2010). Specifications for a syringe-pump extrusion-based 3D printer system with a round outlet approximate the build resolution (i.e. the diameter of the deposited thread) as twice the outlet diameter (the imagine machine, 2013). Based on this assumption, the minimum values for outlet diam. were halved in Table 2.1 to compensate for thread swelling at the outlet of viscoelastic fluids.

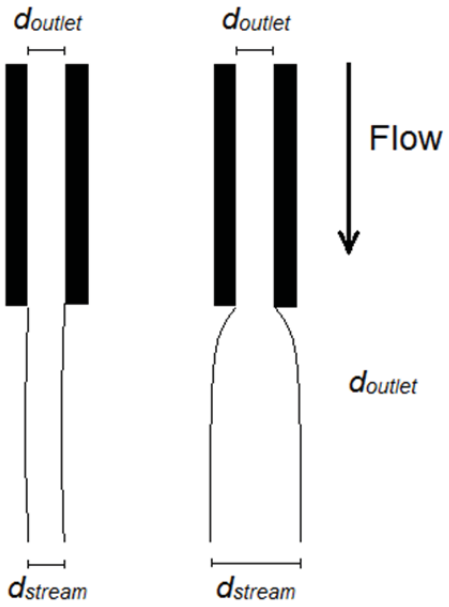

Figure 2.8 Die swell (as diameter of the fluid stream d_{stream} exiting a pipe with outlet diameter d_{outlet}) for a Newtonian fluid (left) compared with a viscoelastic fluid (right).

As well as managing die swell, the outlet flow behaviour of viscous Newtonian and non-Newtonian fluids may also produce random oscillation in flow (Lipton, Boban, et al., 2010), as observed for flow of the model paste exiting the Food-Inks 3D printer prototype during initial print trials (see Fig. 1.3).

2.3.5 Other aspects of pipe flow

In relation to equipment design for a Food-Inks 3D printer, constriction along pipe flow produces secondary flows may result in dead zones and in vortex flows that trap material (Malkin, 2012, p. 185). To deliver an intact voxel, the design of the mixer-to-deposition flow path must remove or minimise any constrictions that stretch or retard the coloured voxel. Extensional shear also stretches fluid components in pipe flow when sudden changes in pipe dimension occur (e.g. outlets, constrictions) (Rao, 2007d; Steffe & Daubert, 2006b). The flow behaviour of structured fluids under extensional shear is important if deposition is through an outlet that differs in diameter from the preceding pipe flow.

2.4 Rheological determination of stop-start-stop flow

2.4.1 Initiation of stop-start-stop flow in Food-Inks

Taking the Food-Ink in the reservoir, the pumping force must overcome the yield stress fluid in order to begin continuous flow into the mixer (stop-START-stop behaviour). If fluid in a reservoir has rested long enough for all structures to be fully relaxed, this is the static yield stress. If the fluid has recently been sheared, the observed yield stress value depends on how much structure has reformed since the previous deformation cycle, so yield stress behaviour (relaxation time for regaining structure) and the capacity to be self-supporting must be evaluated.

On depositing the Food-Ink fluid, a voxel must recover structure very rapidly after deposition (stop-start-STOP behaviour). Food-Inks also need to resist slumping after deposition which results from the hydrostatic pressure of consecutive layers in order to maintain voxel shape and position until setting. A

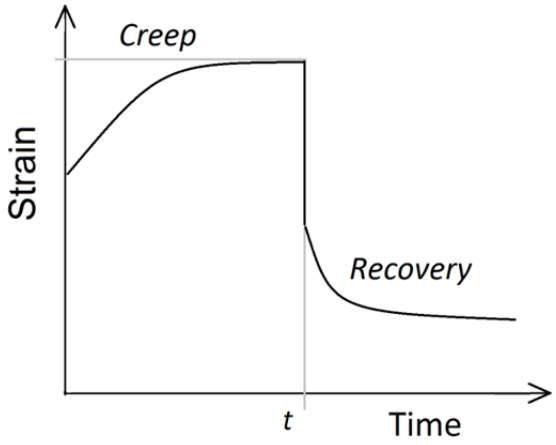

Figure 2.9 Schematic strain-time curve for a time-dependent strutured fluid on loading and removal of a constant low shear deformation (creep-recovery); *t*, time of removal for the deformation force.

review of hydrogel structure-forming solutions (e.g. alginates, gelatin, chitosan) for extrusion-based 3D biofabrication of cells gave a preferred time of 2 s for recovery of hydrogel structure or structure setting after deposition (Murphy, Skardal, & Atala, 2013), although few biofabrication polymer systems in use fall near this value. In the case of biofabrication, structure formation is assisted by activation of cross-linking reactions, either by mixing in activator before deposition, or by deposition into a structure-setting solution (e.g. alginate into salt solution).

2.4.2 Static yield stress determination under increasing rotational shear

One test to determine fluid yield stress applies a rotational shear deformation with a gradual increase in stress rate to a sample which has fully recovered structure after placement into the rheometer test geometry (Malvern Instruments, 2012). The static yield stress is determined from the stress at the inflection point of the flow curve that indicates the start of fluid flow. The static yield stress value is needed for modelling Food-Ink stop-START-stop flow, and predicting fluid velocity profiles during piping.

2.4.3 Creep-recovery testing for Stop-start-STOP flow behaviour

In a creep-recovery test (Fig. 2.9), a constant low-shear rotational or oscillatory stress is first applied to the fluid for a fixed time (*creep* phase), then removed (*recovery* phase). Fluids which exhibit a time-dependent decrease in viscosity under constant strain gradually acclimate, until a steady state is achieved in the stress-strain response. An estimation of structure reformation on the removal of the shear stress can be calculated from the recovery phase response (Rheoplus/32 software, version 2.81). In this case the parameter of most interest is the relaxation time related to structure reformation.

2.5 Post-deposition flow after extrusion-based AM

Minimal relative movement of the deposited material is required between deposition and structure setting to maintain the positional information introduced on extrusion-based AM. The factors influencing structure distortion are fluid flow after deposition, hydrostatic pressure (including the effect

of placing additional layers over deposited material) and the timeframe for the deposition/setting process.

2.5.1 Models for slump and spreading flow

In tests of spread for concrete, the gravitational flow of concrete released on removal of a cylindrical mould is defined as *slump* when post-spread height is greater than the radius, and as *spread flow* when the inverse is true (Pierre, Lanos, & Estellé, 2013). The consistometer test system provides a similar test rheology for fluid foods (Coussot, 2005d). Slumping is a planar flow behaviour with a yield stress component. Complete modelling of fluid behaviour under this extensional flow requires analysis of both radial flow along the XY-plane and downward flow along the Z-axis. Mathematical models for concrete derive values from the radius and height of fluid flow after release from a cylinder for the flow behaviour under extensional shear (response to stretch forces) (Coussot, 2005d), and for the planar yield stress (Malvern Instruments, 2012).

Separate models exists for pure-spread flow with no slump (yield stress σ_{YS} < 18 Pa); pure-slump flow with negligible spread (σ_{YS} > 100 Pa); and for intermediate flows (18 Pa > σ_{YS} > 100 Pa) (Pierre et al., 2013). As these simple slump/spread models do not include a relaxation time parameter, this needs to be determined experimentally: during the timecourse of a print run using extrusion-based AM for example, the relaxation time for appreciable spread to occur before structure setting may be long enough to prevent significant post-deposition distortion.

2.5.2 Post-deposition structure models for hydrogels

2.5.2.1 Influence of extrusion nozzle shape on deposition rate

Chung et al. (2013) modelled typical hydrogel extrusion-based AM through small diameter nozzles (0.1-0.4 mm), using alginate-gelatin mixtures piped into calcium chloride solution as a cross-linking reagent, and compared the post-print formation of structure with flow behaviour modelled under oscillatory shear deformation. Calculated and experimental flow rates of alginate through a tapered nozzle required lower pressures to deliver the same flow rate when compared with a cylindrical nozzle (Li, Tian, Schryer, & Chen, 2011). Therefore, the way the outlet constricts a Food-Ink on deposition is a factor in determining the work W required to generate flow in the Food-Ink printer.

Die swell is also influenced by pipe length before the outlet: a longer residence time allows a structured fluid to reform some structure so that fluid memory of compression within the pipe has decayed, so reducing die swell (Shenoy, 1999b). However, the small scale and short timeframe of the Food-Inks 3D printing application may fall outside fluid relaxation times relevant to decay of die swell behaviour on deposition.

2.5.2.2 Influence of outlet shape on voxel spread

The shape at the outlet will influence voxel spread. By analogy with spread tests, for a continuous thread of deposited material a round outlet reduces the potential for slumping compared with a square outlet (Fig. 2.10), as the round outlet deposits a flattened cylindrical shape, closer to the optimal hemispherical shape at which spreading forces are most evenly distributed. However, a cubic voxel fills the entire volume of the print line when first deposited, whereas a cylindrical thread produced by a circular outlet must spread and slump to some degree to fill gaps between adjacent lines of cylindrical voxel trains. The Food-Ink relaxation time for structure reformation will be important in determining whether the printed material slumps to the correct degree before setting.

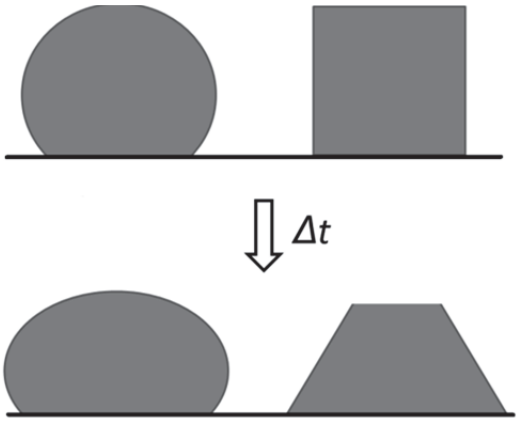

Figure 2.10 Schematic of shape development on slumping with change in time Δt for an unsupported thread produced from a circular or a square outlet.

2.5.3 Model for outlet flow of non-Newtonian fluids

The thread diameter on extrusion-based AM is a function of the fluid flow rate and the outlet travel rate. Khalil & Sun (2007) derived a general expression for the rate of outlet flow Q for power law fluids:

$$Q = \left(\frac{n}{3n+1}\right)\pi\dot{\gamma}_0^{\frac{n-1}{n}}\left(\frac{\partial P/\partial z}{2\eta_0}\right)^{1/n} r^{\left(\frac{3n+1}{n}\right)},$$

where r is the radius of the outlet, P is flow pressure in the system, η_0 the limiting fluid viscosity at shear rate, $\dot{\gamma}_0$ is the shear rate at η_0, ∂z the height drop, and n the power index of the fluid. This equation estimates flow rates required to produce a round thread of radius r for a given rate of outlet travel. The study modelled the flow velocity required to produce extruded threads thinner than, equal to, or thicker than the desired thread diameter.

2.6 Doughs and batters are multiphase foamed dispersions

2.6.1 Fluid components of doughs and batters

The first Food-Inks prototype product is a cake- or bread-type food with an embedded image. To produce the desired structure, a Food-Ink for such a SP must be a pipeable batter with controllable time-dependent behaviour. Dough/batter is a *multiphase* structured fluid, with gas and solids present as

particles in a non-Newtonian continuous liquid phase. The gas, liquid and solid phases interact with each other to influence the flow behaviour, and the interpretation of the bulk rheological properties in any multicomponent fluid must take into account interactions between the components under flow.

In dough/batter a liquid phase rich in solubilised protein and polysaccharide biopolymers provides the continuous phase for both the gas-liquid *foam,* and for the solid-liquid *dispersion* which contains flour cell fragments, starch granules and aggregated solids. Fats may form an emulsion if comprised of liquid fats or of solid fats in the presence of sufficient industrial emulsifier; or may form a discrete soft solid phase in the absence of added emulsifier. Visual observation by light microscopy of fluid flow in SP batters made using different flours (see timecourse videos of batters in .avi format, accessible on the CD insert of this thesis, and discussed in section 4.5.1) illustrates the diverse range of *micro-rheological* events (interactions between individual particles in the fluid under flow) that may contribute to the bulk flow behaviour in SP formulations.

While in this section focuses flow behaviour of multiphase SP doughs and batters, the discussion is also relevant to other multiphase food fluids which may be used as Food-Inks, and more generally, to particle-containing fluids under extrusion-based AM.

2.6.2 Examples of multiphase fluid flow behaviour models

There may be suitable bulk rheological models to describe aspects of batter dispersion behaviour under piping, mixing and deposition during extrusion-based AM. However, fundamental models for micro-rheological interactions between bubbles, particulates and the liquid phase in multiphase are only just being developed, (e.g. Chateau, Ovarlez, & Trung, 2008). Mader et al. (2013) described the rheological properties of lava magma systems in terms of two separate models, one for the behaviour of the gas-liquid component, and a second for the particulate-liquid component. Molten lava is a simpler multiphase system than dough/batter, as the liquid phase is Newtonian. Kogan et al. (2013) modelled micro-rheological interactions in a foam with an emulsion in the liquid phase. In this multiphase fluid the non-gas particles were not rigid particulates but deformable emulsion drops. These are a few recent examples - multiphase fluid behaviour is a rapidly expanding area of research.

2.6.3 Flow models for particulate dispersions

When solid particulates are added to a polymer fluid, depending on the type of particulate the fluid response with increasing volume fraction of the particulates is modified to that of a yield stress power law fluid at low shear values (Rayment, Ross-Murphy, & Ellis, 1995), or to more complex models of flow behaviour (Shenoy, 1999c, 1999f). Spherical particulates in a Newtonian liquid produce non-Newtonian flow behaviour so that the apparent viscosity of the dispersion changes with particle volume fraction and number density. The length-scale of particulate-particulate interactions is important in determining the overall flow response of dispersions. For a concentrated dispersion made using plastic polymer melts and added particulates, when the dispersion particulate size is < 10 μm the apparent viscosity increases logarithmically with a decrease in particulate size; but when particulate size is > 10 μm the apparent viscosity increases linearly with particle size (Shenoy, 1999a). In an food example involving small rice starch granules (6-10 μm diam.) in semi-dilute guar solution, flow behaviour could be best

fitted to a Cross fluid flow model (see Fig. 2.5) with the addition of a relaxation time parameter to the yield stress component (Rayment, Ross-Murphy, & Ellis, 1998).

In modelling dispersion flow, differences in the maximum possible particulate packing fraction ($\phi_{\text{Particulate max}}$) that result on varying particulate shape and size can be accounted for by normalising the particulate volume fraction ($\phi_{\text{Particulate}}$) to give a *normalised particulate volume fraction*, $\phi'_{\text{Particulate}}$:

$$\phi'_{\text{Particulate}} = \phi_{\text{Particulate}} / \phi_{\text{Particulate max}}.$$

Similarly, a normalised dispersion viscosity ($\eta'_{\text{Dispersion}}$) can be derived by dividing dispersion viscosity by the viscosity of the particulate-free liquid phase:

$$\eta'_{\text{Dispersion}} = \frac{\eta_{\text{Dispersion}}}{\eta_{\text{Liquid}}}.$$

One model for the relationship between particulate volume fraction and dispersion viscosity is the Krieger-Dougherty equation, derived from the theoretical interaction between single spheres of similar size (Rao, 2007c):

$$\eta'_{\text{Dispersion}} = (1 - \phi'_{\text{Particulate}})^{-\eta(\phi_{\text{Particulate max}})}.$$

As the particulate volume fraction is difficult to quantify for soft deformable food particulates, the phase contribution of the particulate fraction may be calculated by replacing particle volume fraction with the particulate dry mass fraction (Lopez-Sanchez & Farr, 2012) or by estimating the maximal particulate fraction from the viscosity increase with increasing concentration of particulates in dilute solution (Van Der Vaart et al., 2013).

Shenoy (1999c, 1999e, 1999f) discussed relevant models for particulate interactions in detail and identified the following factors as influencing the viscosity response of dispersions:

- Particulate size, shape and roughness
- Number density of contacting particulates
- Particulate size distribution
- Electrostatic interactions that cause repulsion or attraction between particulates
- Rotation of individual and agglomerated particulates and effect on liquid phase flow.
- Association of polymer or surfactant molecules on the particulate surface that modulate electrostatic behaviour.

The deformability of particulates (e.g. the elasticity of blood cells) will also modulate fluid viscosity by introducing an elastic component into the fluid response.

Some *polydisperse* dispersions of electrostatically neutral particulates may display better pipe flow characteristics than expected. For example, dispersions containing coarse particulates (size > 100 µm) within a dispersion of finer particulates generally exhibit a minimum in apparent viscosity at a mass ratio of 25: 75 of coarse-to-fine particulates (Shenoy, 1999f). The fine particulates delay settling of the coarse particulates if the liquid phase has insufficient yield stress to counteract gravitational settling (Coulson, Richardson, Backhurst, & Harker, 1999b). They shield particulate-particulate interaction between larger particulates, lubricating dispersion flow (Shenoy, 1999c). Farris (1968) produced a model for the viscosity of polydisperse mixes of electrostatically neutral spherical particulates that predicted

experimentally-measured viscosity values. Recently Choi, Young & Kwon (2013) added terms derived from the pipe flow behaviour of cement mixes to Farris's model to account for shape deviation from sphericity.

Particulate dispersions in doughs and batters are polydisperse. Ungelatinised starch granules can be considered as electrostatically neutral. Cell wall fragments may have some charge on hydration (generally cationic for plant polysaccharides), but the salt conditions typical in SP batters (50-100 mM NaCl) discourage the development of extensive electrostatic interaction between charged biopolymers. Flour particulate polydispersity would be predicted to modulate dough/batter flow, depending on the particulate size distribution and packing fraction, and assuming no electrostatic particulate interactions. Adding electrostatically neutral particulates to polymer plastics may decrease viscoelastic behaviour on high-pressure extrusion (Shenoy, 1999e), suggesting that Food-Ink flow behaviour on piping and post-deposition spread could be modulated by particulate addition.

2.6.4 Foam structure and flow

Foams may be produced as *monodisperse* bubble distributions of similar size or as polydisperse distributions, depending on the mode of production (Weaire & Hutzler, 1999). A foam is a non-equilibrium system and bubble number density and size distribution change as bubbles interact, coalesce and collapse on aging. Monodisperse bubble populations are more stable on standing than polydisperse populations (Sahu & Niranjan, 2009). An important attribute of foams is the interfacial surface tension of the bubble (Γ), a measure of the capacity of molecules at the gas-liquid interface to cohere and contract. Interfaces with lower surface tension have greater capacity to minimise the bubble surface area and to reform a spherical shape after deformation.

Foams can be separated into three categories, depending on the density of bubble packing (Cohen-Addad, Höhler, & Pitois, 2013). *Bubbly liquids* have a bubble population in which all bubbles can move freely and generally are spherical. At a critical maximal bubble packing fraction ($\phi_{\text{Critical Bubble}}$) bubble movement begins to be constrained by neighbouring bubbles and the bubbly liquid transitions to a *wet foam*. As points of contact develop between bubbles and spherical bubbles distort, the wet foam is in transition to a *dry foam,* in which fluid channels between two bubbles thin to form classic *Plateau borders* containing the minimal amount of liquid to retain the bubble structures. Bubbles develop polyhedral shapes to minimise the surface energy on packing as foams become drier. In SPs, polyhedral voids with typical dry foam structure are usually present only near the top of highly-expanded breads. The mesostructure of most SP products retains packing features and bubble shapes typical of wet foams or wet foams in transition to dry foams.

A *normalised foam viscosity* (η'_{Foam}) can be calculated as for normalised dispersion viscosity (see section 2.6.3) by dividing foam viscosity by liquid phase viscosity (η_{Liquid}). The value for η'_{Foam} is related to fluid flow rate, gas phase volume (ϕ_{Gas}) and to the typical relaxation time for the bubble, λ_{Bubble}. For an ideal bubble the relaxation time is related to the viscosity of the surrounding fluid, the radius of the undeformed bubble r, and interfacial surface tension Γ, by:

$$\lambda_{\text{Bubble}} = \frac{\eta_{\text{Liquid}} \cdot r}{\Gamma},$$ (Mader et al., 2013).

Under flow, a bubble deforms due to friction of the fluid on the bubble surface (*drag*), while surface tension acts to minimise surface area, returning the bubble to a spherical shape. The Capillary number (Ca) is used as a predictor of bubble shape at a set flow velocity. Ca is a dimensionless ratio of the viscous versus surface forces, derived from the bubble surface tension, liquid phase viscosity and fluid phase velocity, v:

$$Ca = \frac{\eta_{\text{Liquid}} \cdot v}{\Gamma}.$$

2.6.5 Behaviour of foams under shear deformation

Herzhaft, Kakadjian, & Moan (2005) examined steady state foam flow in a pipe system (i.d. 20 mm) at shear rate between 10^1-10^3 /s (a range relevant to oil pipeline flow), for a Newtonian fluid with continuous generation of surfactant bubbles, and ϕ_{Gas} between 20-85%. Below a ϕ_{Gas} of 50% the foam was a bubbly liquid, and flow behaviour was similar to that modelled for moderately concentrated emulsions. Above 60% ϕ_{Gas}, when foam bubbles start to transition to a dry foam and bubble crowding begins, the foam pipe flow became highly shear-thinning. Finally, between 60-70% ϕ_{Gas} the apparent viscosity became proportional to Ca, the foam Capillary number. The ϕ_{Gas} of a foam greatly influences both piping flow and yield stress behaviour.

Air inclusion into for egg-rich sponge batter uncooked SP batters by whisking typically generates ϕ_{Gas}at ~50% (e.g. Chesterton et al., 2013; Massey, Khare, & Niranjin, 2001). The maximum ϕ_{Gas} value reaches a plateau value during beating that depends on the emulsifying capacity of the formulation (Sahu & Niranjan, 2009). The ϕ_{Gas} may be < 50% in batters produced with a minimal physical incorporation of air by beating, or which depend on solely on heating to drive foam expansion. Ca was found to be a poor predictor of flow under shear deformation for foamed batter flow (Chesterton et al., 2013), unsurprising given Ca is most relevant to high ϕ_{Gas} foams.

2.6.6 Between-domain interactions in biopolymer-containing fluids

As previously discussed (section 1.5.2), mixtures of soluble biopolymers may have limited co-solubility, producing separate domains within a structured fluid (Tolstoguzov, 2003). This may generate additional structure within the bulk liquid phase to influence flow behaviour.

2.6.7 Yield stress behaviour of dispersions and foams

When the particle density is high enough, inter-particle networks must be disrupted before flow begins (i.e. yield stress behaviour). Fluids in this state have been described as *soft-jammed* systems (Coussot, 2005b). Yield stress behaviour can be exhibited by polymer solutions and particulate dispersions, with yield stress behaviour depending on the relative influence of between-particle short-range attraction and polymer/particulate content (Emady et al., 2013). *Colloidal glasses* with yield stress behaviour form when polymers or dispersions with uncharged particulates (e.g. toothpaste) develop fluid structure as particles become so crowded that particulate movement is hindered by physical interaction between neighbours. If the particulates carry a charge (e.g. clays, charged polysaccharides),

structure is formed by electrostatic repulsion and attraction between particles, or by particulate aggregation that encourages charge shielding, resulting in yield stress *colloidal gels* and *sols* (e.g. shampoo) when particle-particle interactions become significant (Emady et al., 2013). Yield stress behaviour develops when these fluids develop enough structure to resist initial shear deformation.

Foams do not exhibit significant yield stress behaviour until undeformed bubbles are fully packed at $\phi_{\text{Critical Bubble}}$ (i.e. only in wet and dry foams) (Cohen-Addad et al., 2013). The initial resistance of the foam to shear above $\phi_{\text{Critical Bubble}}$ is primarily due to elastic energy stored by the gas-liquid interface (Cohen-Addad et al., 2013; Rust & Manga, 2002) which also results in viscoelastic behaviour of wet and dry foams under oscillatory shear deformation (Mader et al., 2013).

2.6.8 Uneven development of flow in foams and dispersions

Measurements of flow behaviour in yield stress and structured fluids must be interpreted cautiously, especially at the start of fluid flow. Wall slip has previously been mentioned, and refers to the development of a lubricating layer at the boundary between vessel and fluid in structured fluids. Particles are at lower density near the wall because they cannot pack fully against the boundary surface. Similarly, for polymer solutions the friction of the wall on the polymer network disentangles individual polymer molecules, reducing local network structure (Coussot, 2005a). The use of roughened plates with deep indentations in rheometric test systems in place of smooth surfaces reduces wall slip by providing pockets in which particles and polymer networks can maintain packing density.

When the flow on shear deformation occurs initially in only a thin band of a structured fluid, this *shear-localisation* behaviour means that until flow develops fully the measured value for apparent viscosity may represent only a small part of the fluid response (Coussot, 2005a). *Shear-banding* refers to the transitional fluid behaviour between the first initiation of localised flow and full initiation of flow across the rheometer gap (Coussot, 2005a). Bonn & Denn (2009) consider that all non-ideal yield stress fluids exhibit a discontinuous transition (shear-banding) under deformation, as the structures that contribute to yield stress experience structure-healing and structure-breaking events simultaneously under shear deformation.

2.6.9 Rheological testing of Food-Ink flow behaviour

Multiphase Food-Ink formulations containing bubbles, concentrated emulsions and/or particulates) will have a complex response under stop-start-stop flow; while different stages of the Food-Inks 3D printing application require markedly different flow behaviours. To characterise Food-Ink formulation flow in the Food-Inks 3D printer system and to test prototype Food-Ink formulations requires development of an integrated suite of rheological tests to evaluate pipe flow behaviour, stop-start-stop flow characteristics, dye mixing and post-deposition slumping of Food-Ink formulations.

2.7 Rheometric test systems

2.7.1 Test systems for pipe flow behaviour

Steady-state pipe flow is often measured in a closed-loop pumping system, with pressure transducers to determine pressure drop in the test system. Capillary flow geometries evaluate steady

state fluid flow under pumping. These systems generally require large volumes of fluid and long pipe lengths (> 100 x pipe radius) in order to establish steady state flows (Coulson et al., 1999a). At small volumes the Vilastic-3.1 controlled stress capillary rheometer (Vilastic Scientific, Austin, US) determines fluid response to both oscillatory and extensional deformation by pumping fluid back and forth in a small-bore capillary fluid. It has been used to characterise flow behaviour of fluids such as blood and ketchup, and this dual-use rheometer system is potentially the best option for characterising Food-Ink flow characteristics.

In this study, access to rheometric test systems for shear deformation was limited to plate-plate, cone-and-plate and, cup-and-bob fundamental test geometries, and an empirical back extrusion test geometry.

2.7.2 Back extrusion test system

The back extrusion test system measures the force taken to compress and withdraw a piston into a cylinder filled with the test fluid, with a gap of at least 2 mm between piston and cylinder. Back extrusion is an imperfect squeezing flow test (Coussot, 2005c) and is used in quality testing of foods such as mayonnaise. Both compression and withdrawal stages are used as indicators of fluid consistency and cohesion. The back extrusion response curves quantify initial resistance of the fluid to displacement and the force value for material flow once any yield stress is overcome.

On compression the point of maximum force is a measure of relative fluid firmness, the area under the curve is a measure of consistency, while on withdrawal the maximum negative value is a measure of fluid cohesiveness (see Fig. 2.11 bottom). The area under the negative curve is related to both cohesiveness and viscosity (Angiolini & Collar, 2008). With more extensive data acquisition, back extrusion parameters can be correlated to the corresponding shear deformation values determined using a vane-and-cup geometry (a mathematically modelled geometry) (Perrot et al., 2011), and may be used to estimate fluid yield stress (Coussot, 2005c).

As an example of back extrusion carried out in this study, uncooked idli batter prepared as described in section 3.4.1 was tested before sodium bicarbonate addition (i.e. with no CO_2-generated aeration from leavening agent). Rice2 idli batter is easily pourable, blackgram batter is a stiff, sticky paste, while sorghum batter is less stiff than blackgram batter, but not yet pourable.

The back extrusion force-time curves shown in Fig. 2.11 top are for the three batters, on measurement using the method in section 2.7.2.1. The roughness of the blackgram batter curve on withdrawal corresponds to shear-localisation events in which the batter is caught between two shearing surfaces (TA Instruments, 2014). Fig. 2.11 bottom shows the zones used to calculate back extrusion parameters. The area under the compression curve between the start of deformation and the line at position 2, from start of deformation to start of steady state, quantifies the work required to reach the steady state plateau.

In this study, the values reported were the maximal force, F1, the work done to reach steady state and the mean steady state force between points 2 and 3 (blue line). The work done to reach the steady state plateau includes the yield stress component. The value at F2 is a measure of fluid cohesiveness once the structure of the fluid at rest has been disrupted.

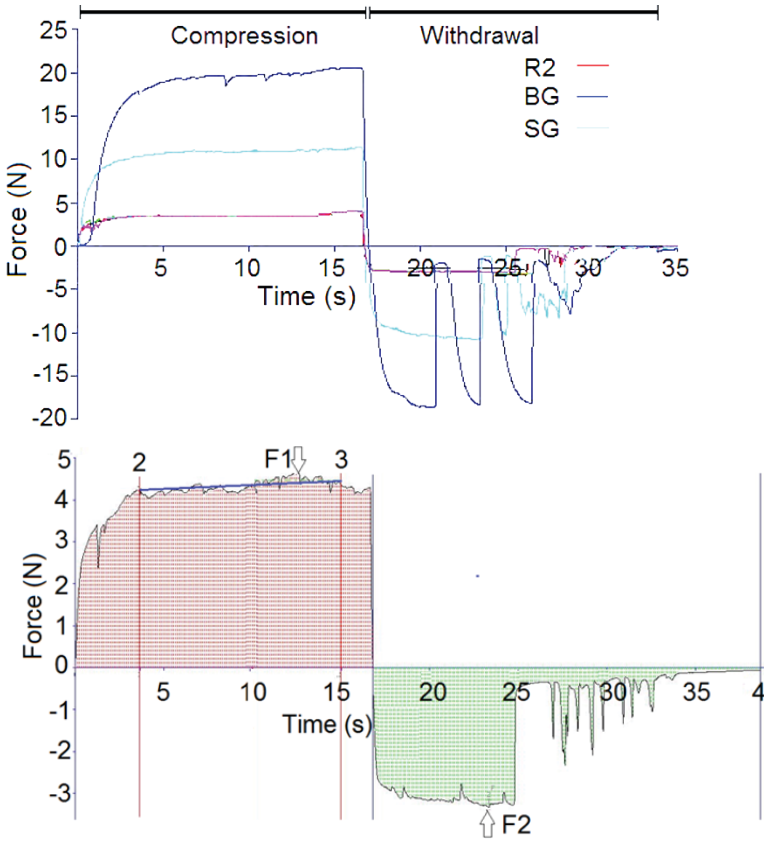

Figure 2.11 Top: typical force-time curves on back extrusion for rice2 (R2), blackgram (BG), and sorghum (SG) idli batters (before sodium bicarbonate addition). Bottom: zones used to calculate back extrusion parameters. F1 = Firmness, F2 = Consistency value.

2.7.2.1 Method for back extrusion rheological testing

- *Flow was analysed in a back extrusion cell (diameter 43 mm, volume 86 mL) with piston (diameter 41 mm) fitted to a TA.XT.plus texture analyser system with 50 kg load cell (Stable Microsystems, Goldaming, UK), and subjected to piston displacement to a depth of 25 mm at 1.50 mm/s, followed by a return to starting position at 4.0 mm/s.*
- *TA.XT.plus software was used to calculate back extrusion parameter (see Fig. 2.11 bottom).*

2.7.3 Pipe flow of pastes

Wilson & Rough (2012) described the use of a Benbow-Bridgewater ram-extrusion rheometer (a syringe pump with a narrow outlet) to model paste flow parameters for design of extrusion equipment. Both bulk fluid yield stress and a yield stress at the outlet wall (*wall yield stress*) can be derived, assuming the fluid flows primarily as an unsheared plug. Vane rheometry is also commonly used to evaluate yield stress for spreading flow behaviour, and to evaluate flow properties of foams.

2.7.4 Test systems for slump and spread

Possible test systems for fluid spread and slump under gravitational and extensional shear include the consistometer test system (Coussot, 2005d), (in which a cylinder of fluid is released from the bottom and allowed to spread), squeezing flow between two plates (Rao, 2007d) sliding plate

rheometry, and inclined plane rheometry (Bonnoit, Darnige, Clement, & Lindner, 2010).

2.8 Design considerations for pipe flow in the Food-Inks 3D printer

The pipe flow behaviour of non-Newtonian yield stress fluids must be taken into account when designing for Food-Ink flow during mixing and post-mixing flow. All material from a coloured voxel must be removed from the walls of the mixer chamber and post-mixer tubing before mixing and depositing the next voxel. Additionally, the profile of the fluid front migrating in the pipe must be as flat as possible. The potential solution space to minimise unwanted retention of coloured Food-Ink materials at the wall includes both equipment and formulation design options. If small-volume voxels are to be deposited accurately, any non-Newtonian, yield stress or viscoelastic flow behaviour of Food-Inks on exiting the pipe outlet must be considered.

An optimal mixer design should deliver a discrete voxel in a way that cleans out the mixer chamber without being part of a continuous flow (with associated flow profile). Strategies for the design of flow behaviour between mixer and deposition site include:

- Minimisation of the fluid path between mixer and deposition site. For example, mounting the mixer, dye metering and deposition outlet on a static head, while the deposited material is moved on a platen to provide the Z-axis motion for 3D printing.
- Minimisation of the radius of the sheared region compared with the radius of the unsheared core in pipe flow (by minimising yield stress of the Food-Inks, or maximising plug flow behaviour).

2.9 Flow behaviour in model xanthan-particulate dispersions on shearing

2.9.1 Initial pumping trials for the first 3D printer prototype.

A dispersion of xanthan solution incorporating rice flour was trialled as a model paste for the Food-Inks 3D printer prototype on pumping and mixing (see section 1.3.1). The paste could be pumped through the first printer prototype using a peristaltic pump, as long as a static mixer was not attached to the system (which increased the pumping pressure required above the capacity of the pump). The model paste did have reasonable deposition properties (Fig. 2.12 left). It maintained continuous piping for three layers without excessive spread within the specified print time for printing a Food-Ink structure (8 min; Table 1.1). It produced a bread-like structure on microwave cooking when chemical leavening was added (Fig. 2.12 right). However, the piping and deposition properties of this xanthan-rice flour dispersion were sensitive to small differences in hydration and mixing history during preparation. Small increases in aeration during preparation reduced pumpability markedly.

For further rheological studies, xanthan-based particulate dispersions were chosen to model stop-start-stop flow behaviour in a batter-based Food-Ink. Xanthan polysaccharide solution is added to some toothpaste formulations to give typical stop-start-stop flow behaviour. It is also used extensively as a food grade viscosifying agent, and to substitute for the structure-forming functionality of gluten in gluten-free SP formulations. Aeration (added gas phase to produce gas-particulate-liquid multiphase fluids) was omitted as a variable from rheological testing.

Figure 2.12 Left: example of a three-layer shape (the number 7) printed using the first iteration of the Food-Inks 3D printer (minus static mixer) and a xanthan-rice flour model Food-Ink, at ten min after printing. Right: the same formulation after addition of chemical leavening and cooking by microwave heating.

2.9.1.1 Method for xanthan stock preparation

- *A source of xanthan with well-characterised rheological behaviour and ready solubility was used to produce xanthan solution (Tixican Texture Smooth Pro, DIC, Hawkins and Watts, Auckland, New Zealand). Xanthan powder (20. 0 g) was added rapidly in a thin stream into 980 g filtered water. The powder was dispersed using an overhead stirrer over 2 h. Stirrer speed was varied during mixing to minimise xanthan lumping and any aeration during solubilisation. Once solubilised, 0.1% potassium sorbate (food grade) was incorporated by stirring as an antimicrobial agent. The 2% xanthan stock was stored at 4 °C for up to one week. Care was taken to minimise gas phase introduction during preparation.*

2.9.2 Xanthan solutions adapt rapidly to static and dynamic states

The development of xanthan-mediated stop-start-stop flow behaviour occurs even at low concentrations of polysaccharide. Xanthan has a high solution viscosity at low concentration due to the formation of (non-gelled) self-associated domains of long, stiff molecules in the presence of salts (Wyatt, Gunther, & Liberatore, 2011; Wyatt & Liberatore, 2009). The viscosity of xanthan-only solutions can drop 5, 000-10, 000-fold on application of shear stress (Viebke, 2004). The first transition from a disordered to an ordered polymer configuration occurs at very low polysaccharide concentration (0.024%) compared with other polysaccharides (Wyatt & Liberatore, 2009). Solution behaviour is affected strongly by the xanthan manufacturing process and heating history.

The addition of ionic components in solution masks xanthan side-chain interactions and encourages between-chain pairing, increasing the apparent viscosity of xanthan solutions. Ionic conditions reduce the activation energy required for xanthan molecules to transition to a more rigid conformation (Viturawong, Achayuthakan, & Suphantharika, 2008) and also stabilise the rigid conformation on heating (Viebke, 2004).

Xanthan solutions retain yield stress behaviour to much higher temperature than other food polysaccharides, up to 80 °C in the presence of 0.5% NaCl (Marcotte, Taherian, Trigui, & Ramaswamy, 2004). Xanthan polymer networks collapses readily under shear (highly shear-thinning), do not bind water tightly, and retain some structure on heating. These properties are important in the presence of ingredient transformations such as starch gelatinisation which depend on local water availability during heating.

2.9.2.1 Method to prepare model xanthan-particulate dispersions

- *A portion of 2% xanthan stock was centrifuged at 6, 500 g for 20 min at 20 ˚C before use to remove air bubbles. For xanthan-salt-rice flour dispersions (X-RF2), rice2 flour (previously characterised for composition and particle size, see Table 5.2) was dispersed into deaerated xanthan stock by gentle mixing in a 25 mL plastic vial with a plastic micro-spatula, to give an evenly mixed paste with minimal aeration. For xanthan-salt-microcrystalline cellulose dispersions (X-MCC), a few drops of acetone were first added to non-soluble microcrystalline cellulose (Avicel® PH105, FMC BioPolymer, Newark, US) to reduce hydrophobic clumping of the insoluble particulates on mixing with xanthan stock. Filtered water equivalent to the weight of xanthan stock was added, along with 0.5% NaCl, and mixed gently by spatula, to produce a final particulate dispersion and containing 1% xanthan, and 0.05% K sorbate and 0.5% NaCl (w/w) (both food grade), unless otherwise stated. The sample was slowly stirred to minimise aeration, using a small overhead stirrer which passed into the vial through a cover of Parafilm (Pechiney Plastic Packaging, Illinois, US) to limit water loss. After stirring for 15 min (microcrystalline cellulose) or 60 min (RF2), the sample vial was capped, and left at 20 °C until used for rheological testing (within 0-3 h). A xanthan-salt solution representing the liquid phase of the dispersion (X-salt) was also prepared by diluting xanthan stock solution to 50% and adding 0.5% NaCl.*
- *Dispersion density was determined by measuring four independent aliquots in a container of 0.500 mL volume (determined by weighing water at 20 °C), using a 4-place balance.*
- *Particulate maximum packing fraction was determined by determination of the point when the liquid phase becomes discontinuous (Rayment et al., 1995).*

2.9.2.2 Particulate size in model xanthan-particulate dispersions

A 1% xanthan solution prepared with 0.5% NaCl and 0.01% K sorbate (X-salt) was mixed either with non-soluble microcrystalline cellulose (MCC) or with rice2 flour (RF2) containing individual starch granules, large granule aggregates cell wall and endosperm fragments. From manual measurement of light microscopy images (Fig. 2.13 left) the MCC size distribution for the major axis had lognormal size distribution with geometric mean, 25.7 µm (Fig. 2.14 left) and a mean aspect ratio (major axis/minor axis) of 1.98 ± 1.41. Laser diffraction particle sizing of RF2, which is > 80% starch, gave a polydisperse distribution with peaks at 2.3, 20 and 142 µm. The 142 µm peak correlated with ellipsoidal particulates (intact rice grain surface cells filled with individual starch granules). These surface cells moved readily over each other on observing events in RF2 batter over time (Fig. 2.13 right; R2 +BiC .avi video files).

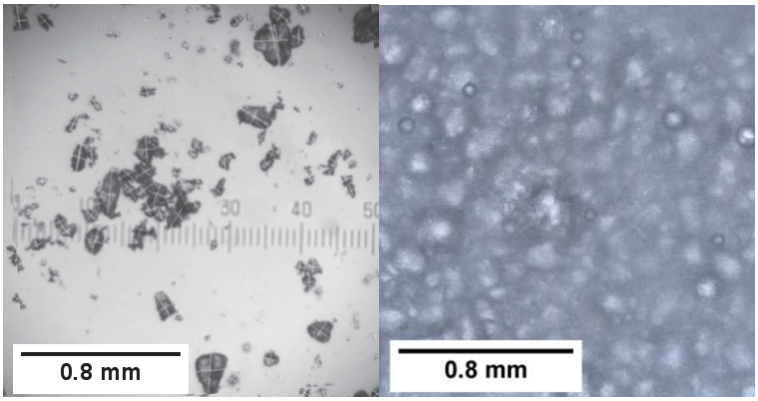

Figure 2.13 Visualisation of particulates used in model xanthan-particulate dispersions. Left: microcrystalline cellulose, MCC. Right: rice2 flour in idli batter. Egg-shaped starch grain cells dominate the particulate fraction; the small spheres with dark outlines are bubbles.

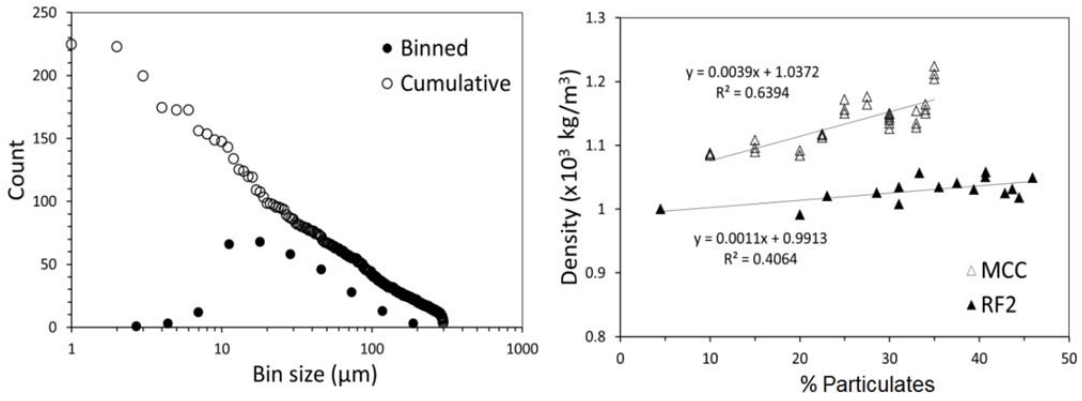

Figure 2.14 Left: MCC particulate size distribution (major axis length) as cumulative count, n = 300 (○), or binned count (●). The X-axis values represent the upper size limit of each bin. Right: the relationship between particulate content and dispersion density for RF2 (▲) and MCC (∆) in 1% xanthan-salt.

The increase in density with increasing particulate content was greater for X-MCC than for X-RF2, which maintained densities around 1 x 10^3 kg/m^3 (Fig. 2.14 right). This similarity in density between the particulate and liquid phases is common in food fluids. Many food dispersions contain neutrally-buoyant particulates (Lareo, Fryer, & Barigou, 1997), unlike the majority of non-food particulate systems for which flow behaviour has been modelled.

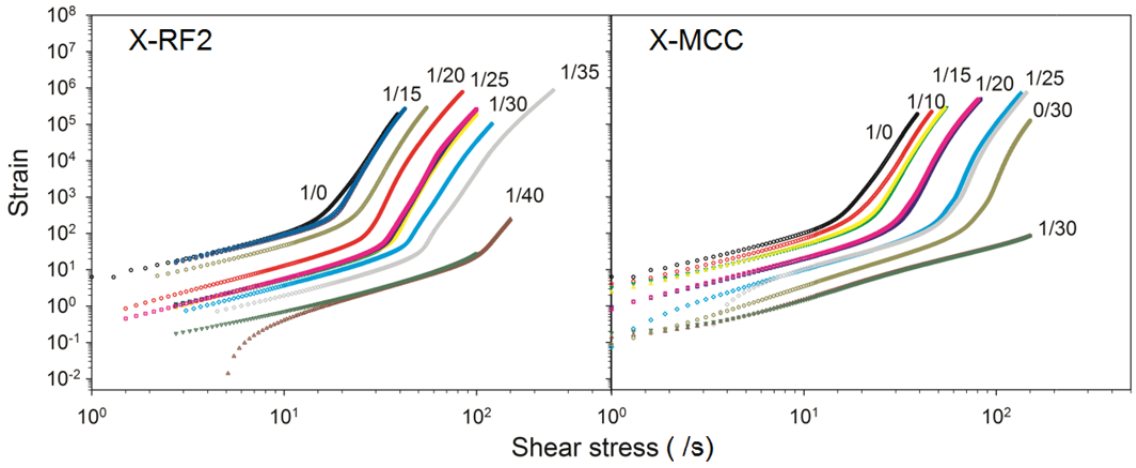

Figure 2.15 Stress-strain curve curves (including replicates) for flow under shear of particulate dispersions in xanthan-salt. Left: xanthan-rice2 flour. Right: xanthan-crystalline microcellulose plates with geometric mean length 26 µm (MCC) Labelling: e.g. 1/40 = 1% xanthan-salts/40% particulates. Data from replicate samples are overlaid.

2.9.3 Behaviour of model xanthan-particulate dispersions under shear

2.9.3.1 Static yield stress determination under rotational shear

Yield stress is measurable as a fluid bulk property as long as the test geometry gap is wider than any molecular events which structure the fluid (Ovarlez, Cohen-Addad, et al., 2013). A continuous shear test, with linear increment in shear rate 0-200 Pa, was run with roughened geometry to decrease the effect of wall slip. Preliminary experiments validated the choice of gap size for the 25 mm plate-plate test geometry, and for a suitable rest time for the sample after aliquotting. A yield stress test was carried out at increasing shear rate to a termination value of 100 /s, to examine flow behaviour of X-salt, X-RF2 and X-MCC. The static yield stress was determined as the inflection point on the stress-strain curve (Fig. 2.15).

Yield stress was first estimated manually from the stress-strain plots of representative samples, and compared with the calculated values produced by different analyses in the Rheoplus 32 software for yield stress determination. The 'Yield stress II analysis (upwards bend)' was chosen as closest to the manual estimates, and was used for further analyses. Normalisation of yield stress data was carried out by dividing by the mean yield stress for X-salt sample (0% particulates). A normalised mass fraction for particulate content (X') was calculated by dividing the added particulate content by the particulate content at maximal packing fraction (determined as 41% mass content for X-RF2, and 35% for X-MCC).

2.9.3.2 Methods for yield stress determination

- *An MCR301 model Anton Paar rheometer with Rheoplus 32/ Ver. 2.81 software (Anton Paar, Lisz, Austria) and a Peltier heating system was used for rheological analysis. Sample was loaded onto PP25 25 mm diam. roughened plates at 20 °C, set to a 1 mm gap. To prevent sample dehydration the gap was covered at the edge with a thin silicon oil layer, and sample was kept in a high-moisture enclosure.*

- *After resting for 30 min, the rotational shear test produced a linear ramp from 0-250 Pa in shear stress, with test termination at 100 /s.*
- *Yield stress was determined automatically using the stress II analysis (upwards bend) option.*

2.9.3.3 Static yield stress behaviour in model Food-Inks

Static yield stress for X-salt (0% particulate content in xanthan solution) (Fig. 2.15, 1/0 samples) was calculated as 18.3 ± 0.3 Pa, which is at the minimum value for fluids to develop self-supporting behaviour (Pierre et al., 2013). This level of xanthan content is around two-fold greater than that generally added to gluten-free SP formulations as a structuring aid. A yield stress well above 18 Pa is needed for a Food-Ink, as the bottom printed layer must support the weight of further layers if free-form printing is carried out.

With increasing particulate content, the yield stress (σ_{YS}) increased more rapidly for X-MCC dispersions than for X-RF2 dispersions (Fig. 2.16 left), to a maximum of 105 Pa and 50 Pa, respectively. Compared with X-salt, σ_{YS} was two-fold higher for 40% X-RF2; and five-fold higher for 30% X-MCC.

Values of σ_{YS} were normalised by subtracting the value of X-salt (with 0% added particulates), and plotted against normalised mass fraction (Fig. 2.16 right). An exponential relationship ($y = ae^z$) could be fitted to the data, with z values of 2.63 for X-RF2 and 6.03 for X-MCC. Rayment et al. (1995; 2000) reported logarithmic relationships for yield stress-particulate content for plots of semi-dilute guar dispersions containing either purified rice starch granules of 6-10 µm diam. or monodisperse MCC composed of rods with length ~25 µm (similar in size, but not shape, to the MCC used in this study).

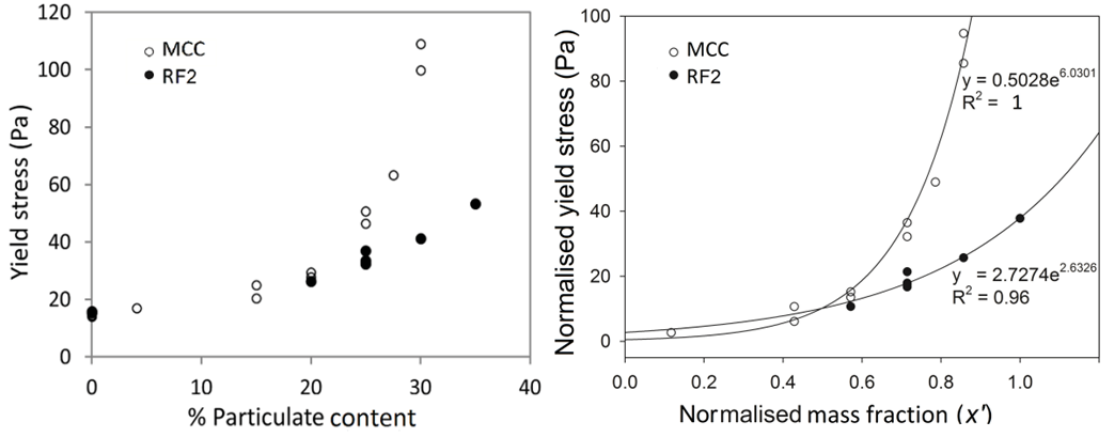

Figure 2.16 Yield stress plotted against particulate content for dispersions made with RF2 or MCC and 1% xanthan, 0.05% K sorbate and 0.5% NaCl. Left: derived from the inflection point of the stress-strain plot on rotational shear using the Rheoplus stress II analysis (upwards bend). Right: the same data plotted using normalised mass fraction x' (calulated by dividing by the mass fraction at maximum packing) and normalised yield stress (calculated by subtracting the yield stress of X-salt). Curves fitted using Sigma Plot 12.5.

2.9.3.4 Modifying slumping behaviour by manipulating yield stress

Addition of particulates may be a potential strategy to increase fluid yield stress in a background of X-salt to improve slumping over spreading behaviour (see section 2.6.3). An equation for self-supporting pastes is given by Wilson & Rough (2012) as:

$$Sl = \frac{\sigma_{\mathrm{YS}}}{\rho g h},$$

where ρ is density, g is gravitational force, and h the height of the paste. The value Sl must be < 1 for slumping to occur. It indicates the magnitude of self-supporting behaviour rather than an absolute value, as the nature of structure failure at the yield point must be considered.

The critical height for self-supporting behaviour was calculated for 25% X-RF2 and X-MCC from σ_{YS} and density values (i.e. solve for h when $Sl = 1$):

$$25\%\ \text{X-RF2} = \frac{3.29 \times 10^{1}\ \mathrm{N/m^2}}{1.0203 \times 10^{3}\ \mathrm{kg/m^3} \times 9.8\ \mathrm{N/kg} \times 1} = 3.2\ \text{mm, and}$$

$$25\%\ \text{X-MCC} = \frac{5.09 \times 10^{1}\ \mathrm{N/m^2}}{1.159 \times 10^{3}\ \mathrm{kg/m^3} \times 9.8\ \mathrm{N/kg} \times 1} = 4.5\ \text{mm.}$$

Assuming a thread height of 1.25-7.0 mm (Table 2.1), the heights at which the dispersions fail to be self-supporting suggest that they cannot support many layers of material. However, there is no relaxation time parameter in this equation - the time for appreciable fluid spread maybe longer than the time between printing and structure setting in the Food-Ink printing application.

Adding dense neutrally charged particulates such as MCC to increase the yield stress also increases the shear rate needed to start dispersion flow. From Fig. 2.16 left, to reach a yield stress above 60 Pa (halfway between 20 and 100 Pa, the yield stress range between spreading and slumping behaviour) requires a particulate content > 30% for MCC, and is never reached before the maximal packing content for RF2. This level of addition will interfere with any SP formulation, and will also be problematic in non-SP food systems. Adding neutrally charged particulates such as MCC to increase yield stress appears to be a poor strategy to improve stop-start-STOP behaviour of Food-Inks.

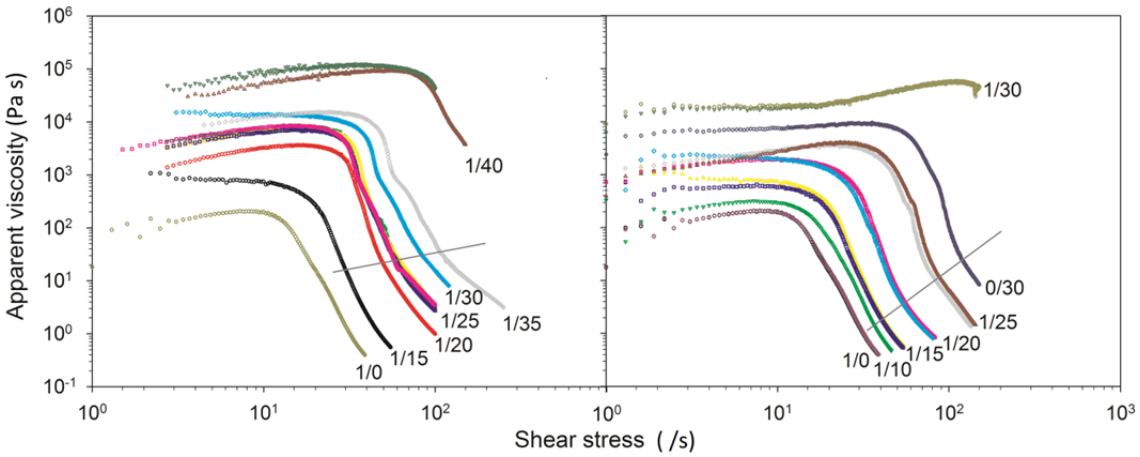

Figure 2.17 Viscosity-shear rate curves for flow under shear of particulate dispersions in xanthan solution with 0.05% K sorbate and 0.5% NaCl. Left: xanthan-rice2 flour (X-RF2). Right: xanthan-microcellulose cellulose (X-MCC) Labelling: e.g. 1/40 = 1% xanthan/40% rice flour (w/w). Lines are drawn on the graphs to indicate the approxiamte end of a log-linear relationship between shear stress and apparent viscosity.

2.9.3.1 Yield stress and shear-thinning flows in model particulate dispersions

On replotting the data in Fig. 2.15 as shear stress-viscosity plots (Fig. 2.17) it could be seen that apparent viscosity increased slightly until the yield point (point of inflection) and then reduced rapidly with increasing shear. The post-yield point slopes of xanthan-salt, MCC-salt only, X-RF2 and X-MCC solutions were generally similar in shape, but offset at increasingly higher yield stress and apparent viscosity values with increasing particulate content. This suggests a similarity in shear-thinning response between the polymer-only, particulate only and polymer-particulate fluids. The slopes for polymer-particulate solutions became less smooth with increasing particulate content, showing one or more inflection points. A line drawn across the slopes in each graph roughly indicates the end of the log-linear portion of the family of flow curves, below which the shear-thinning behaviour of the dispersions can be considered as tending to a plateau viscosity value. The apparent viscosity at the end of the log-linear response to shear deformation ranged between 20-50 Pa s for X-RF2, and 3-30 Pa s for X-MCC.

As a benchmark for the data plotted in Fig. 2.17, the viscosities of some typical flowing foods at room temperature are given in Pa s: water, 10^{-3}; light oil, 10^{-2}; cream 10^{0}; ketchup,10^{1}; rice pudding, 10^{2}; and smooth peanut butter, 10^{5} (Aguilera & Stanley, 1999; Smith, 2014, and others). At their yield points the xanthan dispersions were moderately to highly viscous (10^{2}-10^{5} Pa s) which falls between the apparent viscosity of tomato sauce and rice pudding.

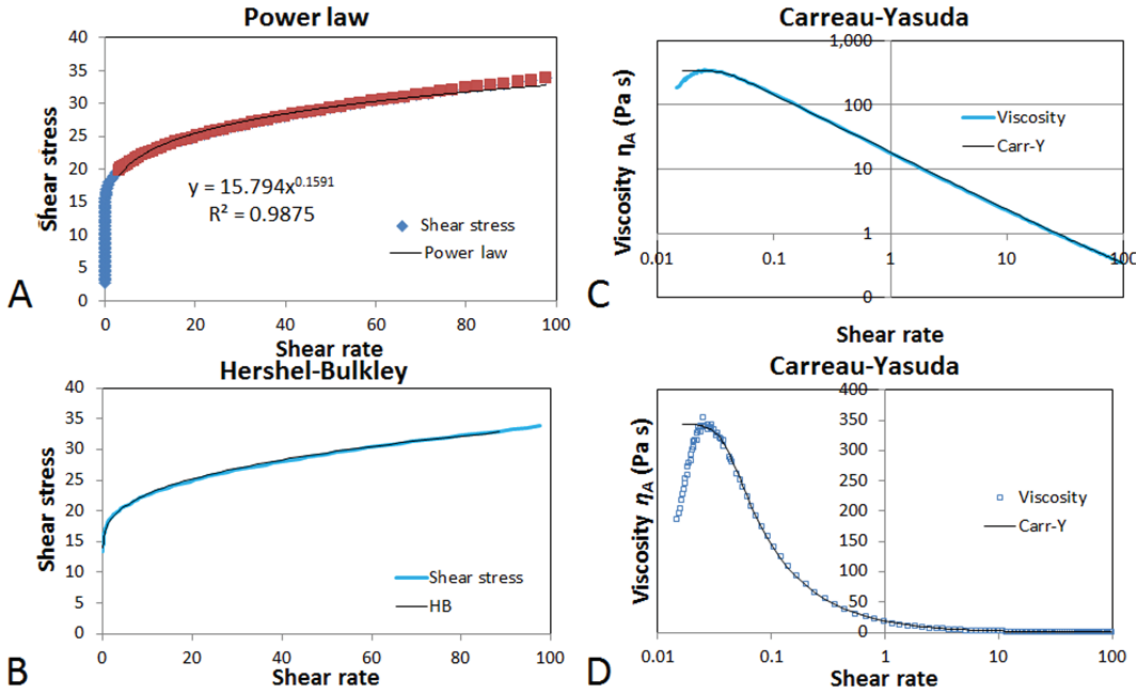

Figure 2.18 **Excel worksheet plots used to determine model curve parameters for data from X-RF2 at 25% RF2 content. A. Excel regression for power law parameters could only be fitted adequately to data at higher shear rate. Herschel-Bulkley (B) and Carreau-Yasuda parameters (C, log-log plot, and D, semi-log plot) were fitted initially using Excel Solver Add-in, then modified manually to the best fit.**

2.9.3.1 Calculated Carreau-Yasuda parameters

Taking data from the yield point onwards, the data did not fit completely to a power law curve (Fig. 2.18 A), but did fit better to a Hershel-Bulkley equation (power law with yield stress component, see section 2.3.2) (Fig. 2.18 B). The Hershel-Bulkley curve is defined by interaction between consistency coefficient B (mostly influencing curve shape) and power index p (mostly influencing slope).

A Carreau-Yasuda curve with five parameters:

$$\eta_{\mathrm{A}} = \eta_{\infty} + (\eta_0 - \eta_{\infty})[1 + (\dot{\gamma}\lambda_{\mathrm{CY}})^a]^{(c-1)/a}$$ (Morrison, 2013)

could be fitted across the entire flow curve above the yield point. The parameter η_0, which is set at zero shear viscosity in the Carreau-Yasuda equation for non-yield stress fluids, gave a value for apparent viscosity at the yield point, and so was assigned to η_{YS} (yield point apparent viscosity). The parameter c gave the slope (see Fig. 2.18 C), a modified the curve shape near the yield point (see Fig. 2.18 D), λ_{CY} was a relaxation time term that determined the X-axis offset, and η_{∞} (the Carreau-Yasuda term for viscosity at infinite shear rate) modified curve shape at the far end. As the value for shear stress in the test was too low at 100 Pa for full development of the stress-strain response of 40% X-RF2 and 30% X-MCC curves (Fig. 2.15), only yield stress data is reported for these samples.

The value of η_{YS} increased logarithmically with particulate content for both X-MCC and X-RF2 (Fig. 2.19 left), ranging from 4.28 ± 1.59 x 10^2 Pa s at 15% MCC content, to 1.09 ± 0.21 x 10^5 Pa s at 40% RF2 content, ~250-fold higher. At particulate contents near the maximal packing fraction the relaxation time parameter λ_{CY} approached 89 s for X-MCC and 450 s (five-fold greater) for X-RF2 (Fig. 2.19 right). The λ_{CY} value is the inverse of the shear rate at maximum viscosity (Shenoy, 1999e) so the larger the value of λ_{CY}, the lower the shear rate at which the fluid begins to flow. Therefore, MCC added more time-dependent structure to xanthan dispersions than RF2, consistent with the greater increase in η_{YS} for MCC with increasing particulate content (see Fig. 2.17). The value for the Carreau-Yasuda relaxation time λ_{CY} should be considered approximate.

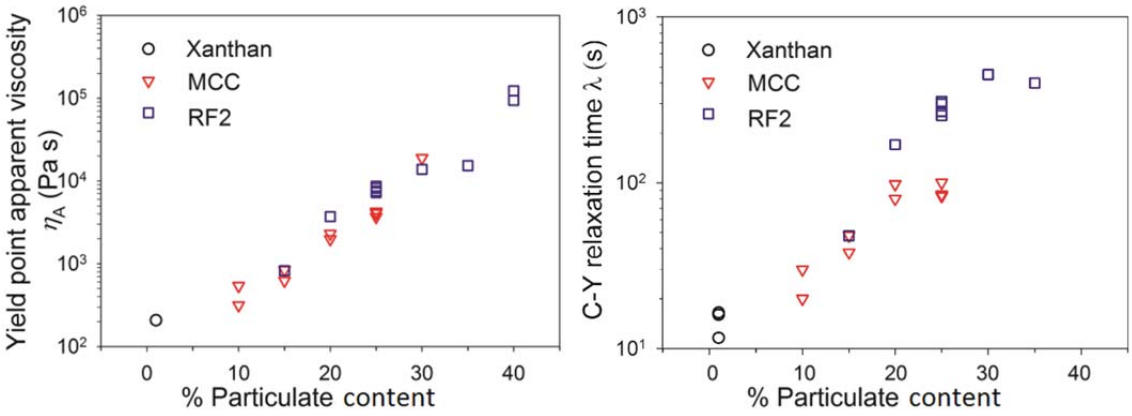

Figure 2.19 Influence of particulate content on the fitted Carreau-Yasuda parameters for (left) apparent viscosity at yield point, η_{YS}; and (right) relaxation time, λ_{CY}, for dispersions of 0-40% MCC or RF2 in 1% xanthan solution containing 0.05% K sorbate and 0.5% NaCl.

2.9.3.2 Calculated power law parameters

Power law parameters for X-salt were calculated as $K = 18.6 \pm 0.8$ Pa s and $n = 0.153 \pm 0.005$, correlated with low apparent viscosity and highly shear-thinning flow behaviour. In xanthan-particulate dispersions the value of K increased rapidly once particulate content was > 20% (Fig. 2.20), ranging between 23-75 Pa s. Values could not be calculated for X-MCC dispersions at > 25%, as the shear rate range of 0-100 /s did not generate a flow response curve after yield point to shear (see Fig. 2.17). Consistent with the noted similarity in curve shape between samples, values for the power index n were similar across samples, at 0.14-0.20, and were close to the values for X-salt, the polymer solution that formed the liquid phase.

As an indication of the shear-thinning behaviour for the particulate dispersions, at shear rate of 1 /s, the apparent viscosity of most samples was < 20 Pa s. All the dispersions were broadly similar in flow behaviour under shear stress, both with and without xanthan. A much broader sample range is needed to differentiate between the contribution of biopolymer and particulate phases to the bulk flow behaviour in model Food-Inks.

The power law equation, with two parameters and poor fit below shear rates of 5 /s, did not characterise the apparent viscosity data as well as the Carreau-Yasuda equation. However, approximations to power law behaviour are often fitted for simplicity of calculation to more complex curves. Steffe & Daubert (2006a) reduced Hershel-Bulkley flow parameters to the power law approximations to calculate pipe flow over a limited range - the functionality of the power law approximation is limited to the fitted shear rate range.

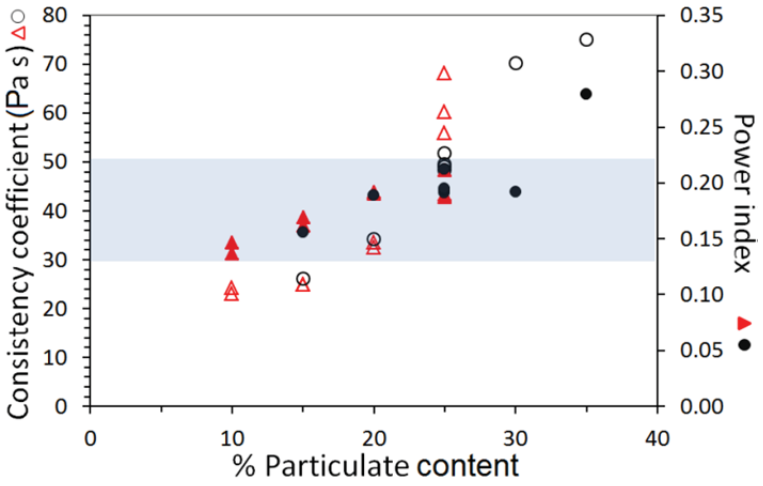

Figure 2.20 Power law consistency coefficient K (open symbols) and power index n (filled symbols) determined for xanthan–particulate dispersions with increasing particulate content (triangles, X-MCC; circles, X-RF2). The shaded box provides a visual aid for grouping n values.

2.9.3.3 Comparison with flow parameters for other structured food fluids

The fitted equation parameters of a and c (Carreau-Yasuda), B and p (Herschel-Bulkley), and K and n (power law) had no direct correlations amongst each other when plotted on the same axes (data not shown). As K has the unit $\mathrm{Pa\ s}^n$, a direct comparison cannot be made between K values for fluids with different n values. Power law parameters for xanthan-particulate dispersions fitted to shear rates above 5 /s were compared with published power law parameters for batters and other food fluids. The calculated power law parameters for xanthan-salt solution and xanthan-particulate dispersions were similar to the reported range of values for tomato-based pasta sauce and pizza sauce ($K =$ 20-60 Pa s, $n =$ 0.18), which were described as thick shear-thinning fluids (Steffe & Daubert, 2006a, p.139).

Bubble incorporation into multiphase batter dispersions decreases the value of the power index n, increasing the shear-thinning behaviour of SP batters. Chesterton et al. (2013) reported values of $n =$ 0.8 for emulsified, high-fat cake batter after complete foam breakage by centrifugation (ϕ_{Gas} at 0%); $n =$ 0.72-0.74 for unwhipped batter (ϕ_{Gas} at 10%); and $n =$ 0.62-0.68 for whipped batter (ϕ_{Gas}at 40-50%). The data were measured using plate-plate geometry. Air bubble incorporation by whisking increased the K values of batters two- to three-fold above those of unaerated batters, from 10-20 to 24-64 Pa s. Meza et al. (2011) measured oscillatory flow behaviour of egg-rich, fat-containing cake batter and batter fractions during whipping. Values for n ranged between 0.61-0.72, and between 30-60 Pa s for K.

Flow behaviour of idli batter at 5: 1 rice flour: blackgram ratio was measured using cup-and bob geometry (Bhattacharya & Bhat, 1997). Yield stress was determined from experimental data as between 4.5 Pa (before fermentation) and 13 Pa (after fermentation, with increase in gas phase fraction unreported). The corresponding K values for unfermented and fermented batters were 12.4 or 22.4 Pa s, with n values of 0.43 or 0.32. Nagaraju & Manohar (2000) used a Brookfield disk rheometer (non-standard geometry) (Steffe & Daubert, 2006a) and derived power law values according to Mitschka (1982). For unfermented idli batter formulations, as the rice flour: blackgram ratio increased from 2:1 to 4:1, K increased from 18 to 25 Pa s. Idli batters with higher K value spread less on deposition. Idli batters with air incorporated by beating initially had $n =$ 0.6 (similar value to beaten cake batter) and dropped to $n =$ 0.3-0.4 after fermentation, when $\phi_{\mathrm{Gas}}$was at 40-50% (i.e. a similar range to the Bhattacharya data).

2.9.3.4 Normal force and torque data did not indicate discontinuous flow

Chesterton et al. (2013) only fitted the power law curve for sponge cake batters to viscosity values below 10 /s shear rate. The reasons given were 1) power law values calculated at shear rate < 20 /s are routinely reported for cake batters; and 2) increasing normal force values (force against the plates measured by the rheometer along the spindle Z-axis) and a discontinuity in measured torque data indicated that at higher shear rates elastic effects became dominant in the whipped batters, pushing fluid out of the measurement gap and negating the value of measured data (Chesterton et al., 2011).

To determine whether normal forces in the xanthan dispersions also invalidated the rheological data, the influence of increasing shear stress on the normal force and torque, normal force and viscosity data were plotted against shear stress for an example dispersion (30% X-RF2) (Fig. 2.21). The normal force (force pushing spindle upwards) peaked as the yield point was reached. A second, more irregular rise in normal force at > 50 Pa corresponded to an inflection observed in the viscosity curve. Changes in normal force were within an acceptable range and there was no discontinuity in torque values, with no expulsion of material from the test geometry as described by Chesterton et al. (2011). Measurements at shear rates > 10 /s were therefore acceptable for the xanthan-particulate dispersions.

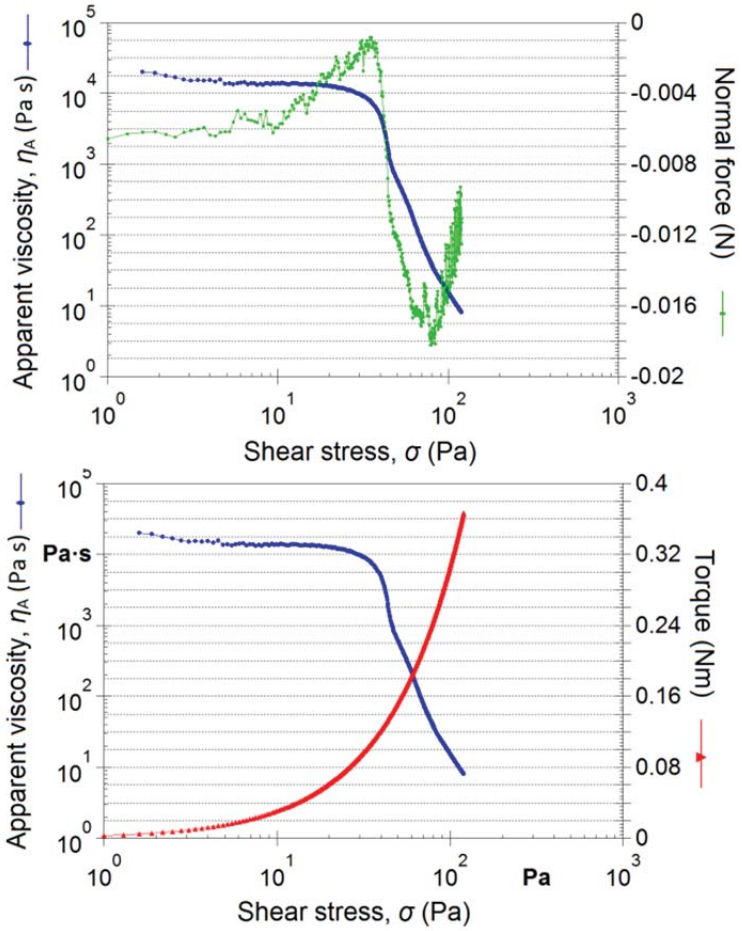

Figure 2.21 Plots for (top) normal force (in green) and (bottom) torque on the spindle (in red), compared with apparent viscosity (in blue); for viscosity-shear stress data from 30% X-RF2. Output image generated using Rheoplus 32 software.

The normal stresses generated in a structured fluid derive from the elastic component of viscoelastic materials (Rao, 2007d) (e.g. chain-chain interactions in polymer solutions, elastic behaviour of wet foams). The normal force magnitude correlates with the degree of fluid expansion on extrusion from an outlet, with higher normal values indicating greater die swell. Chesterton's group used parallel plate and cup-and-bob geometries for rheological testing, which are inappropriate for testing foams. Viscoelastic flow behaviour is best studied under oscillatory shear conditions (Shenoy, 1999e), as transitions in fluid structure are more evident. Foams and other fluids with elastic properties are also better studied using open-top vane test geometries, which have room for expansion at the top of the sample to dissipate some of the normal stresses.

2.9.3.5 Determination of fluid behaviour under elongational (stretching) flow

Fluid behaviour under extensional shear is most relevant to evaluating the behaviour of fluid systems under stretch, for example, the region of dough/batter around a rapidly expanding or contracting bubble (biaxial extensional shear; strain hardening) (Kloek, Van Vliet, & Meinders, 2001). Ink-jet printing produces a series of discrete drops. Characterisation of the breakup of a continuous thread of alginate solution into discrete drops under gravity was used as a form of extensional test to correlate modelled flow behaviour to fluid behaviour on ink-jet printing (Herran & Coutris, 2013). A related test system for pastes and foams followed thread thinning as sample was dropped from an open cylinder (Coussot & Gaulard, 2005; Guillermic et al., 2013). Recently an *elongational yield stress* was also measured for dispersions, foams and particulate-stabilised emulsions by imaging thread thinning as fluid was pulled apart between two plates (Martinie, 2013). The measurement of extensional/elongational flow is dependent in a complex way on transient viscoelastic effects (Shenoy, 1999d). More suitable rheometric tests for extensional flow are the Hyperbolic Contraction Flow attachment for the Instron Universal Testing machine (Instron Corp. Canton, US) (Andersson et al., 2011), or the multifunction Vilastic-3.1 controlled stress capillary rheometer (Vilastic Scientific, Austin, US).

2.9.3.6 Flow curve appearance

In this study, Hershel-Bulkley and power law curves could only be fitted if data below the yield stress were omitted (see Fig. 2.18). The apparent viscosity dropped at least three decades as shear stress increased between 0.1-100 /s (e.g. Fig. 2.15 & Fig 2.17). The dispersion shear-thinning flow behaviour therefore changed markedly over this shear range.

Flow curves in Figs. 2.15 and 2.17 for particulate X-salt dispersions were not very similar in shape to shear rate-viscosity plots described by Chesterton et al. (2013) for foamed cake batter, or by Rayment et al. (1995) for dispersions of individual rice starch granules in semi-dilute guar gum. The curve shape, with a large bend at the yield point and multiple inflection points along the shear-thinning portion of the curve, was similar to that reported by Lopez-Sanchez & Farr (2012) for concentrated dispersions of plant cell wall fragments. In their study when shear rate was ramped from 0.1 to 100 /s and back to 0.1 /s over four min, the inflections disappeared during the return interval, meaning they were the product of structure-influenced flow behaviour destroyed by high-shear deformation.

2.9.3.7 Localised fluid response to shear

The appearance of this type of inflection point in the response of shear-thinning fluids to increasing shear indicates shear-localisation events (non-predictable development of localised bands with increased shear flow, as in wall slip and shear-banding) that Livescu (2012) considers ubiquitous in history-dependent thixotropic fluids under shear deformation. Shear-localisation develops when history-dependent fluids with apparent yield stress are accelerated beyond the capacity of the local structure to reform. The increase in fluid elastic behaviour reported by Chesterton et al. (2013) occurred around an inflection point, which may indicate shear-localisation on foam shear deformation in the cake batter system used in their study.

2.9.4 Managing Food-Ink structure formation during piping, mixing and deposition

To overcome the variable response of Food-inks along the Food-Inks 3D printer flow path, as structures in the Food-Ink break and reform in a history-dependent manner, any strategy which standardises the Food-Ink flow characteristics will be of use in producing more predictable printing behaviour. A possible solution is to limit time-dependent structure reformation within the Food-Inks 3D printer by applying either a rapid high shear deformation of Food-Inks before any critical printing step, or a continuous low shear deformation at all resting steps along the flow path. Breaking down structure will decrease or remove yield stress behaviour, and will reduce the time and power required for Food-Inks to reach fully developed flow during piping.

2.10 Calculated parameters for flow behaviour of a model Food-Ink

This section models some flow behaviour characteristics, based on the power law properties of determined for the model X-RF2 Food-Ink and on published power law values for SP batters. The section focuses on pipe flow and on fluid behaviour as determined by the outlet diameter, which becomes the limiting diameter along the Food-Ink 3D printer flow path. To simplify modelling and to focus on fluid flow behaviour rather than fluid-equipment interactions, the influences of pipe fittings and of pipe friction are ignored and flow is assumed to be fully developed.

2.10.1 Laminar pipe flow range

The *Reynolds number* is a dimensionless parameter describing the ratio of fluid inertial forces to fluid viscous forces (Coulson et al., 1999a). Situation-dependent variants of the Reynolds number are used extensively to simplify fluid flow calculations. A *generalised Reynolds number* (GRe) for power law fluids under pipe flow is calculated from:

$$GRe = \frac{d^n v_z^{2-n} \rho}{8^{(n-1)} K} \left(\frac{4n}{3n+1}\right)^n$$, (Rao, 2007b),

where v_Z is the average fluid velocity across the pipe radius, d is pipe/outlet diameter, p is fluid density, and n and K are the power law parameters. The GRe value indicates whether fully-developed fluid flow will be laminar or turbulent. Laminar flow is preferred for Food-Ink pipe flow, as turbulent flow generates eddies within the flow stream. Laminar flow in a power law fluid takes place at GRe < 2100 when $n = 1$ (Newtonian fluid), increasing with decreasing n to GRe < 2880 at $n = 0.1$ (Steffe &

Daubert, 2006b, p. 53); in other words, the threshold for turbulent flow increases by around a third as fluids become highly shear-thinning in behaviour.

The critical GRe for laminar flow was calculated over a range of values for n under conditions relevant to the Food-Inks 3D printer. From Table 2.1, deposition rate was set at 200 or 600 mL/min. Parameters for the model particulate Food-Ink were set at 1020 kg/m^3 for fluid density, with $n = 0.20$ and $K = 48.2$ Pa s. A value of $n = 0.2$ was chosen, to represent a highly shear-thinning fluid likely to transition to turbulent flow. A pipe diam. of 2.75 mm was chosen: this is smaller than the likely pipe diameter during pumping along the flow path before the mixer chamber, but larger than the minimum round outlet of 1.4 mm diam. outlet which will deliver a Food-Ink voxel at 10 dpi in the absence of die swell (see Table 2.1).

The range for flow velocity (v) along a straight pipe of diam. 2.75 mm and area 2.29 x 10^{-5} m, with printing rate between 200-600 mL was calculated as:

Flow rate: 200 mL/min =3.33 x 10^{-6} m^3/s; 600 mL/min = 1.0 x 10^{-5} m^3/s.

Velocity at 200 mL/s = (Flow rate)/Area = 0.140 m/s; at 600 mL/min = 0.421 m/s.

For a 2.7 mm diam. pipe, flow rate from 200-600 mL/min and $n = 0.2$, GRe falls between:

$$\frac{(2.75 \text{ x } 10^{-3}\text{m})^{0.2} \text{ x } [0.140 \text{ or } 0.421]^{(2-n)} \text{ m/s x } 1.02 \text{ x } 10^3 \text{ kg/m}^3}{(8^{0.20-1} \text{ x } 48.2 \text{ Pa s}^{1-n})} \text{ x } \left[\frac{4 \text{ x } 0.20}{3 \text{ x } 0.20 + 1}\right]^{0.2}.$$

Therefore, 2.0 < GRe < 14.5 between the two flow rates. The critical GRe value for laminar flow in a power law fluid with $n = 0.20$ is 2800 (Steffe & Daubert, 2006b, p. 53). Increasing K from 48 to 90 Pa s decreased GRe by around two-fold. Increasing n to 0.4, 0.6 and 0.9 reduced GRe from 2.0 to 1.3, and 0.5, respectively. None of these changes calculated GRe above the critical threshold for turbulent flow. As a comparison, calculating GRe at flow rate 200-600 mL in a 2.75 mm diam. pipe using $n = 0.153$ and $K = 18.6$ Pa s, the power law parameters determined experimentally in this study for the 1% X-salt solution produced 4.6 < GRe < 38.9.

Increasing the pipe diameter d between 0.05-8.0 mm at flow rate of 200 mL/min decreased GRe from 2028 to 0.8. Calculated GRe values fitted to a power law function, $y = [4 \text{ x } 10^{-8}].d^{-3.541}$, showing the critical influence of decreasing pipe diameter on the flow behaviour of power law fluids. The probability of turbulent flow increases at smaller pipe diameters and faster flow rates.

2.10.2 Pressure drop of a power law Food-Ink in a small diameter pipe

From the Mechanical Balance equation (section 2.2.1.1), the pressure drop ΔP in a pipe system relates to the work needed to move fluid through the system if pipe friction and hydraulic effects are ignored. The pressure drop value therefore provides information on the interaction between fluid structures and pipe dimension. The pressure drop was calculated as described in section 2.3.2 (see Fig. 2.22 legend) using K and n values corresponding to a highly shear-thinning fluid ($n = 0.1$), and to power law values reported for unaerated and aerated SP batters ($n = 0.2$, 0.6 and 0.9). Pipe diameter range was chosen to be consistent with a deposition outlet pipe of small diameter and low void volume. Flow rates were set at values up to twice the maximal flow rate in the design specifications given in Table 2.1.

Each parameter was set at four values, and calculated under conditions where all other parameters were set at either their minimum, intermediate or maximum values (conditions 1-4 on the X-axis in Fig. 2.22). Increasing flow rate Q and pipe length L did not produce a great spread in ΔP when calculated for each condition; these parameters did not produce a great change in pressure drop. Increasing the consistency coefficient K increased the value of ΔP linearly going from condition 1 to 4.

At higher flow rates, the greater shear rate across the pipe encourages shear-thinning, resulting in a decrease in fluid resistance to flow in the pipe. Changing the n value produced the greatest spread in ΔP within a specific condition, up to four orders of magnitude at condition 1 between n = 0.1 and n = 0.9. The increase in ΔP values within each n value varied only slightly between condition 1 and 4; $n = 0.6$ and 0.9 had similar ΔP values across all conditions. When friction and hydraulic effects are discounted, the power index n is therefore the most influential factor on the work required to move a power law fluid in a pipe, and decreases in influence as n increases.

Modulating pipe diameter d gave the greatest spread of ΔP between conditions 1 and 4 (eight orders of magnitude). As the greatest range in pressure drop was associated with the smallest pipe diameter, pipe diameter along the flow path is therefore a critical parameter for the 3D Food printer design, even without consideration of the influence of fluid yield stress in generating plug flow (see section 2.3.1).

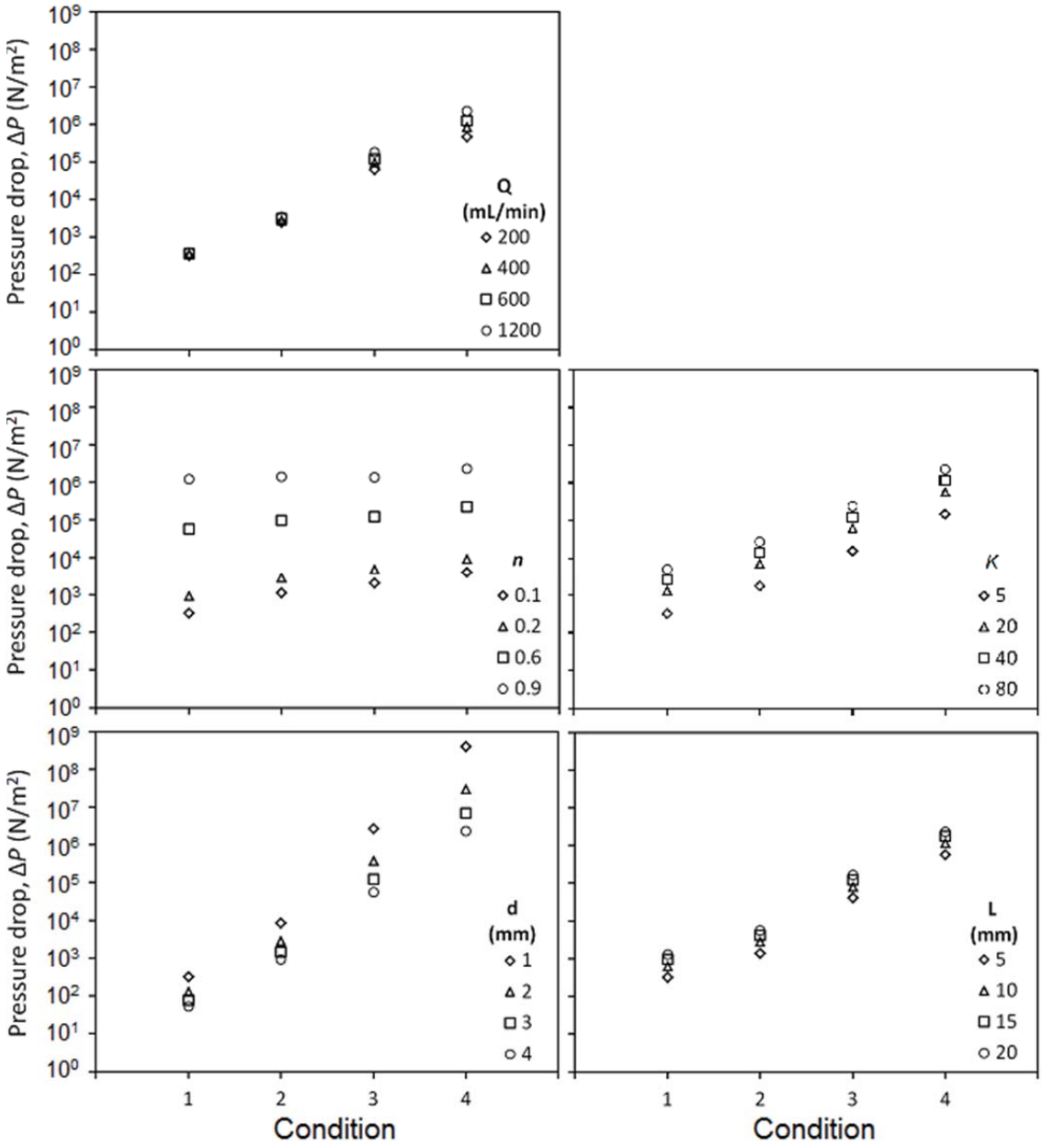

Figure 2.22 Influence of increasing flow rate Q, power law parameters K and n, pipe diameter d and pipe length L on pressure drop under laminar flow. Parameter values were calculated for a power law fluid using $\Delta P = \frac{2KL}{(d/2)}\left[\left(\frac{3n+1}{4n}\right)\left(\frac{4}{\pi(d/2)^3}\right)^n\right]Q^n$, (Steffe & Daubert, 2006b). Conditions 1-4 on the X-axis refer to minimum (1), intermediate (2, 3) and maximum (4) values set for all other equation parameters.

2.10.3 Estimation of maximum shear rates for pipe flow

Using parameter values within those specified for the Food-Inks 3D printer the value of $\dot{\gamma}_{\text{Wall}}$, the maximum shear rate at the wall under pipe flow, provides an estimate of suitable shear rate limits for rheological testing of Food-Ink pipe flow behaviour (Steffe & Daubert, 2006b). Under steady state conditions the minimum shear rate for a power law fluid is zero at the pipe centre, while $\dot{\gamma}_{\text{Wall}}$ can be calculated from:

$$\dot{\gamma}_{\text{Wall}} = \left(\frac{2n+1}{4n}\right)\left(\frac{4Q}{\pi r^2}\right), \text{ (Steffe \& Daubert, 2006a, p. 8).}$$

Given $n = 0.2$ (e.g. xanthan-RF2), pipe diameter of 2 mm (radius $r = 0.001$ m), and flow rate Q of 200 mL/min (= 3.33 x 10^{-6} m^3/s), the maximum shear rate at the wall is calculated as:

$$\dot{\gamma}_{\text{wall}} = \left[\frac{((3 \text{ x } 0.20)+1)}{4 \text{ x } 0.20} \text{ x } \frac{4 \text{ x } 3.33 \text{ x } 10^{-6} \text{ m}^3/\text{s}}{3.142 \text{ x } (1 \text{ x } 10^{-3}\text{m})^3}\right] = 8480 \text{ /s.}$$

The influence of n, Q, and d on wall shear rate was calculated at d = 2 mm and 4 mm (Table 2.2). The calculated wall shear rates were very large, primarily due to the influence of pipe diameter.

Increasing flow rate increased $\dot{\gamma}_{\text{wall}}$ values proportionally. Doubling pipe diameter decreased the wall shear rate 8-fold. For a given value of n, wall shear rate increased proportionally with flow rate. Fluids with increased shear-thinning behaviour produced a greater wall shear rate under the same pipe flow conditions. Wall shear rates at n = 0.2 were 1.7-fold greater than at n = 0.6, and 1.9-fold greater than at n = 0.9. The limits are relevant only for flows above the shear rate of the fluid yield point: the calculated shear rates are well above shear rate values at the yield points of model Food-Ink dispersions, which fell between 10-100 /s (e.g. see Fig. 2.15).

At $d = 20$ mm, the wall shear rate fell within 8-26 /s at all power index values (data not tabulated). Small pipe diameters < 2 cm generate significantly greater shear gradients from wall to the pipe centre than larger pipes.

The parameter values calculated in this section give only a general guide to pipe flow behaviour for SP Food-Inks, as they assume steady state flow and ignore the contribution of yield stress. As noted for pressure drop calculations, the calculated values of wall shear indicate that the most important influences on shear deformation during pumping of particulate-containing food pastes are the pipe diameter and the power index n. The wall shear stress is also sensitive to flow rate, where pressure drop is not. Test systems for pipe flow in the Food-Inks 3D printer at outlet size compatible with delivery of clear printed images suggests that Food-Ink flow behaviour should be measured at high shear rates.

Table 2.2 Influence of power index (n), flow rate (Q) on calculated wall shear rate $(\dot{\gamma}_{\mathrm{Wall}})$ at two pipe diameters, d = 2 mm and 4 mm.

d (mm)	n	Q (mL/min)	$\dot{\gamma}_{\mathrm{Wall}}$ (/s)		d (mm)	n	Q (mL/min)	$\dot{\gamma}_{\mathrm{Wall}}$ (/s)
2	0.2	200	8480		4	0.2	200	1060
2	0.2	400	16960		4	0.2	400	2120
2	0.2	600	25465		4	0.2	600	3183
2	0.6	200	4947		4	0.6	200	618
2	0.6	400	9893		4	0.6	400	1237
2	0.6	600	14854		4	0.6	600	1857
2	0.9	200	4358		4	0.9	200	545
2	0.9	400	8715		4	0.9	400	1089
2	0.9	600	13086		4	0.9	600	1636
2	0.153	200	10108		4	0.2	200	1263

2.10.4 Relevance of pipe flow models to observed flow of structured fluids

The fluid velocity profile in the pipe and the relative radius of unsheared flow can be calculated for Herschel-Bulkley fluids. However, in a study of the flow of synthetic clay suspensions which contained charged particulates, the data for yield stress and fluid viscosity measured experimentally near the pipe wall were an order of magnitude lower than values predicted on rheological modelling (Escudier & Presti, 1996). Localised inhomogeneity in the degree of structure breakdown (i.e. shear-localisation) was suggested as the reason.

Yoghurt in steady-state pipe flow, characterised on modelling rheological data as a yield stress power law fluid with $K = 3.7$ and $n = 0.3$, (i.e. not particularly thick, quite shear-thinning) was predicted to develop a bullet-shaped velocity profile under wall shear stress. Experimentally however, the measured flow travelled as an undeformed plug that almost filled the pipe diameter, with no great reduction of velocity towards the wall (Henningsson, Östergren, & Dejmek, 2006). This suggested a thin wall slip layer with high localised shear helped to lubricate the entire plug flow at the pipe wall. The authors concluded that yoghurt flavour variations could be switched over during piping in the equipment without resulting in significant between-batch mixing. Similar plug flow behaviour in a Food-Ink could potentially be harnessed to deliver a continuous thread of independently-formed voxels along a pipe. As modulation to create plug flow is rarely reported, the targeted design of such behaviour to Food-Inks 3D printing represents a significant challenge.

The disconnection between experimental and modelled values for pipe velocity profiles indicates that wall yield stress velocity profiles are sensitive to development of wall slip zones close to the wall, which can lubricate flow and produce flow behaviour unrelated to that estimated by calculation and velocity profile modelling (de Souza Mendes, 2013). The transition regime between a fluid with a structure that breaks down under flow and a paste that travels in plug flow is clearly of importance in determining pipe flow profiles in Food-Ink applications. Equation-based estimation of flow parameters needs to be done alongside a valid experimental test system for flow behaviour during printing in the Food-Inks 3D printer.

As well caution in applying models for large-volume, steady state pipe flow to Food-Inks 3D printing,

time- or work-dependent changes in flow behaviour must be minimised. For example, using an industrial dosing machine to portion muffin batter modified the K value of a wheat flour muffin formulation from 17.3 to 21.9 Pa s, but did not affect the power index ($n = 0.6$) (Baixauli, Sanz, Salvador, & Fiszman, 2007). The dosing equipment developed gluten networks beyond the optimal point for muffin batters, altering the cooked muffin meso- and microstructure.

2.11 Rheological testing of stop-start-STOP flow behaviour

2.11.1 The Three Interval Thixotropy test

Where yield stress and viscosity under increasing rotational shear predict stop-START-stop flow behaviour the recovery phase of a creep-recovery test predicts stop-start-STOP fluid behaviour. Creep-recovery tests can be carried out under rotational and oscillatory shear deformation. For the Rheoplus Three Interval Thixotropy Test with Osc-Rot-Osc (Rheoplus 32 software) the fluid is left to reach steady state flow under low amplitude oscillatory shear, given a short high-shear deformation, and returned to low amplitude oscillatory shear (methods in section 2.2.2.1). Rheoplus 32 software calculates a recovery time for structure reformation based on the fluid flow behaviour in the time period after the high-shear rotational deformation.

2.11.2 Method for the Three Interval Thixotropy test

- *Testing geometry, rheometer details and general setup, and sample preparation of X-salt and X–RF2 were as described in section 2.9.3. After 45 min rest to recover structure after loading, a dynamic stress with amplitude 1%strain and frequency 1 Hz was applied for 20 min and 60 data points recorded (interval 1). A rotational shear of 100 Pa was applied for 60 s, increasing from shear rate 86 /s to 324 /s (interval 2), with 10 data points recorded. Dynamic shear was applied at 5%strain and 1 Hz (interval 3) for 60 min, and 300 data points recorded. Storage modulus, loss modulus and complex viscosity were automatically calculated by Rheoplus 32/ Ver. 2.81 software.*

2.11.3 Stop-start-STOP response of rice flour–xanthan dispersions

This test was applied to X-RF2 dispersions to examine the influence of rice flour content on structure recovery. Samples were prepared as for static yield stress determination (section 2.9.3.2) at 0-39% RF2 content (as g/(total g)). In Fig. 2.23 left (storage modulus for elastic behaviour, G') and right (loss modulus for viscous fluid behaviour, G''), plots having the same colour represent the same analysis run. For X-salt solution and for low RF2 content, the viscosity change observed at the start of interval 3 (start of structure recovery) initially trended upwards, eventually reaching a steady state plateau as structure reformed under low-shear oscillation. This response is typical of shear-thinning fluids. As the RF2 content increased, the upward trend at the start of interval 3 gradually flattened for both G' and G'', becoming a downward trend at RF2 > 33.5%. This transition from an upwards to a downwards trend signals a change in flow behaviour immediately after high-shear deformation, from shear-thinning to shear-thickening as RF2 content approaches the maximal packing fraction. At higher RF2 content, discontinuities in the liquid phase are more likely to develop under high-shear deformation, contributing

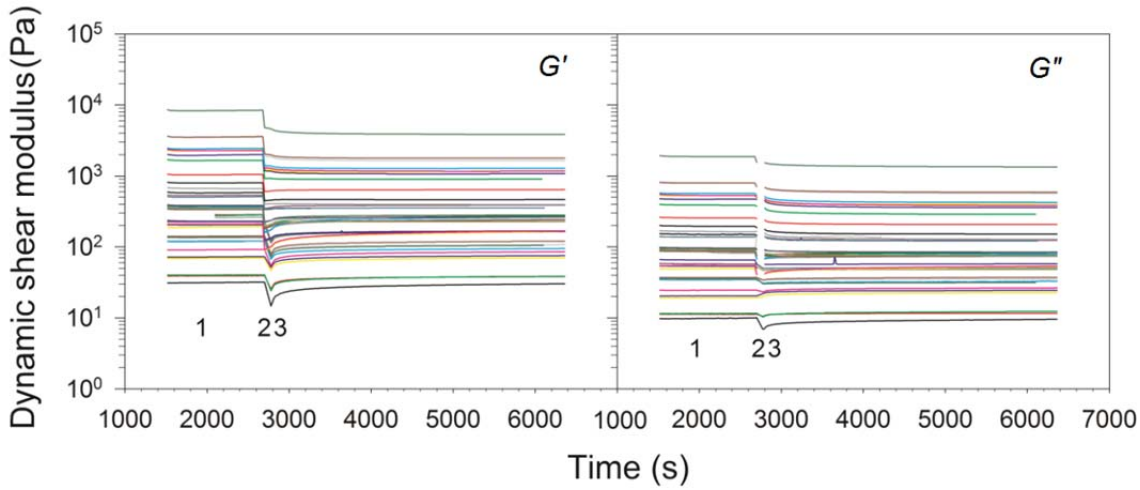

Figure 2.23 Left, storage modulus (G') and right, loss modulus (G") response curves under a Three Interval Thixotropy test (Rheoplus 32 software), applied to 1% X-RF2 dispersions containing 0.5% NaCl and 0.05% K sorbate. The three test intervals (Low Osc-High Rot-Low Osc) are labelled 1, 2 & 3. RF2 content increases from 0-39% moving from bottom to top, and G' and G'' plots having the same colour represent the same analysis run.

to shear-thickening flow behaviour. After high-shear deformation structures gradually relax under low-shear oscillation, and/or the liquid phase flows back into discontinuities.

Concentrated starch granule-water dispersions are typical shear-thickening food fluids, in which increasing the shear deformation pushes dispersion/solution particles together to jam the flow of the structured fluid (Fall et al., 2008). Even though the liquid phase remains continuous, the development of particle 'traffic jams' slows flow and increases the dynamic viscosity. In structured fluids the jammed particles may be drops, bubbles or particulates. The critical particle concentration to observe jamming of shear-thickening fluids is related to deformation force, but also to the gap size of the test rheology (Fall et al., 2008). The available space for a fluid undergoing shear-thickening becomes too limited to contain fluid expansion in the rheometer test geometry. Jamming in fluids may occur as a gradual transition, or may be immediate: abrupt jamming is more likely in particulate dispersions (Ovarlez et al., 2013).

Shear-thickening flow behaviour should be avoided in the extrusion-based AM, as greater work (W) is required to pipe an equivalent volume of fluid at high flow velocities, and fluid may jam at higher flow rates. Any SP Food-Inks formulation should have particulate content well below the maximal packing fraction, while flow rates for the Food-Inks 3D printer system should be modulated to limit the wall shear rate value (see section 2.10.3).

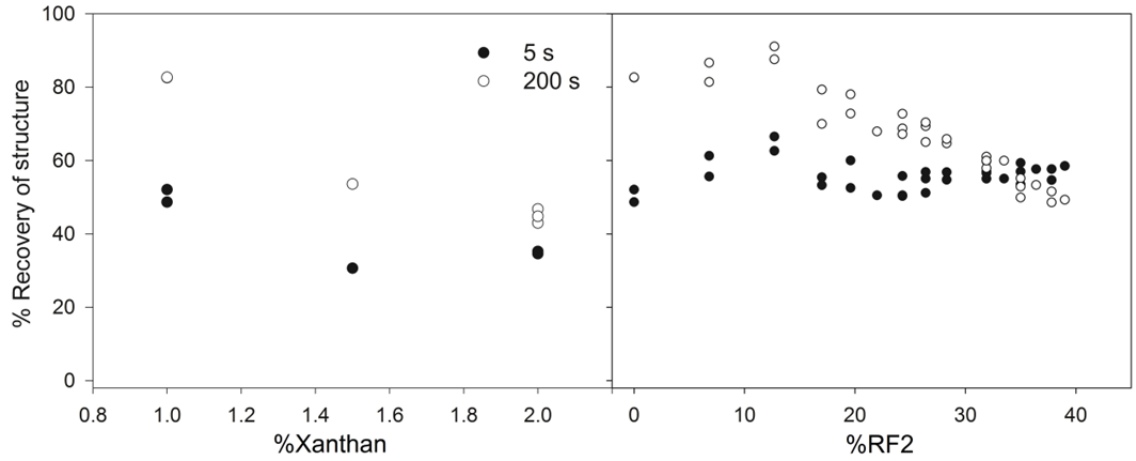

Figure 2.24 Percentage of structure recovery for xanthan-RF2 on return to low shear oscillation after a rapid high rotational shear deformation. Left: for X-salt solutions at increasing xanthan content. Right: for X-RF2 dispersions with increasing RF2 content. Calculated using Rheoplus 3.2 software function 'Calculate recovery after x seconds'.

2.11.4 Time to recovery of structure in fluids

In Fig. 2.23 the gradual plateau of G' and G'' values represents the reformation of fluid structure after high rotational shear deformation. A relaxation time for this structure reformation can be calculated as described in 2.11.4.1. For X-salt solutions, structure recovery after the high-shear deformation interval decreased with increasing xanthan content, to 30-50% of previous values after 5 s (Fig. 2.24 left). By 200 s after high shear deformation, structure recovery reached 82.6 ± 0.1% for 1% xanthan, reducing to 44.8 ± 1.9% for 2% xanthan. For X-RF2 dispersions, recovery by 200 s first increased with increasing RF2 content, to 12.7% RF2, then decreased linearly to 50.0 ± 2.1% at 37.8% RF2 (Fig. 2.24 right). Increasing particulate content did not influence structure recovery of X-RF dispersion greatly in the period immediately after high-shear deformation (most relevant to stop-start-STOP behaviour on extrusion-based AM), but did decrease the degree of structure recovery over a longer timeframe.

Structure recovery should optimally occur in a short time interval (e.g. within 5 s rather than within 200 s) for extrusion-based AM deposition. Murphy et al. (2013) suggested a target reformation time of 2 s for hydrogels used in biofabrication. For dispersions in biopolymer solutions that develop structure in the liquid phase, structure recovery due to reformation of biopolymer networks, rather than to redevelopment of particulate network structures, may determine stop-start-STOP behaviour within a timeframe relevant to extrusion-based AM deposition. Looking more generally at the stop-START-stop response of Food-Inks when pumping is first initiated, for Food-Inks which develop structure with standing, the requirement to overcome the Food-Ink yield stress will benefit from strategies that reduce the time-dependent build-up of structure - for example, by keeping Food-Inks under constant low agitation or oscillatory shear in the Food-Ink 3D printer reservoirs, and at any point in the equipment configuration where the fluid pauses during the print cycle. Reducing this initial resistance of a Food-Ink to flow at the start of pumping should improve the predictability and control of Food-Ink flow during printing.

2.11.4.1 Method to calculate structure recovery in the Three Interval Thixotropy test

- *Structure recovery was calculated with Rheoplus Three Interval Thixotropy Test analysis, using 'Steady State check' at default settings, and 'Calculation for recovery interval' as 'Calculate recovery after x seconds' (Rheoplus 32 software).*

2.12 Models for flow of structured fluids in small-diameter pipes

The complexity in behaviour expected for structured fluids under pipe flow can be judged from sophisticated models developed for small diameter pipe flow in non-food systems. For example, the rheology of blood flow has been extensively modelled. Blood is a shear-thinning, yield stress dispersion of deformable cells in a Newtonian fluid ($n = 0.95$; flow viscosity of ~3 mPa s). In small arteries (pipe diam. of 0.05-0.10 mm) the bulk of blood cells travel as an unsheared core (Sankar, 2011). Multi-component mathematical models have been developed to estimate the change in plug flow radius under shear deformation gradients that arise in arteries narrowed by fat deposits (i.e. decreased pipe diameter). Blood flow is under continual acceleration and deceleration (pulsation). Elastic energy stored in blood cells modifies the fluid response at low shear rate (i.e. start and stop of pumping), but not at higher flow rates. The elastic component is not detected under steady state flow, and more than one set of parameters is needed to fit the flow model across all shear rates (Wikipedia, 2014). This reinforces the message that steady state flow models are only a starting point for modelling Food-Ink behaviour, particularly if the Food-Inks 3D printer design includes short bursts of small volume Food-Ink deposition.

The development of particulate concentration gradients across the pipe radius, as in the model for blood flow, is a general feature of particulate dispersion pipe flow. The shear gradient generated on fluid flow pushes particulates away from the wall; a counter-effect is an increase in yield stress and viscosity with the increased particulate content at the flow centre that hinders particulate crowding. The particulate concentration gradient across the pipe is determined by the balance between these effects (Choi et al., 2013). A recent theoretical model predicts that the velocity profile generated by wall shear (see Fig. 2.7) becomes sharper as the volume fraction of particulates increases (Ramachandran, 2013), with the effect increasing at small pipe diameter.

The specifications for hydrogel printing in biofabrication differ from those to produce the Food-Inks 3D printer project prototype product: printing viscosity is much lower, print times can be much longer, structure setting is preferably immediate (a target in hydrogel printing is for structure formation within 2 s), and non-food grade ingredients can be used to instigate rapid structure formation after deposition (Malda et al., 2013). According to Chung et al. (2013) published studies on hydrogel printing behaviour for bio-fabrication are few. Models for modelling deposition rate in extrusion-based biofabrication report outlet diameters of 0.1-0.4 mm, with zero-shear viscosity of 2 Pa s considered as a high viscosity value for the hydrogel fluid (Chung et al., 2013; Li et al., 2011). Extrusion-based AM may be used at higher viscosities, or for viscoelastic materials (Chung et al., 2013). The zero-shear rate viscosity in the Carreau-Yasuda model (η_0), which gives the intrinsic viscosity of polymer solutions, is an important parameter for calculation of flow behaviour in biopolymer-based hydrogels.

2.13 Limitations in testing approach for piping and deposition

The study focused on identifying key factors in Food-Ink flow for control of thread and voxel deposition on extrusion-based AM, in the context of a pipeable, formable two-phase model Food-Ink to approximate SP formulation behaviour.

Optimisation of test systems was limited and the reported results are preliminary in nature. A more extensive study is required for print system modelling, once a suitable prototype for the mixer-deposition component of the Food-Inks 3D printer is available.

- The behaviour of potential Food-Ink fluids was examined under conditions relevant to Food-Inks 3D printer specifications. Calculations assumed simple pipe flow and excluded the effects of pipe friction and hydrostatic pressure (both of which are dependent on equipment configuration). As both influence pipe flow, these factors must be included in an in-depth analysis of flow behaviour.
- Evaluation of flow behaviour under shear deformation was carried out using a model Food-Ink dispersion made from rice flour in 1% xanthan-salt solution. The xanthan content was around two-fold higher than that generally used in SP formulations as a structuring aid. Evaluation of model SP Food-Inks at xanthan content < 1% should identify the lower limit of effectiveness for xanthan in a Food-Ink liquid phase.
- Access to test geometries in the study was limited. Vane-and-cup geometries are most suitable for rheological testing of foams and fluids containing large particulates, as increased gap width averages shear-localisation events, reducing the influence of shear-banding and wall slip on measurement of bulk flow behaviour. Rheological tests to measure extensional/elongational deformation (as described for foams and yield stress fluids, e.g. Chesterton et al., 2013; Guillermic et al., 2013; Herran & Coutris, 2013) are the most appropriate test for any voxel deposition process which includes the deposition or break up of a continuous thread of Food-Ink fluid.

2.14 Considerations for Food-Ink flow on mixing

2.14.1 Voxel colour-matching is a micro-mixing task

Voxel colour-matching in the Food-Inks 3D printer application requires mixing and metering at very small scale (perhaps to sub-µL level) and must be finished within a time period consistent with a point-of-sale product (see Table 1.2). This is a much smaller scale of mixing process than normally encountered in food manufacturing, or on mixing fluid material streams in extrusion-based AM applications, for example when adding cross-linking reagents to hydrogels.

The mixing process can be split into three attributes (Kukukova, Aubin, & Kresta, 2009). The first is the density of segregation (the density of unmixed clusters); the second, the scale length of the clusters; and the third, the time requirement for adequate mixing. In the design of a mixing system to colour-match voxels the measure of mixing effectiveness must include all three dimensions. Production of a correctly-coloured voxel (with volume between 16-270 µL) is a micro-mixing task dependent on the rate of molecular diffusion, which is a function of diffusion coefficient multiplied by the surface area of the fluids to be mixed and the gradient of species concentration (Hessel, Löwe, & Schönfeld, 2005).

Turbulent mixing is not a general feature of micro-mixing (Hessel et al., 2005). The mixing approach most suitable for Food-Ink colour mixing, assuming structure-forming Food-Inks with high apparent viscosity and yield stress is *laminar mixing*, that is, mixing which distributes material from two or more fluid streams by 'imposing laminar shear, elongation (stretching), and squeezing (kneading) deformation' (Tadmor & Gogos, 2002, p. 323). The result is an ordered redistribution of material that maximises interfacial area between individual material streams. Mixers used for laminar mixing therefore differ from standard chamber-impeller mixer designs usually encountered in food processing. In laminar mixing of two fluids the critical variable is the total strain imposed on the system (Tadmor, 2002).

2.14.2 Options for mixing Food-Ink with food colour

The colour-matching options for individual Food-ink voxels include:

- Adding colour-matched concentrated liquid dye into uncoloured structure-forming fluid (small volume of low-viscosity dye into large volume of high-viscosity fluid with yield stress).
- Four- or five-colour mixing of pre-coloured Food-Ink base with similar high viscosity and yield stress, which involves mixing of multiple material streams with similar flow behaviour at sub-micrometre volumes.
- Adding concentrated solid particulate dye into uncoloured Food-Ink base (mixing of solid particulates into high-viscosity fluid with yield stress.

This section examines the theoretical basis of fluid flow requirements for mixing under the first two conditions. A joint mixing trial designed within the Food-Inks 3D printer project (experimental outline in Appendix C) was not completed, as a test mixing rig developed for the trial did not deliver controlled flow.

2.14.3 Static mixing as a model for Food-Ink flow behaviour on mixing

Static mixers are examples of passive mixing systems that depend on the energy of fluid flow into the mixing chamber to provide the motive force for mixing. Mixing is carried out by reorientation of two (or more) material streams entering the mixer. Fixed physical barriers, the static mixer *elements,* manipulate the fluid streams (F1, F2) to split and orient the flows, producing a striated, laminated mixture. At least one of the fluid streams to be mixed is already under flow (inline passive mixing). As the energy for static mixing is supplied by the material stream, there is a significant pressure drop between mixer inlet and outlet (Rielly, 1997).

Static mixers can mix gas-liquid or solid-liquid material streams into multiphase flows (Thakur et al., 2003) and are suitable for mixing viscous flows, such as viscous dispersion and pastes. Computation flow dynamics models for static mixing have been developed to examine the impact of fluid flow behaviour on mixing effectiveness. The process of mixing in static mixers provides a relatively simple system to evaluate mixing between fluids with different flow properties under lamination and stretching flow. Factors that affect mixing effectiveness include the rate of material flow through the static mixer, the mass ratio $q_1 : q_2$ of Fluid 1 and Fluid 2, and the ratio of the fluid viscosities, $\eta_1 : \eta_2$. Models of static mixer flow are scalable, so long as the geometries of mixer elements and flow entry pathways are maintained and the flow rate ratio $q_1 : q_2$ is the same (Taylor, Penney, & Vo, 2005).

Computational fluid dynamics modelling of the degree of mixing was carried out for a Lightnin Series 45 static mixer (Regner, Östergren, & Trägårdh, 2008). A second fluid was introduced at the centre of the flow of the first fluid. Flow conditions were at Reynolds number 1 and 70, i.e. the ratio of inertial forces to viscous forces was calculated for a Newtonian fluid flowing through the mixer using:

$$Re = \frac{\rho v_z d}{\eta},$$

with fluid density ρ set at 1.0 kg/m^3. As fluid density is invariant in the Regner model, at $Re = 1$, the fluid viscosity η has an equal influence to $v_z d$, the product of average fluid velocity x pipe diameter (i.e. gives an absolute value for fluid inertial forces); while at $Re = 70$ the inertia of the fluid flow influences mixing much more than fluid viscosity. However, the Lightnin static mixer diam. of 40 mm is much larger than the likely pipe diameter requirements for voxel production in the small diameter Food-Inks 3D printer equipment.

In section 2.10.1 a generalised Reynolds number was calculated for a non-Newtonian model Food-Ink dispersion (25% X-RF2 with $n = 0.2$ and $K = 49.0$ Pa s) as GRe = 14.5 at flow rate of 600 mL/min in a 2.7 mm diam. pipe. Under the conditions of the Regner study, the X-RF2 dispersion tends towards an increasing influence of fluid inertial forces with increasing flow rate. This suggests that mixing in a static mixer (or any similar laminar mixing process) may represent a bottle-neck for fluid flow in the Food-Inks 3D printing application.

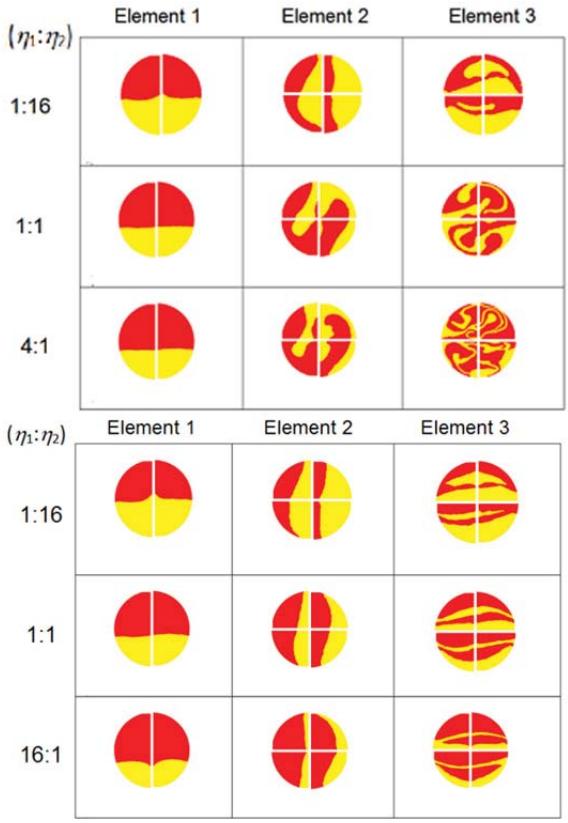

Figure 2.25 Computational fluid dynamics modelling of mixing effectiveness at consecutive elements of a Lightnin series 45 static mixer (with i.d. 40 mm and length diameter ratio of 1.5) when only the viscosity ratio $\eta_1 : \eta_2$ is changed. Top: Reynolds number = 1. Bottom: Reynolds number = 70. The inline fluid is red and introduced fluid is yellow. Adapted with permission from Regner et al. (2008), © 2008 American Chemical Society.

The Regner modelling study concluded that mixing effectiveness (quantified as thinness of striations, see Fig. 2.25) was reduced as difference in viscosity between the two fluids increased, and when the introduced fluid was more viscous than the main fluid flow. This is consistent with the general observation that laminar mixing of high-viscosity fluids is more difficult on introducing a more viscous fluid into a less viscous fluid. Generally, mixing was more effective as $q_1 : q_2$ and $\eta_1 : \eta_2$ approached 1. Increasing Re resulted in the development of vortices and disruption of laminar mixing. The Regner study results suggest that mixing batches of pre-coloured Food-Ink in a 4- or 5- colour system will provide a better mixing outcome than mixing small volumes of highly concentrated liquid dyes into a significantly more viscous Food-Ink base.

GRe values were calculated for SP batters under conditions relevant to the Food-Ink 3D printer (flow rate of 200 mL/min in a 3.5 mm diam. pipe) and n values derived from the literature (see section 2.9.3.8): GRe = 10 at n = 0.6 (e.g. batter before whipping or fermentation), and GRe = 45 at $n = 0.4$ (e.g. aerated batter). As mixing effectiveness in the Regner study was reduced at $Re = 70$ compared with $Re = 1$ (Fig. 2.25 bottom vs. top), the GRe values for SP batters suggest that the effectiveness of laminar mixing decreases with increasingly shear-thinning behaviour.

2.14.4 Residence time in mixers

The previous section described the radial distribution of fluids during flow through an in-line mixer. The temporal distribution of materials (i.e. the axial distribution of in-line mixers) must also be considered, introducing a *residence time* parameter into evaluations of mixing effectiveness (Nauman, 2004). Flow through a positive displacement piston pump that sweeps all material from the barrel produces a residence time of 1 (i.e. position of material is retained along the barrel during flow), while static mixers show a trailing edge (Fig. 2.26), indicating that portions of the mix become spread along a static mixer barrel as they transit through the mixer. Residence time is a critical parameter in designing the mixing chamber of the Food-Inks 3D printer to produce a stream of discrete voxels.

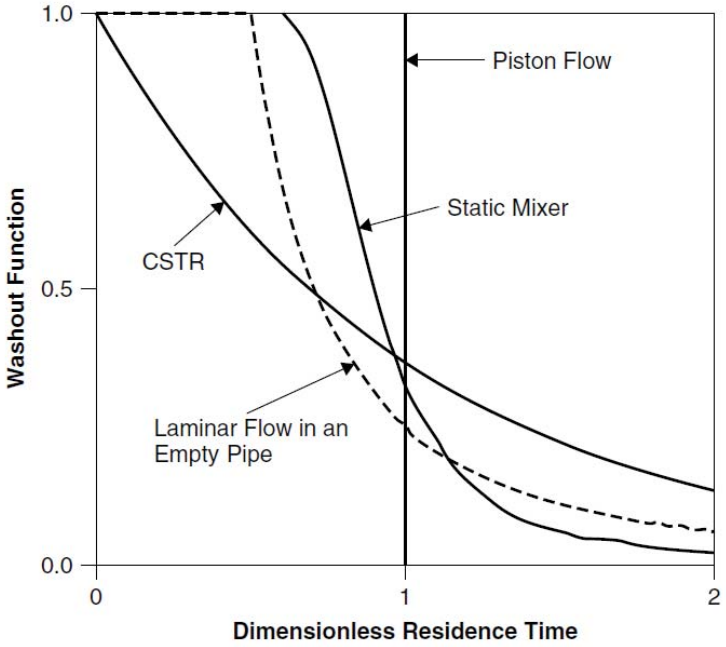

Figure 2.26 Theoretical residence times for a molecule travelling through different pipes and mixers. CTSR, continuous stirred tank reactor. Reprinted with permission from Nauman (2004), © 2004 John Wiley & Sons, Inc.

Figure 2.27 Output threads from a static mixer on adding 10 µL (A) or 1 µL (B) of concentrated food dye into a stream of idli batter. The static mixer barrel (90 mm with i.d. 8 mm and 4.5 mL volume) and the 10-element mixer insert (removed from barrel) are shown in the red box.

An example in this study of colour mixing using a Kenics-type static mixer (Fig. 2.27 red box, with the static mixer insert containing multiple mixer element repeats removed from the barrel) shows the output threads from the mixer when concentrated food dye was added into a stream of idli batter. Output from the mixer was collected from the point that dye (10 µL, A, or 1 µL, B) was applied at the top of the mixer barrel. The thread partitioned into 1) a run of undyed batter (mixer void volume); 2) a run of highly-dyed batter; 3) a trail of gradually diluted colour; and 4) a return to uncoloured batter. The total colour in an initial 1 µL or10 µL dye volume became distributed into > 10 mL batter. As static in-line mixers are designed to deliver a continuous and not a discrete mixing function, and given the trailing residence time highlighted in this example, static mixing is unsuitable for producing discrete low-volume voxels within a continuous thread of fluid. Targeted mixer design is therefore required as part of the Food-Inks 3D printer project to address colour matching and voxel formation.

2.15 Critical flow properties for Food-Ink design: Summary and conclusions

Starting from the simple equipment schematic in Fig. 2.1, a more detailed analysis of the equipment (end-user) requirements for Food–Ink formulations was developed over the course of the chapter.

- The main interaction stages between formulation and printer in the Food-Inks 3D printing application were: stabilisation of Food-Ink in the reservoir before printing; initiation of pipe flow from the reservoir; continuous or intermittent pipe flow to the mixer; mixing to achieve colour-matching by lamination; and deposition of the coloured Food-ink as a thread onto previously-deposited material. The initiation and development of fluid flow in the Food-Inks 3D printer up to the mixer depends on the stop-START-stop behaviour of the Food-Ink (static yield stress). After deposition, the retention of voxel structure depends both on the stop-start-STOP response of the Food-Ink (dynamic yield stress) and the associated relaxation time for structure recovery.
- Particulates, bubbles and soluble biopolymers add structure to the Food-Ink formulation design for a SP with embedded image. The simplest model to be considered for a Food-Ink is a shear-thinning power law fluid with yield stress (Hershel-Bulkley fluid, n > 1). From the published data, SP batters are thixotropic shear-thinning Hershel-Bulkley fluids with n between 0.2-0.8.
- Modelling of Food-Ink flow behaviour should be at a scale relevant to the pipe flow process for deposition. The suite of rheological tests should integrate methods for pipe flow behaviour, mixing effectiveness, voxel deposition, and voxel slump to characterise all aspects relevant to the printing and mixing behaviour of prototype Food-Inks.
- Apparent yield stress includes a time factor in the yield stress response, with independent relaxation times for resistance to flow initiation (stop-START-stop flow) and for deposition and structure setting (stop-start-STOP). Yield stress is markedly influenced by the particle volume fraction, size distribution and degree of polydispersity. Particulate addition is not a suitable strategy to increase Food-Ink yield stress (and potentially, load-bearing capacity) due to the high level of particulate addition required. The elastic properties of the gas-liquid interface in a particulate-gas-liquid multiphase fluid additionally modify flow behaviour by producing yield

stress behaviour at gas phase volume > 60%.

- The critical Food-Ink design elements for extrusion-based AM are the degree of shear-thinning flow behaviour and the yield stress behaviour during structure breakdown and reformation. Rapid changes in flow velocity (e.g. a rapid deposition step) have the capacity to induce marked changes in the apparent viscosity of structured fluids along the Food-Ink 3D printer flow path, and this must be taken into account in defining Food-Ink specifications.
- The critical Food-Ink design element for post-deposition retention of voxel structure is the capacity to resist spread and to support additional structure under short timeframes (high resistance to spread, high dynamic yield stress and short structure reformation time).
- Equipment design for the Food-Inks 3D printer must include flow path modelling of potential designs. The critical equipment design elements are pipe diameter during pumping, outlet diameter, the rates of fluid acceleration and deceleration on transit through different printer zones, and components that introduce resistance to flow (e.g. valves, mixer) and alter flow velocity. The flow path design requirements for Food-Ink transfer from reservoir to mixer, mixing for colour-matching and voxel deposition are independent.
- Assuming fully-developed pipe flow, the power index n and the pipe diameter are the most critical factors for printer pumping capacity; and pipe diameter and flow rate for the shear rate at the pipe wall.
- A shear stress gradient from pipe wall to centreline under pipe flow produces a curved velocity gradient across the pipe on modelling fluid behaviour, which distorts voxel shape on piping. This excludes a Food-Inks 3D printer design with extensive pipe flow between mixer and deposition head, and strongly suggests that producing trains of voxels within a continuous extrusion thread is unachievable. However, the actual velocity profile may differ markedly from the predicted profile, and needs to be tested experimentally alongside model calculations.
- Reducing the amount of fluid structure in Food-Inks (e.g. by rapid pre-shear or by constant low oscillation) will reduce pumping power requirements and standardise flow behaviour in yield stress Food-Inks. Continuous breakdown of fluid structures of Food-Ink in the printer reservoirs may also prevent separation of multiphase Food-Inks before printing.
- Unless the Food-Ink is a purely Newtonian fluid (which is unlikely in extrusion-based AM applications), in a continuous thread of material the fluid will expand on exiting the outlet, requiring an outlet diameter smaller than the target thread diameter. Random oscillation patterns generated in high-viscosity fluids may reduce the fidelity of thread deposition.
- Voxel colour-matching requires micro-mixing at low volumes, which is primarily a lamination mixing process. Models for mixing effectiveness in static mixers, which mix by extensive lamination, provide a useful first approximation of the rheological constraints on Food-Ink design to meet colour mixing requirements. Laminar mixing is more effective between fluid flows with similar density and viscosity, suiting a system where pre-coloured Food-Inks are mixed together for colour-matching.

The choice of a SP Food-Ink as the first design target added the extra steps of post-deposition voxel expansion and setting to the production of Food-Ink voxels (see section 1.4.2.1). Design task analysis (see Tables 1.1 & 1.2 and section 1.4.2.3) identified SP foam expansion and setting at the 'Microwave cooking' production step as influencing the most quality factors in SP Food-Ink formulation design. Therefore, the control of SP structure development during foam expansion and cooking becomes the highest priority design task in the design of a SP Food-Ink to produce a recognisable embedded image using the Food-Ink 3D printer application.

In Chap. 1 an analysis of the literature on SP structure development excluded wheat-based SP Food-Ink formulations from consideration, due to the work-sensitive and time-dependent nature of gluten-containing formulations, and a knowledge gap was also identified for structure development in SP formulations made using non-wheat flours and not cooked by baking.

The next three chapters examine the key events in SP structure development under microwave cooking, deconstructing a non-wheat SP formulation under microwave cooking in order to identify the critical design elements. Part of the design process is side-by-side development of test systems to evaluate design prototypes. Chap. 3 therefore describes a suite of test methods developed to examine critical events during SP product structure development, while methods to quantify SP macrostructure, mesostructure and microstructure are reported in Appendix D.

Chapter 3. A suite of tests for SP structure development

3.1 Testing batters and cooked sponge products

This chapter describes test methods chosen to deconstruct a non-wheat SP formulation cooked using microwave energy. The test formulation chosen for the study was a blackgram-rice flour-buttermilk batter, chemically leavened with sodium bicarbonate (BiC) on acidification with buttermilk acids. Other flours were substituted for rice flour to generate SP structure variants. As part of the product design process is to decide on suitable test methods for prototype design evaluation, the rationale for the choice of a particular method is explained where relevant. Chaps. 4 & 5 detail the rationale for the deconstruction experimental approach, and present results on applying the experimental methods described in Chaps. 2 & 3 and Appendix D to the idli formulations.

3.1.1 Key events in the development of sponge product structure

Chap. 1 examined the current knowledge on transitions and transformations in SP formulations during the development of macrostructure (shape, volume), mesostructure (foam organisation) and microstructure (organisation of the non-gas phase in doughs/batters and cooked SPs). In a simple solid-gas foam produced from a heat-set gas-liquid foam, structure develops in three stages: foam formation (dependent on the density of bubble initiation sites introduced into the liquid phase), foam expansion (growth in bubble size on gas expansion, or on gas transfer into bubbles), and foam setting (transformation of the liquid phase into a solid). These were identified in Chap. 1 as the three top-level functional elements in SP formulation design. In complex food formulations each of these stages represents multiple interactions between ingredient components.

Doughs and batters are closed-cell foams, containing a liquid phase with solubilised protein and non-starch polysaccharides (NSPs), sugars and soluble oligosaccharides, salts and organic compounds. Surface-active molecules in dough/batter partition to the gas-liquid interface and modulate the bubble population dynamics. Dispersed in the liquid phase is a particulate phase comprised of starch granules, cell fragments and protein bodies which fills a significant fraction of the non-gas volume. Liquid fats and lipophilic compounds may also be present as an emulsion in the liquid phase. In the absence of added emulsifiers, solid fats (butter, shortening) form a separate soft-solid phase in the uncooked dough/batter until the fats melt during cooking.

The Hadiyanto study identified the key events on baking as “starch gelatinization, protein denaturation, water evaporation, starch retrogradation, water crystallization and glass transition” (Hadiyanto et al., 2007). Starch retrogradation and glass transition are not relevant to this study, as the first relates to loss of quality on storage after baking and the second differentiates between the crisp crust and the soft crumb. The heat-mediated liquid-to-solid transition to a set structure setting involves gelatinisation of hydrated starch granules to produce swollen granules and extruded starch polymers; protein denaturation/aggregation and NSP reorganisation in the liquid phase to produce an elastomeric gel; and water loss from the liquid to the gas phase. These changes require an appropriate spatiotemporal temperature-moisture gradient to coordinate the individual transitions. The solidified

structure must also transform from a closed-cell to an open-cell foam, releasing gases and heated water vapour to the atmosphere.

3.1.2 Abbreviations

Generally, abbreviations are defined where they first occur. wwb, wet weight basis; dwb, dry weight basis. Data are reported as wwb unless otherwise stated.

3.2 Methods for general statistical tests

- *Statistical analyses were conducted using SAS Enterprise Guide 3 Version 4.2 software (SAS Institute, Cary, US). Separate batches of idli were treated at replicates for statistical analysis. One-way ANOVA analysis and Duncan's Multiple Range Test was used to determine statistical difference between means.*

3.3 Ingredient characterisation

3.3.1 Compositional analysis

Flour compositional analysis is highly standardised across the baking industry to enable benchmarking of individual flour batches and the influence of wheat flour composition on desired functionalities of this flour in food systems is well characterised. However, flours with the same total starch, protein and lipid content by compositional analysis may not behave the same way in a formulation. For example, Mohamed et al. (1998) was able to vary amylose: amylopectin ratio (and therefore starch granule response) in a rice cake formulation without change to other flour components, by replacing a portion of the standard rice flour with glutinous flour having an almost identical non-starch composition by analysis, but which contained no amylose.

3.3.1.1 Methods for compositional analysis

- *Sample moisture content was determined by drying to constant weight at 105˚C. Starch content was determined with a Total Starch assay kit after removal of oligosaccharides and solubilisation of resistant starch (Megazyme, Wicklow, Ireland). Protein was determined as nitrogen using Kjeldhal analysis, N x 5.95 (rice flours), 6.25 (sorghum flour) or 5.80 (bean flour). Lipid content was determined by Soxtec extraction (AOAC International, Method 991.36) (AOAC International, 1992); and dietary fibre content by the Enzymatic-gravimetric method (AOAC International, Method 991.43) (Lee, Prosky, & DeVries, 1992) in a commercial laboratory.*

3.3.2 Particle size analysis

Particulates such as flours can be sorted by size using

- Measurement of the apparent particle diameter in dispersed solutions by automated laser diffraction particle sizing (LDS).
- Digital image analysis of light micrographs of dry flour particles
- Sifting through a sieve set with decreasing mesh size.

LDS gives a measure of the largest particle diameter under rotation in solution, while sieving measures the second-largest diameter. Image analysis gives the truest evaluation of particulate

dimensions. Both sieving and digital image analysis are time intensive, while sieving requires a large sample for reproducible results. LDS provide a simple, rapid way to compare particulate size distribution in flours and dispersions.

3.3.2.1 Methods to analyse particle size

- *Flour particulates or concentrated dispersions were sized within one minute of vigorous dispersion into water at room temperature, using a MastersizerS long bed Laser Diffraction Particle Sizer (Malvern Instruments, Surrey, UK) and a 300F or a 1000 lens. Using Malvern Instruments Version 2.19 software, particle size distribution was derived as %volume ($D_{4,3}$) as the blended mean of three separate determinations at each lens size.*
- *Some particulates were sized by direct measurement in digital images, as described in Appendix D.6.*

3.4 Preparation of idli batters and testing fractions

As much as feasible, batter testing fractions were prepared reproduce the conditions experienced in whole batter for formulation handling, pH changes and ionic concentration. For some testing fractions large bean particulates and buttermilk flocs were first removed by centrifugation before adding remaining ingredients, to enhance the response of flour components on testing.

3.4.1 Method to prepare idli batter

- *Hulled split blackgram beans, chickpea, pea, blackgram, sorghum, and rice flours, cultured buttermilk (BM) (Tararua, Goodman Fielder, Auckland, New Zealand) and baking soda (BiC) (Hansells, Masterton, New Zealand) were purchased from retail outlets. All preparations in this study made with flours sourced from a single batch. Flour weights are given as wwb, unless otherwise stated.*
- *Beans were treated in 0.05% hypochlorite for 10 min, rinsed well, and soaked overnight in water. For batter, 265 g of well-drained beans was ground for 10 min with 171 g cold BM at 4 ˚C in a Magimix Compact 3100 food processor (Magimix, Vincennes, France). A further 295 g BM was added and ground briefly, to give a bean-buttermilk fraction (BBM) which was stored at 4 °C for up to 4 h before use. For each idli batch, 203 g of batter +BiC was prepared by folding in 48.7 g flour into 154.3 g cold BB (BBM: flour at 0.758: 0.242). The flour was hydrated at 20 ˚C, folding in 0.5% NaCl (w/w) at 45 min, and 1.0% BiC (w/w) at 60 min, immediately before aliquotting. The batter just before BiC addition is the –BiC batter fraction, and that at 5 min after BiC addition (the start of cooking) is the +BiC batter fraction.*

3.4.1.1 Method to prepare supernatant fractions of buttermilk and bean-buttermilk

- *For some preparations, BM or BBM were centrifuged at 5,000 **g** for 30 min at 4 ˚C and the supernatants retained. The supernatant pH was adjusted with 4 M NaOH to pH 5.3 (the mean pH of batters after flour addition), to give BM_{Liq}-5.3 and BBM_{Liq}-5.3. The volume fraction of BBM supernatant was 0.521 ± 0.007, with mass fraction of 0.476 ± 0.007 and density of 1.05 g/mL. On visual analysis by light microscopy, it was comprised of a liquid phase and small buttermilk protein aggregates, but was deaerated and without starch granules, bean fragments or large BM flocs.*

3.4.2 Preparation of batter fractions

3.4.2.1 Method to prepare fractions for low amplitude oscillatory shear testing under batter-equivalent conditions

- *Batter fractions were prepared using BBM_{Liq} (see previous section) in place of BBM, to enhance the influence of the flour by removing the contribution of large BBM particulates to the batter. To account for the increased liquid phase mass volume on removal of particulates, NaCl content to the batter was increased proportionally. In place of BiC (which complicates the rheological response by adding a gas phase to the system), the batter fraction pH was adjusted with 4 M NaOH just before rheological testing to pH 7.0, the mean pH of batters soon after BiC addition.*

3.4.2.2 Method to prepare fractions for flour pasting under batter-equivalent conditions

- *Flours were pasted under batter-equivalent conditions by mixing flour and BBM_{Liq} in a canister to a total of 28.0 g. After 15 min hydration, NaCl was added to give the equivalent of 0.5% salt content in whole batter. At 30 min, batter was titrated to pH 7.0 with 4 M NaOH immediately before pasting.*

3.4.2.3 Method to prepare washout fractions for foaming tests

- *Flour (36.0 g) was added to cold BBM_{Liq} (40.0 g), and left to hydrate for 45 min at 20 °C before adding 0.7% NaCl (w/w). After a further 60 min hydration, 20-70 mL BBM_{Liq}-5.3 was added, to produce supernatants with 70-100 mL volume after centrifugation at 5,000 **g** for 30 min. It was assumed that NaCl and soluble components of flour and BBM partitioned completely into the liquid phase during centrifugation. Supernatant volumes were made to 100 mL with BM_{Liq}-5.3. The resultant washout fractions contained soluble components from flours equivalent to those in 116.2 g whole batter, with a similar background of BBM and NaCl.*
- *The BBM washout fraction for foaming was prepared by adding 0.7% NaCl to BBM_{Liq}-5.3.*

All washout fractions had a consistency similar to thin pouring cream (i.e. no fluid structure before whipping).

3.4.2.4 Method to prepare batter samples for light microscopy analysis

- *BBM-5.3 (5.0 g of BBM-5.3 sample) or small batter preparations (1.2 g flour added to 3.8 g BBM) were sealed in lidded 25 mL plastic cups. After 15 min at 20 °C, NaCl (25 mg) was mixed in. At 30 min a small portion was removed and analysed (–BiC sample), then 50 mg BiC was mixed in gently and a further portion analysed immediately (+BiC sample). A coverslip was placed over samples on the slide and gently pressed before viewing.*

3.4.3 Batter characterisation

3.4.3.1 Method for batter density determination

- *The specific volume of batter before bicarbonate addition (-BiC batter) was determined at 20 °C from the weight of batter in a container of known volume (Sahu & Niranjan, 2009). After BiC addition, batter density was estimated as [π x average batter height at circumference x ((cylinder diameter)/2)^2]/ batter weight, taking five estimates of idli height around the beaker circumference just before cooking.*

3.4.3.2 Method to determine flour titration capacity

- *Batter fractions without BBM particulates prepared for rheological testing (see section 3.4.1.1) had varying flour content. The increase in pH with incremental addition of 4 M NaOH was recorded during neutralisation of these fractions to pH 7.0. To determine the influence of flour on batter titratability, a linear regression was applied to the combined data to quantify the relationship between moles of added base and flour content.*

3.4.3.3 Method to measure water activity of batter

- *Water activity was measured in batters before BiC addition using a standard commercial water activity meter, and sample volume < 5 mL.*

3.4.3.4 Method to determine flour water binding capacity on hydration

During preparation idli batters are hydrated for 1 h at room temperature after flour addition. Soluble protein and NSP biopolymers become hydrated and may swell to form a gel. Some water also moves into starch granules, dependent on the permeability of the granule coat, although loss of order in starch polymers does not take place until heat is applied. Extended flour hydration before cooking is considered to be important for successful breadmaking using rice flours (Song & Shin, 2007). The water uptake capacity of the different flours was evaluated under non-batter conditions.

- *Flour (1.000 g, wwb) was hydrated with stirring in 15 mL of deionised water at 18 °C, then centrifuged for 10 min at 3,000 **g**. The weight of the pellet was measured to determine water binding capacity at room temperature, as [100*(Pellet weight – flour weight wwb))/(Flour weight)].*

3.5 Methods to determine batter foaming properties

Foaming capacity and foam stability were tested as described by Marco & Rosell (2008). Heat treatment was applied to a proportion of washout fraction before foaming, to evaluate the effect of cooking on batter foaming properties. BBM and batter washout fractions were prepared as described in section 3.4.2.3.

3.5.1 Method for heat treatment of batter washout fractions

- *50 mL of washout fraction was heated intermittently with stirring over 30 s at 80% microwave power, monitoring temperature until 55˚C was reached (approximation of early batter cooking). The heated washout fraction was cooled rapidly in water, and foaming properties determined at room temperature.*

3.5.2 Method for foaming capacity determination

- *0.58 g BiC (w/w) was added to 50 mL of batter washout fraction or to 50 mL BBM washout fraction at 20 ˚C (prepared as in 3.4.2.3). The solution was whipped immediately for 90 s using a standard commercial milkshake maker, the foam immediately decanted into a 150 mL measuring cylinder and the volume recorded. Foaming capacity was calculated as 100 x (Foamed volume)/(Initial volume).*

3.5.3 Method for foam stability determination

- *Foam stability was determined as the resistance of the foam to drainage on standing in the*

measuring cylinder at 20 ˚C. The total (foam+ liquid) volume and the volume of the drained liquid were recorded over 60 min.

3.6 Cooking conditions

3.6.1 Characterisation of microwave oven

Domestic microwave ovens are not designed for prolonged cooking times as output drops off with extended use (Swain, James, & Swain, 2008; Swain, Spinassou, & Swain, 2008). The model of microwave oven used in this study was tested for average power output and for output variation on extended use. Power output was determined by a standard water heating test for microwave power determination (Buffler, 1992). Average power usage was determined as 677 ± 10 W.

When started from cold, the average power output of the oven was around 110% of that after pre-warming the oven for 5 min (data not shown). During a continuous load period the power output reduced gradually over 25-30 min by 25-35% compared with average power usage of a pre-warmed oven (Fig. 3.1 left). To standardise cooking conditions the oven was first run for five min if it was more than 1 hour since its last use.

The design of the oven door excluded the monitoring of batter rise during cooking by direct visualisation of samples using photography.

3.6.1.1 Method to determine microwave oven energy

- *Microwave cooking was done in a 2450 MHz Kenwood Multifunction microwave oven Model MW786 with average power output determined by the 2 litre IEC method adaptation of Buffler (Buffler, 1992).*

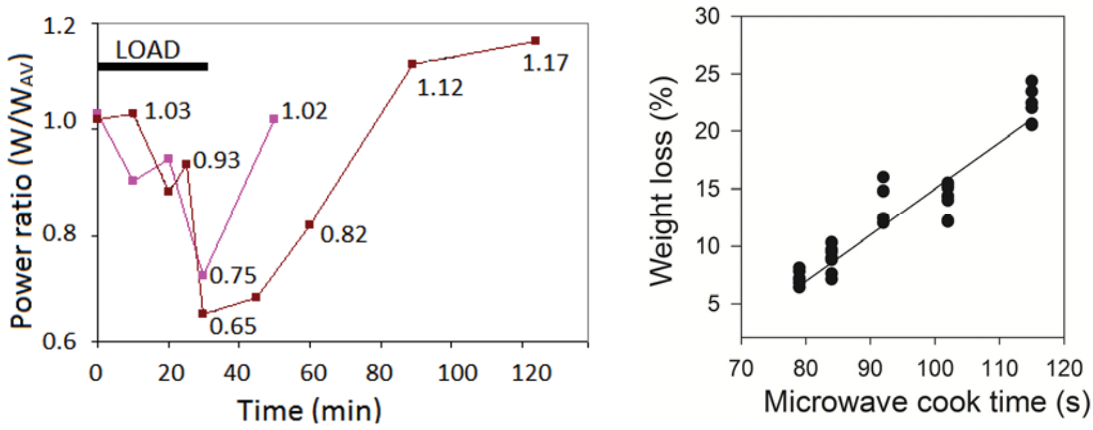

Figure 3.1 Left: typical loss and recovery of microwave power output in the Kenwood Multifunction oven. Power usage was tested during 30 min continuous use (labelled load) and after load removal (two replicate runs). Right: weight loss from idli batter as %(initial weight) plotted against cook time, for 10.0 ± 0.1 g batter aliquots in 19 mL silicon mini-muffin pans cooked at 80% power; slope: y = 0.40 x, R^2 = 0.82 (n = 4 runs). 'Cook time' refers to cumulative exposure to microwave energy, not to time setting on the oven.

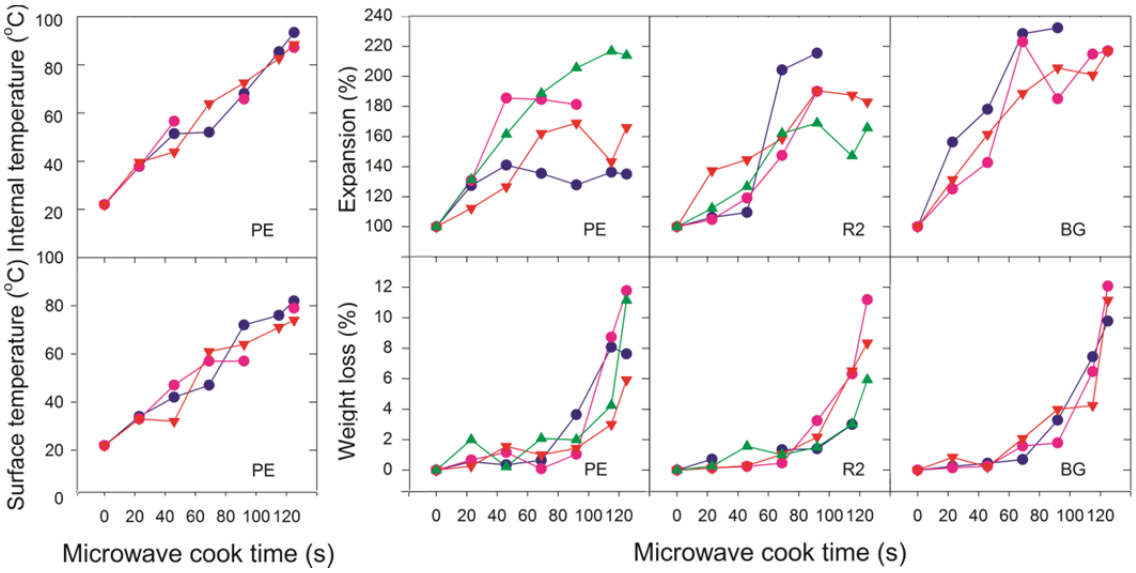

Figure 3.2 Changes in idli batter temperature, volume and weight on microwave cooking, for 45.0 g batter cooked in 64 mm diam. beakers at 80% power. Left: typical idli heating profile (Internal and surface temperature) for pea idli batter (PE). Right: idli batter weight loss and expansion for batters made with pea, rice2 (R2) or blackgram (BG) flour. 'Cook time' refers to cumulative exposure to microwave energy, not to time setting on the oven. Data points represent a sample removed at 30 s intervals during cooking (= 27 s of microwave cook time at 80% cycle).

3.6.2 Batter weight loss, heating rate and expansion on cooking

Cook time for a specific set of batter samples was set to a time/power setting which gave adequate structure setting without browning, to a weight loss of 10% unless otherwise stated. Fig. 3.1 right gives test cook data for batches of eight batter samples (10.0 g portions in 19 mL silicon mini-muffin pans). Batter setting was complete by 80 s - increasing the cook time after this produced a linear increase in weight loss.

To compare batter heating rates, the batter temperature was recorded internally at the beaker centre and at the batter surface, for batches of six beakers containing 45.0 g batter. Between-batch values were determined by removal and measurement of randomised samples during cooking, for n = 3 or 4 batches; each batch was freshly prepared. The linear batter heating profiles at the batter centre and the surface shown for pea idli batter (Fig. 3.2 left) were typical of heating profiles for other batters. Heating rates were consistent across batches under the same cooking conditions. The batter heating rates were similar across different batter formulations, ranging between 31-37 °C/min for internal temperature at the batter centre, and between 27-29 °C/min for batter surface temperature. The heating rate of a low-fat food material on microwave cooking is determined primarily by the content of dipolar and ionic molecules, including water (see section 1.3.2). As the different idli formulations had the same water content and negligible fat content, microwave-responsive molecules in bean-buttermilk, NaCl and BiC, not flour, were the main source of components controlling microwave heating rate, explaining the similarity in heating rate between batter formulations.

The start of extensive water loss was correlated with the setting of the batter surface as observed

by eye. Batter weight loss began on the release of water vapour during the transition from a closed-cell to an open-cell foam. Between-batch weight loss was consistent for the same batter (Fig. 3.2 right, bottom row) but the degree of batter expansion was highly variable, between individual samples and between batches (Fig. 3.2 right, top row). This variability can be explained primarily by oven position effects and by a time lag after BiC addition between portioning the first and the last aliquots in a batch. Earlier batch aliquots expanded within the cooking container, while later aliquots were portioned when batter was already partly expanded. During cooking batter expansion was observed to occur within 5 s.

One-way ANOVA analysis of cooked idli properties (moisture content, volume, texture) confirmed there was no detectable influence of batch number, batch preparation order or sample cooking position on final cooked product physical properties ($p < 0.05$). Care was taken during cooking to run a balanced design for replicate batches, to pre-warm the oven if not used within the previous hour, to position samples consistently on the microwave turntable, and to assign the oven position of aliquotted samples randomly. The variability in batter expansion data suggests that sample number would need to increase greatly for a reproducible determination of expansion rate and, by extension, for batter transformations on microwave cooking.

3.6.3 Method for microwave cooking of idli batters

- *For samples of 45.0 ± 0.2 g batter, four borosilicate beakers per batch were evenly-spaced, with the beaker outer edge placed 20 mm from the turntable edge. Samples were cooked at 80% power for 3.0 min, with a half turn of the beakers at 1.0 min intervals. Batter heating rate, water loss and expansion during cooking were determined in 45 g samples, six per batch, and samples were removed at 30 s intervals, and turned at 1.0 min intervals.*
- *For samples cooked in silicon mini-muffin pans with volume of 19 mL (3 pans in a strip, 2 or 3 batter aliquots per strip), four strips were placed immediately against the edge of the turntable at four equidistant, standard positions on the turntable, and cooked for 120 s at 80% power.*

3.7 Cooked product attributes

3.7.1 Volume, shape and mesostructure characterisation

Product shape is a diagnostic tool in industrial test baking which provides information about dough/batter expansion during cooking, and whether the cooked structure has collapsed on cooling (incorrect setting).

3.7.1.1 Methods to determine weight, volume and water content of cooked products

- *Each cooked product was characterized separately, and stored at 10 min after cooking in a sealed container before analysis of cooked volume, with a minimum of 12 independent samples. Batter weight and height (at four positions around the beaker circumference) was recorded before cooking and at 10 min after cooking. Cooked sample volume was measured by the seed displacement method (Griswold, 1962). Cooked product moisture content was determined by drying to constant weight at 105˚C.*

3.7.2 Mechanical properties of sponge products

Standardised tests of SP mechanical properties are used industrially for SP quality evaluation, primarily for prediction of sensory quality. Deformation tests may give reproducible quantitative differences between samples, but do not necessarily have a direct relationship between sensory evaluation of texture; while the lack of a quantitative difference does not guarantee there is no difference in structure or sensory texture (Szczezniak, 1987). To quantify texture differences between muffin formulations, Baixauli, Sanz, Salvadore & Fiszman (2008) used both a *Texture Profile Analysis* test and an industry test for muffins, modified to compress a cylindrical plug from the muffin with a probe larger than the sample. Most industry tests of baked products use a probe smaller than the sample, to expose the sample to a tearing action as well as to compression (emulation of biting and chewing) (Trinh & Trinh, 2009b).

Compression test settings commonly applied to baked sponge products were evaluated for usefulness in comparing the cooked idli. Idli samples were cut to a standard size from the product centre, and taped to the stage to prevent adhesion to the compression probe. Following the example of Baixauli et al. (2008), the probe was larger than the sample.

3.7.2.1 Texture Profile Analysis

Texture Profile Analysis (TPA) administers cycles of compression and withdrawal to a set strain. A compression strain value is chosen which falls at just beyond the point of sample failure (Trinh & Trinh, 2009b) so that recovery of the sample is incomplete between compression cycles. To approximate the destructive effects of chewing, a *two-bite* test with two cycles of compression-withdrawal (Bourne, 1978) is generally applied, but more cycles can be added to observe the sample to destruction (Trinh & Trinh, 2009b). Baixauli et al. (2008) summarised the TPA compression cycle settings from a number of studies on SPs. The %strain used ranged between 30-60%, and was most commonly set to 50% of sample height.

3.7.2.2 Method for Texture Profile Analysis of cooked sponge product

- *The texture of individual cooked products was determined as described for muffins (Baixauli, Salvador, & Fiszman, 2007) using Texture Profile Analysis (Bourne, 1978). Idli had top and bottom surfaces removed and were trimmed to 25 mm cubes (for 64 mm diam. products cooked in beakers) or 12 x 20 x 20 mm cubes (for products cooked in mini-muffin pans). The TA.XT.plus Texture Analyzer (Stable Microsystems, Goldaming, UK) was fitted with a 5 kg or 50 kg load cell and a 37 mm diameter cylindrical probe. Note that the compression probe was larger than the sample, as used by Baixauli et al*. (2008).
- *Each cube received one or more cycles of compression to the %(initial height) defined for each test, at a constant crosshead speed of 1.0 mm/s and with 5 s lag time between cycles.*

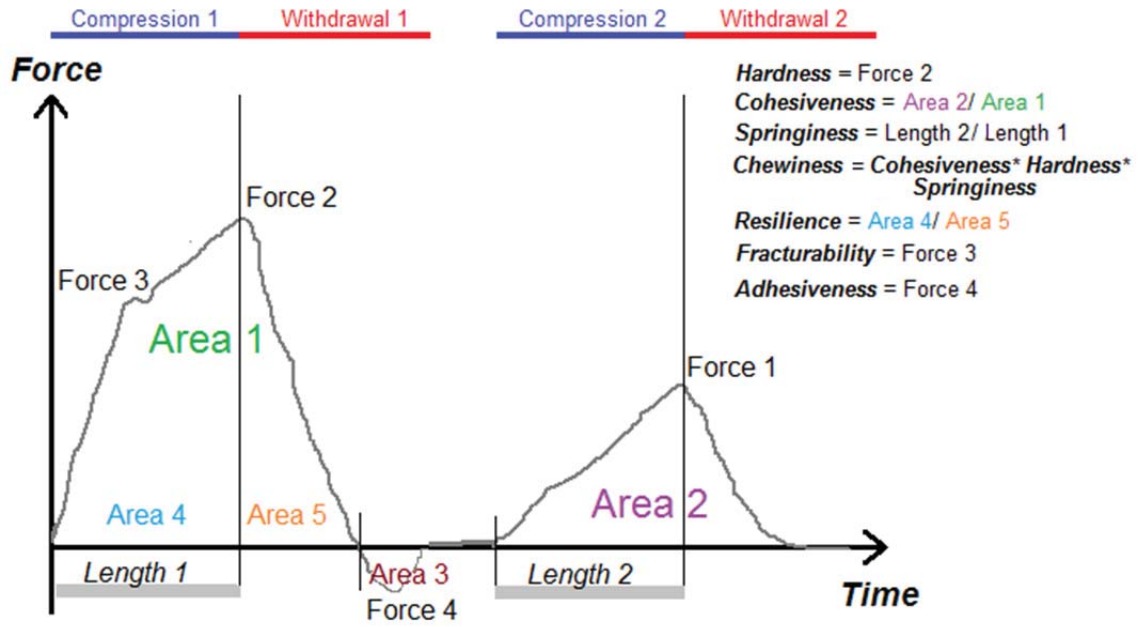

Figure 3.3 Texture Profile Analysis force-time curve and calculated TPA parameters, based on Bourne (1990).

Fig. 3.3 describes the stages in a generic two-bite TPA test, and shows the calculation of (arbitrary) texture parameters derived from the TPA curve. The TPA parameters used in this study were calculated as defined in Texture Technologies (2008) and Bourne (1990):

- *Hardness*: the peak force on the first compression of the product.
- *Cohesiveness*: the ratio of the area under the second deformation curve to that of the first curve (sample resistance to multiple deformations)
- *TPA Springiness: the* ratio of the time taken to reach maximal force on the second compression cycle to that of the first cycle (elastic recovery after first compression).
- *Chewiness*: the product of Hardness x Cohesiveness x Springiness (composite value suggestive of texture on chewing).
- *Resilience*: the ratio of the area on the first compression curve after the compression is removed to the area of the curve before release (structure recovery after first compression).
- *Adhesiveness* is the maximum negative force associated with disengagement of the probe from the food surface after the first compression (stickiness).
- On the first compression a part of the sample may fracture before reaching the maximum force on compression. The inflection point in the compression 1 curve is the TPA *Fracturability* parameter.

3.8 Flow behaviour of batter fractions

The aim of rheological testing of SP formulations was to compare the different formulations during SP production, to understand the contribution of batter flow behaviour to SP structure formation and setting. The rheological tests applied before cooking and on heating were:

- Back extrusion of whole uncooked batters before bicarbonate addition (-BiC batters) (no heating, to compare bulk flow response of the multiphase batter before CO_2-driven foam expansion).
- Dynamic oscillatory rheological testing under low amplitude oscillatory (to compare batter viscoelastic behaviour, before and after heating).
- *Pasting* of batter fractions with equipment used commercially to evaluate flour quality for SP applications (to compare the relative timing of rapid viscosification in batters). Pasting is the controlled heating of flour under stirring (shear deformation) until starch granule disintegration.

3.8.1 Back extrusion test on whole batter before bicarbonate addition

The sample fills a cylinder of set volume and flow is induced by inserting a narrower piston to a set depth at a controlled speed. The gap through which material flows is 2 mm for the setup in this study (see section 2.7.2 for method and example graphs).

3.8.2 Low-amplitude oscillatory shear testing of batter fractions

- *Rheological properties were evaluated for starch-hydrocolloid dispersions or batter fractions using a Paar Physica RC1 Rheometer and plate-plate geometry (Anton Paar, Graz, Austria), under low amplitude oscillatory shear at 1 /s (previously determined to be within the linear viscoelastic range).*

Batter fractions were prepared for testing as in section 3.4.2.1. Test methods are given in section 2.2.4.1.

3.8.3 Testing for wall slip

Low amplitude oscillatory shear deformation tests to quantify changes in dynamic viscosity should have a gap between moving surfaces at least ten times the size of the largest particle to reduce particle-wall interactions (Rao, 2007f). Flours are generally graded to 250 µm mesh size (i.e. the largest particulates have a second largest dimension of 250 µm as determined by sieving), while the usual gap in standard cup-and-bob geometries is 1,000 µm. Additionally, particulate dispersions are prone to slip at the boundary of moving surfaces under shear: that is, a lubricating layer of particulate-free liquid phase close to the wall results in a lower value for apparent viscosity of the dispersion (Rao, 2007f). Wall slip can be detected by change in viscosity parameters with increasing gap size (Wein, 2005; Yeow, Leong, & Khan, 2006). Roughened plates reduce the occurrence of slip by compensating for the reduction of particle density that occurs when a flat planar boundary forms a barrier to complete particle packing.

The behaviour of –BiC batters under low amplitude oscillatory shear was tested for wall slip effects by changing the size of the gap between 1.0, 1.5 and 2.0 mm. There was no difference in flow behaviour when different batter fractions were tested (data not shown).

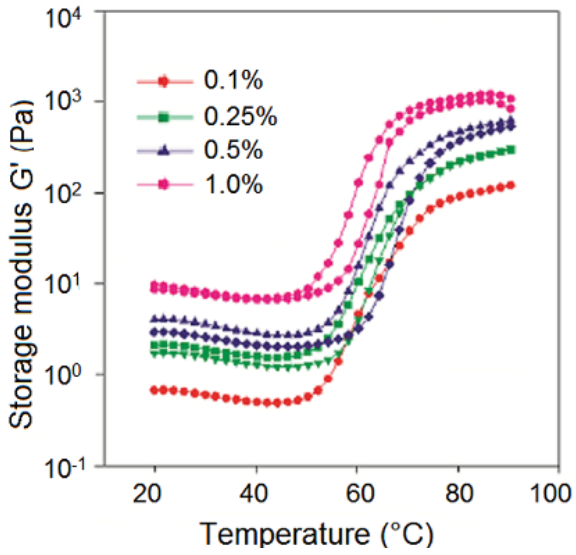

Figure 3.4 **Storage modulus values (*G'*) under low amplitude oscillatory deformation at increasing %strain, on heating of blackgram batter fraction (at pH 7.0, prepared without bean-buttermilk particulates and sodium bicarbonate). Plate-plate roughened geometry was used.**

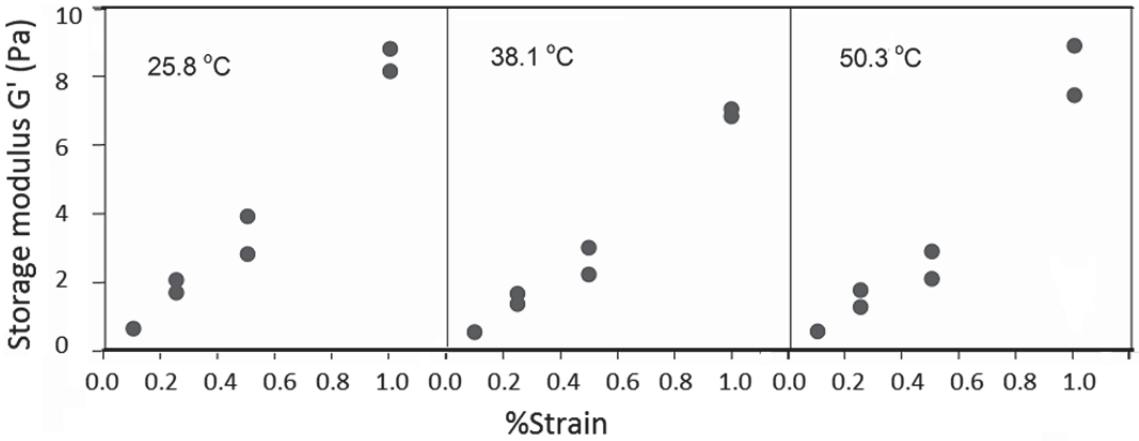

Figure 3.5 **Storage modulus data from Fig. 3.4 plotted as a function of %strain with increasing temperature.**

3.8.4 The linear viscoelastic range under low amplitude oscillatory shear

An example of flow behaviour under fixed frequency and increasing strain on low amplitude oscillatory shear deformation from this study is shown in Fig. 3.4, for an idli batter fraction prepared without BiC or blackgram bean-buttermilk particulates (see section 3.4.2.1). Components contributing to batter fraction flow behaviour included starch granules and bean fragments from added BG flour; and soluble polysaccharides, proteins, ionic solutes and other small solutes from BG beans, BG flour and buttermilk.

In the early stage of batter heating, before rapid viscosification due to starch gelatinisation, both storage modulus (*G'*) and loss modulus (*G"*) decreased at a linear rate between 25-50 °C (Fig. 3.4), consistent with an initial increase in batter fluidity on heating, as reported to occur in other SP formulations (e.g. Gaines & Donelson, 1982). Below 50 °C, increasing the %strain between 0.1-1.0 for

this sample produced a linear increase in storage modulus and loss modulus with increasing strain (storage modulus data is plotted in Fig. 3.5), indicative of little loss of structure in the BG batter under low strain oscillation before the onset of rapid viscosification.

3.9 Observation of events in structure setting

The visualisation of structure setting by direct observation of structure change in situ is the preferred approach to monitoring events on structure development and setting during SP cooking. However, in this study energy fluctuation over the microwave duty cycle, together with dependence of heating rate on turntable position, generated enough between-sample variation in expansion and setting rates to exclude the use of direct observation methods. Instead, monitoring of events during starch gelatinisation was chosen as an indirect test of the relative timing of structure setting, based on the rapid viscosification of SP batter as a result of starch granule swelling. Differential scanning calorimetry (DSC) can be used to identify the initiation of granule gelatinisation as a loss of starch polymer order on heating in the presence of water. With increasing starch polymer hydration, granules swell to fill the dispersion volume, sequestering water from the liquid phase. Analysis of the rate of increase in viscosity of batter fractions on heating allows between-batter comparison of the relationship between batter temperature and the rate of structure setting.

3.9.1 Water binding capacity of flour on hydration at room temperature

Idli batters are hydrated for 1 h at room temperature after flour addition. On hydration insoluble proteins and NSPs sequester water and influence the viscosity and the volume of of the liquid phase.

- *Flour (1.000 g) was hydrated with stirring in 15 mL of deionised water at 18 °C, then centrifuged for 10' at 3,000* ***g*** *(Singh, Kaur, Sodhi, & Sekhon, 2005) and the weight of the pellet measured to determine Water Binding Capacity at room temperature as 100*(Pellet weight – flour weight wwb))/(Flour weight). The flour weight was measured on a wwb.*

3.9.2 Onset of starch gelatinisation by differential scanning calorimetry

DSC measures changes in specific heat capacity with structure ordering/disordering during physical state changes and chemical reactions. For purified starch granules in excess water, a single peak of exothermic enthalpy change is generally observed in the DSC profile, and calculated gelatinisation enthalpy values for purified starches represent the sum of endothermic granule swelling, crystallite melting, and exothermic hydration (Eliasson, 2003). DSC analysis can identify the initiation of granule gelatinisation from the onset of this enthalpy change.

DSC methods have also been used to characterise the behaviour of ingredients, doughs, and batters on heating (e.g. Donovan, 1977; Fessas & Schiraldi, 2000; Wilderjans et al., 2010) and to examine SP ingredient interactions (e.g. in a GF formulation, Kobylanski et al., 2004). The data from sealed-pan DSC does not represent events after the start of water loss from the formulation (Eliasson, 2003), as the sealed DSC pan stops water loss from the sample.

Gelatinisation is a non-equilibrium process sensitive to the availability of local water to individual starch granules (Waigh, Gidley, Komanshek, & Donald, 2000). The water content in wheat-bread doughs falls around 40-50% on a mass basis and batters generally contain water content of at least 60% (with a

significant proportion of this water lost as water vapour during cooking). Other dough/batter components may also compete for water. Therefore starch polymers are generally not completely hydrated in cooked SP dough/batter (see section 1.5.9 & Fig. 1.16). Gelatinisation is also sensitive to heating rate (see section 1.5.8.2). A very rapid heating rate (as on microwave cooking) will restrict the degree of starch gelatinisation in SPs.

DSC analysis of potato starch on heating produced two exothermic peaks at water content below 14 water molecules per glucose residue (the maximal hydration capacity for each residue, at a mass ratio of glucose: water of 1:2.5). The second peak, which shifted to higher temperature as water content decreased further, recorded melting of starch crystalline structures in the absence of sufficient water (Donovan, 1977). A similar two-peak gelatinisation profile occurs for wheat starch under limiting water conditions (e.g. Kaletunc & Breslauer, 2003), while pea starch gelatinisation in 6 M KCl also generated two overlapping peaks (Bogracheva , Wang, Wang, & Hedley, 2002).

More complex enthalpy profiles are produced in flour samples, as enthalpy changes due to structure reorganisation of non-starch components may overlap with those on granule gelatinisation. For example, chickpea flour and water at 9:32 mass ratio produced a DSC profile with two main peaks, the first attributable to granule gelatinisation, and a second partly-overlapping peak to protein denaturation (Meares, Bogracheva, Hill, & Hedley, 2004). Wheat-flour protein denaturation is poorly detectable under the water conditions found in doughs and batters (León, Rosell, & Benedito de Barber, 2003) and so is usually ignored on reporting DSC data for wheat-flour SP formulations.

DSC was performed on freeze-dried batters after a short rehydration, which produced similar profiles and peak positions to freshly-prepared samples, but which generated larger enthalpy values (data not shown). All work on batters was carried out with freeze-dried material to maximise the DSC output signal. The influence of heating rate on the DSC peak definition was evaluated using rice1 batter. A heating rate of 40 °C/min is close to the bulk heating rate of 31-37 °C/min measured at the centre of batters during microwave cooking (section 4.4.4). However, the pan limit on DSC sample size meant that peaks were poorly differentiated at this heating rate (Fig. 3.6 left). Enthalpy quantification in batters was therefore carried out at 10 °C/min. A typical DSC profile for blackgram batter (Fig. 3.6 right) shows the manual partitioning of peaks, with the first enthalpy peak (gelatinisation) defined by extension of the heating baseline as shown. The DSC temperature of gelatinisation onset and DSC peak temperature are the key parameters for events in early starch gelatinisation.

3.9.2.1 Method for Differential Scanning Calorimetry of batter fractions

- *Batters used to prepared idli, after BiC addition were frozen, freeze-dried under vacuum, and stored at room temperature in a sealed container before analysis.*
- *Thermal analysis of freeze-dried or freshly prepared material was performed using a model DSCQ100-1060 differential scanning calorimeter (TA Instruments, New Castle, Delaware, US). Freeze-dried materials were broken up in a mortar and reconstituted to original moisture with Milli-Q® water (Millipore, North Ryde, Australia). A sample (15-25 mg) was crimped in a 40 µL aluminium pan and heated from 15-125˚C at 10˚C /min, beginning 10 min after water addition. Sample dry weight was determined after drying the pierced pan for 24 h at 105˚C. Endothermic heat change (ΔH, as J/g dry*

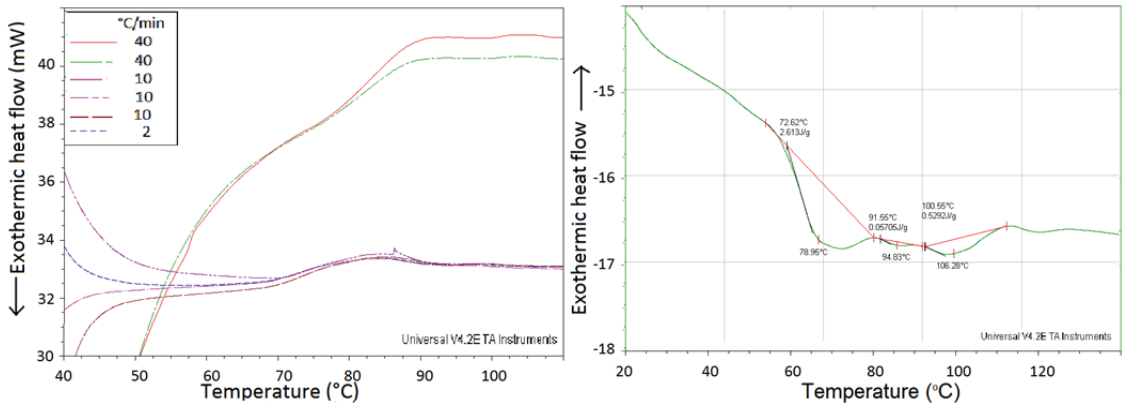

Figure 3.6 Differential scanning calorimetry profiles for freshly-made rice1 flour batter, (left) heated at 2, 10, and 40 °C/min; (right) a typical trace for blackgram batter showing peak analysis details (output from TA Universal Analysis software).

weight batter), onset and peak temperatures were derived using Universal Analysis 2000 Version 4.2E software (TA Instruments). The instrument was calibrated against a sapphire standard and samples were run in tandem with an empty reference pan. Data are reported as dwb.

3.9.3 Timing of rapid viscosification by rheological testing

Starch granules swell as more water enters the granule for polymer gelatinisation, and with the loosening of semi-crystalline structures with increasing temperature. Minor components such as proteins and lipids associated with the granule coat can also influence granule swelling behaviour on gelatinisation (Debet & Gidley, 2006). The volume fraction that granules occupy in the dispersion increases geometrically with granule swelling. A rapid increase in the apparent viscosity of the dispersion occurs as the liquid phase fraction is reduced. On gelatinisation at a specific flour content (~14.0% wwb, or 10.6% dwb, for wheat flour) fully-expanded granules will completely fill the dispersion volume without compressing each other (Navickis & Bagley, 1983).

3.9.3.1 Rapid viscosification of batter fractions under low amplitude oscillatory shear

In idli formulations tested using low amplitude oscillatory shear, once temperature rose above 40-50 °C (start of significant viscosification with starch gelatinisation) the reproducibility between replicate preparations reduced markedly, particularly for CP batter fractions.

The low reproducibility is due in part to the sensitivity of starch-based rheological tests at small volume to small changes in starch concentration (A. Rao, pers. comm.). Additionally, the Paar Physica rheometer used cannot compensate for a change in normal force on the top plate when sample volume changes rapidly, as during rapid starch gelatinisation. As a result, this test system was only used to quantify changes in flour and batter flow behaviour on heating below the point of rapid batter viscosification.

3.9.3.2 Pasting of batter fractions

In pasting studies, flours are heated in excess water with stirring until starch granule disintegration. Expanded granules are sensitive to shear and break up under stirring at high temperature, resulting in a

drop in solution viscosity. As the cooked starch mass starts to set into a gel on cooling, the dispersion viscosity increases again. The time-temperature response of wheat flour on pasting is used industrially to predict flour behaviour in SP formulations. A pasting test is indicative of flour quality, and is not necessarily correlated with events during SP preparation. Starch granules in SPs 1) are not in excess water, and 2) may be under squeezing deformation, but do not experience the shear deformation that occurs in pasting tests.

The Rapid ViscoAnalyser™ (RVA) is a robust pasting device used extensively in industry for pasting wheat flours to characterise baking quality. The geometry has a curved vane (paddle) to maintain ungelatinised starch granules in suspension until swelling. Changes in viscosity are measured as a change in torque. An estimate of the average shear rate can be calculated by multiplying revolutions/s by 20.1 (Lai, Steffe, & Ng, 2000), but the lack of strain data means the test system cannot be used to derive fundamental rheological properties of non-Newtonian fluids (Steffe & Daubert, 2006d). RVA results in this study are therefore reported as RVA units rather than standard viscosity units.

While the RVA system generates a variety of parameters related to wheat flour quality (Batey, 2007) the portion of the pasting curve relevant to SP structure setting is the first part of the pasting curve rising to the first peak (RVA *Peak Viscosity*, PV), the period of rapid viscosification on starch gelatinisation. Under non-limiting water conditions the PV parameter is the point at which granule breakdown begins to overtake granule expansion processes (Newport Scientific, 1998). To make a useful comparison between different flour types in the idli batter system, modified batter preparations were pasted at flour contents which produced a PV value of 6000 ± 500 RVA units. Visualisation of changes in RVA apparent viscosity values was enhanced by plotting RVA data as the 1st derivative curve (Meadows, 2002), after normalising each data point for change in viscosity by dividing by the maximum rate of observed positive change in RVA viscosity.

3.9.3.2.1 Method for RVA pasting of batter fractions

- *Pasting properties of flours and batter fractions (sample + liquid to 28.0 g) were determined using the Rapid ViscoAnalyser™ RVA-Super 4 and Thermocline for Windows version 2.6 software (Newport Scientific, Warriewood, Australia). For pre-hydration, dry samples were weighed into the canister with the liquid, shaken, and material scraped off the sides with a Teflon spatula. The heating-cooling profile was based on the Thermocline STD1 protocol, with an extended cooling stage. Paddle speed was run for 10 s at 960 rev/min and then maintained at 160 rev/min. The sample canister was held at 50 °C for 2 min, heated at a constant rate from 50 °C to 95 °C over 4 min and held for 2 min at 95 °C to complete gelatinisation. The paste was cooled to 50 °C over 4 min, unless otherwise state, and held for 2 min at 50 °C.*
- *The first derivative of the data was calculated as the normalised rate of change in RVA viscosity,* $\Delta RVA'$ *:*

$$\Delta RVA' = [(RVA_n - RVA_{n-1})/(t_n - t_{n-1})]/\Delta RVA_{Max},$$

where RVA_n *is the RVA viscosity value at measurement time* t_n*, and* ΔRVA_{Max} *is the maximum value of the positive rate of change in RVA viscosity over the measurement period.*

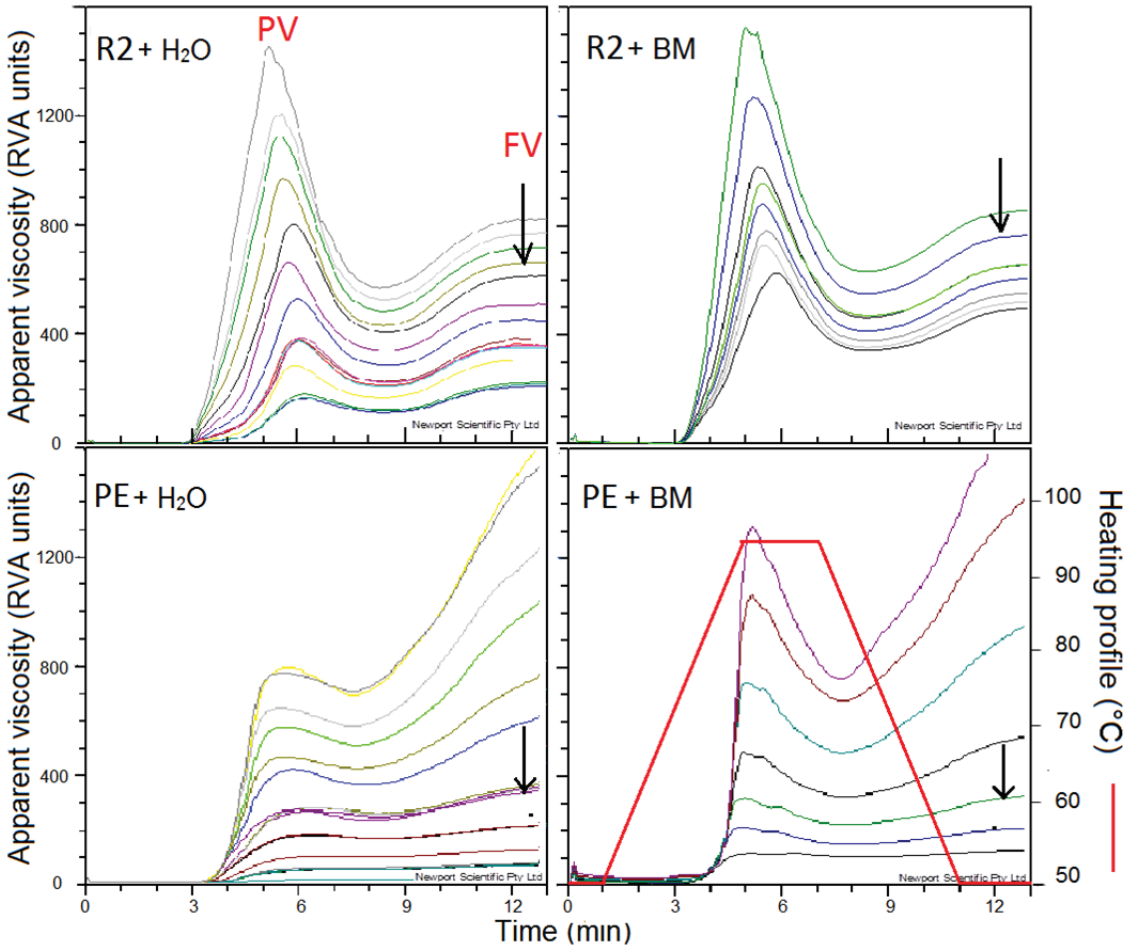

Figure 3.7 Viscosity profiles produced by RVA software on RVA pasting of rice2 (R2) and pea (PE) flours at increasing flour concentration, pasted with water (left) or with buttermilk (BM) at pH 5.3 (right). Arrows point to viscosity curves generated at 14% wwb flour. Red line: heating profile; PV, Peak Viscosity; FV, Final Viscosity.

3.9.3.3 Flour and batter fraction response on pasting

The typical stages of the RVA pasting curve are: 1) onset temperature (temperature at the start of rapid viscosification); 2) the first peak viscosity (PV in Fig. 3.7 top left), at which granule disintegration begins to overtake granule swelling, producing a loss of viscosity due to reduction in granule-granule interactions; 3) the trough following PV, which represents the viscosity at completion of granule breakdown; and 4) the final viscosity (FV in Fig. 3.7 top left) as the pasted flour thickens on cooling to 50 ˚C (Newport Scientific, 1998). With extended cooking, flour pasting viscosity is also influenced by protein denaturation and aggregation from solution on heating, which plays a greater role in protein-rich flours (e.g. pulse flours) than in low protein flours (e.g. cereal flours).

3.9.3.4 Influence of flour content on RVA pasting response

Clear differences in pasting behaviour in the RVA were observed between a pulse flour (pea; PE) and a cereal flour (rice2; R2) (Fig. 3.7). Many studies analyse pasting of non-wheat flours by following the standard RVA wheat flour pasting protocol at 14% wwb. While PV for R2 flour was well differentiated at 14% wwb (arrowed), PE flour had poorly differentiated RVA peaks (3.7) at the same flour content.

The differentiation between PV, the trough value and FV improved with increasing flour content in both flours. Differences between the pasting responses of the two batter fractions with increasing flour content are a combination of differences in flour starch content and protein content, and granule size and shape. R2 flour had greater starch content than PE flour (86%, vs. 52.2% wwb) and lower protein content (6.5%, vs. 22%). Based on measurements taken from light microscopy images of idli batters (see Appendix D.6) R2 flour contained individual small starch granules, granule composites of intermediate size, and intact grain surface cells > 100 µm packed with small granules. In comparison PE contained many small, disk-shaped starch granules with major diameter of 28 µm by laser diffraction particle sizing, and some larger composite granules.

The viscosity in solution is determined primarily by starch granule swelling. When granules are large, the particulate number density (and corresponding flour content) at which extensive particle-particle interactions begin is lower than for the same mass of smaller granules. However, once small granules begin to interact the rate of viscosity increase with increasing flour content will be more rapid than for flours with larger granules, as the number of between-particle interactions is correspondingly higher. Starch granule shape may also alter the relationship between flour content and dispersion viscosity, as disk shapes in solution have a different maximal packing fraction than spherical or ellipsoidal shapes (see sections 2.6.3 & 2.9.3.3). Finally, in high protein flours (e.g. PE flour) any viscosity increase that occurs on protein denaturation and aggregation within the same temperature range as gelatinisation may mask the depression in viscosity with granule breakdown.

3.9.3.5 Influence of liquid fraction on RVA pasting response

The RVA pasting curves for R2 and PE flour also changed when water was replaced with buttermilk at pH 5.3, the pH of the idli batter formulation before flour addition (Fig. 3.7 right), with a much sharper initial slope (increase in rapidity of swelling) and a different response to increasing flour content. Buttermilk contained both soluble milk proteins and those coagulated on fermentation, milk lipids, lactic acid and salts, all which influenced the water availability and the ionic conditions during granule gelatinisation and protein denaturation in batters. This observation is important, as while the correlation between pasting response and functionality in SP applications is well-characterised for wheat flour, the same is not true for other flour types. To compensate for the lack of validated indirect test systems for flour functionality of non-wheat flours, pasting must be under conditions as they occur in the SP formulation during production (*batter-equivalent* conditions).

3.10 Gel formation in pasted flours

The gel-forming capacity of pasted flour samples was evaluated by leaving pasted mixtures to set for 24 h at 20 °C. On visual inspection, pasting in the presence of buttermilk decreased the flour content at which the pasted mixture set (Fig. 3.8) and increased the opacity of the product colour. The RVA parameter Final Viscosity (FV, arrowed in Fig. 3.7) is an indirect measure of gel formation in the dispersion before cooling. Flour components that contribute to gel formation include protein fractions in pea and chickpea (Papalamprou, Doxastakis, Biliaderis, & Kiosseoglou, 2009), and rice (Baxter, Zhao, & Blanchard, 2010). As pulse flours were three- to four-fold higher in protein content, gel formation was more evident in pasted pulse flour gels. Flour proteins may also act synergistically with denatured buttermilk proteins to strengthen the elastomeric gel formed by flour components on pasting.

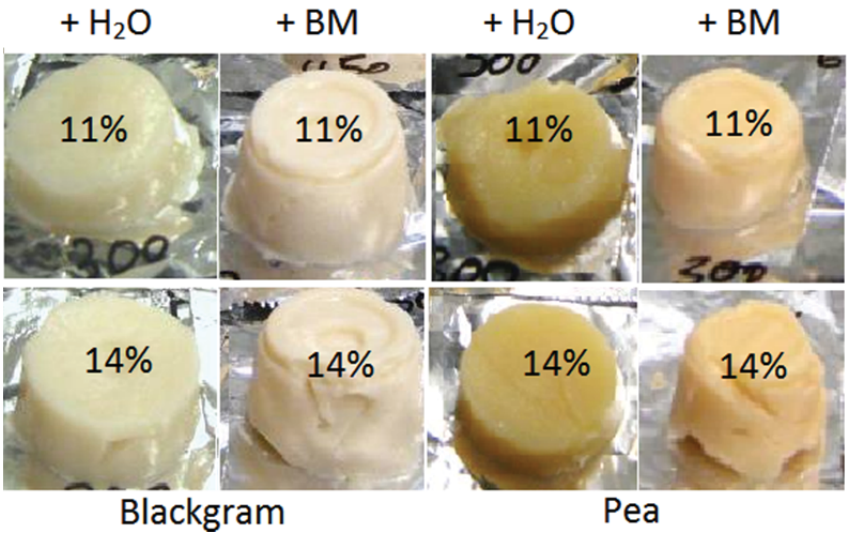

Figure 3.8 Examples of gel formation, at 24 hours after pasting, for flours pasted at 11% and 14% flour concentration with either water (H_2O) or 85% buttermilk adjusted to pH 5.3 (BM).

3.11 Testing limitations

Two methods applied in this study would benefit from improvement. To remove the need for the washout step in preparing batter fractions for foaming, which may alter the partitioning of surface-active components to the interface, centrifugation at high-speed (> 100, 000 *g*) to separate the liquid phase and soluble polymers would be preferable. The upper viscosity limit of the RVA pasting system constrained flour content to below that present in batter. Tests for rheological behaviour in standard geometries would allow flow modelling and determination of structure relaxation times.

The data would benefit from:

- Quantitative estimation by high-speed centrifugation of the gas, liquid and solid phase volumes in batters after hydration and after BiC addition
- Visualisation and sizing of flour particles by microscopy
- Laser diffraction particle sizing of hydrated batters in a standard volume, to estimate particulate number density after hydration under batter conditions.

3.12 Summary of SP test systems

Test systems were developed to quantify the batter and cooked product attributes (physical and chemical changes) associated with the top level functional design elements in sponge structure development of foam formation, foam expansion and structure setting.

- Due to the unevenness of sample heating on microwave cooking, foam expansion on heating and physical and chemical changes on structure setting were examined indirectly, rather than by sampling during cooking.
- Visual observation by light microscopy of the interaction between particulates, bubbles and the liquid phase in batters, and of the cooked product microstructure in the solid phase provided critical information about events during SP structure development.
- Batter fractions for testing batter attributes were prepared to reflect, as much as feasible, the composition, handling history and heating rates for whole batter during preparation and cooking.
- Foam properties of batters were measured indirectly in batters washout fractions standardised to the same volume.
- Changes in batter mesostructure were quantified by measuring size and number density distributions of bubbles in batter and of voids in cooked products.
- The temperature dependence of structure setting was compared by indirect measurement of rapid viscosification in batter fractions.

Table 3.1 lists the methods developed in this study to characterise the three top-level functional elements identified in Chap. 1 as contributing to SP structure development.

Chap. 2 covered methods to characterise batter flow behaviour; Appendix D, methods for mesostructure and microstructure quantification in batters and cooked products by image analysis; and Chap. 3, methods to follow component transformation in batter during structure setting. The next two chapters apply these test systems to examine the critical events in structure development on deconstruction of a non-wheat SP formulation under microwave cooking.

Table 3.1 Events on structure development of sponge products, with test attributes and chosen methods of characterisation in sponge product batters and cooked products. BiC = sodium bicarbonate.

Event	Attribute	Method	Section
Foam formation/foam expansion before cooking	Batter density -/+ BiC	Volume & weight measurement	3.4.2.1
	Liquid-particulate-gas phase interaction in batter -/+BiC	Observation of batter behaviour by light microscopy	Appendix D.6
	Bubble number and size in batter -/+BiC	Quantification of bubble distributions in light micrographs by digital image analysis	Appendix D.6
	Ingredient particulate size distribution	Laser diffraction particle sizing	3.3.2.1
	CO_2 desolubilisation in uncooked batter	Titration of batter fraction to neutral pH	3.4.3.2
	Flow behaviour in uncooked batter	Back extrusion rheology of –BiC batter Low-amplitude oscillatory shear of –BiC batter	3.8.1 3.8.2
	Batter foaming capacity	Preparation of washout fractions by centrifugation before whipping +BiC to measure foam	3.4.2.3, 3.5.2
	Batter foam stability on drainage	Monitoring foam and liquid volume over time	3.5.3
Foam expansion in early cooking	Bubble number and volume in batter +BiC	Quantification of bubble distributions by light microscopy after 5 min	Appendix D.6
	Effect of heating on foaming capacity and stability	Repeat of foam tests with washout fraction heat-treated to 55 ˚C	3.5.1-3
	Viscoelastic properties of batter before rapid viscosification	Low amplitude oscillatory shear of batter fractions with heating below rapid viscosification temperature	2.2.4 3.8.2
Structure setting (transition to open-cell, solid-air foam from liquid-particulate-gas, closed-cell foam)	Batter heating rate	Measure water activity of batters	3.4.3.3
		Measure batter temperature during cooking	3.6.2
	Void size distribution in cooked product	Digital image analysis of 2D slices on x-ray computed microtomography	Appendix D.7.2 & D.8
	Enthalpy change on associated changes in starch granule and protein organization	Differential scanning calorimetry of batter fractions	3.9.2
	Rapid viscosification on starch gelatinisation & protein denaturation	Rapid ViscoAnalyser™ pasting of flour under batter conditions	3.9.3.2
	Batter water loss	Weight before and after cooking	3.6.2
	Formulation compositions	Ingredient compositional analysis	3.3.1
	Domain organisation in solid phase of cooked product	Light microscopy of cryotome sections with domain-specific staining	Appendix D.6
	Physical properties of cooked sponge product	Volume by seed displacement, weight and water content	3.7.1.1
		Texture Profile Analysis 2-cycle compression test	3.7.2.1

Chapter 4. Deconstructing a non-wheat sponge product

4.1 Approach rationale

Wheat-flour formulations do not meet Food-Ink specifications for work- and time- independent flow behaviour, while baking produces a cooked SP with a browned crust. The replacement of wheat flour in SP formulations with other flours, and of baking with microwave cooking or steaming in order to set SP structure without surface browning, are potential strategies to deliver a successful 3D printed food image from a SP Food-Ink formulation. Chap. 1 identified a knowledge gap for structure development in non-baked, non-wheat SP formulations. It was also clear that understanding structure development in a SP Food-Ink, both on deposition and during heat-mediated foam expansion on cooking is essential to develop suitable SP Food-Inks for FLM applications. Therefore the decision was made to re-evaluate formulation design for non-wheat SP formulations using microwave cooking. The deconstruction of a non-wheat, non-baked SP system in Chap. 4 & 5 aims to identify the key functional elements (formulation structuring operations) and physical elements (ingredient components) which modulate mesostructure and microstructure development in non-wheat SPs under microwave cooking. Once the key functional elements and physical elements that modulate mesostructure and microstructure development are identified, these will provide information for an appropriate design strategy for SP Food-Inks.

4.1.1 Approaches to deconstruct the development of sponge product structure

The complexity of ingredient interactions in SP formulations excludes the existence of a generic SP model system. Study approaches fall into these categories:

- Whole-system observational studies to examine many events in the same formulation.
- Fractionation-reconstitution experiments to identify component function, which isolate ingredient components and add them back into the formulation.
- Substitution experiments which replace components with like or unlike substitutes to identify component function.
- In situ modification of composition and functionality of ingredient components.
- Indirect tests to correlate ingredient or formulation attributes with SP quality.

Observational studies may require specialist equipment for direct visualisation of events on cooking. For example, as part of a whole-system observational study on cake batter (Mizukoshi, 1983; Mizukoshi, Kawada, & Matsui, 1979; Mizukoshi et al., 1980) the group designed an equipment setup to measure viscosity changes and starch gelatinisation simultaneously during batter heating. A fractionation-reconstitution approach was used by MacRitchie's group (MacRitchie, 1985; Sroan & MacRitchie, 2009) to identify flour lipid functionality in stabilisation of the bubble interface in wheat-bread dough. A substitution experiment replaced wheat lipid fractions with purified lipids, to confirm that lipid polarity determined the stabilising (or destabilising) function of specific wheat-flour lipids at the interface. As an example of an in situ modification study, Primo-Martin et al. (2006) added exogenous lipase and xylanases to wheat-bread doughs to modify the structure of surface-active lipids and arabinoxylans

during proving, altering cooked bread volume.

The functionality of a given batch of wheat flour in SP formulations depends on the cultivar and on environmental, post-harvest storage and flour processing conditions. To enable useful prediction of flour functionality, correlations between wheat flour composition and the quality of baked cakes and breads have been well characterised in traditional SP manufacturing. The study of Moiraghi et al. (2013) is an example of an effective correlative study. Industry-wide, the American Association of Cereal Chemists publishes standard protocols for both indirect tests (e.g. flour composition, pasting) and direct tests (test baking) to quantify (and mitigate) between-batch wheat flour functionality in SP manufacturing.

4.1.2 Novel system-level designs to control sponge product structure

Very few published studies have produced new system-level design schemes for SP product architecture with the aim of identifying novel solutions for SP manufacture. The 'Expert Cake System' developed at the Campden and Chorleywood Food Research Institute is one example (Cauvain & Young, 2006c; Young et al., 1999). To model the relationship between ingredient functionality and ingredient ratios, Cauvain's group evaluated cooked product quality of > 1000 ingredient formulation variations for sponge cakes aerated by whisking, and for standard cakes more dependent on chemical leavening for aeration. The group developed algorithms to define the limits of ingredient ratios in order to achieve good product quality, and produced a balance calculation programme for cake formulation design. According to the designers, this software has the capacity to generate novel formulation solutions for cakes and sponges. It has not been updated since release, but existing copies are still in use industrially, primarily as a tool for training novice formulators (S.P. Cauvain, pers. comm.).

The thesis work of Hadiyanto on development of predictive tools to optimise production in a small multi-product bakery is another example. Hadiyanto synthesised existing bakery industry expertise with published data on bakery item properties (including SPs and biscuits) into a set of fundamental equations to describe transformation events on cooking. Although the primary target of the Hadiyanto study was not formulation design, the identification of key events in bakery item manufacture from a chemical engineering perspective produced a novel and informative deconstruction of ingredient influence on the development of texture and colour in bakery goods.

4.2 Filling the knowledge gap: deconstructing a non-wheat bread

An observation-substitution approach was chosen, using a bean-buttermilk-rice flour idli formulation which produces an elastomeric cake-like structure on microwave cooking. The variability reported in section 3.6.2 for idli replicates during microwave cooking excludes the use of direct observation during cooking and limits the study to observation of events before and after cooking and to indirect measurement of transformation events on cooking.

The targets for observation and quantification are those attributes of batter formulations and cooked products that contribute to mesostructure development (foam gas-phase organisation) and microstructure development during the batter-to-sponge transition (setting of multiphase batter to form a multi-domain composite solid). The suite of test methods developed to quantify key batter and

product attributes on foam formation, foam expansion and structure setting during idli production were summarised in Table 3.1.

4.2.1 Idli: a steamed non wheat bread with white colour

Idli are steamed breads from the Indian sub-continent, with a cohesive, soft and elastic cooked texture and a mesostructure similar in appearance to wheat-based sponge cake (Joseph, Crites, & Swanson, 1993; Reddy, Sathe, Pierson, & Salunkhe, 1982). Cooked idli are an opaque white colour when made with white rice and hulled blackgram beans, i.e. they do not carry a significant background colour. Food-Inks based on idli formulations may be suitable as uncoloured bases for colour-matching voxels. In this study, idli structure variants were generated by substituting rice flour with non-wheat flours from different plant sources.

4.2.2 Idli ingredient preparation and function

There are few studies on idli structure development, but the majority are of high quality and the main functional components have been identified. In traditional idli production soaked blackgram beans are wet-milled with parboiled or ground rice at an optimal ratio of 1:3 blackgram to rice (Reddy et al., 1982). Lactic acid-forming *Leuconostoc* bacteria in salted idli batters act as the main endogenous fermentation agents, over an extended fermentation period (Bkorkroff & Holzapfel, 2006). The fermented batter is steam-cooked in small moulds (Reddy et al., 1982). Commercial 'instant idli' mixes contain rice flour and blackgram flour, replacing fermentation with chemical leavening and acidulants. Fractionation studies (Changala Reddy, Susheelamma, & Tharanathan, 1990; Susheelamma & Rao, 1978, 1979) identified that synergistic interactions of blackgram components, between a protein globulin-rich fraction with foaming properties and a high-viscosity, heat-resistant blackgram arabinogalactan-rich fraction, were the main contributors to mesostructure development in idli formulations. Blackgram also contains, surface-active saponins (small structures of triterpenoid or steroid linked to carbohydrate) (Jood, Chauhan, & Kapoor, 2006). As the fractionation methods used in these studies did not exclude small molecules during preparation of globulin-rich foaming fractions, saponins may also contribute to the foaming activity of idli formulations.

4.2.3 Preliminary study

In a preliminary screening experiment chickpea (CP), pea (PE), sorghum (SG) and blackgram (BG) flours were identified as able to produce a suitably-expanded and set idli product when substituted for rice (RI) flour on a wet weight basis (i.e. no change in ingredient ratios). Idli batters and cooked products made using these flours were compared with those made from two types of rice flour (R1 & R2). As each flour produced a different cooked idli mesostructure, flour substitution in the idli formulation provided a useful tool to study factors contributing to structure development in cooked idli products.

4.2.4 Idli formulations used in this study

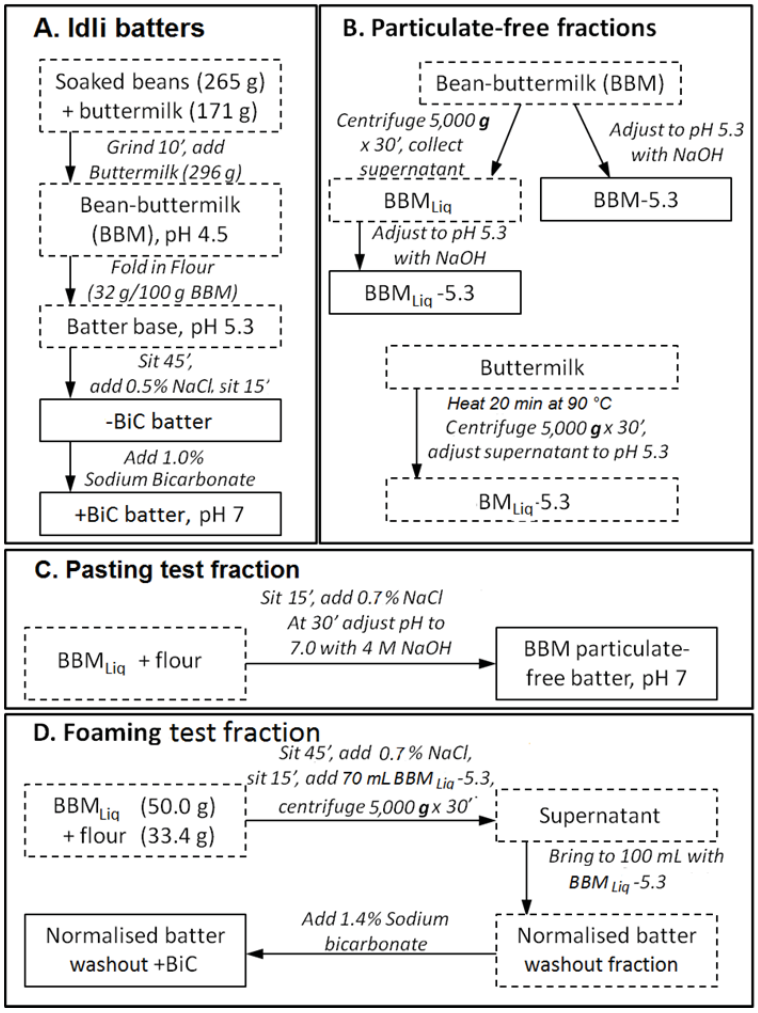

Figure 4.1 Schematic of preparation methods for idli batters and batter fractions. Solid boxes identify those used in testing, while dotted boxes identify intermediates during preparation.

The idli formulation used in this study was a hybrid adapted for rapid batter preparation and microwave cooking (Sahni, 1990). Ingredients were purchased from local retail outlets. BG, CP, PE, SG, and R1 and R2 flours were all from a single batch, with BG flour was made from dehulled beans. Soaked hulled BG beans were wet-milled in a food-processor with a commercial low-fat buttermilk (BM) (described as 'cultured' by the manufacturer) (see Fig. 4.1 A for the process outline, and section 3.4.1 for batter and batter fraction preparation details). The stiff bean-buttermilk foam which resulted (BBM) was stored for up to 4 h at 4 ˚C, before folding in individual flours and leaving the idli batter base to hydrate at 18 ˚C. Sodium chloride (NaCl) was folded in gently after 45 min hydration. Sodium bicarbonate (as domestic-grade baking soda, BiC) was added after 60 min. Batters were aliquotted immediately after adding BiC and cooked within 5 min. Microwave cooking conditions of the formulations were standardised as much as possible, with standard turntable positions and randomised sample placement on the turntable (method in section 3.6.3).

To study the influence of specific batter components indirectly, a range of batter fractions were

prepared for specific tests, including fractions in which BBM large particulates were removed (Fig. 4.1 B-D, see section 3.4 for preparation methods). The NaCl and BiC contents of batter fractions were adjusted to reflect the concentration in the liquid phase of whole batter.

4.2.5 Idli batter fractionation-reconstitution

When BBM was cooked by itself the mixture expanded slightly on heating, producing a flat elastic cake after cooking. Addition of NaCl and BiC to BBM produced rapid and extensive foam expansion and bubble coalescence during cooking, followed by bubble collapse, and also gave an unexpanded elastic cake after cooking. Adding NaCl and BiC increased the ionic content of BBM, increasing the uptake of microwave energy by batter (see section 1.3.2). Cooking RI flour and buttermilk together without NaCl or BiC produced a starch paste, while adding NaCl and BiC produced a fluffy, expanded mashed-potato structure which lacked cohesiveness. RI flour is therefore required to set the structure of the highly expandable BBM structuring foam in idli formulations, while components in BBM are required to stabilise the bubble population during foam expansion, and to form an elastomeric biopolymer gel on structure setting to cohere the gelatinised RI starch granules together. This behaviour is analogous to the relationship in wheat bread production between gluten proteins and wheat starch granules (Kusunose et al., 1999).

4.3 Overview of events in SP mesostructure formation

Chap. 1 summarised the development of SP mesostructure (section 1.5) and identified forces acting on individual bubbles and on whole bubble populations (Fig. 1.14). A more detailed description of bubble population dynamics relevant to the idli formulation in this study provides a necessary framework for interpretation of the experimental results.

4.3.1 Characterisation of sponge product bubble populations

Parameters related to foam development in foamed foods include the formulation foam-forming capacity, gas phase volume (ϕ_{Gas}), foam density (as mass/volume, or *specific gravity,* volume/mass), and the stability of the foam on standing (Campbell & Mougeot, 1999). The concern of most industrial bakery studies is the quality of the cooked SP product as rated by the consumer. The regularity of cooked product mesostructure, and the density and regularity of cell sizes discernible by eye are most relevant to consumer evaluation of SP character (Angiolini & Collar, 2009). Void size in SP studies is usually not quantified below 0.08-0.10 mm. This limits the analysis of bubble population dynamics, which requires population data across the whole length scale for correct interpretation of events during foam development (Shea et al., 2010). The choice of bin size on partitioning a continuous bubble distribution into discrete size classes greatly affects the information content of bubble population data. A linear bin size progression may be too expanded and an exponential bin size progression too compact to evaluate trends in bubble population distribution data. Increasing bin size by a multiplicative coefficient is a useful compromise (see Appendix D 5.1).

Data for SP bubble distributions are often reported as quantile values or as linear (or geometric) mean and variance, sometimes with skewedness and kurtosis values (moments of size distribution related to tailing and peak width-to-height proportion) (Leng & Calabrese, 2004). Normal and log normal

bubble size distributions can be described by a mean value and deviation, as they have a characteristic length scale. According to Blower et al. (2002) and Bellido, Scanlon, Page & Hallgrimsson (2006), non-steady state bubble growth with a power law distribution cannot be described statistically in the same way.

4.3.2 Bubble formation in sponge products

Wikipedia defines nucleation as "the first step in the formation of either a new thermodynamic phase or a new structure via self-assembly or self-organisation" (Wikipedia, 2015) (underlined emphasis added). The term nucleation as applied to bubble formation may be split into *homogeneous nucleation*, formation of new bubbles from a solution of super-saturated gas (which is energetically very costly in terms of surface energy), and *heterogeneous nucleation*, with de novo bubble formation on rough surfaces (including particulate surfaces), which greatly reduces the energetic cost of interface formation. In the case of SP production, pre-existing separate bubbles into which gas molecules transfer from the liquid phase during CO_2-driven foam expansion are often referred to as *nucleation sites*. This is an incorrect use of the term as defined here. In this study, in place of *nucleation site* the term *microbubble* is used for very small existing SP bubbles that take up gas during CO_2- or water vapour-driven SP formulation expansion.

The primarily formation of the initial bubble population in SP dough/batter takes place when air introduced under shear deformation is fragmented into smaller bubbles, e.g. by kneading dough or whisking batters. Air inclusion by whisking may be by single-stage mixing (all ingredients together), by multi-stage mixing (e.g. fat and sugar, or eggs and sugar, or eggs, sugar and flour beaten first before other ingredients are added by folding or beating) (Bennion & Bamford, 1997; Wilderjans, Luyts, Brijs, & Delcour, 2013), or by sparging gas into the formulation through rotating or static orifices (e.g. Haas-Mondo 'Mondo Mix' equipment used for cake batter preparation). The dependence of SP ϕ_{Gas} on gas breakup by shear deformation is highlighted by a decrease in SP cooked product volume when gas introduction and fragmentation takes under reduced air pressure (i.e. the concentration of gas available for incorporation is reduced) (Baker & Mize (1937), Dunn & White (1939), quoted in Campbell & Martin, 2012).

Each process of gas inclusion by shear deformation generates a different initial bubble size distribution (Weaire & Hutzler, 1999). Air introduction by sparging gas produces a monodisperse bubble distribution in SP formulations (Poortinga, Koman-boterblom, & Wijnen, 2005), while kneading bread dough develops a bubble population with log normal size distribution (Campbell, Rielly, Fryer, & Sadd, 1998; Mills, Salt, & Wilde, 2007; Scanlon & Zghal, 2001; Shimiya & Nakamura, 1997), which is typical of particle fragmentation (Leng & Calabrese, 2004). Air incorporation and breakup under whisking or beating is a complex process, generally producing bubble populations with a positively-skewed log normal distribution (Sahu & Niranjan, 2009). During batter whisking the smallest mean bubble size and narrowest size range occur at the point that ϕ_{Gas} reaches a maximum value (Massey et al., 2001). After this, the mean bubble diameter rises again, as bubble-bubble contact and coalescence become frequent. The ϕ_{Gas} decreases with increasing whisking time due to surface degassing and bubble collapse, until it reaches a steady-state value (Massey et al., 2001). The content of surface-active

molecules directly determines the steady state values for ϕ_{Gas} (Cauvain & Young, 2006e; Meza et al., 2011).

A portion of the initial bubble population forms when air trapped on and between particulates added to the dough/batter becomes surrounded by the liquid phase during ingredient hydration, forming discrete bubbles when the particulates separate. Air entrainment by flour particulates into SP formulations has been surmised from changes to dough/batter volume on flour addition, but has not been proven by first-principles experimentation (Shimiya & Yano, 1987; R. Carl Hoseney, pers. comm.). SP formulations such as angel food cake that depend solely on water vapourisation to drive expansion during cooking require flour to be sifted multiple times for successful structure development (Confroti, 2006). Air entrainment on particulates is particularly critical for these cake formulations.

Air may also be introduced as microbubbles trapped in cavities on particulate ingredients. Shimiya & Yano (1987) measured the air trapped on and in flour particles in water under extended vacuum extraction. Wheat-flour particulates 74-125 μm in diameter were associated with 10-15 μL of air/mg, most of which was trapped as microbubbles within cavities ~30 nm diam., as estimated by pycnometery. In particulate-containing plastic polymer foams expanded by a chemical reaction analogous to the BiC reaction in SPs, bubble numbers in the foamed product are two- to three-fold greater than the number of added particulates. To account for the difference Feng & Bertelo (2004) proposed that particulate cavities act as heterogeneous nucleation sites, producing multiple bubbles from the same cavity during gas desolubilisation. Cavities in and on starch granules (and flour particulates) that harbour air microbubbles may potentially act as *nucleating agents* in SP formulations if the CO_2 desolubilisation rate is high enough.

As an example of particulates used industrially to modulate SP structure, adding insoluble microcrystalline cellulose to pre-packaged microwave cake mixes produced a finer cake crumb. It was assumed the rough particulates were acting as nucleating agents (Jackson & Roufs, 1989), but the addition of the particulates may have also increased the number density of the initial bubble population by air entrainment during ingredient hydration.

4.3.3 Bubble population change on standing

Unless the bubble population is trapped within a solid phase (as in formulations with a creamed fat phase), the initial bubble population size distribution broadens with standing, and may generate bimodal or multimodal distributions. Bubble coalescence (merger of two bubbles to form a larger one), disproportionation (transfer of gas from a smaller bubble into an adjacent larger bubble) and bubble collapse can all modify the bubble population. The change in bubble size and number distributions over time can indicate which predominates (Shea et al., 2010) (see Fig. 1.12).

Bubble population dynamics in expanding bread dough during proving are well studied. The initial monomodal bubble size distribution in bread dough becomes increasingly bimodal with time as ϕ_{Gas} becomes high enough for bubble coalescence to become frequent (Shimiya & Nakamura, 1997). Gas movement from smaller to larger neighbouring bubbles driven by disproportionation was also reported in wheat dough (van Vliet et al., 1992). Transfer of CO_2 from smaller to larger bubbles is promoted by a reduction in the surface energy of the system, and also by the concentration gradient-driven diffusion of

solubilised CO_2 towards larger bubbles, which are more depleted of solublised CO_2 in the adjacent liquid phase (Shimiya & Nakamura, 1997; van Vliet et al., 1992).

Some incorporated air is lost by surface degassing on standing, at a rate dependent partly on bubble buoyancy. The buoyancy of an individual bubble increases with size and with decreasing viscosity and/or yield stress of the liquid phase, so that the degassing rate increases if the initial bubble population is prone to coalescence. Surface degassing may also occur when gas diffuses from the liquid phase in the presence of a marked pressure differential with the external atmosphere, e.g. as when doughs and batters mixed under high pressures are returned to 1 atm.

The initial bubble population is also sensitive to downward drainage of the liquid phase under gravity through channels between bubbles, which thins the material between bubbles in a gradient from the top down. Strategies to decreases drainage rate, e.g. increasing liquid phase viscosity, or adding small particulates which block the drainage channels, increase foam stability (Rouyer et al., 2014).

4.3.4 Attributes determining the size of a bubble at equilibrium

In uncooked dough/batter not experiencing CO_2-driven expansion (system tending towards dynamic equilibrium), the internal gas pressure in an individual bubble is dependent on the pressure on the bubble from the external medium, surface tension at the bubble interface and the bubble radius of curvature (i.e. bubble size), as well as the local hydrostatic pressure around an individual bubble (Stading, Franzoni, & Johansson, 2012). The internal gas pressure required for a bubble to maintain a specific radius r under dynamic equilibrium conditions is calculated from:

$$P_{\mathrm{Bubble}} = P_{\mathrm{Medium}} + P_{\mathrm{Hydrostatic}} + (2\Gamma_{\mathrm{Bubble}})/r,$$ (Stading et al., 2012).

P_{Medium} is the pressure on the bubble from the external medium and $P_{\mathrm{Hydrostatic}}$, the pressure from the material column above the bubble. The existence of larger bubbles is energetically preferred. The surface tension (Γ), a measure of the cohesiveness of the bubble interface, is determined by the population of surface-active molecules migrating to the interface during and after bubble formation. For a set value of P_{Bubble}, increasing P_{Medium} reduces the value of r, i.e. increasing the pressure of the external medium reduces bubble size at equilibrium.

Interface-stabilising proteins at high concentration at a bubble interface have equilibrium values ~45 mN/m for Γ, but still significantly reduce the value of Γ at lower concentrations. A transient and rapid reduction in surface tension during gas incorporation, resulting from the initial migration of proteins to the interface during shear deformation, is an important property of foam-forming protein solutions (Foegeding, Luck, & Davis, 2006). In a complex mixture the interface properties are sensitive to turnover of surface-active molecules at the interface, with less-diffusive, but more surface-active components (such as flour glycerides and free fatty acids formed in response to lipase) replacing this initial population over time (Walstra, 2003b).

Xu et al. (2012) reported that pea protein isolate solution (1.0 g/L in water at 23 ˚C) had Γ of 56 mN/m shortly after solubilisation (initial interface non-equilibrium conditions). The surface tension of deionised water at the same temperature is 72 mN/m (Vargaftik, Volkov, & Voljak, 1983), i.e. interface-stabilising molecules lower the value of Γ_{Bubble}. Assuming set values for all pressure terms in the Stading

equation, $P_{\text{Bubble}} \propto 1/r$, and $r \propto \Gamma$. At dynamic equilibrium, smaller bubbles require higher internal gas pressure to maintain a specific size. Lowering surface tension by adding suitable surface-active molecules results in smaller bubbles for the same value of bubble internal gas pressure. Conversely, an increase in the partitioning of surface-active molecules to the interface also reduces the internal gas pressure required to maintain a bubble at a specific size.

For a bubble with diameter 0.010 mm formed from PE protein isolate under the previously stated conditions, the term $2\Gamma/r$ is calculated as [2 x (5.6 x 10^{-2} N/m)]/ (5 x 10^{-6} m) = 2.24 x 10^{4} N, acting at a bubble surface area of 3.1 x 10^{-10} m^2. In comparison, a bubble with diameter 0.100 mm has 100-fold greater surface area and a ten-fold reduction in the value of $2\Gamma/r$. Larger bubbles resist shrinkage due to external pressure better than smaller ones when they have the same value for surface tension.

4.3.5 Induction of bubble expansion with bicarbonate addition to idli batter

Up to this point in dough/batter preparation the bubble population tends toward dynamic equilibrium with time. With fermentation or with reaction of chemical leavening some solublised CO_2 transfers into the gas phase, providing a non-equilibrium chemo-motive force for bubble expansion in uncooked dough/batter. The degree of CO_2-driven expansion depends on the amount of CO_2 released: the expansion volume of wheat-bread dough made with chemical leavening in place of fermentation was linearly related to leavening content (Bellido, Scanlon, & Page, 2009). An increase in ϕ_{Gas} increases the frequency of bubble-bubble and bubble-particulate interactions. In volcanic lava melts, bubble coalescence begins to be observed at ϕ_{Gas} > 35%, the point at which bubble-bubble contacts become frequent (Herd & Pinkerton (1997), quoted in Blower et al., 2002).

No new bubbles are thought to form during CO_2-driven expansion in bread dough on fermentation (Baker & Mize (1941), quoted in Bloksma, 1990a) and in cake formulations with chemical leavening activated before cooking (Carlin (1944), quoted in Wilderjans et al., 2013). Rather than undergo energetically-costly bubble formation by nucleation, CO_2 gas transfer appears to be into the existing SP bubble population.

The relationship between bubble population distributions in dough/batter and void size distributions in cooked products is often incompletely reported and, frustratingly, no study has tested this assumption robustly to date, despite excellent 3D data acquired for bread dough and cooked SP structures in recent years (e.g. Bellido et al., 2006; Wang, Karrech, Regenauer-Lieb, & Chakrabati-Bell, 2013). The incomplete reporting of bubble/void size data in doughs and cooked SP structures may hide formation of bubbles by nucleation during cooking. As an example, a sub-population of small voids of 10-80 μm diam. is evident between large voids in electron micrographs of wheat bread (Gonzales Barron & Buteler, 2008), and may potentially form by heterogeneous nucleation from cavities on flour particulates.

The elasticity of the surrounding fluid medium, and not fluid bulk rheology, is the main influence on bubble expansion rate in models of bubble growth in structured fluids (Joshi, 1998; Kloek et al., 2001). The influence of the external medium on bubble growth in a viscoelastic material was modelled by Yano & Shimiya (1987) for bread dough on proving, based on the equation:

$$\Delta P/E = \frac{1}{6}\left\{5 - \frac{4r_0}{r} - \left(\frac{r_0}{r}\right)^4\right\} + (2\Gamma)/E,$$

where ΔP is the pressure difference between bubble internal and external pressure, E is the instantaneous elastic modulus of the medium, r_0 is the radius of the bubble when E = 0, and Γ_{Bubble} is the equilibrium surface tension. The value of r_0, the critical radius below which bubbles are predicted to shrink and disappear, can be calculated as $3\Gamma/E$. For bread dough, r_0 was calculated as 12.7 µm (for bubbles of air, not CO_2), with E set at 1 x 10^4 N/m^2 and Γ at 42.3 mN/m (Yano & Shimiya, 1987). This model predicts that P_{Bubble} > 5/6 E before expansion can occur: this can be viewed as a type of yield stress requirement for bubble expansion in a viscoelastic medium.

Under conditions when bubble surface area changes greatly the expansion properties of the bubble interface become more influential than surface tension in determining bubble stability. The *dilatational modulus* is a measure of interfacial viscoelastic properties under oscillating expansion and contraction, and gives rise to a corresponding interfacial complex viscosity (Foegeding et al., 2006). On modelling bubble population stability, increasing the value of E/Γ decreases bubble shrinkage rate (Kloek et al., 2001), and also decreases the frequency of disproportionation (Langevin, 2014). Small particulates that partition to the interface can increase the interface elasticity considerably, increasing foam stability.

Mixed lipid-protein interfaces, as occur in bread dough bubble populations, have a lower dilatational modulus, are less elastic than films made with protein alone, and therefore are less capable of self-repair (Mills et al., 2007). Lipase addition to a cake formulation made with egg and high-ratio cake shortening decreased Γ_{Bubble} slightly, but decreased the interfacial complex viscosity by 40-60%, presumably due solely to an increase in simple lipid moieties at the interface. The net effect was to increase batter bulk viscosity by 3-10% for the same ϕ_{Gas} (primarily the result of a finer batter mesostructure), increase cake expansion by 7-11%, and decrease the void count/cm^2 and the frequency of large voids at the cut surface of the cooked product (Guy & Sahi, 2006).

Mesostructure development is sensitive to bubble number density and size distribution and to the rate of CO_2 production. Bubble expansion on bread dough proofing, a slow process closer to equilibrium than that in chemically-leavened idli batter, was modelled by Narsimhan (2012) while varying initial bubble number density and size distribution, dough viscoelastic properties and rate of CO_2 production on fermentation. After an initial lag phase in bubble growth, an exponential rise in ϕ_{Gas} eventually plateaus as CO_2 production is exhausted. Increasing CO_2 production rate decreases the lag time before discernible ϕ_{Gas} increase, but also decreases the rate of bubble growth after the lag phase (i.e. more rapid initial expansion results in a slowed rate of overall expansion). Narsimhan's model also predicts faster uptake of CO_2 by a population of smaller bubbles than of larger ones, and a more rapid increase in ϕ_{Gas} with increasing dough viscoelasticity.

CO_2 solubility in BiC-containing solutions decreases by 70% between 30-70 °C (Tang, Bian, Du, &

Wang, 2015). The rapid increase in temperature experienced on microwave cooking should produce an almost explosive expansion of SP foams, particularly in small items, as was observed in bread rolls cooked using microwave energy (Keskin et al., 2004). CO_2 desolubilisation is the main driver of bubble expansion early in in cooking, but at higher temperatures the increase in the partial pressure of heated water vapour migrating into the bubble becomes more important (Bloksma, 1980).

The events on thinning of the material surrounding bubbles in dough/batter during rapid bubble expansion have some similarity to events on wall thinning during drainage under gravity in a foam system at equilibrium. Particulates dispersed in the foam liquid phase tend to align so that the longest axis lies parallel to the bubble interface within thinning channels between bubbles, as observed in light micrographs of wheat bread sections (Bloksma (1990a), see Fig. 1.9 top left). Larger particulates are more likely to be swept into the intersections between multiple bubbles, which have more room for particulate packing than thinning channels under extensional shear deformation (see Fig. 1.7): this feature of foams can be used to fractionate particulates into different size categories (Cohen-Addad, Krzan, Höhler, & Herzhaft, 2007). Particulates of a size equal to the width of drainage channels in highly expanded foams can jam the channel, reducing drainage flow, and markedly increasing foam stability in foamed systems at equilibrium (Rouyer et al., 2014).

4.3.6 Bubble formation and expansion in the idli formulation

In the preparation method for idli batter used in this study, bubbles were first formed on inclusion and fragmentation of air on wet-milling of soaked blackgram beans with buttermilk (BM). The wet-milled bean-buttermilk fraction (BBM) had a gas volume fraction of 0.14 ± 0.03, liquid mass fraction of 0.48 ± 0.07 and liquid phase density of 1.05 (as determined by low-speed centrifugation of BBM). The pH of BM was 4.6 and rose to pH 5.2 in BBM.

Flour was folded into the wet-milled BBM fraction. The mix was left to hydrate for 60 min at 18 °C. During this time, flour surface-active components could migrate to the interface of existing bubbles. Addition of 1% NaCl (~100 mM) part way through hydration modified the ionic environment of the BBM-flour idli base, with the increased ionic concentration favouring biopolymer solubility. After hydration, batter density ranged between 0.94-1.09 kg/m^3 (~13% difference between batters) and batter pH fell between pH 5.3-5.6.

From this process description, the initial bubble population in the idli formulation is formed by wet-milling, with interface stabilisation provided by BG bean and BM surface-active components. The extended period of flour hydration allows flour biopolymers (proteins, NSPs) to solubilise into the liquid phase, flour surface-active components to migrate to the bubble interface, and any bubbles formed by air entrainment on particulates to develop. With BiC addition to idli batters, acidification by BM acids produces CO_2 gas to drive bubble expansion. Further CO_2 desolubilisation on heating, together with the increase in water vapour partial pressure, drives foam expansion on cooking.

4.4 Idli flour and batter characterisation

4.4.1 Ingredient composition

Based on calculations made from the ingredient compositional data blackgram (BG),

Table 4.1 Composition of flours and commercial buttermilk; and water binding capacity of flours on hydration in excess water at room temperature, (± SD). [a]Manufacturer's data. [b]Commercial analysis, coefficient of variance < 5%.

	Content (g/100 g dry weight)						Water binding capacity (%)
	Water	Starch	Carbohydrate	Protein	Dietary fibre[b]	Lipid[b]	
R1	11.50 ± 0.07	86.4 ± 0.6	-	7.30 ± 0.03	0.1	0.6	214 ± 2
R2	11.21 ± 0.07	83.7 ± 0.6	-	6.50 ± 0.03	0.5	0.5	207 ± 8
BG	9.84 ± 0.12	44.9 ± 0.5	-	22.36 ± 0.02	23.7	0.5	295 ± 2
CP	9.61 ± 0.16	44.7 ± 0.4	-	23.20 ± 0.01	8.0	4.8	148 ± 5
PE	10.61 ± 0.13	52.2 ± 0.4	-	20.05 ± 0.09	6.2	1.3	167 ± 4
SG	9.36 ± 0.07	66.8 ± 1.1		9.60 ± 0.06	6.4	1.4	258 ± 5
BM[a]	90.97	-	4.3	3.4	-	0.8	-

chickpea (CP), and pea (PE) pulse flours contributed significantly less starch and more protein to batters than sorghum (SG), rice1 (R1) and rice2 (R2) cereal flours (Table 4.1). RI flours contained around twice the starch content of pulse flours (84-86%, vs. 45-52%) and one-third the protein content (6.5-7.3%, vs. 20-23%), while sorghum (SG) flour had intermediate starch and protein levels.

The BBM fraction contribution to batter composition was calculated from BG flour data and the manufacturer's composition data for buttermilk (BM) (Table 4.1). BBM contributed ~50% of the protein content to pulse batters, and > 66% to cereal batters. The corresponding figures for BBM starch contribution to batters were ~30% and ~25%, respectively. As a fraction of the BBM components remained sequestered within BG bean fragments, not all the BBM contribution was available in the batter as solubilised protein or free BG starch granules.

CP flour contained more lipid (4.8%) than other flours (0.6-1.4%). This high CP lipid content may disrupt batter foaming capacity at the interface (Toews & Wang, 2013). Lipids can also reduce starch polymer leaching from the granule during starch gelatinisation by forming free fatty acid-amylose complexes (Raphaelides & Georgiadis, 2007).

BG flour had dietary fibre content of 23.7% dwb, more than twice that of SG, CP, and PE flours at 6.2-8.0%, consistent with the presence of significant NSP content in BG beans. BG NSPs are pectic polymers with arabinogalactan side chains (Tharanathan et al., 1994) which contribute significantly to the structuring function of BG bean as a food ingredient (Changala Reddy et al., 1990). The BG flour content of BG batter increased total batter BG content by 115% compared with other idli batters (dwb), but increased the functional contribution of BG components more than this, due to more effective hydration of soluble BG components from finely-ground BG flour than from coarsely-milled BG beans.

The idli batters are hydrated at room temperature after flour addition. On extended hydration in water (see section 3.9.1 for method), BG flour had the greatest water binding capacity, binding almost three times its own weight of water, and was followed closely by SG flour (Table 4.1). CP and PE flours had half and RI flours two-thirds of BG flour water binding capacity. Most of the water binding of BG flour can be attributed to non-starch biopolymers, as Singh, Kaur, Sadhu and Guraya (2004) reported isolated BG starch granules sequestered only 75-85% water by weight under similar conditions.

Table 4.2 and Figure 4.2 Peak size and quartile size values on laser diffraction particle sizing of unhydrated flours and soaked BG beans after wet-milling. Laser diffraction particle sizing of flours, reported as %volume. Data are the blended means at two detection ranges ($n = 3$ analyses at each range).

	Peak size (µm)	Quartile size values (µm)			
		Q_{25}	Q_{50}	Q_{75}	Q_{100}
BBM	2.2, 16, 175, 523	10.4	88.9	302	879
R1	2.3, 18, 108	33.0	70.9	112	207
R2	2.3, 20, 142	60.9	112.1	152	248
BG	2.6, 18, 105	11.3	24.3	70.9	207
CP	2.5, 16, 120	9.7	20.9	60.9	207
PE	2.6, 28, 106	15.4	28.4	52.2	177
SG	2.4, 26, 121, 694	20.9	44.8	112	817

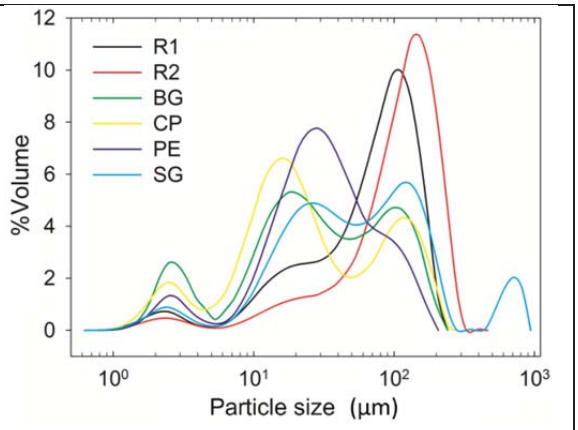

4.4.2 Size distribution of batter particulates

Particulates in unhydrated flours and BBM sized by laser diffraction particle sizing (LDS) had multimodal size distributions (Fig. 4.2, reported as volume fraction of particulates). The second modal peaks for PE, CP and BG flours (16, 28 and 18 µm, respectively, Table 4.2) fell within size ranges reported for individual starch granules in these pulses (Hoover & Sosulski, 1991; Huang et al., 2007). RI flours contained a greater volume of particulates in larger size classes than other flours. In rice flour individual RI starch granules are reported to range between 2-24 µm, with larger aggregate granules around 20 µm. Larger RI flour fragments (LDS peak 108 and 142 µm) corresponded to whole starch grain surface cells > 100 µm diam., which contain many granules within an intact cell wall (Araki et al., 2009; Puncha-arnon et al., 2008). R2 flour was milled more coarsely than R1 flour based on fragment size distribution. Liu et al. (2012) reported that two-thirds of SG starch granules fell between 1-30 µm in size, corresponding to the 26 µm LDS peak in SG flour. A small volume fraction of particulates > 400 µm in size in SG flour were identified as tannin-rich bran fragments (visible by eye as dark flecks in SG flour).

The size distribution of particulates from wet-milled BG beans was spread over four roughly equal-sized peaks with peak diam. of 2.2, 16, 175 and 523 µm (data not plotted). Mean particulate size in traditionally-prepared idli batter was reported as 500-600 µm (Nagaraju & Manohar, 2000).

4.4.3 Flow properties of uncooked idli batter

Fractions before BiC addition were evaluated for flow behaviour. A structured fluid initially resists flow until the extrusion force is large enough to overcome the yield stress. In backward extrusion testing, the fluid in a hollow cylinder is displaced by a central piston, flowing through the gap between piston and cylinder. Typical backward extrusion test curves for batters and the calculation of test parameters are discussed in section 3.8.1. Back extrusion parameters include maximal force at steady state, mean steady state force, and the area under the force-time curve (representing total change in momentum during a cycle of piston insertion or withdrawal).

Table 4.3 Rheological testing of –BiC idli batters and batter fractions. Back extrusion parameters for –BiC idli batters: maximal and mean force at steady state plateau, and change in momentum required to reach steady state plateau (n = 3 preparations, each with 5 replicate measurements). Storage and loss moduli on low amplitude oscillatory shear deformation of idli batter fractions minus particulates at 1 Hz and 5% strain, with 1 mm gap and roughened plates (n = 3 determinations). Means ± SD.

	Maximum force (N)	Mean steady-state force (N)	Area under curve (N s)	$G'_{20^\circ C}$	$G'_{40^\circ C}$	$G''_{20^\circ C}$	$G''_{40^\circ C}$
R1	3.25 ± 0.16	3.11 ± 0.17	50.09 ± 2.37	86	74	43	36
R2	3.94 ± 0.49	3.74 ± 0.44	58.34 ± 5.72	54	43	30	23
BG	20.73 ± 1.66	20.12 ± 1.52	304.89 ± 22.60	1515	1063	558	409
CP	4.04 ± 0.51	3.48 ± 0.32	54.67 ± 4.28	83	67	46	37
PE	4.48 ± 0.65	3.75 ± 0.33	58.56 ± 5.68	103	80	53	39
SG	11.65 ± 065	11.26 ± 0.63	175.52 ± 9.64	805	705	327	290

R1, R2, CP and PE –BiC batters behaved as soft and readily spoonable foams, while SG and BG batters behaved as stiff pastes, consistent with the values recorded for back extrusion parameters (Table 4.3). R1, R2, CP and PE batters produced similar values for maximal force and mean force at the steady state plateau. The corresponding values were three-fold higher for SG batter, and five-fold higher for BG batter. The momentum change required to reach steady state was five- to six-fold greater in BG batter and more than three-fold greater in SG batter than in other batters.

These back extrusion results correlated with the results on low amplitude oscillatory shear deformation testing of batter fractions from which BBM particulates were removed (see Fig. 4.1 C for batter fraction preparation and section 3.8.2 for test conditions). There was a direct linear relationship between batter storage modulus at 20 ˚C (elastic behaviour; $G'_{20^\circ C}$) and all back extrusion parameters, while the corresponding relationships for loss modulus (viscous behaviour; $G''_{20^\circ C}$ were close to linear (data not shown). At 20 ˚C, back extrusion parameters for whole –BiC batters were directly correlated with the elastic behaviour of the corresponding BBM particulate-free batter fractions.

4.4.4 Batter expansion, heating rate, weight loss and product volume

Heating rates at the batter surface and centre during cooking were relatively constant over the cooking period for batters and ranged between 0.5-0.6 °C/s (30-36 °C/min). Between 9-10% of batter mass was lost on cooking as water vapour (Table 4.4). There was no significant difference between idli types for weight loss, consistent with the primary role of the non-flour fraction in determining microwave heating rate (see section 3.6.2). As batter water activity was not significantly different between formulations (data not shown), flour composition did not greatly influence water partitioning in uncooked batters, even though they varied markedly in viscoelastic properties. This suggests that water is not tightly bound to extensive biopolymer networks contributing to BG and SG batter stiffness.

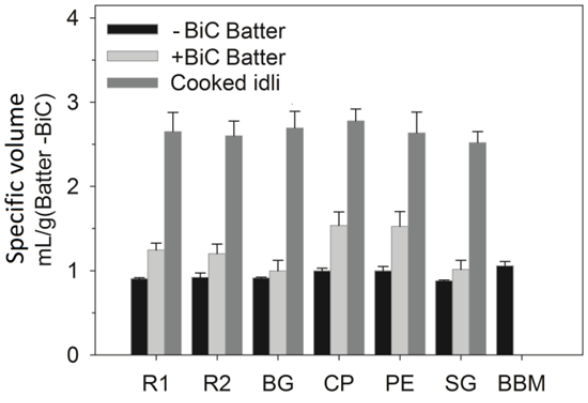

	Weight loss (%)	Cooked volume (mL)
R1	9.60 ± 0.60	119.2 ± 10.1
R2	10.27 ± 0.69	114.8 ± 6.2
BG	9.79 ± 0.97	119.2 ± 5.4
CP	9.73 ± 0.77	123.9 ± 5.2
PE	10.20 ± 0.94	119.6 ± 10.0
SG	9.47 ± 0.91	113.0 ± 5.5

Figure 4.3 & Table 4.4 Left: idli batter expansion before sodium bicarbonate addition (-BiC batter), 5 min after addition (+BiC batter), and in cooked idli, normalised to the initial mass of –BiC batter (n = 12 ± SD) and compared with the specific volume of BBM before flour addition (n = 6 ± SD). Right: weight loss from batter on cooking, and cooked idli volume (n = 12 ± SD).

To compare the effect of flour hydration on BiC expansion of uncooked batters and product expansion after cooking, the specific volume at each batter preparation step was standardised to the weight of batter before BiC addition (Fig. 4.3). –BiC batters generally had a specific volume similar to BBM, apart from values for SG and BG batters which were lower by ~13%. +BiC batters represent the batter just before cooking. When compared with the specific volume of BBM there was little change in batter specific volume with flour addition and hydration. With BiC addition, CP and PE batters expanded the most, SG and BG batters expanded the least and RI batters had intermediate levels of expansion. The reduced rate of expansion of SG and BG batters on BiC addition was associated with the significantly greater viscoelasticity of these batters, which resulted in higher values for P_{Medium} and for batter elastic modulus, G'. Increasing the elastic modulus of batter would be predicted to reduce minimum bubble size under equilibrium conditions, such as in –BiC batters (see section 4.5.3).

4.4.5 Flour buffering capacity

The pH of -BiC batters ranged between pH 5.28-5.40 and rose soon after BiC addition to around pH 7.0. On neutralisation the equilibrium of solubilised CO_2 is pushed towards the carbonic acid form, which has a lower energetic requirement for CO_2 transfer into the gas phase (Pool Water Treatment Advisory Group). To compare the influence of flour type on batter titratability, batter fractions free of BBM particulates were titrated with NaOH to pH 7.0 (see section 3.4.2.2 for method). The linear regression slope of the combined data for PE flour titration under batter-equivalent conditions gave 6.8 pH units/mmol [OH^-]/g flour (R^2 = 0.82), compared with values of 5.5 for CP (R^2 = 0.83); 5.2 for SG (R^2 = 0.90); 5.0 for BG (R^2 = 0.97); 4.5 for R1 (R^2 = 0.90); and 4.6 for R2 (R^2 = 0.90) flours. A greater value for ΔpH on titration indicates a reduced buffering capacity of the flour for OH^- ions under batter conditions. Therefore, CO_2 transfer from the liquid to gas phase should be most rapid in PE batter and slowest in RI and BG batters in +BiC batters soon after BiC addition.

4.4.6 Change in batter viscoelastic properties with heating

Heating batter fractions from 20 ˚C to 40 ˚C at 10 ˚C/min decreased both G' and G'' (Table 4.3), with values for BG batter dropping by a third. This pattern of decreasing viscosity during early batter heating is commonly reported in bread dough (Bloksma, 1980) and in cake batter (Brooker, 1996; Gaines & Donelson, 1982). The decrease in complex viscosity decreases the elastic value of P_{Medium}, the pressure of the external medium on the bubble, and the value of $5/6E$, the elastic yield stress value of the medium to be overcome before a bubble can expand. Consequently, this increase in batter fluidity in early cooking enhances the rate of bubble expansion, particularly in highly viscoelastic batters.

4.4.7 Batter foaming capacity and foam stability

In-depth studies on the relationship between the properties of the bubble interface in batters and doughs and SP cooked product structure (e.g. Handleman et al., 1961; Primo-Martin et al., 2006) have generated no clear correlation between interfacial properties and SP structure formation. To provide a comparison of flour component functionality at the idli bubble interface, simple functional tests of foaming capacity and foam holdup may be more helpful for between-batter comparisons than more detailed analysis of the bubble interface composition.

4.4.7.1 Foaming of batter washout fractions

To compensate for the wide variation in idli batter viscosity, flours were hydrated under batter conditions and soluble components extracted under centrifugation (see fig. 4.1 D; preparation details in section 3.4.2.3). Liquid phase components from the same amount of flour were present in a standard background of non-flour liquid phase components in the washout fractions. A BBM foaming fraction, representing non-flour components in the liquid phase, was prepared by adding NaCl to particulate-free BBM fraction at pH 5.3 (BBM_{Liq}-5.3). Half of each prepared fraction was heat-treated to 55 °C and cooled before whipping (method in section 3.5.1). All fractions had the consistency of thin pouring cream (i.e. foaming properties were due primarily to surface-active components, not to solution viscosity).

Foaming capacity and foam stability were evaluated by whipping washout fractions after BiC addition and monitoring the ratio of drained liquid to foam on standing (sections 3.5.2 & 3.5.3). When unheated washout fractions were whipped in the presence of BiC, most had foaming capacity and foam stability comparable to those of BBM-5.3 foaming fraction (Figs. 4.4 & 4.5). BG washout fraction (with two-fold more soluble BG content on a weight basis than other batters) had both increased foaming capacity and resistance to drainage, while PE washout fraction had a similar increased resistance to drainage.

PE flour particulates and PE isolated starch granules have been reported to increase the stability of foamed solutions by blocking liquid drainage through channels between bubbles (Fruhner, Wantke, & Lunkenheimer, 2000). As batter washout fractions were prepared by low-speed centrifugation, fine particulates were not excluded from the washout fractions and may have contributed to foam stabilisation, although the content of fines was small. Fines were most evident in PE, SG and CP supernatants. The presence of a thin layer of orange droplets in the fines of CP washout fraction was consistent with the high lipid content of CP flour (see Table 4.1). A small reduction in foam stability of

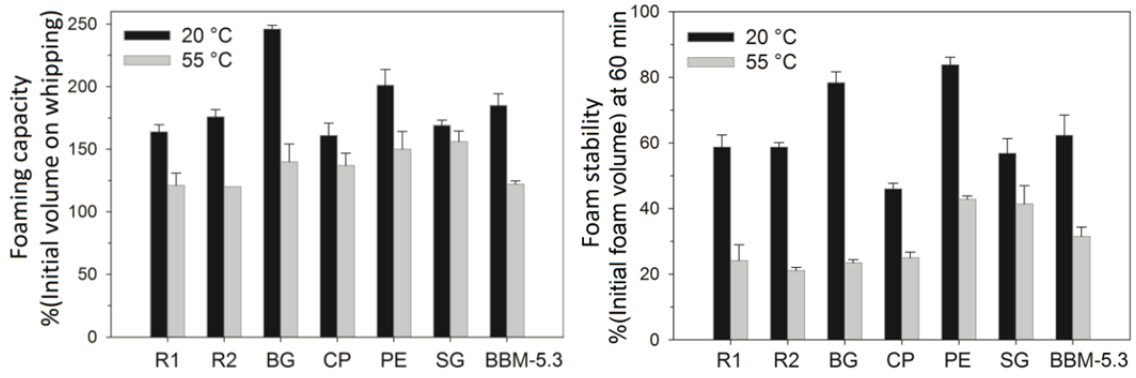

Figure 4.4 **Foaming properties of idli batter washout fractions held at 20 ˚C, or heated to 55 ˚C and cooled, on whipping in the presence of BiC. Left: foaming capacity. Right: foam stability on standing at 20 ˚C, (n = 2, prepared on separate days).**

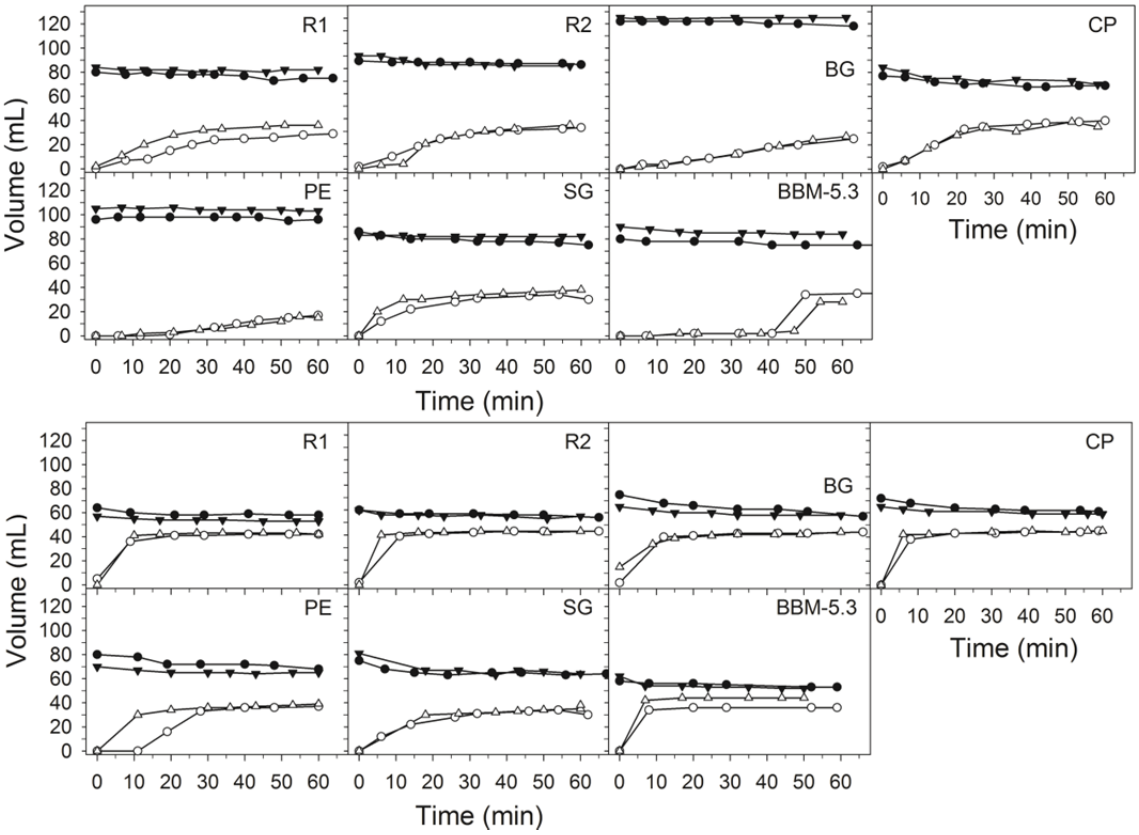

Figure 4.5 **Stability of foams produced from idli batter washout fractions over time. Top: unheated fractions at 20 ˚C; bottom: heated to 55 ˚C and cooled before whipping. Closed symbols, volume of (foam + liquid); open symbols, liquid volume only. Data are for 50 mL of washout fraction, prepared on separate days.**

the CP washout fraction may be related to CP lipid, which was reported to destabilise the foaming properties of isolated chickpea proteins (Toews & Wang, 2013).

Heat treatment reduced foaming capacity in BG and RI washout fractions to similar or lower values than the BBM-5.3 foaming fraction, which reduced in foaming capacity by a third and in foam stability by half after heat treatment (Fig. 4.4 left). The loss in foam stability over time for most heat-treated

washout fractions followed the pattern of BBM-5.3 washout fraction, with a rapid initial increase in drained liquid to a plateau value (Fig. 4.5). Note that the apparent stability of unheated BBM-5.3 foam until 40-50 min is an artefact of the high opacity of BBM foam, which masks events in the foam until drainage is advanced.

Based on the rapid rate of liquid drainage, much of the BG bean foam-stabilising capacity was lost after heating to 55˚C. SG and PE washout fractions differed in heat stability to other fractions, with a reduced rate of drainage on standing. Several mechanisms can be suggested to explain these observations: the SG fraction generated a new foam-stabilising component on heat treatment (as described by Hamaker & Bugusu (2003) for heat-dependent solubilisation of kafirin proteins from SG protein bodies), and/or it protected BBM foam-stabilising components during heating; while the PE washout fraction retained a PE-specific foam stabilising component after heating, and/or heat treatment generated a new PE stabilising component.

4.4.7.2 Surface-active components in idli batters

Most BG soluble proteins are globulins with an isoelectric point between pH 6.15-6.65; albumins, prolamins and glutelins are minor protein fractions (Padhye & Salunke, 1979). BG NSPs are comprised predominantly of pectic polysaccharides with arabinogalactan side chains (Tharanathan et al., 1994) and produce highly viscous solutions. The high content of BG NSP may also concentrate the soluble protein fraction in the liquid phase, by a pH-dependent process of biopolymer exclusion which generates separate NSP-rich and protein-rich domains within the liquid phase. The driving force for the process is the limited co-solubility of the biopolymers (Tolstoguzov, 2003). This exclusion effect may also positively influence protein partitioning to the bubble interface.

While a liquid phase pH close to the isoelectric point encourages partitioning of surface-active proteins to the interface (Foegeding et al., 2006), this is not the case if proteins are not yet solubilised. The main foam-forming proteins in PE flour are the globulins vicilin and legumin. Most surface-active CP and PE proteins are poorly soluble between pH 4.0-5.5 (Liang & Tang, 2013; Sánchez-Vioque et al., 1999) and the solubility of RI protein isolate is reduced by about half between pH 4 and pH 6 (Romero et al., 2012). However, these solubility values are for water, and may improve under batter ionic conditions (~100 mM NaCl + BM ionic moieties). Most protein in SG flour remains unsolubilised in protein bodies until heated (Hamaker & Bugusu, 2003). The pH on flour hydration is ~pH 5.3. Until the increase in idli batter pH to 7 on BiC addition, BG globulins will be more soluble in batters than PE or CP surface-active proteins, encouraging the retention of the BG protein-rich interface generated during wet-milling.

A protective role was recently described for pectin in stabilising the β-sheet structure of surface-active pea proteins during heating (Gharsallaoui et al., 2012). Large particulates produced after charge neutralisation and co-aggregation between PE polysaccharides and PE proteins altered the fluid viscosity and also stabilised the expansion of the bubble interface to a greater radius (Sagis & Scholten, 2014). Like pectin, BG NSPs also carry negatively-charged galacturonic acid groups (Tharanathan et al., 1994), so a similar mechanism may also stabilise BG foams on heating.

The major influence of the BBM fraction on the foaming properties of idli batters suggests that the concentration of BG surface-active components may be high enough to out-compete those from non-BG

flours. Alternatively, surface-active proteins from non-BG flours may perform interchangeably with BG proteins, resulting in little overall change in batter foaming properties, apart from those noted for the CP, PE and SG washout fractions. Therefore, a hypothesis can be proposed for the variant idli formulations prepared in this study: that batter globulin proteins (primarily BG globulins) are the predominant surface-active components contributing to foam formation and stabilisation during batter preparation. Based on the differences in batter foaming properties reported in the previous section, the contribution of SG and PE flour surface-active components in particular may improve the stability of the bubble interface in these batters during cooking.

Blackgram NSPs (> 20% by weight in BG flour) act together with a foam-forming protein fraction to stabilise BG-based idli batter foams on heating (Susheelamma & Rao, 1974). In a study comparing the functionality of blood plasma proteins in fat-free cake formulations to replace egg-white, plasma globulin fractions were the most effective in supporting batter expansion and structure setting (Raeker & Johnson, 1995). Therefore, idli batter globulins are also likely to dominate in the formation of an elastomeric gel during idli structure setting.

4.5 Structures in uncooked idli batter

4.5.1 Observation of batter behaviour by light microscopy

Observing interactions at the different stages of SP formulation preparation - between bubbles, particulates (cell fragments, freed starch granules and granule aggregates) and the liquid phase (containing solubilised proteins and NSPs) - is essential to understand idli structure development. The behaviour of the uncooked formulation at the macroscopic level (e.g. porosity, bulk flow behaviour) is otherwise open to misinterpretation due to the dynamic nature of bubble populations and to interactions between batter components at small scale. Bubble populations of idli samples in this study could be observed by light microscopy in relatively thick sections, as idli batters were less opaque than wheat-flour batters. Generally, disproportionation was observed when small bubbles came close to or docked onto a much larger bubble, while coalescence was more common between two larger bubbles.

Time series video clips were prepared from micrographs of +BiC batters to simplify the interpretation of particle interactions in batter. The .avi video files attached to the cover of this thesis give timecourse records of component interactions in typical +BiC batters within 90-150 s after BiC addition. (Note: the .avi files should be viewable in Windows media player as a continuous loop, or other default viewing software. If not, check that the .avi format is in the list of accepted formats.)

Bubble populations were observed by light microscopy in idli batters and BBM (see section 3.4.1 and Appendix D.6 for preparation and analysis methods). BBM-5.3 (pH adjusted to the mean pH of idli batters after flour hydration) represented the contribution of the non-flour fraction to batter bubble populations after wet-milling and standing. The whole-batter samples were –BiC batters, representing the effect of flour addition and hydration, and +BiC batters at 5 min after BiC addition, representing bubble population dynamics on foam expansion during CO_2 influx into bubbles after BiC acidification. +BiC samples also represent events at the start of microwave cooking and during early cooking (as microscopy samples were warmed by the microscope light).

BBM-5.3 (Fig. 4.6) had ready bubble movement and expansion within a low viscosity liquid phase, as observed in timecourse videos on streaming flow. The largest particulates in BBM (also evident in batters, labelled P in micrographs) were large BG bean fragments produced on wet-milling BBM. Coagulated BM protein was observed in the liquid phase of BBM and batters as soft deformable threads in mats that did not greatly impede bubble or particulate movement.

CP and PE batters were most like BBM-5.3 in behaviour. Individual CP granules could not be easily discerned, while many small granules packed PE batter (CP & PE +BiC. avi). Bubble movement and bubble expansion were not greatly affected by CP or PE flour particulates, and each liquid phase flowed readily.

Flour particulates of medium size (> 100 µm, but smaller than large BG bean fragments) were detected by LDS in all flour distributions (see Fig. 4.2) and were particularly evident in RI and SG cereal batters (arrowed in the corresponding micrographs in Fig. 4.6). In time lapse images (see .avi files) bubbles in these batters moved within a reduced volume of liquid phase compared with bubbles in CP and PE batter, and were surrounded by many medium-sized particulates that restricted bubble expansion and reduced the frequency of bubble-bubble contact (e.g. R2 +BiC. avi). Medium-sized flour particulates in RI batters were egg-shaped, with length 130 ± 3 µm and width 80 ± 2 µm on direct measurement from micrographs. They corresponded to a LDS peak in unhydrated flours of 142 µm (R2 flour) and 108 µm (R1 flour) (Table 4.2). Based on the description of Araki et al. (2009) these are intact rice grain surface cells packed with small individual starch granules. The liquid phase in RI batters, while reduced in volume, still flowed readily.

Medium-sized flour particulates were common in SG batter (Fig. 4.6 SG, arrowed) and had a pyramidal or angled shape, with mean length of 250 µm and mean width of 140 µm in micrographs (corresponding to an LSD peak of 125 µm in unhydrated SG flour). These were irregular aggregates of roughly cubic granules in which one or more granules had broken off. Compared with the behaviour of RI batters, bubbles in SG batter were not only separated by irregular flour particulates, but also moved within a more viscous liquid phase (SG +BiC.avi).

In BG batters (Fig. 4.6, BG +BiC.avi) many small bubbles and a few large bubbles were trapped in a gel-like liquid phase that moved as a continuous sheet. This can be interpreted as the flow of a yield stress fluid in which the yield stress is not reached under streaming flow conditions on the slide, while sheet movement is lubricated by a thin slip layer at the glass-batter interface. BG bubbles maintained position relative to each other within the sheet, inhibiting between-bubble contact. Based on flow behaviour of BBM particulate-free batter fractions on low amplitude shear deformation (see section 4.4.3), the liquid phase in both SG and BG batters was significantly viscoelastic.

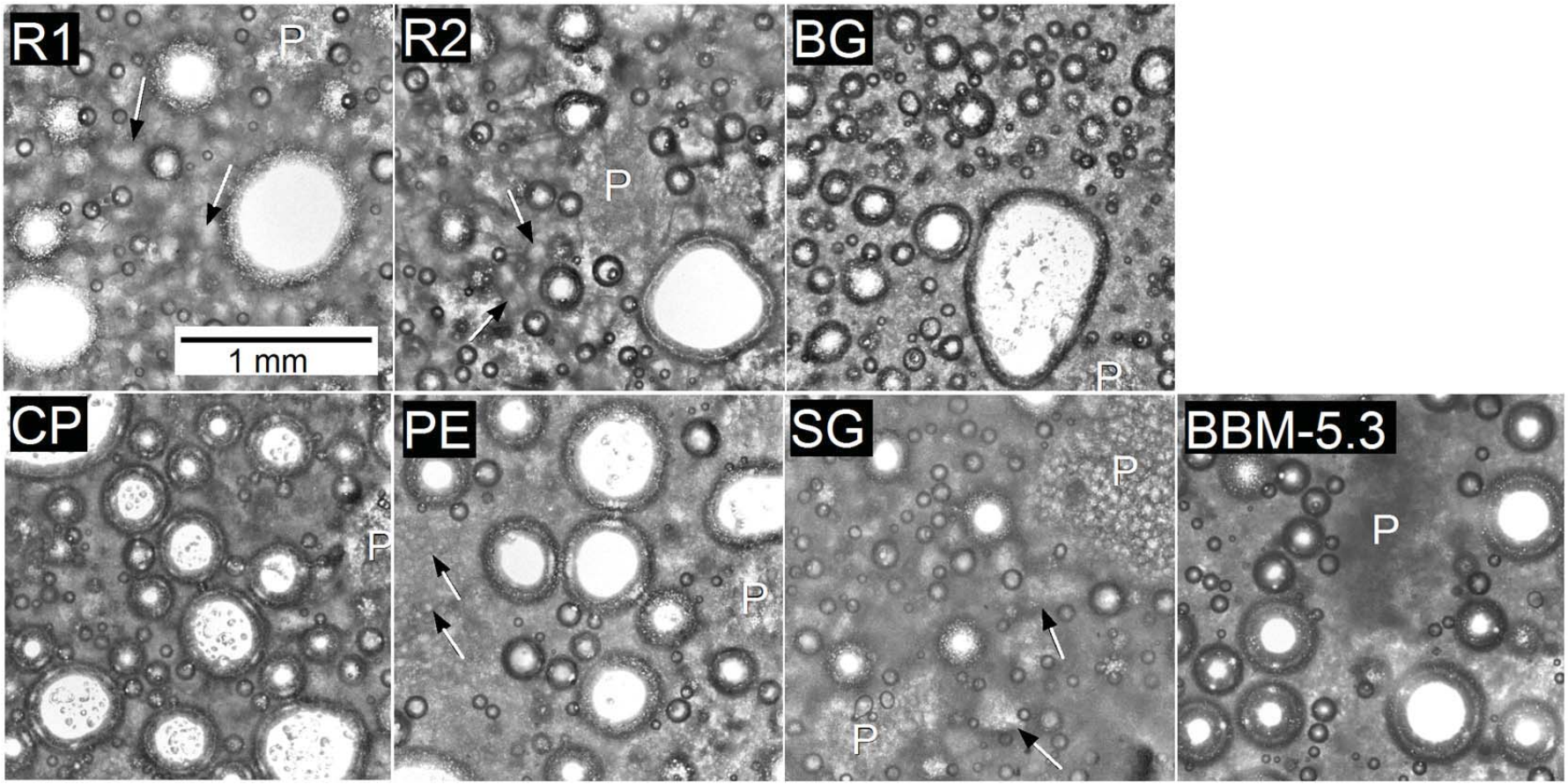

Figure 4.6 **Light microscopy of idli batters and bean-buttermilk fraction at pH 5.3 (BBM-5.3), all at five min after bicarbonate addition. Arrows point to starch granule aggregates where evident; large blackgram particulates are labelled P. Bubbles with white centres have diameter greater than the gap between slide and coverslip. Click here for high-resolution image.**

4.5.2 Bubble size and number distributions

Manual counting to quantify bubble number density and size distributions gave between 200-1500 bubbles per measured replicate. Note that the precision of the reported data in describing the whole bubble population diminishes with decreasing bubble size, as smaller bubbles migrate into the batter out of view or behind large particulates. However, the lack of absolute bubble distribution data does not invalidate between-batter comparisons based on the measured data, as the magnitude of under-reporting will be the same in all samples. Measured diameters of large bubbles flattened between slide and coverslip over-estimated the true bubble diameter and were corrected as described in Appendix D.6.2. The volume of non-spherical bubbles was estimated from the average of the volume calculated for the sphere with diameter equivalent to the long axis of the bubble, and that calculated for the short axis.

By convention particle distributions are binned into linear or geometric size classes. However, information about bubble population trends may be lost for small size classes in linear plots, and for large size classes in geometric plots (see Appendix D.5.1). To retain information on population trends, the continuous bubble distribution data was binned into 24 size classes which increased by a multiplicative coefficient, producing a regular increase in size class across the logarithmic scale on the plots.

4.5.3 –BiC bubble populations

Idli batter bubble populations were produced by a combination of bubble fragmentation and air entrainment on flour particulates. The initial bubble population in BBM produced by wet-milling was corrected to reflect BBM contribution to batters. The model bubble populations described by Shea et al. (2010), in which bubbles form by nucleation from a supersaturated gas solution, produce bubble number density distributions decreasing logarithmically, or by a power law relationship with increasing bubble size. In BBM-5.3 the bubble population had a broad bimodal size range size distribution (Fig. 4.7), as expected for an initial lognormal distribution produced by fragmentation which had broadened on standing.

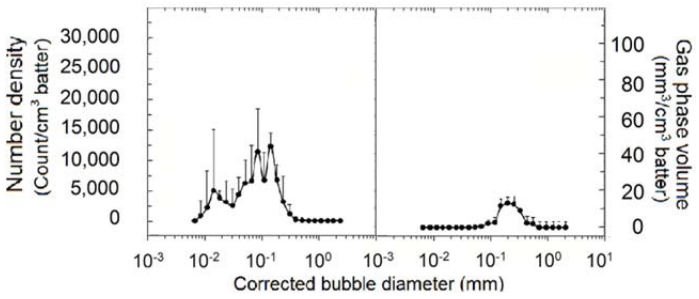

Figure 4.7 Bubble number density and gas phase volume distribution of bean-buttermilk fraction (BBM-5.3), corrected to represent the contribution in whole batter (n = 3 + SD).

Table 4.5 Idli batter bubble distributions, as Total number density, Total gas phase volume and Total surface area before and after BiC addition, all normalised to 1.0 g whole batter, n = 4 ± SD.

	Total number density (Count x 10^{-3}/g batter)		Total gas phase volume (mm^3/g batter)		Total surface area (cm^2/g batter)	
	-BiC	+BiC	-BiC	+BiC	-BiC	+BiC
BBM-5.3	36.3 ± 25.7	-	23.9 ± 12.0	-	-	-
R1	18.6 ± 0.6	66.1 ± 16.8	22.0 ± 6.1	151.5 ± 56.8	0.60 ± 0.07	3.23 ± 0.69
R2	12.5 ± 4.3	94.9 ± 15.3	10.8 ± 2.9	160.5 ± 19.5	0.39 ± 0.09	3.96 ± 0.65
BG	83.0 ± 10.5	118.1 ± 9.3	9.2 ± 3.0	102.8 ± 40.4	0.56 ± 0.10	3.13 ± 1.21
CP	106.6 ± 14.9	162.0 ± 37.3	26.9 ± 9.6	426.3 ± 102.5	3.13 ± 1.21	9.05 ± 1.43
PE	142.9 ± 23.3	92.5 ± 16.1	45.2 ± 6.8	373.5 ± 26.9	1.70 ± 0.26	7.73 ± 4.97
SG	16.7 ± 3.2	78.6 ± 11.3	7.6 ± 2.7	128.9 ± 5.8	0.28 ± 0.08	6.12 ± 0.60

Batter bubble populations were plotted as cumulative bubble number density and cumulative gas phase volume on a logarithmic scale (Fig. 4.8 left-hand Y-axes, over page). These cumulative plots describe general trends in bubble distributions before and after BiC addition. The corresponding values for individual size classes were plotted on a linear scale (right-hand Y-axes) to emphasise distribution features. Bubble number density distributions in individual size classes identified bubble population features better than the corresponding gas phase volume distributions.

The plateau values in cumulative plots represent the total bubble gas phase volume as mm^3/cm^3 batter or the total bubble count as Count/cm^3 batter. To correct for varying degrees of foam expansion as advocated by Shea et al. (2010), plateau values were normalised to a /(g batter) basis (Table 4.5) by correcting for –BiC and +BiC batter density. Normalised values are reported as Total gas phase volume and Total number density. The Total surface area was estimated as the sum of bubble surface areas, calculated individually as (6 x bubble volume)/(corrected bubble diam.) (Walstra, 2003a), and normalised to a /(g batter) basis (Table 4.5).

Idli batter bubble populations were produced by a combination of bubble fragmentation and air entrainment on flour particulates. Pulse flours entrained many new bubbles into BBM, increasing the number density of detectable bubbles (Table 4.5; Fig. 4.8 top & -BiC overlay plot). Total gas phase volume was higher than that of cereal batters (Fig. 4.8 bottom & -BiC overlay plot). Shimiya & Yano (1987) suggest the proportion of air entrained with flour particles is related to the total surface area of added particulates. On LDS sizing pulse flours contained a greater volume of small particulates (see Table 4.2), and consequently had greater particulate surface area than cereal flours.

Adding RI or SG flours to BBM decreased Total number density ~ten-fold compared with pulse batters. The number density distributions of RI and SG batters were broadened and flattened in scale compared with those in BBM-5.3 and pulse flours; this profile is typical of a model bubble population undergoing collapse (Shea et al., 2010) (see Fig 1.12). As judged by eye, cereal batters contained large particulates which filled a greater volume of the non-gas phase. They also showed reduced liquid phase volume (presumably as a result of liquid uptake by cereal flour particulates), contracting the volume in which bubbles can exist, and so encouraging the loss of bubbles from BBM-5.3 on flour hydration. Larger particulates will also inhibit both bubble movement and expansion.

For an individual bubble to expand the internal gas pressure must be greater than the pressure of the external medium. In the presence of much larger particulates, it also must also provide enough force to displace surrounding particulates. The larger the individual mass of particulates surrounding a bubble, the greater the force the internal gas pressure must exert to expand beyond the limit of the space between them. R2 flour contained a higher %volume of large particulates than R1 flour as determined by LDS (section 4.4.2), and lower Total number density and Total gas phase volume (Table 4.5).

BG and SG batters were observed to have more gel-like liquid phases that flowed less readily than in other batters, and were also markedly more viscoelastic on bulk rheological testing before BiC addition (see Table 4.3). BG –BiC batter had a high proportion of bubbles in the smallest size class compared with the other pulse batters, while SG –BiC batter had a similar increase in small bubbles compared with other cereal batters. This is consistent with a reduction in mean equilibrium bubble size due to the influence of the elastic component E of the viscoelastic medium (see section 4.3.4). The elastic component of structured fluids also stabilises small bubbles by resisting bubble shrinkage (Kloek et al., 2001).

4.5.4 +BiC bubble populations

In all batters at 5 min after BiC addition, > 90% of the added CO_2 gas phase volume had partitioned into bubble sizes > 0.1-0.2 mm diam. (Fig. 4.8 bottom, individual size classes). Unexpectedly, the relative proportion of bubbles in each size category (i.e. shape of the cumulative curve) generally became more similar on BiC-driven expansion (Fig. 4.8 + BiC overlay plots).

For cereal batters, an increase in gas phase volume after BiC addition was evident as an upwards shift across all size classes (Fig. 4.8 bottom) which resulted in cereal +BiC cumulative curves overlapping those of pulse batters (+BiC gas phase volume, overlay plot). This was associated with an increase in cereal batter number density in the corresponding size classes (Fig. 4.8 top) (i.e. curve was translated upwards). Bubble counts for individual size classes in cereal batters separated into two sub-populations, with a main peak at ~0.1 mm diam. A flat shoulder of smaller bubble size was evident below a point of inflection at 0.03-0.04 mm diam.

There are two potential mechanisms for the development of this bimodal population in cereal batters. 1) Adjacent large particulates physically constrain CO_2-driven growth of larger bubbles by increasing the internal pressure (and hence the energetic cost) required for bubble expansion, so favouring the growth of existing microbubbles to a detectable size in the space between particulates. 2) The reduced liquid phase volume in cereal batters increases local CO_2 gas concentration to the point that a new sub-population of bubbles can form by heterogeneous nucleation from cavities associated with RI and SG flour particulates. As the flat shape of the small sub-population is typical of a model bubble population undergoing continuous nucleation (Shea et al., 2010), conditions in cereal batters appear to favour heterogeneous nucleation over maturation of previously undetected microbubbles as the probable mechanism.

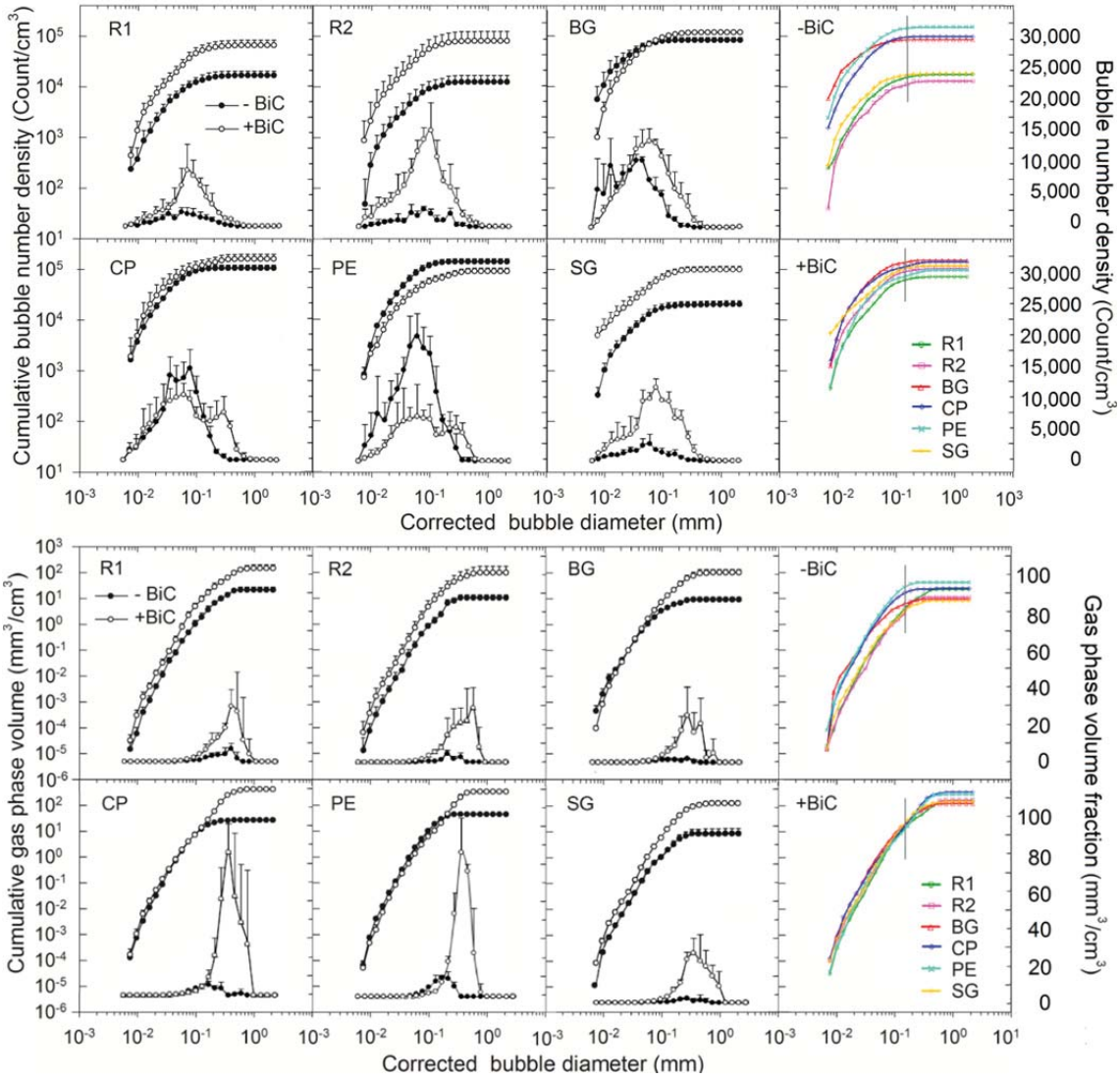

Figure 4.8 Cumulative bubble distributions (plotted against left-hand axis) and individual size class values (plotted against right-hand axis) for batters before bicarbonate addition (-BiC, closed circles) and at 5 min after addition (+BiC, open circles). Top: bubble number density. Bottom: bubble gas phase volume. Colour plots on the far right overlay the cumulative plots for all batters before BiC addition (labelled -BiC) or after addition (labelled +BiC). Grey lines indicate the lowest value for sample thickness h_{Mean}, (n = 4 + SD).

Total number density in CP and PE –BiC batters was 8-10 fold more than in cereal batters, and Total surface area was three-to five-fold more than in other batters (Table 4.5), increasing the surface available for CO_2 diffusion. Total gas phase volume increased two- to three-fold more on BiC addition in CP and PE batters than in other batters, consistent with specific volume measurements (see section 4.4.4). Together with the low viscosity of the liquid phase as observed in light micrographs, bubble expansion driven by CO_2 is predicted to be more rapid in CP and PE batters. Rather than stimulating a round of expansion in small bubbles, as observed in cereal batters, the bubble populations were biased towards expansion of bubbles larger than 1 -2 mm diam.

CP and PE bubble counts in individual size classes after BiC addition (Fig. 4.8 top) also displayed a

bimodal distribution typical of coalescence (two peaks, with the one at larger size somewhat truncated, see Fig. 1.12). Total gas phase volume in PE and CP +BiC batters was > 350 mm^3/cm^3. In volcanic melts bubbles begin to coalesce at ϕ_{Gas} above this value (Herd & Pinkerton (1997), quoted in Blower et al., 2002). A ~30% decrease in PE Total number density after BiC addition indicated a higher incidence of coalescence than in CP batter at the same timepoint in batter preparation. Before BiC addition, the Total gas phase volume of PE -BiC batter was almost two-fold more and Total surface area one-and-a-half times more than in CP –BiC batter (Table 4.5). It is probable that the process of coalescence was less advanced in CP batter, so that CP Total number density remained high at the time of measurement. In such a complex whole-food system, the influence of other factors on bubble stability cannot be ruled out, and more extensive timecourse data is required to confirm the supposition that PE batter advances more rapidly to the stage of extensive bubble coalescence than CP batter after BiC addition.

Both SG and BG +BiC batters, with more viscoelastic liquid phase, had greater bubble number density at small size than other batters. The regular shape of BG +BiC batter number density in individual size classes is typical of an expanding bubble population formed in a single nucleation event (Shea et al., 2010) (see Fig. 1.12), with a stock of bubbles below detectable range under continual recruitment for expansion after BiC addition.

SG batter had number density and gas phase volume distributions similar in overall shape to RI batters. However, while the viscoelasticity of the liquid phase appears to be the major influence on bubble population dynamics in BG +BiC batter, the bimodal distribution shared by SG and RI +BiC batters suggests that the large particulate content and/or a reduced liquid phase are more influential in determining bubble population dynamics in SG batter than the flow behaviour of the liquid phase.

The differences observed for bubble population dynamics between cereal and pulse batters point to a marked influence of larger particulates before and after BiC addition. Potential mechanisms by which large particulates may modify bubble population dynamics include 1) a reduction in bubble-bubble interactions by physically screening bubbles from one other; 2) creating the need for a localised minimum force (critical bubble internal gas pressure) to move apart the masses of adjacent particulates forming barriers to bubble expansion; 3) sequestration of liquid phase within particulates on flour hydration, leading to bubble collapse; and 4) acting as sites for heterogeneous nucleation of new bubbles during CO2-driven expansion.

The fate of individual bubbles (do they grow, shrink or stay the same?) was evaluated in a small preliminary analysis by measuring bubble areas at 20 s intervals in a section of a +BiC batter micrograph (Figs. 4.9 & 4.10). At least half of all batter bubbles decreased in measurable size over the 3 min observation period. The relative incidence of bubble shrinkage to bubble growth trended higher in CP, PE and R2 batters, and was more equal in R1, BG and SG batters (Fig. 4.9). There was no clear difference between the cereal batters and other batters. However, the disappearance of smaller bubbles into the batter and out of view cannot be differentiated readily for many (but not all) of the apparent shrinkage events. A systematic relationship between bubble size, liquid phase viscosity and bubble fate under conditions of rapid bubble expansion was not clear in this small-scale analysis. Further study would require larger sample size and include baseline timecourse data for –BiC batters.

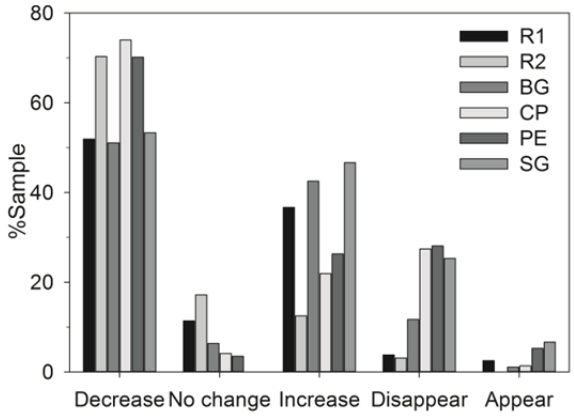

Figure 4.9 Incidence of bubble size change in +BiC batters. Bubble areas were measured at 20 s intervals in one quarter of a field of view (1.8 x 1.3 mm). Bubble numbers: R1 (46), R2 (84), BG (94), CP (73), PE (57) and SG (75).

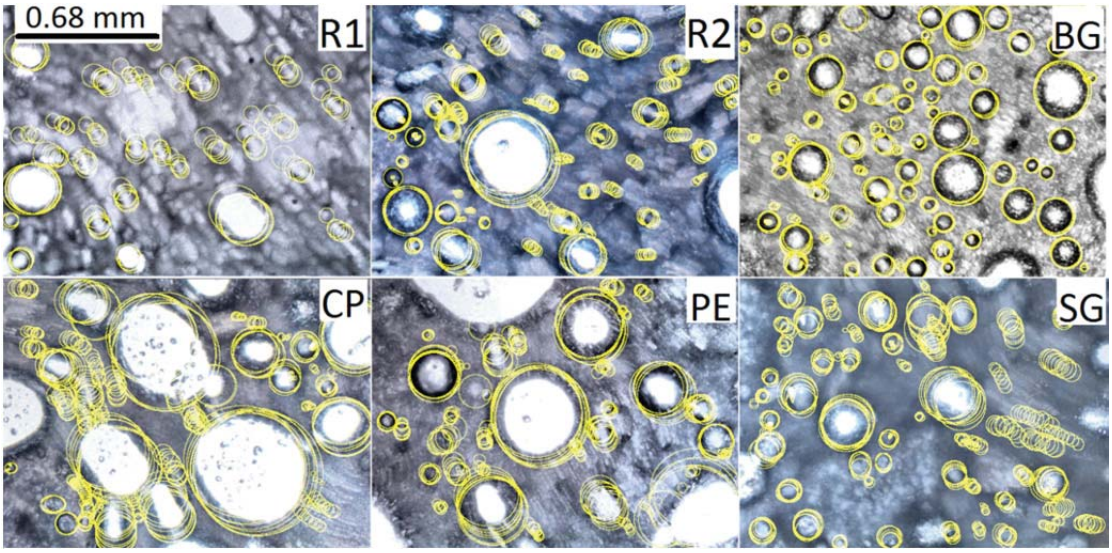

Figure 4.10 Overlay images for micrographs taken at 20 s intervals to follow the change in bubble size and position with batter streaming on the slide (quantified data shown in Fig. 4.9). Produced using ImageJ Stack/Z-project/Max intensity. R1 = 6 images; other batters = 9 images.

4.5.5 Idli bubble population dynamics and models for bubble growth

The behaviour of the idli batters can be compared with models for both food and non-food systems of bubble populations and individual bubbles undergoing growth driven by gas desolubilisation (Bikard, Coupez, Della Valle, & Vergnes, 2008, 2012; Everitt, Harlen, & Wilson, 2006a, 2006b; Joshi, 1998; Narsimhan, 2012; Shehzad et al., 2010). Models of bubble population growth predict that high bubble number density at the onset of rapid CO_2-driven expansion (with correspondingly high surface area) should accelerate the increase in gas phase volume early in expansion, as observed on comparing of CP and PE +BiC batters with other idli batters. A high initial bubble number density also produces a narrower size range once the leavening agent is fully reacted and gas–driven expansion ceases, which is consistent with the observed void size distribution in CP & PE batters compared with other batters (see

section 5.4).

In models of bubble growth in viscoelastic fluids, after overcoming an initial lag period the growth rate of an individual bubble increases as the liquid phase becomes more viscoelastic – contrary to an intuitive expectation that viscoelasticity might reduce the extent of foam expansion. With BiC addition, the cumulative gas phase distribution plots of SG and BG batters, with a high viscosity liquid phase on microscopy observation and a significantly increased viscoelasticity on bulk rheological analysis of the batter, began to converge with those of less viscoelastic batters. This is consistent with the behaviour of bubble populations in increasingly viscoelastic fluids. Bubble population growth models also predict that with the reduction of chemo-motive force driving expansion (e.g. on carbonate ion depletion) newly-expanded microbubbles will experience more rapid growth than larger bubbles (Feng & Bertolo, 2004). Batters such as RI and SG +BiC batters with a bimodal or multimodal bubble distribution may therefore experience different expansion rates between sub-populations, dependent on the relative size and number density of each sub-population and on competition for expansion gases from adjacent bubbles (Yue, Feng, Bertelo, & Hu, 2007).

4.5.6 Bubble population dynamics in uncooked idli batters: conclusions

To summarise the conclusions drawn from the behaviour of uncooked idli batters and batter fractions:

- Idli batters are complex multiphase fluids. The liquid phase can range from a thin fluid to a highly viscoelastic fluid (which may be gel-like). It contains threads of BM denatured protein present as soft deformable mats; flour particulates in the form of starch granules, granule aggregates, and larger grain/seed fragments; and BG bean fragments with a broad size distribution.
- Bubbles are formed in the idli batter formulation used in this study at three stages: wet-milling of BBM; when air entrained between flour particulates forms new bubbles during flour hydration; and possibly by heterogeneous nucleation from particulate cavities In the presence of CO_2-driven bubble expansion.
- With flour addition the number density of measurable bubbles increases for pulse flours containing many small particulates, and decreases for cereal flours containing large particulates that crowd the batter and reduce the liquid phase volume on hydration.
- At the same timepoint in batter preparation bubble growth is more advanced in batters with ready bubble mobility and expansion. In these batters adding BiC does not increase bubble number density, but rather increases the gas phase volume to the point that bubble-bubble contact and coalescence become frequent, generating a bimodal distribution with a truncated peak at larger size.
- Adding BiC to batters with low liquid phase volume and low bubble number density either 1) stimulates bubble expansion in previously undetected microbubbles, or 2) possibly initiates formation of new bubbles by heterogeneous nucleation on cavities of flour particulates. Although most of the CO_2 gas partitions into larger bubbles, enough partitions

into smaller bubbles over the course of observation to expand both the existing population detected before BiC addition and the newly-detectable sub-population, generating a bimodal distribution.

- Modelling suggests that increasing the liquid phase viscoelastic properties slows initial bubble expansion, but also stabilises bubble expansion at later stages, reducing bubble coalescence and collapse. Snapshots of bubble distributions in viscoelastic idli batters support this mechanism.
- The relationships between bubble size and cumulative gas phase volume and number density converge for batters once BiC is added. Despite significant between-batter differences, all batters reached a similar cooked volume (see Chap. 5). This suggests some common mechanism controls bubble growth and expansion in the idli batter system, and that the mechanism remains stable despite considerable variation in composition and flow behaviour between batter formulations.

Chap. 5 quantifies the structure of cooked idli products, examines structure setting, proposes mechanisms to explain the variation in cooked idli structure, and defines functional and physical elements in the design of idli formulations.

Chapter 5. Cooked idli structure and events on batter cooking

5.1 Events on cooking and synthesis of idli structure development

Chapter 4 examined bubble formation and foam expansion in uncooked idli. On cooking SP foams expand further as the rise in temperature reduces CO_2 solubility and initiates foam expansion driven by water vapour transfer into bubbles. The process of bubble expansion ceases as biopolymers in the liquid phase denature/alter structure on heating. Heat denaturation also alters the properties of the bubble interface. The key events on microstructure setting are swelling of starch granules, loss of water from the liquid phase in the form of water vapour and on uptake by gelatinising granules, and protein denaturation and NSP reorganisation to produce an elastomeric protein-rich gel. When bubbles rupture on structure setting to form an open-cell foam, the gas-pressure differential between the bubble interior and the external medium driving bubble expansion is lost and batter expansion ceases (Whitworth, 2008).

The aim of this chapter is a whole-system analysis based on the experimental observations of structure development in idli formulations in which flour type was changed without altering ingredient ratios. This requires correlation of the cooked idli macro-, meso- and microstructure with bubble formation and foam expansion before cooking (Chap. 4) and with further expansion and structure setting on cooking (examined in this chapter). As direct measurement of transformation in idli batters on cooking could not be carried out (see section 3.6), instead indirect measures of starch granule gelatinisation and protein denaturation are used to compare the timing of structure setting in the different batters. Void mesostructure and cooked microstructure are compared between the idli formulations. The information from all stages of idli production is synthesised into a conceptual model identifying the key functional and physical elements in idli structure development, in relation to bulk product expansion on cooking, void size distribution and wall thickness distribution, void shape and void regularity within the idli cooked product.

5.2 Cooked idli macrostructure: product shape and volume

On visual inspection, pulse flour idli had an even cylindrical shape with a flat top, slightly sunken in the centre of BG and CP idli. RI and SG idli rose to a small peak of 3-4 mm. The peaked shape of muffins was attributed by Whitworth (2008) to a combination of early setting of muffin batter at the edges and retention of a fluid core that continued to expand upwards late in cooking. Even though the degree of expansion in idli batters ranged from 200-300% on cooking, cooked idli products all had similar final volumes (see Fig. 4.3 & Table 4.4). This supports the primary influence of the non-flour fraction, rather than flour components or batter viscosity, on bulk batter expansion.

5.3 Visual assessment of cooked idli mesostructure

The mesostructure at the cut surface of the cooked idli was clearly differentiated between the different idli formulations on visual inspection (Fig. 5.1 top, over page), and the distinctive features in each formulation were retained between samples and between batches. Internal mesostructure was

recorded by x-ray computed microtomography (μCT) of typical idli samples. The μCT output gave a consecutive series of 2D image slices (e.g. Fig. 5.1 middle) at a resolution of 13.3 μm/pixel and slice thickness of 13.3 μm (see Appendix D.7). Different digital image analysis methods to quantify idli void size and wall thickness were evaluated (Appendix D). Fig. 5.1 bottom shows 3D renditions of 2D μCT data after void size analysis using the ImageJ plugin Local Thickness. ImageJ is an open-source platform for digital analysis of scientific images (Abramoff, Magalhaes, & Ram, 2004).

The μCT images for R1 and R2 idli (Fig. 5.1 middle) showed large ellipsoidal voids and regular thinning of the solid phase walls, typical of a readily-foaming material with a rapid recovery of bubble sphericity after distortion. BG idli had a few very large, mostly ellipsoidal voids, with many smaller ellipsoidal voids flattened along the Z-axis in a u-shape curve from edge to centre to edge. BG idli had walls with little evidence of between-void interconnection. Observation of BG batter after BiC addition indicated a few large bubbles were formed on mixing flour into batter. These then expanded preferentially at later stages of batter preparation, as their expansion was energetically favoured over neighbouring smaller bubbles. Preferential growth of infrequent very large bubbles introduced during batter handling is a fault in batter cake production (Cauvain & Young, 2000b).

CP and PE idli structure had a finer appearance than other idli, with a greater proportion of small voids, and fewer medium- and large-sized bubbles (Fig. 5.1 top). As modelled for a small bubble population in proving bread dough by Bickard, Coupez, Della Valle & Vergnes (2008) increasing bubble number density predisposes a bubble population to reach a narrower size distribution by the end of expansion, which is consistent with the observations of batter number density and void size distributions for these idli formulations. PE idli voids appeared more spherical than those in CP idli, with little evidence of wall loss between voids. Voids in the CP sample were more irregular and, as also observed in SG idli, were more likely to be missing walls between voids - some were probably below the resolution of the μCT analysis. The irregular shape of larger SG voids suggests that coalesced voids that formed on the merger of adjacent bubbles along their thinnest walls were hindered from regaining an ellipsoidal shape by surrounding partially-set material.

5.4 Idli void size distribution by digital image analysis

Terms and methods for digital image analysis are explained in Appendix D.1. Idli void size in μCT image slices was estimated using two approaches. Quantification of particle size from μCT sections with voxel size of 13.3 μm was carried out as described in detail in Appendix D., using binarised denoised 2D images and 1) FOAMS, a freeware package to determine void size distributions in lava rocks from microscopy sections (Shea et al., 2010) (Appendix D.9.6), and 2) Local Thickness analysis (LT) (Dougherty & Kunzelmann, 2007a) (Appendix D.9.4). FOAMS separates the continuous voids in binarised 2D μCT slices into discrete *particles* for automated counting, by completing missing walls as described in Appendix D.8.4. Note the term *particle* in digital image analysis is not the same as used to describe particles in emulsions, foams and dispersions. LT sizes voids by fitting a sphere into voids without first separating the voids into discrete 2D particles, giving an approximation of 3D void size from aggregated voxel data.

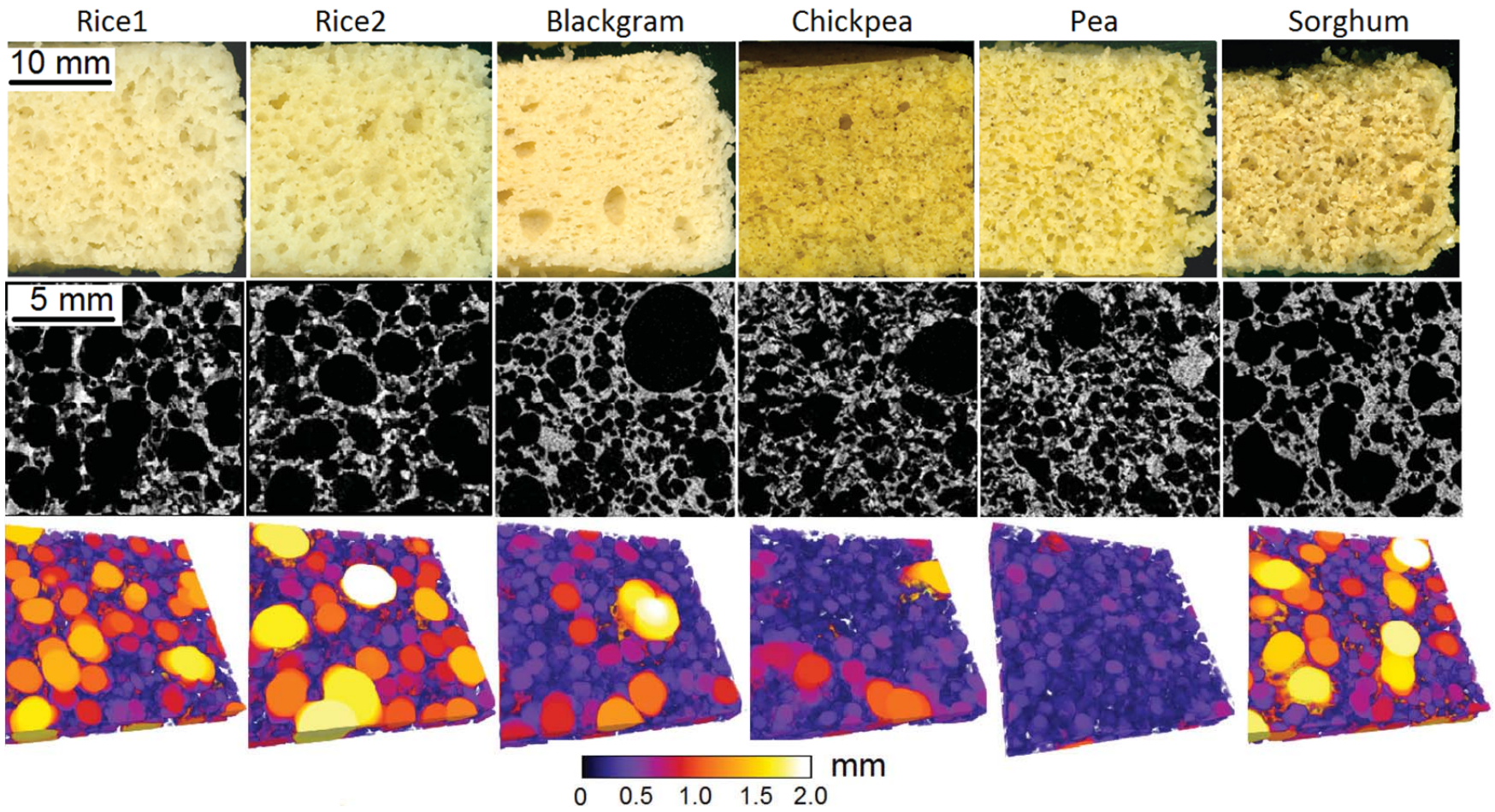

Figure 5.1 Visualisation of idli mesostructure. Top: digital scans of idli cut surface from a vertical slice through the product centre. Middle: XY-plane slice on x-ray computed microtomography. Bottom: 3D reconstruction of voids in cooked idli determined by Local Thickness as the equivalent fitted sphere for a sample of 10 x 10 x 1.3 mm.

5.4.1 Local Thickness analysis

Local Thickness analysis was plotted on linear axes after sorting into 114 bins increasing linearly in size (Fig. 5.2 top line, over page). The increased number of size classes for LT data accentuates events at larger size compared with the 24 geometrically-increasing size classes produced on FOAMS analysis (Fig. 5.2 remaining lines) (see Appendix D.10 for a comparison of these methods).

RI and SG void populations differentiated clearly into two sub-populations with an inflection point at ~1 mm diam. The BG void population showed a regular log-normal distribution, while CP and PE void populations had a narrow, positively-skewed log-normal distribution (Fig. 5.2 top line, quartile values in Table 5.1). A shoulder peak on the right-hand side of this distribution suggested a bimodal distribution. Additionally, there was a low incidence of voxels assigned to void diameters > 3.8 mm diam. in all samples (Fig. 5.2; Table 5.1), with the largest diameters assigned to the two idli formulations with viscoelastic liquid phases. However, maximal bubble size depends not only on bubble stability in idli batters during expansion but also on the timing of structure setting, which may limit the degree of bubble expansion.

5.4.2 Quantitative measures of void size and surface area

The size classes for peaks in idli void size distributions determined on LT analysis of μCT data are listed in Table 5.1, along with void peak sizes and distribution quartile values. BoneJ is an ImageJ distribution for analysis of porous bone structure (Doube et al., 2010). The BoneJ Isosurface function identified voxels associated with the gas-solid interface to quantify the surface-to-volume ratio, by mapping binarised 2D μCT slices onto a 3D mesh. The order from lowest to highest surface-to-volume ratio in cooked idli was R1 ≈ R2 < SG < BG < CP < PE (Table 5.1).

Table 5.1 Diagnostic features of void populations in typical samples of cooked idli. Total void volume and quartile values refer to LT data plotted in the top line of Fig. 5.2. LT peak sizes show (shoulder peaks) in brackets. Void volume, and BoneJ Isosurface function were determined on seven consecutive sections of 100 slices (n = 7 ± SD), and BoneJ Degree of anisotropy function was applied to the entire 700 slice sample.

	Void peak size (mm)	Void volume (mm^3/cm^3)	LT void diameter (mm)				Surface area (mm^2/cm^3)	Degree of anisotropy
			Q_{25}	Q_{50}	Q_{75}	Q_{100}		
R1	0.24, 1.70	746 ± 6	0.63	1.42	2.18	4.13	63.9 ± 0.9	0.199
R2	0.24, 1.53	736 ± 8	0.63	1.70	2.60	5.79	64.2 ± 2.0	0.153
BG	0.52	679 ± 17	0.52	1.00	1.84	7.95	76.8 ± 3.5	0.368
CP	0.24, (0.80)	736 ± 17	0.31	0.73	1.16	6.55	81.5 ± 4.1	0.298
PE	0.24, (0.52)	659 ± 32	0.28	0.55	0.87	5.55	85.8 ± 4.7	0.463
SG	0.24, 1.80	685 ± 35	0.71	1.46	2.19	8.0	68.7 ± 1.5	0.331

5.4.3 FOAMS analysis

The FOAMS output (Fig. 5.2 under line) is plotted from top to bottom as

- Void volume
- Cumulative void volume
- Ln(number density): plotted by Shea et al. as the natural log values to enable growth rate determination
- Log(cumulative number density): this plots the count of voids greater in size than the X-axis value.

FOAMS data are plotted using a logarithmic X-axis that emphasises events at small bubble size, except that ln(number density) are plotted on a linear X-axis to enable visualisation of growth rate curves. Trends in void distributions indicative of events such as disproportionation, collapse, etc., as identified by Shea et al. (see Fig. 1.12), were assigned to distribution features in Fig. 5.2 FOAMS plots. More than one event was sometimes suggested in the same distribution. LT analysis and FOAMS analysis resembled bubble population features observed in the corresponding uncooked +BiC batters (see section 4.5.4). The bimodality in void size distributions of R1, R2 and SG idli, particularly evident in number density plots, supported the occurrence of expansion in two distinct sub-populations, as described in the corresponding +BiC batters. Both sub-populations underwent exponential growth, the first to an upper size of ~0.7-0.9 mm diam. and the second to ~3 mm diam. The regularity of the BG void distribution, also observed in uncooked BG batter, was consistent with a single initiation of bubble expansion. The drop in bubble number above 3 mm diam. in R1, R2 and SG idli void distributions suggests a general size limit to bubble expansion in these idli batters. The inflection in the number density curve in CP and PE number density plots suggests that coalescence was common in bubbles > 3.5-4.0 mm diam.

5.4.4 Regularity of idli mesostructure

The deviation in void size between 100 slice sections was smallest in RI idli, and largest in PE and CP idli. The BoneJ function Degree of anisotropy function was applied to µCT data to evaluate the regularity of void organisation, which decreased from most to least regular in order R2 > R1 > CP > SG > BG > PE (Table 5.1). In foam structures with the same gas phase volume but with differing size distributions, BoneJ Isosurface value was higher in SPs with smaller voids and lower in SPs with more regular void shape.

Mesostructure regularity was evaluated from the bottom to the top of the cooked product by measuring particle number and mean particle size in µCT slices sampled uniformly along the idli Z-axis. Continuous voids were counted after watershedding to partition voids into discrete particles (see Appendix D.8.4 and D.8.5 for discretisation and measurement methods). The gas phase volume/porosity (ϕ_{Gas}) of the open-cell cooked idli foams as calculated by counting of void/non-void pixels did not vary significantly from top to bottom (data not shown).

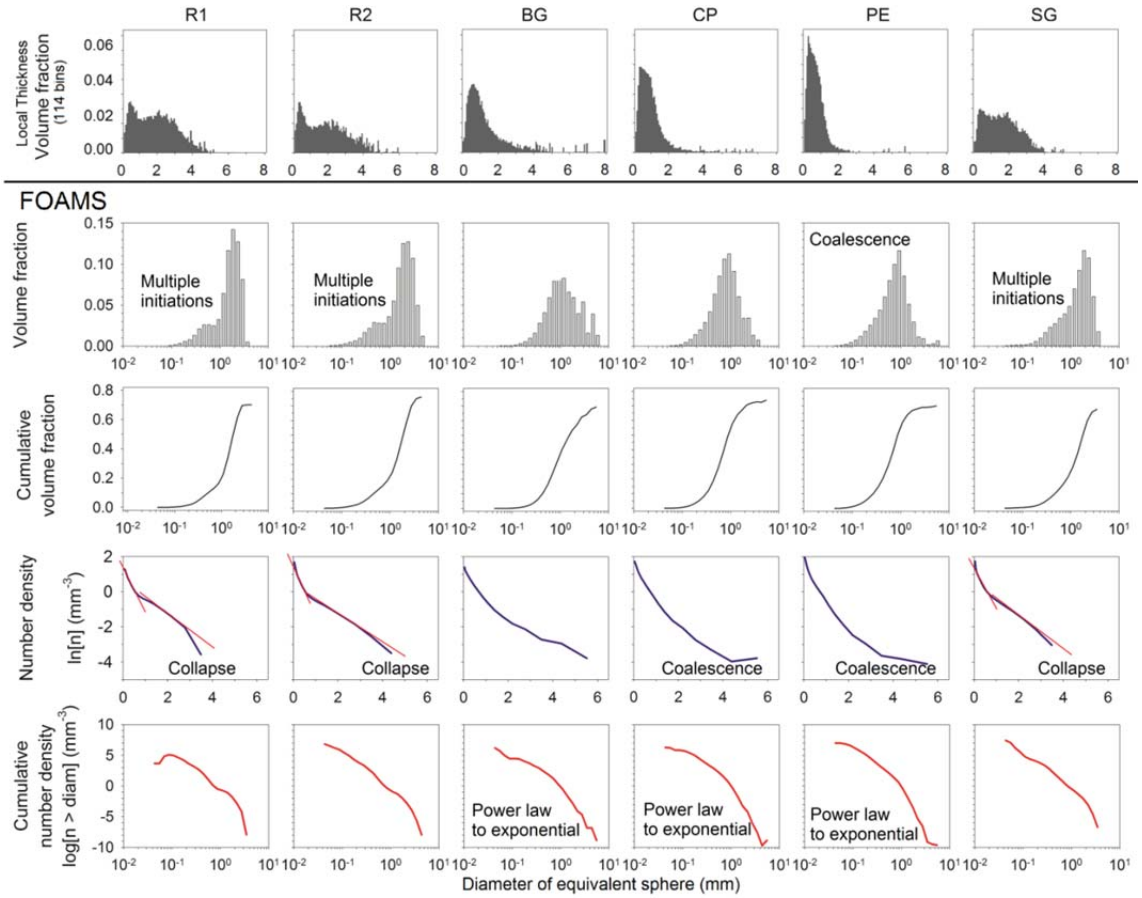

Figure 5.2 **Void size distribution in cooked idli as the output of Local Thickness analysis (top line) and FOAMS analysis, carried out on a 700 slice stack (15 x 15 x 13.3 mm) of images captured by x-ray computed microtomography analysis on a larger sample cut from a typical idli. Red lines on the number density plots are a visual guide to exponential growth rates. Descriptions on plots are based on diagnostic features assigned by Shea et al. (2010) to model bubble populations (see Fig. 1.12). Local Thickness: n =7, each of 100 consecutive slices, sorted into 114 linear bins. FOAMS: n = 25 slices chosen with random start and uniform interval, sorted into 24 geometric bins.**

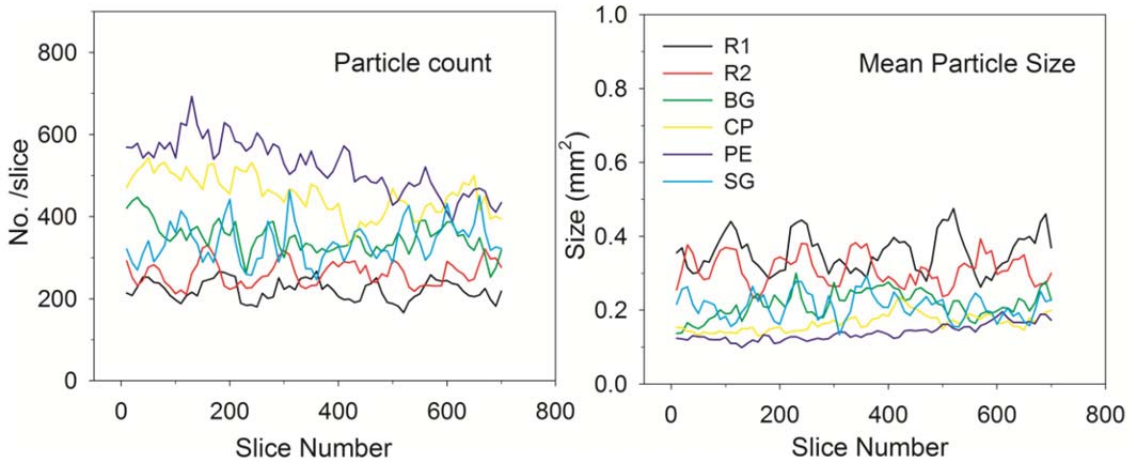

Figure 5.3 Variability in particle count and mean particle size from bottom to top in a 700-slice µCT idli sample sampled every 10 slices. Size distributions determined using ImageJ AnalyseParticle function and Unbiased Count, after voids were discretised by binarisation, denoising and watershedding.

Idli samples varied markedly between consecutive slice sections, particularly in RI idli (Fig. 5.3). CP and PE idli showed a consistent change in void distribution from the sample bottom to the top, with a 20-30% decrease in particle count (Fig. 5.3 left) correlated with an increase in mean particle size (Fig. 5.3 right). As a similar value for ϕ_{Gas} was maintained along the Z-axis in all samples, the increase in particle size balanced the decrease in particle count, suggesting some systematic mechanism generated this size/number gradient in CP and PE idli.

Several possible mechanisms may act separately or together to generate the linear gradient in count/size distribution. As the variation in hydrostatic pressure was negligible between all idli batters (range = 137.3-138.1 kPa, calculated using $P_{\mathrm{Hydrostatic}} = \rho \,.\, h \,.\, g$, where ρ is bulk fluid density, g is gravitational acceleration and h, batter height) a linear gradient generated by the difference in hydrostatic pressure can be excluded as a factor. Another potential mechanism is the generation of a linear heating gradient on cooking with increasing height. The large variability between individual samples observed for the time of initiation in batter expansion during microwave cooking (see Fig. 3.2 right) excludes this as a factor.

In a mathematical model of foam drainage, the frequency of bubble coalescence and collapse increased as liquid drained from channels and intersections between bubbles. Correspondingly, bubble number density decreased and bubble mean size increased linearly along the Z-axis (Narsimhan & Ruckenstein, 1996, p. 174). The flow behaviour observed for PE and CP batters supports the development of a drainage gradient in the time between aliquotting batter and structure setting as the probable mechanism producing a Z-axis gradient in void size and count in CP and PE idli.

5.4.5 Void shape distortion

On scrolling through the LT analysis output stacks, the development of voids could be visualised along the Z-axis. Based on a visual examination of void position and shape, the increasing size of CP idli voids along the Z-axis was associated with larger bubbles with an elongated shape, which formed on

upwards migration through the batter (upwards *tunnelling*), while the corresponding larger voids in PE idli were less elongated and more spherical.

The Bond number describes the relative importance of surface tension at the bubble interface, Γ_{Bubble}, to the effect of external forces acting on the whole bubble (Tsamopoulos et al., 2008). Under dynamic equilibrium conditions it is defined as:

$$Bo = (\rho_{\mathrm{Medium}}\, g r^2)/\Gamma,$$

where ρ_{Medium} is the density of the external (Newtonian) medium, g is gravitational acceleration and r, the radius of the sphere with equivalent volume. For a buoyant bubble travelling upwards through a liquid, decreasing Γ_{Bubble} results in more ready bubble distortion, becoming more extreme with increasing bubble size. This increased capacity for distortion with decreasing Γ_{Bubble}/increasing Bo also enables bubbles to squeeze more readily though the medium (Tsamopoulos et al., 2008).

As the definition of Bo suggests, deformation of buoyant bubbles depends on the relationship between interface properties and medium density. Fluids with yield stress or viscoelastic flow behaviour also affect the ease of bubble movement and bubble shape. A more thorough evaluation of the influence of bubble interface properties to void shape development in SP batters requires detailed information of interfacial properties and batter multiphase flow behaviour on heating. To date, there are no models for bubble growth in a medium that includes a large volume fraction of particulates.

As an initial hypothesis, the increased foam stability in PE batter fractions on heating, along with the heat stability reported for PE protein foams in the literature, suggests that PE bubbles may maintain a spherical shape during cooking due to increased robustness of the bubble interface at higher temperature; the lower robustness of the CP bubble interface increases upward mobility of buoyant bubbles through the medium by tunnelling, and also encourages greater bubble distortion.

5.5 Visualisation of idli microstructure

Starch and protein-NSP domains in the idli microstructure were well differentiated in light micrographs of lightly-fixed and -stained cryotome sections (Fig. 5.4, over page). In RI, PE, and SG idli starch domains formed extensive continuous regions within the solid phase microstructure. Individual starch granules and granule aggregates (stained dark blue or purple) were easily identified. Thin domains of protein-NSP material (counter-stained light blue) surrounded the starch domains (see Fig. 5.5 for detail, thin regions of protein-NSP arrowed). In comparison, the microstructure of BG and CP idli had smaller, non-continuous starch domains embedded within a predominant protein-NSP domain. The area ratio of protein-NSP domain to starch domain in the BG sponge structure was roughly similar to that visualised in (unaerated) wheat bread after similar preparation (Hug-Iten et al., 1999). While the protein-NSP domain appears homogenous on counter-staining, there will be distinct protein and NSP subdomains at smaller scale.

BG bean fragments (BF) produced on wet-milling BBM were evident as a microstructural component in all idli. Larger BF (0.1-0.3 mm wide) contained intensely blue, curled dish-mop structures inside thick, poorly stained cell walls, which represented BG starch granules restricted within bean cells during gelatinisation. CP and BG idli, without extensive starch domains, had larger BF reinforcing the void wall

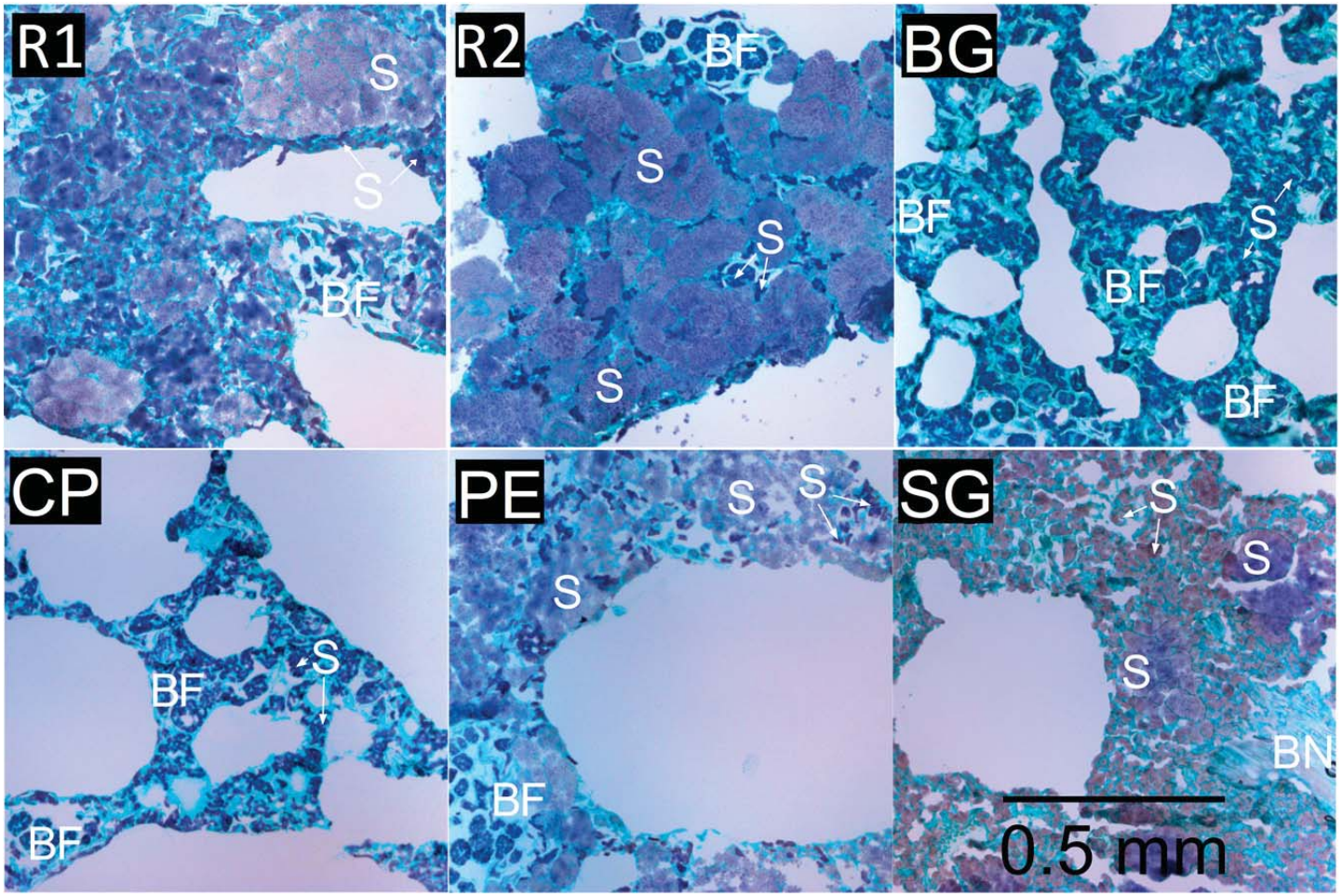

Figure 5.4 Micrographs of cryo-sectioned idli samples. BF: bean fragments; S (unarrowed) starch composite granules; S (arrowed) - arrows indicate individual distorted granules of blackgram starch; BN: sorghum bran flake. Sections were stained with iodine solution and counter-stained with FastS Green. Click here for high-resolution image.

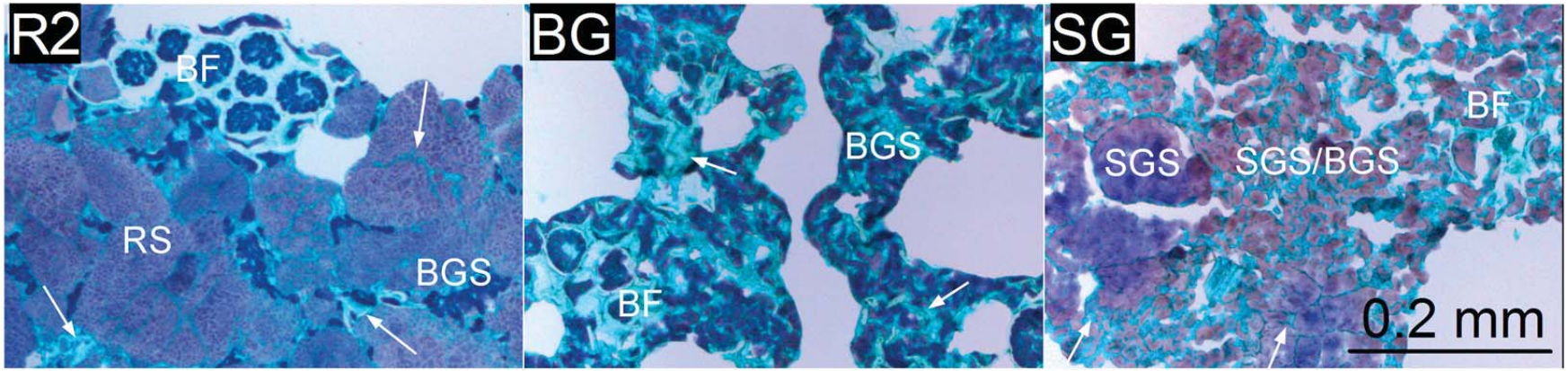

Figure 5.5 Closer views of cooked idli microstructure. RS: composite rice starch granule. BGS: blackgram granules. BF: blackgram bean fragment. Arrows indicate a thin continuous layer of protein-non-starch polysaccharide gel. Click here for high-resolution image.

structure at bubble intersections. These large BF must determine the frequency and position of the largest intersections between bubbles during foam expansion in CP and BG batters. Rye cell fragments up to 1 mm in size were reported to reinforce rye bread structure (Pomeranz et al., 1984), but non-granule flour fragments are generally not considered as contributing to the integrity of SP microstructure.

BG beans in the BBM fraction contributed from a quarter to a third of the starch content in batters (section 4.4.1). Dish-mop structures of dark-blue gelatinised BG granules were readily identifiable inside BF, and when these appeared free BG granules in idli microstructures were often compressed and distorted (arrowed granules in Fig. 5.4). On heating mixtures of starches from different sources under limiting water conditions, starch granules with lower gelatinisation temperature gelatinise more fully than granules with higher gelatinisation temperature (Puncha-arnon et al., 2008). Free BG granule distortion will be a combination of physical constraint by adjacent swollen flour granules and limited BG granule gelatinisation due to the reduced availability of local water.

Starch domain organisation in cooked idli microstructure can be related to observations of batter by light microscopy (section 4.5.1). Irregularly shaped large starch domains in RI idli (~200 μm at the widest point, RS in Fig. 5.5) are the gelatinised form of large rice grain surface cells filled with small individual RI granules (see section 4.5.1). Amylose efflux is a feature of PE starch pasting (Raphaelides & Georgiadis, 2007). The numerous, small, disk-shaped granules observed in PE batter expanded and fused to produce a continuous starch domain in PE idli microstructure.

In SG idli microstructure, a cluster of blocky granules, as seen near the scale bar in Fig. 5.5, was the gelatinised form of irregular aggregates of roughly cubic SG granules observed in SG batter (see section 4.5.1). Based on the shape of cooked SG granule remnants described by Obanni & BeMillar (1996), the amorphous SG starch domains (stained less intensely and labelled SGS/BGS in Fig. 5.5) probably represent a mixture of small SG granules, BG granules and leached SG starch polymers. Larger ellipsoidal purple-staining starch structures (labelled SGS in Fig. 5.5), were also described by Obanni & BeMillar.

The SG idli protein-NSP was more fragmented in appearance compared with the domains in other idli. Webbed and sheeted structures reported in cooked SG grain are produced when the coat around protein bodies melts at higher temperatures, releasing kafirins for solubilisation (Chandrashekar & Kirleis, 1988; Hamaker & Bugusu, 2003). Kafirins are structurally similarly to fibril-forming glutenin proteins in wheat-flour doughs but have higher T_g (Andersson et al., 2011). This will predispose kafirin-rich protein-NSP domains to adopt a glassy rather than a rubbery state after cooking and cooling (see Fig. 1.15). SG idli were also more crumbly and less cohesive on handling than other idli, consistent with a loss in microstructure integrity. SG-based breads are reported to be poorly cohesive - partial digestion of kafirins during extended fermentation improves the cohesiveness of SG bread (Schober, Bean, & Boyle, 2007). SG bran fragments (labelled BN in Fig. 5.4 SG) were also incorporated into the SG microstructure.

Finally, R1 idli appeared to have a greater volume of amorphous starch domain and fewer large intact starch surface cells than R2 idli, consistent with the smaller maximum size of particulates in R1 flour on laser diffraction particle sizing (see Table 4.2 & Fig. 4.3), suggesting a higher content of disrupted surface cells.

5.6 Transformation events in idli structure development

The gelatinisation of starch in batters and doughs on heating is responsible for the rapid viscosification of dough/batter associated with structure setting in SPs. The temperature range for starch gelatinisation influences the time and temperature range for bubble expansion in the batter on heating.

5.6.1 Initiation of granule gelatinisation

Differential scanning calorimetry (DSC) identifies the first stage of starch granule gelatinisation as a change in sample enthalpy (see section 3.9.2). In wheat-based doughs and batters DSC does not detect a great change in enthalpy on gluten network denaturation with heating (Arntfield & Murray, 1981), but this is not necessarily so for flours from other sources, particularly high-protein flours: DSC analysis of chickpea flour (Meares et al., 2004) produced a negative enthalpy peak linked to loss in starch crystallinity. A second overlapping peak was due to PE protein structure reorganisation on denaturation.

Freeze-dried +BiC batters were reconstituted with water for DSC analysis. A fresh BBM fraction was prepared with NaCl and BiC at concentrations consistent with whole batter, to represent conditions in the non-flour fraction of batter (see Fig. 4.1 & section 3.4.1 for method). Note that under standard baking conditions the temperature in SPs on cooking does not generally reach > 100 ˚C except at the browned crust (see Fig. 1.15). The enthalpy-time curves in Fig. 5.6 left represent the response of 1.0 g of whole batter. Most DSC profiles had one major peak and a later shoulder. The major DSC peak in PE batter was well differentiated from a second, smaller peak.

The order of DSC onset temperature for the major peak was PE << R2 ≈ R1 < CP ≈ SG ≈ BBM < BG, and the order of DSC peak temperature was PE < R2 < SG ≈ R1 ≈ BBM-5.3 ≈ CP <BG (Table 5.2, over the page). Peak DSC values for CP and BG starch gelatinisation were within the range, or a few degrees higher, than reported for isolated pulse starch granules (Hoover & Sosulski, 1991). DSC peak temperatures for starch granules isolated from smooth pea fell between 60-75 ˚C, depending on pea variety (Kosson, Czuchajowska, & Pomeranz, 1994; Ratnayake, Hoover, & Warkentin, 2002). R1, R2 and SG peak temperatures were close to values reported for isolated RI and SG starches in the presence of salt or NSPs (Alamri, Mohamed, & Hussain, 2012; Samustri & Suphantharika, 2012). Based on reported starch gelatinisation temperatures, the profiles represent an initial starch gelatinisation event, overlapped by later partial starch polymer melting under limiting water conditions and protein denaturation.

PE protein isolates were reported with onset temperatures of 82-83 ˚C (vicilin) and 92 ˚C (legumin) (Liang & Tang, 2013). The vicilin value corresponded to the second peak of the PE batter DSC curve, although the DSC profile of isolated PE starch granules also tailed at higher temperature (Ratnayake et al., 2002). A shoulder/peak at 90-97 ˚C in BG batter almost certainly represents BG protein reorganisation with heating; a small shoulder at a similar position in all other samples can be attributed to BG in BBM. Protein denaturation at higher temperature is useful for SP formulation design: a later gelation of the liquid phase increases the number of possible starch sources for the formulation (i.e. initiation of starch gelatinisation should precede initiation of protein-NSP gelation).

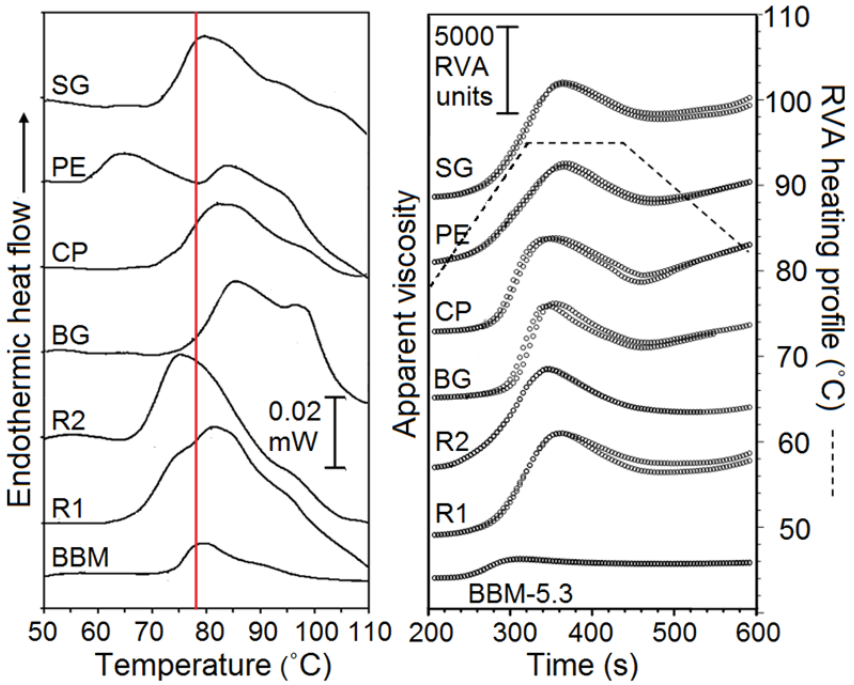

Figure 5.6 **Left: typical traces of enthalpy change on differential scanning calorimetry at 10 °C/min, for reconstituted freeze-dried +BiC batters and BBM-5.3 at 0.5% NaCl (equivalent to 1 g fresh batter). Right: RVA viscosity of flours pasted in particulate-free BBM under batter conditions at flour content to give peak viscosity of 6,000 ± 500 RVA units. Data are overlays of duplicate flour preparations. The dotted line is the heating profile on pasting. The red line on the DSC plot corresponds to RVA temperature at 200 s.**

Table 5.2 Differential scanning calorimetry parameters for reconstituted freeze-dried batters and for BBM-5.3 at 0.5% NaCl. Values equivalent to 1.0 g fresh batter, n = 3 ± SD.

	R1	R2	BG	CP	PE	SG	BBM-5.3
Onset temperature (°C)							
Peak 1	67.3 ± 0.3	67.4 ± 0.4	77.7 ± 0.4	72.8 ± 1.3	59.1 ± 0.6	73.3 ± 1.2	73.8 ± 1.7
Peak 2			93.1 ± 0.4		81.4 ± 1.5		
Peak temperature (°C)							
Peak 1	80.9 ± 0.5	75.5 ± 0.4	85.1 ± 0.4	81.8 ± 1.0	65.7 ± 1.2	80.5 ± 1.1	78.9 ± 0.7
Peak 2	-	-	98.2 ± 0.7	-	85.8 ± 1.3	-	-
Shoulder	95.3 ± 0.8	90.7 ± 1.4	-	96.3 ± 1.2	-	96.2 ± 1.7	97.0 ± 1.0
Activation energy (J/g)							
Peak 1	6.24 ± 0.91	6.00 ± 0.86	5.50 ± 0.26	4.30 ± 0.11	1.53 ± 0.10	3.57 ± 0.10	2.7 ± 0.08
Peak 2			0.52 ± 0.15		0.62 ± 0.38		
Peak range (°C)							
Peak 1	30.6 ± 0.5	23.0 ± 1.3	24.2 ± 0.4	27.8 ± 1.8	21.1 ± 1.5	31.2 ± 1.9	22.4 ± 0.6
Peak 2			7.3 ± 0.7		14.6 ± 0.7		

5.6.2 Batter viscosification on heating

5.6.2.1 Relationship between pasting and batter viscosification

Starch granule expansion during heating in the presence of water produces a rapid rise in batter and dough viscosity, due primarily to extensive starch granule swelling (BeMillar, Derby, & Trimbo, 1973). Wheat flour suitability for SP formulations is tested indirectly by evaluating viscosity changes in flour dispersions on heating in excess water under stirring (pasting). Starch granules on pasting experience greater shear deformation than those in batters during cooking. Even so, analysis of the early part of the viscosity-time curve on pasting provides a valid indirect measure of rapid viscosification in flour dispersions. The influence of idli flour content on viscosity increase was first established for flours pasted in water before comparing the timing of rapid viscosification in flours pasted under batter-equivalent conditions, in the absence of BBM particulates and BiC-driven foam expansion.

5.6.2.2 Pasting conditions

Batter fraction preparation and pasting methods are detailed in sections 3.4.2.2 & 3.9.3.2 Pasting was carried out with the Rapid ViscoAnalyser™ Super-4 system, used commercially for wheat flour analysis. Temperature increased linearly from 50 ˚C to 95 ˚C, followed by a period at 95 ˚C to ensure completion of granule gelatinisation and breakdown under shear, before cooling to 50 ˚C. Fig. 5.6 right shows typical RVA pasting curves for flours and a BBM fraction, under batter-equivalent conditions and with flour content chosen to produce a similar peak viscosity. The part of the pasting curve relevant to rapid batter viscosification runs from the onset of the viscosity rise to the first peak in viscosity (RVA Peak Viscosity; PV). Note that under batter-equivalent conditions and similar heating rate of 10 ˚C/min for DSC and RVA analyses, the loss of starch crystallinity as determined by DSC was a poor predictor of the onset of rapid viscosification on RVA pasting (Fig. 5.6 left vs. right), particularly for PE batter fractions.

5.6.3 Influence of starch on flour pasting response

The starch granule number density, size and shape all influence the viscosity increase on pasting. Starch content was highest in RI flours, intermediate in SG flour, and lowest in BG and CP flours, based on compositional analysis (see section 4.4.1). Under light microscopy, many small disc-like granules (similar in shape to the large A granule fraction of wheat starch (Li et al., 2013) could be seen in PE batter, while RI batters contained many large rice grain surface cells filled with small individual granules. The addition of BG starch granules to batter in the BBM fraction also introduced heterogeneity into the granule population.

The influence of flour content on viscosity was examined on pasting in buttermilk adjusted to pH 5.3, the mean pH of flour + BBM (see section 3.9.3.5). RVA Peak Viscosity (PV) was plotted on semi-log scale against increasing flour content (Fig. 5.7). The measured flour contents fall below the flour content in idli batter formulations of 24%, as the plotted values were limited to the highest flour content able to produce a smooth viscosity profile over a complete pasting cycle in this test system.

A linear increase in flour content produces a geometric increase in flour starch granule volume fraction (Steeneken, 1989). When this volume fraction is high enough that particulate-particulate contact between gelatinising granules becomes frequent on pasting, a logarithmic increase in PV should be generated with a linear rise in flour content (log-lin regression), until the point at which flour particulates start to overcrowd the volume at PV, when the relationship breaks down. Flours with small granule size and/or lower starch content (e.g. pulse flours) must achieve a higher flour content to reach this contact threshold.

PV values for R1 and R2 flours overlapped, indicating that R1 and R2 flours were milled from similar cultivars (Meadows, 2002). The upper limit of a log-linear response for PV with flour content was at ~10% for R1 and R2 flours (with ~80% starch content), while this was the lower limit for the log-linear response in pulse flours (with 45-52% starch content) and SG flour (with 67% starch content).

Flour granule content was not the sole factor contributing to flour viscosification. Non-starch components such as denatured proteins and aggregated NSPs also contribute to viscosification in whole flours, particularly in low-starch, high-protein pulse batters. Extrapolation back to the Y-axis along the log-linear portion of the viscosity response gives a rough indication of the contribution of protein-NSP components to PV. The order of Y-axis intersection for PV (in RVA units) was R1 (2.2) = R2 (2.2) << PE (90) < CP (120) = SG (120) < BG (280). This parameter is similar to the background viscosity contributed by the liquid phase to the flow behaviour in particulate-containing polymer solutions (e.g. see section 2.9.3), but with the addition of temperature as a factor. Interestingly, the relationship between PV and flour content for SG flour is more similar to the pulse flours than to RI flours.

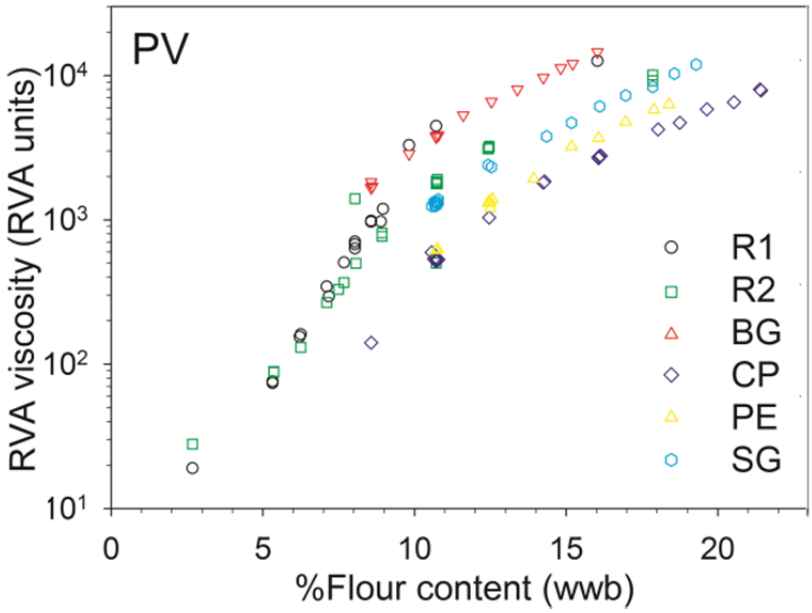

Figure 5.7 RVA Peak Viscosity values with increasing flour content with pasting in the presence of 85% buttermilk adjusted to pH 5.3.

5.6.4 Timing of batter viscosification

Whole batters were too viscous on pasting for RVA measurement. For between-batter comparison flour contents were chosen to produce PV values at 6,000 ± 500 RVA units (within optimal response range for the RVA Super-4). Plotting viscosity-time data as the 1st derivative curve extracts more information from pasting curves (Juhász & Salgó, 2008). Fig. 5.8 plots the 1st derivative values calculated for flours pasted with water, buttermilk adjusted to pH 5.3 (BM-5.3), the pH of batter before flour addition, or with BBM_{Liq} after adjustment to pH 7 (batter-equivalent conditions). For batter-equivalent conditions, flours were hydrated with particulate-free BBM and 1.6% NaCl and adjusted to pH 7.0 with NaOH before pasting (preparation described in Fig. 4.1 D). Data for the rate of change in viscosity were normalised by dividing each data point by the maximum rate of change in viscosity below PV.

In the normalised 1st derivative curves of RVA data in early pasting, the initial point of inflection indicates the onset of rapid viscosification. The first peak value is the point of most rapid viscosity increase, before the start of extensive granule disintegration. The zero point on the Y-axis at the far end of the peak corresponds to the RVA PV value.

The 1st derivative curves for batter fractions had either a narrow, rapid increase in rate of viscosity change (BG and CP flour, BBM-5.3) or a broader, more gradual increase (RI, SG and PE flours).The 1st derivative curves for flours pasted with BM-5.3 and BBM_{Liq} pH 7 were generally similar in shape to the corresponding pasting curves with water, but shifted to higher onset temperature. This was primarily in response to salts, organic acids (and possibly free fatty acids) in BM-5.3, as deproteinated BM-5.3 produced a similar shift (data not shown). Samustri & Suphantharika (2012) reported that the ionic fraction was most influential in modifying gelatinisation of RI flour in the presence of salts and NSPs. Free fatty acids may retard gelatinisation, with retardation being specific for free fatty acid length and amylose polymer size (Raphaelides & Georgiadis, 2007). Based on these results, the most influential non-starch component modulating the onset temperature of starch granule swelling in idli batters is the non-protein fraction of the BBM liquid phase.

On pasting in BM-5.3 (representing batter minus BG bean contribution) or BBMLiq adjusted to pH 7.0 (batter-equivalent conditions) BG and CP flour produced 1st derivative curves similar in shape and timing to the pasting of the BBM-5.3 fraction, i.e. buttermilk components had more influence on pasting than BG bean components. BG and CP idli both had microstructures with reduced, non-continuous starch domains, suggesting that gelation of the protein-NSP domain contributed more to the rise in batter viscosity than in other batters. Under batter-equivalent conditions (pasting with BBMLiq pH 7) the onset temperature for rapid viscosification increased in order R1 < R2 < PE < SG < CP < BBM-5.3 ≈ BG and the temperature at peak viscosity increased in order PE ≈ SG < R1 ≈ R2 ≈ CP ≈ BG (Table 5.3, over page). The broader flatter peaks for RI, PE, and SG flour indicated that viscosification took place over a wider temperature/time range in these samples. PE and SG idli microstructures both had an amorphous, continuous starch domain indicative of starch polymer leaching during gelatinisation.

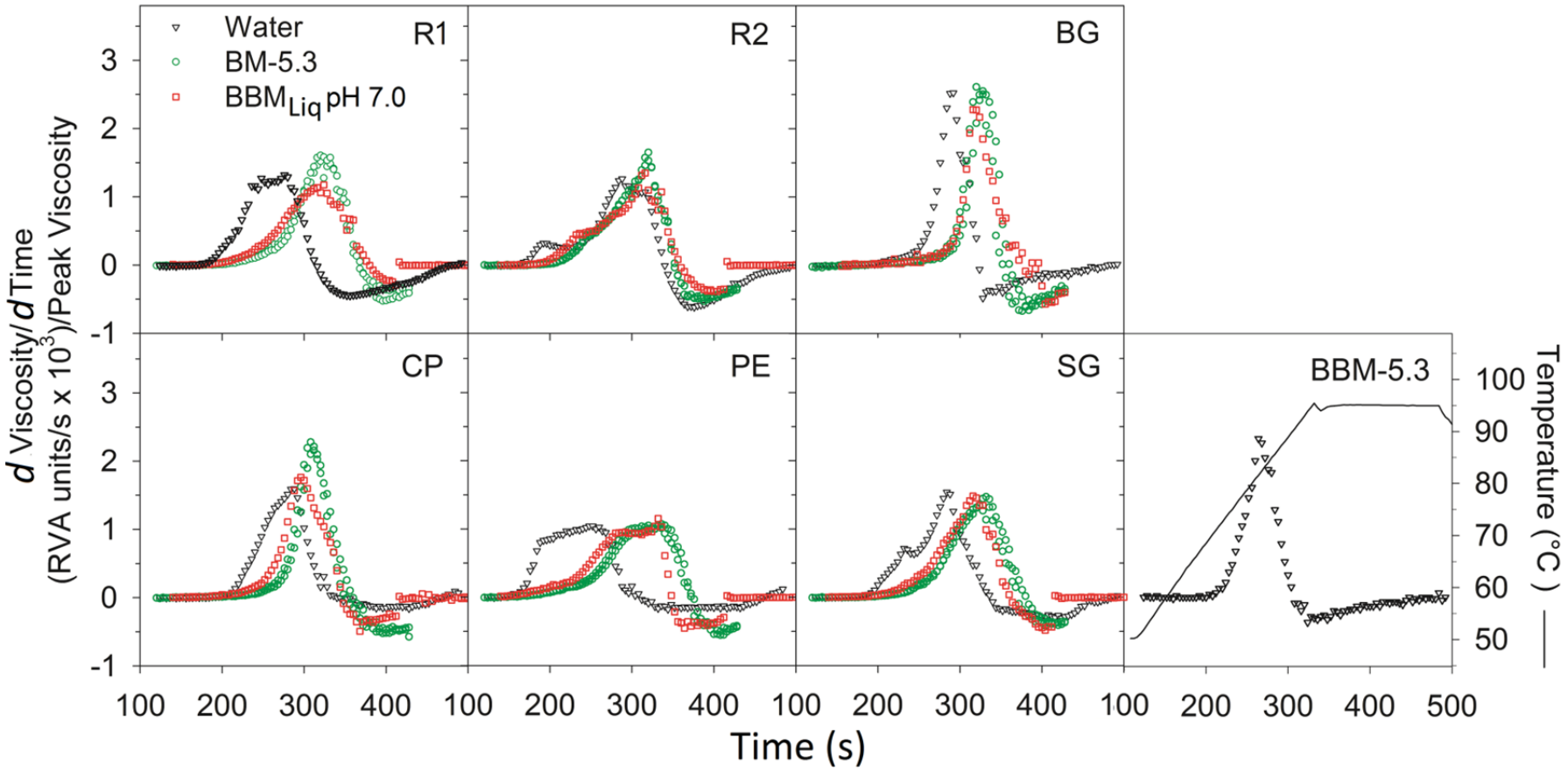

Figure 5.8 Rate of change in viscosity on RVA pasting of flours and BBM-5.3 as the 1st derivative curves. Flours were pasted with water, particulate-free buttermilk at pH 5.3 (BM-5.3), or particulate-free BBM, at 1.6% NaCl and adjusted to pH 7.0 (BBMLiq pH 7.0). Data from two independent preparations are plotted as the 1st derivative after normalisation, by dividing the rate of viscosity change between each timepoint (ΔRVA units/(time interval)) by the maximal rate of change over this period.

When Meadows (2002) pasted RI flours with varying amylose and protein content, the amylose: amylopectin ratio (which gives a rough guide to relative granule sensitivity to shear disruption) influenced the slope and complexity of the RVA pasting curve, while the effect of increasing the rice flour protein content was to shift curves to higher temperatures. Possible reasons for an extended period of starch granule swelling in idli formulations include: heterogeneity in the granule population (Puncha-arnon et al., 2008); inhibition of gelatinisation, by binding of NSP or protein to the granule surface (e.g. Gonera & Cornillon, 2002) or by competition for water; or slowed rate of water uptake into large starch aggregates, such as those in RI and SG batters.

Flour RVA PV values on pasting under batter conditions fell between 89-95 ˚C, close to the probable denaturation temperature of 98 ˚C identified by DSC analysis for BG protein. The main difference between batters is the temperature/time range for viscosification, a physical event that must significantly influence the pattern of bubble expansion during the middle and late stages of cooking. Around a quarter of the cooking process in SP formulations occurs as steaming after removal from the microwave oven (Dodson, 2001). Post-cooking starch gelatinisation due to water absorption by granules from steam after bubble disruption may be a significant feature of SP microwave cooking.

5.7 Texture Profile analysis of idli structure

Mechanical testing provides information on structure organisation and the strength of the solid phase in elastomeric foams (see section 1.5.6.2). Cooked idli were tested using Texture Profile Analysis (TPA) (see section 3.7.2). Samples cut from cooked idli experienced two cycles of compression and release along the Z-axis, where deformation force on the first compression was just enough to damage idli structure. TPA force-time curves are shown for R2, BG, CP and SG idli (Fig. 5.9) and were typical of elastomeric foams. The response curves for R1 and PE idli were similar in shape to those of BG and R2 idli, respectively.

A small peak or an inflection point in the first TPA compression curve indicates an irreversible fracture in structure (*fracturability*) (Trinh & Trinh, 2009a). TPA curves for SG idli had an inflection point (arrowed in Fig. 5.9), suggesting that the SG idli formulation produces a more fragile and less elastic microstructure than other idli. By eye, SG idli had a greater proportion of very thin walls compared with other idli on µCT analysis (see Fig. 5.1), and a fractured protein-NSP domain, presumably due to the high T_g of SG proteins (see Figs 5.4 & 5.5). These factors may contribute to the fracturability of SG idli foams on compression.

TPA parameters were calculated from the TPA curves (see section 3.7.2). The TPA Hardness parameter reflects the peak force on the first compression cycle. Hardness refers to sample firmness (as maximal compression force), Cohesiveness is a composite measure of structure resistance to multiple deformations and Springiness is a measure of elastic recovery after the first compression. Chewiness is a composite parameter suggestive of resistance to chewing, Resilience a measure of structure recovery after the first compression, and Adhesiveness a measure of sample stickiness.

Table 5.3 **Temperature values at the first point of inflection (onset of granule swelling) and peak time (maximal rate of viscosification) of RVA 1st derivative data. Data in (brackets) refer to secondary peaks or shoulders. [1]As time in seconds.**

	Medium	R1	R2	BG	CP	PE	SG	BBM-5.3
	Water	3.25	3.25	4.6	4.5	4.0	3.00	
	BM-5.3	3.00	3.20	5.1	5.25	4.5	3.50	
	BBM_{Liq} pH7							
Inflection point, T_O (˚C)	Water	65.2	62.6	79.8	68.5	60.7	65.6	-
	BM-5.3	69.4	68.0	84.4	81.6	75.9	75.9	70.6
	BBM_{Liq} pH7	68.5	70.0	80.9	80.3	73.0	74.6	-
Peak (˚C)	Water	84.0 (76.8)	83.1 (67.0)	86.7	86.0	79.8	86.0 (74.8)	-
	BM-5.3	93.9	91.7	90.9	90.7	95.3	92.4	82.8
	BBM_{Liq} pH7	92.3	91.7 (75.9)	89.5	91.8	95.3	94.9	-
Time range (s)[1]	Water	137	222	140	160	172	176	-
	BM-5.3	192	190	156	178	196	196	100
	BBM_{Liq} pH7	165	190	172	170	198	197	-

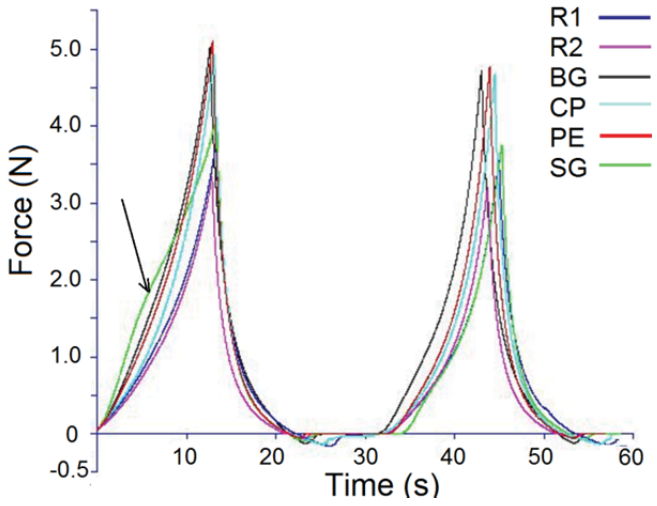

Figure 5.9 **Typical Texture Profile Analysis output plot for a two-cycle compression test on 25 mm^3 cubes of cooked idli. The arrow indicates an inflection point typical of structure fracture. Test conditions: to 50% compression with 5 s hold.**

Table 5.4 TPA parameters measured at 24 h after storage in a sealed pot at 20 ˚C, n = 12 ± SD. Values in the same column with different letters are significantly different according to Tukey's test (p < 0.05).

	Hardness	Springiness	Cohesiveness	Resilience	Chewiness	Adhesiveness
R1	4.83 ± 0.95 a	0.94 ± 0.05 a	0.76 ± 0.05 ab	0.40 ± 0.00 a	3.45 ± 0.63 ab	-0.19 ± 0.08 ab
R2	3.54 ± 0.62 b	0.94 ± 0.05 a	0.78 ± 0.02 ab	0.40 ± 0.01 a	2.62 ± 0.45 c	-0.39 ± 0.13 c
BG	4.83 ± 0.95 a	0.94 ± 0.05 a	0.76 ± 0.05 ab	0.40 ± 0.00 a	3.45 ± 0.63 ab	-0.19 ± 0.08 ab
CP	4.59 ± 0.81 a	0.89 ± 0.03 bc	0.75 ± 0.04 b	0.35 ± 0.02 c	3.04 ± 0.51 bc	-0.12 ± 0.08 a
PE	5.81 ± 1.06 c	0.91 ± 0.03 ab	0.73 ± 0.03 b	0.34 ± 0.02 c	3.75 ± 0.58 a	-0.17 ± 0.1 ab
SG	6.08 ± 1.17 c	0.87 ± 0.05 c	0.60 ± 0.03 c	0.25 ± 0.01 b	3.12 ± 0.65 bc	-0.21 ± 0.14 ab

The magnitude of the TPA data (Table 5.4) indicated that idli had a more elastic and cohesive texture than muffins made with resistant starch and tested using a similar TPA protocol (Sanz, Salvador, Biaixauli, & Fiszman, 2009). Idli Hardness increased in order R2 < CP ≈ BG = R1 < PE < SG. SG idli were firm on compression and had the least recovery of structure. R2 idli were significantly softer, more cohesive and stickier than other idli, including R1 idli.PE idli, which contained the highest solid phase fraction were firmer than other idli except for SG idli. Considering the wide variation in idli mesostructure and microstructure, the response of idli on TPA compression testing did not vary greatly apart from R2 and SG idli, suggesting that soon after cooking the elastomeric protein-NSP gel makes a greater contribution to foam mechanical response than the starch domain or void organisation.

5.8 Relationship between idli wall thickness and void size distribution

5.8.1 Idli wall thickness distributions

Idli wall thickness was determined by Local Thickness analysis of µCT image slices (Fig. 5.10 left). The slopes of the wall width curves increased in order R1 ≈ R2 < SG < BG < CP < PE; a lower slope value correlated with a broader wall width range. Table 5.5 lists quartile values for wall thickness distribution and the parameters for a Weibull 5-parameter curve that fitted best to the cumulative width data, using SigmaPlot 11 (Systat Software Inc. San Jose, US) (Appendix D 11.3). The Weibull equation generates an S-shaped exponential distribution with rapid increase and decrease at curve ends. Weibull probability functions are used for time-dependent processes and particle size distributions. Weibull parameters x_0 and y_0 relate to the curve inflection points, *a* gives the plateau value of the fitted curve (cumulative volume), while *b* and *c* define the slope. The corresponding void volume cumulative data did not fit readily to a single type of distribution curve, reflecting the more complex multimodal void distributions (Fig. 5.10 left).

The wall thickness distribution curves for R1 and R2 idli were almost identical. CP and PE cumulative wall volume curves overlapped at small size, but diverged at larger sizes. Maximum wall thickness in idli, at 120-150 µm, could be attributed to the presence of large BG bean fragments at the intersections between multiple bubbles, and was most obvious in CP and BG idli microstructures.

Compared with CP idli, which had a low volume of wall material (259 ± 3 mm^3/cm^3, a in Table 5.4) PE idli had the highest wall volume (334 ± 2 mm^3/cm^3). CP and PE uncooked batters shared similar multiphase batter flow behaviour and response to flour hydration and foam expansion. The marked

difference in wall volume can be attributed to extensive swelling of the starch domain in PE batter, vs. limited swelling of CP starch granules. The low value for CP idli wall volume was close to values for R1 and R2, even though RI flours contained a broad particulate size distribution and CP flour had few larger granule aggregates. This suggests that expanded flour particulates in set RI idli batters were optimally packed into channels and intersections between bubbles (polydisperse packing efficiency in RI batters vs. bimodal packing of many small CP granules with a few large CP particulates and BG bean fragments). The overlap in BG and SG cumulative wall volume curves, where SG microstructure contained large particulates and BG did not, suggests that the increased content of soluble biopolymer in the liquid phase of BG and SG batters which produces viscoelastic behaviour must also increase the mass (and phase volume) of set elastomer. The shallower slope for the SG distribution curve below 0.050 mm width is consistent with a more rapid rate of increase in the wall thickness than in BG idli, suggesting a contribution of SG particulates in limiting the proportion of very thin walls.

The disconnection between the patterns of wall and void size distributions (Fig. 5.10 left vs. right) suggests that the controlling factors for foam formation and wall thinning are independent to some extent. R1 and R2 idli, for example, were almost identical in wall thickness distribution but dissimilar in void width distributions (Fig. 5.10 left). This suggests similar constraints and mechanisms control wall thinning in RI batters, but different mechanisms control RI bubble population dynamics.

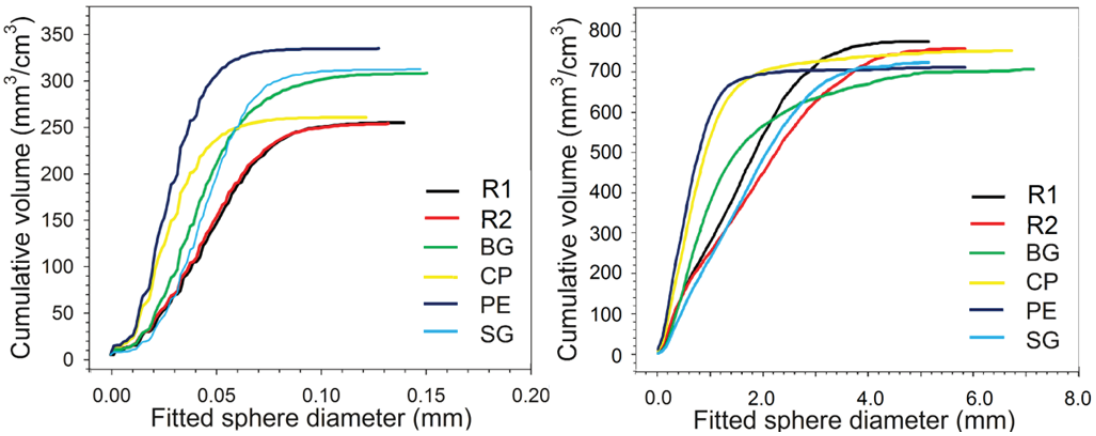

Figure 5.10 Cumulative volume data in cooked idli for wall solid phase (left) and for void gas phase (right), determined by ImageJ Local Thickness analysis. Distribution curves finish at the value of the largest fitted diameter.

Table 5.5 Quartile size class values and Weibull curve fitted parameters (R^2 > 0.999, curve fitting in SigmaPlot 11 ± SE of fit) for wall thickness distributions shown in in Fig. 5.10.

	Wall thickness (µm)				Weibull curve parameters				
	Q_{25}	Q_{50}	Q_{75}	Q_{100}	a	b	c	x_0	y_0
R1	23	35	48	120	253 ± 2	0.0372 ± 0.0016	2.06 ± 0.09	0.0353 ± 0.0002	0.32 ± 2.2
R2	23	35	48	117	252 ± 2	0.0369 ± 0.0016	2.11 ± 0.09	0.0352 ± 0.0002	0.32 ± 2.1
BG	24	33	44	127	307 ± 2	0.0249 ± 0.0008	1.44 ± 0.06	0.0329 ± 0.0002	6.29 ± 2.03
CP	17	23	31	98	259 ± 3	0.0185 ± 0.0008	1.56 ± 0.07	0.0229 ± 0.0002	4.18 ± 2.73
PE	18	24	54	171	334 ± 2	0.0203 ± 0.0006	1.58 ± 0.06	0.0253 ± 0.0001	6.55 ± 2.36
SG	27	35	46	117	311 ± 2	0.0312 ± 0.0012	2.18 ± 0.10	0.0365 ± 0.0001	2.37 ± 1.57

5.9 Design elements in idli structure development

The aim of the experimental work in Chaps. 4 & 5 was the deconstruction of SP structure development of under microwave cooking, using a non-wheat idli formulation substituted with different flours to vary product structure. A whole-formulation/whole flour study approach was chosen in place of fractionation, with the focus on attributes related to the stages in SP structure development of foam formation, foam expansion and structure setting. Synthesis of the whole-system observations produces a general analysis of the design elements which contribute to idli structure development.

5.9.1 The influence of flour components on idli mesostructure

While product volume is not influenced by the type of flour in the idli formulation, flour type does influence development of the idli mesostructure and microstructure. A useful way to correlate idli batter attributes with cooked idli structure is to compare idli pairs which share some structural features, examining similarities and differences in batter behaviour.

5.9.1.1 CP and PE idli: readily-flowing liquid phase, unconstrained bubble expansion

The smallest void size ranges for idli cooked products were in CP and PE idli. The timing of rapid batter viscosification can be ruled out as the critical factor for determining void size, as it began at low temperature and extended over a long period in PE batter, but began at high temperature and finished rapidly in CP batter. Significant numbers of stable bubbles were introduced on CP and PE flour particulates during flour hydration, along with an increased gas phase volume from entrained air. Uncooked CP and PE batters expanded 20-30% more on BiC addition than other batters, due to ready bubble expansion within the non-gas phase. BiC addition initiated preferential expansion in larger existing bubbles over an increase in bubble number density. As a result of the greater gas phase volume, coalescence events became more common by 5 min after BiC addition, as based on the bubble distribution shape.

The cylindrical, even shape of CP and PE idli supported an even process of macrostructure expansion on cooking. Even expansion and minimal convection during foam expansion and setting is critical for foam-based Food-Ink formulations. However, a gradient of increasing void size/decreasing void number along the Z-axis in CP and PE cooked idli was consistent with liquid drainage in the batter foam before structure setting, indicated the development of an uneven foam mesostructure in these idli. The common factors determining the narrow size void range are the high initial bubble number and gas phase volume at the start of CO_2-driven foam expansion, and the preference for CO_2-driven expansion of bubbles > 0.10 mm, with lower surface tension and a lower energy barrier to expansion than smaller bubbles (compare –BiC and +BiC individual size class plots in Fig. 4.9 bottom).

CP idli voids appeared more irregular in shape than PE voids. Bubble expansion in CP batter continued to a higher temperature before viscosification, so that bubbles had longer to expand, coalesce and migrate during the cooking period. The less-distorted spherical shape of PE voids, even larger voids produced towards the end of cooking, together with the greater heat stability of PE foaming fractions, suggest that Γ_{Bubble} in PE batter was stabilised more effectively to the point of structure setting (see section 5.3.5in PE batter).

In the CP microstructure individual starch granules were poorly expanded and the protein-NSP domain was dominant. The high lipid content of CP flour may inhibit starch polymer leaching from CP granules by free fatty acid complexation with extruding starch polymers (Zhang & Hamaker 2003; Raphaelides & Georgiadis, 2007), reducing CP granule swelling during gelatinisation. Starch granules were at low enough concentration that the lower limit of wall thinning was not greatly constrained to the width of individual granules, but could thin further than in PE batter during foam expansion

A continuous amorphous starch domain filled most of the PE idli microstructure was derived from the expansion of many mobile disk-shaped starch granules that packed the liquid phase in PE batter. Rapid batter viscosification began at lower temperature in PE batter and was also spread out over a longer period. This suggests that during wall thinning on foam expansion PE granules swelled slowly to fill all the possible space in between-bubble channels and intersections. PE granules lining the voids could also be more amenable to water uptake from steam in the void space, extending the period on microwave cooking for granule expansion. The standing period after microwave cooking (post-microwave steaming) is considered an important part of microwave cooking (Dodson, 2001).

For Food-Inks with foam structure that undergo post-deposition expansion, the design target of minimal voxel distortion requires that the foam structure has the smallest possible void size range while also delivering the required food texture. To produce a SP Food-Ink formulation design with small void size range, without also producing a vertical void size gradient due to liquid phase drainage as observed in CP and PE idli, requires more modelling of interactions between foam liquid phase viscosity, bubble number density before foam expansion, and the influence of particulates on void size distribution in the set foams.

5.9.1.2 RI and SG idli: many large flour particulates, low liquid phase volume

Larger flour particulates in SG and RI batters (sized between 120-250 µm in length) destabilised existing BBM bubbles by reducing the liquid phase volume available to the bubble population, and reduced bubble growth by forming physical barriers that isolated bubbles and hindered bubble coalescence. RI and SG idli exhibited a bimodal void size distribution with two distinct sub-populations (Fig. 5.2). The second sub-population became detectable on BiC addition, with CO_2–driven expansion increasing the number density of small bubbles above that of the –BiC batters. This second sub-population possibly arose due to new bubbles formed by heterogeneous nucleation at flour particulate cavities in response to a higher concentration of solubilised CO_2 in the reduced volume fraction of liquid phase.

Alternatively, there may have been preferential maturation of previously undetected microbubbles due to the increased energetic cost of expansion for larger bubbles when physically constrained by surrounding large particulates. Physical partitioning of bubbles in early foam expansion by large flour particulates (which increases the diffusion path for solubilised CO_2) may also encourage bubbles to develop independently in all size categories on BiC addition, compared with the lack of increase in bubble number density at small size observed in pulse flours. However, more experimentation is needed to clarify the predominant mechanism(s).

The batter attributes associated with a bimodal distribution and appearance of new bubbles are:

the reduction of the liquid phase volume by adsorption onto flour particulates during hydration; a particulate size/mass that inhibits bubble expansion below some critical size and bubble-bubble contacts leading to coalescence; and the presence of large particulates with cavities that may enable heterogeneous nucleation on CO_2-driven bubble expansion. A bimodal void distribution in cereal batters is not a useful attribute for SP Food-Ink formulations.

SG idli voids had a narrower void size range than RI idli. This is consistent with the behaviour of bubble growth models in which increasing viscoelasticity of the medium produces a narrower final size distribution (Bikard et al., 2008). The outcome also depends on the range in bubble sizes present before gas-driven expansion. In a three-bubble model of growth with large and small bubble size, increasing medium viscoelasticity broadens the size differences in the final distribution (Everitt, Harlen, & Wilson, 2006c).

Larger voids were even and ellipsoidal in RI idli and more irregular in shape in SG idli. The return to spherical shape after events such as coalescence in SG batter would be slower due to the longer relaxation time of the viscoelastic medium. If bubble coalescence occurred late in cooking, then partial setting of material surrounding distorted bubbles would also maintain bubble distortion.

The partitioning of flour particulates in channels and intersections between bubbles during bubble expansion will be modulated by 1) the viscosity of the liquid phase, and 2) the size range distribution and concentration of granules and other particulates within the non-gas phase. RI batters had a less viscoelastic liquid phase and a greater %volume of smooth rice surface grain cells. Particulate shape may contribute to the ease of bulk particulate flow in dispersions (e.g. see section 2.9.3.3). Large, smooth, ellipsoidal rice surface grain cells would be predicted to move past each other more readily than more angular large SG starch composites during rapid foam expansion and wall thinning on microwave cooking. If larger RI particulates were swept readily into intersections between bubbles in preference to being trapped in channels, compared with more irregular SG particulates of similar size in a more viscoelastic liquid phase, this would produce a broader wall size range in RI idli than in SG idli, as observed in Fig. 5.10 left.

5.9.1.3 BG and CP idli: predominant protein-polysaccharide domain and limited starch granule swelling

The protein-NSP domain dominant in the microstructure of both BG and CP idli was able to set SP structure successfully even in the absence of an extensive starch domain. The probable mechanism is the late onset on heating of BG and CP starch granule gelatinisation compared with other batters, which limits the time period for granule swelling, starch polymer extrusion and starch network formation before protein denaturation sets the foam structure.

BG batters effectively carry more BBM structuring capacity than other batters, perhaps more than two-fold more based on the greater solubility of components from BG flour compared with soaked BG bean. The void size distribution in cooked idli was monomodal for BG idli, while CP idli had a shoulder suggestive of bubble coalescence at larger size (Fig. 5.2 top), and a broader cumulative wall thickness distribution (Fig. 5.10 left). The gel-like BG batter liquid phase (which contained additional BG bean components from BG flour) trapped bubbles in place, while bubbles in CP batter liquid phase had ready

movement. The viscoelastic yield-stress liquid phase in BG batter was more effective in stabilising bubble expansion and limiting bubble coalescence, with greater resistance to wall thinning on rapid foam expansion, and so was able to retain a log-normal size distribution with minimal coalescence in the cooked products.

A SP structure with predominant protein-NSP domains and limited starch domains may increase the intensity of colour from added dyes, as many food dyes have high affinity for protein. Isolation of the BG protein-rich domain as a food ingredient may provide an uncoloured, yet opaque medium for Food-Ink dye addition that can stabilise heat-set Food-Ink foams. However, highly viscoelastic fluids are not suitable for extrusion-based 3D printing.

5.9.1.4 BG and SG idli: viscoelastic medium modulates bubble growth and shape

The cumulative wall size distribution was similar in both BG and SG idli (Fig. 5.10 left). On modelled bubble wall thinning in viscoelastic polymers, Yue, Feng, Bertolo & Hu (Yue et al.) identified that "…viscoelasticity is shown to initially enhance film thinning but later resist it… polymer strain-hardening, namely the steep increase of extensional viscosity with strain, helps stabilize the foam structure by suppressing bubble-bubble coalescence and bubble burst at the foam surface". Maximal reduction of wall thinning in Yue's model occurred when the viscoelastic relaxation times for both initial fluid flow and for the development of fluid resistance to extensional shear (strain hardening) fell within the timeframe of bubble expansion.

In contrast, the cumulative void size distribution of SG idli was most similar to those of RI idli, while that of BG idli had more similarity to other pulse idli, but with a broader distribution and more voids > 2 mm diam. (as assigned on FOAMS analysis). Where larger SG voids in cooked idli were irregularly distorted, BG bubbles were generally ellipsoidal in shape. A mechanism can be proposed to account for the greater sphericity of BG voids compared with SG voids. Before cooking, the frequency of bubble-bubble interactions leading to coalescence was markedly reduced by the gel-like BG batter liquid phase compared with bubble interactions in SG batter. Infrequent very large bubbles were observed in BG batters on physical handling during flour addition. The high viscoelasticity of the BG batter would encourage growth of pre-existing larger bubbles by disproportionation rather than by growth and eventual coalescence of medium-sized bubbles. In comparison the incidence of distortion as a result of coalescence late in cooking was more frequent in the less viscoelastic SG batter.

In more viscoelastic SP batters a detailed analysis of batter response on extensional shear to identify liquid phase relaxation times is needed to explain how this aspect of the multiphase batter may modulate void organisation and wall thinning.

5.9.1.5 R1 and R2 idli: similar composition, differing component behaviour

The compositions of R1 and R2 flours were very similar on analysis. R1 and R2 batters produced identical wall width distributions, but R2 idli had a broader void size range than R1 idli (Fig. 5.10). R2 starch aggregates in the idli microstructure appeared to have greater integrity and to be less amorphous than those in R1 idli, consistent with the presence of more intact granule composites and rice grain surface cells in the cooked microstructure. R2 flour was ground more coarsely than R1 flour, with a lower %volume of smaller particulates (i.e. reduced particulate number density in batter). Flour

fragment size (or a decreased proportion of intact rice surface grain cells) may have a marked influence on void size development. R2 flour also produced fewer detectable bubbles on hydration in BBM. The period of rapid batter viscosification was more extended in R2 batter than in R1 batter (Table 5.3), and bubble expansion may have continued for longer before R2 structure set. A decrease in expected void number density (as assigned by FOAMS analysis) at large void size suggested a higher incidence of bubble collapse in R1 idli compared with R2 idli during cooking (Fig. 5.2, number density plots).

On texture analysis R2 idli were significantly softer, stickier and more elastic than other idli, including R1 idli. Flour components can modulate the robust elastomeric gel produced on BBM setting. It is probable that differences in minor protein components of the non-starch fraction in R2 flour contributed to the textural differences between R1 and R2 idli; these may also have contributed to differences in foam stability between the two RI flour batters.

5.9.2 Summary of flour component influence on idli mesostructure

Flours contribute a number of structuring functions to modify the mesostructure of the BBM fraction under microwave cooking:

- Flours with small flour particulates introduce a significant fraction of entrained air, increasing the number of detectable bubbles on flour hydration. When the liquid phase viscosity is low, these batters produce small voids with narrow size distribution, with preferential CO_2 partitioning into existing bubbles on foam expansion. Flours with large flour particulates with high hydration requirement reduce initial bubble number and inhibit bubble expansion. They produce a bimodal void distribution on BiC addition, with an increased number density of small bubbles. This bubble sub-population is possibly newly formed by heterogeneous nucleation.
- Soluble proteins and NSPs which increase the viscoelasticity of the liquid phase encourage a more even void size distribution, but at broader wall size range than batters with readily-flowing liquid phases.
- The pattern of bubble distribution in batter is retained in cooked idli void populations. This may be due in part to the short timeframe for foam expansion and structure setting during microwave cooking of small volumes of idli batter.
- Modification of void shape (towards or away from energetically optimal spherical shape) depends on the presence of heat-stable surface-active components, on the relaxation time of the liquid phase compared with foam expansion, and on the relative timing for bubble coalescence and for setting of the liquid phase.

5.10 Summary of events in idli structure development

This deconstruction of a non-wheat, non-baked SP system examined a resilient SP structuring system which was able to produce a successfully expanded SP in the absence of added NSPs, wheat gluten or egg protein, and in the presence of flours with a wide range of protein and starch content, starch gelatinisation temperature and content of surface-active components when substituted at the same ingredient ratios.

The idli batter formulation used in this study generated initial batter bubble populations during two

stages of bubble formation, wet-milling and entrainment on flour particulates. The timeframe for these two stages was long enough for surface-active components in BBM and flour to hydrate, and to equilibrate at the bubble interface. Rapid expansion at the +BiC/cooking stages pushed bubble populations far from equilibrium, possibly generating a third stage of bubble formation in cereal batters by heterogeneous nucleation at particulate cavities.

Idli foam expansion occurred over a short period when compared with expansion times during traditional baking and steaming. The void populations in the cooked idli retained size distribution features observed in the corresponding batter bubble populations. Therefore mesostructure development under rapid microwave cooking of batter systems can be manipulated by controlling bubble population dynamics in the batter. A similar correlation has been reported between bubble distribution in proved wheat-bread dough and the mesostructure organisation of the cooked bread (as quantified by μCT analysis) (Babin et al., 2006), even though idli microwave cook time is much shorter than on baking and internal spatiotemporal temperature-moisture gradients also differ on microwave cooking.

This study differentiated between the introduction of idli batter bubble initiation sites by shearing of incorporated air, as air entrained by and on flour particulates, and possibly as heterogeneous nucleation in the presence of CO_2-driven expansion. While flour components reduced the detectable bubble population in some batters, the addition of BiC overcame any initial reduction in detectable bubble number density, although there was evidence of disproportionation/shrinkage. Bubble size and number density distributions converged in overall shape during expansion, suggesting a common process of bubble growth in the idli batter system.

5.10.1 The blackgram-buttermilk fraction determines idli cooked volume

The most important observation in the deconstruction of idli batters under microwave cooking was that all batters reached a similar cooked volume despite significant differences in batter protein and starch content, batter flow behaviour, the temperature of structure setting, and the proportion of the starch domain in the cooked microstructure. Based on the current knowledge of ingredient functionality in SP formulations, these differences would be expected to markedly influence the cooked product structure. The common factor for this consistent behaviour was the non-starch component of BG bean. BG structuring function was not affected by switching between flours with high starch-low protein contents (RI and SG flour) and high protein-medium starch contents (CP and PE flour). A five- to six-fold difference in batter resistance to flow had little overall effect on cooked product volume, as did doubling the content of BG components. This consistency of behaviour was also observed in the convergence of bubble gas phase volume size distributions on BiC addition.

The gluten network that supports foam expansion in wheat bread production is developed by hydration, extensional deformation combined with shear deformation, and enzymatic and redox-assisted breakage and reformation of protein-protein bonds in a complex time- and work-dependent process (Joye, Lagrain, & Delcour, 2009). The stiffness of wheat-bread dough is very sensitive to water content: for dough at 43% water content, storage modulus at low amplitude oscillatory shear was modified two-fold by a difference of ± 2% in water content (Phan-Thien & Safari-Ardi, 1998), significantly

altering dough expansion on proving and baking. A difference in the wheat dough hydration level also alters the accessibility of surface-active compounds and solubilised gas molecules to the bubble interface. Finally, water molecules become strongly associated with gluten proteins, so that small differences in flour hydration significantly affect the amount of free water available for starch gelatinisation and other processes during structure setting.

Idli batter is not sensitive to flour hydration levels compared with bread dough. The similarity in water activity measured for idli batters suggests that additional soluble proteins introduced on flour hydration do not greatly affect the tightness of idli batter water-binding capacity. Based on the effective structure setting in all idli batters, even in high-viscosity idli batters the water associated with soluble proteins and NSPs in the idli batter liquid phase is not tightly bound and remains available for key transformation events during structure setting. The high temperature of BG protein denaturation also increases the flexibility of the idli formulation to added starch type, by increasing the temperature range over which starch granule swelling can occur for successful structure setting.

In comparison with wheat gluten system, idli batter does not depend on work to develop structure in the non-gas phase, only to introduce air into the batter, giving a formulation that is much more resilient to conditions of work, standing time and water content. The idli formulations encompass a liquid phase viscosity flow behaviour ranging between that of low-viscosity, readily draining wheat-flour cake batters and higher viscosity stiff wheat-flour doughs within a single system that maintains very similar cooking behaviour across the formulations.

In the presence of a reasonable content of blackgram bean soluble components, and with adequate content of starch granules to take up excess water from the liquid phase within the temperature range of BG protein denaturation, the expansion capacity of CO_2-water vapour in the batter appears to determine idli cooked volume. In the preliminary experiment to screen flours for structure formation, substitution with potato flour, cassava flour and cross-linked wheat starch in place of rice flour did not support structure setting (data not shown); therefore properties of the starch granules also determine flour suitability as a setting agent in the idli formulation.

The role of the BG fraction is to form and stabilise the foam. It also sets into a continuous protein-NSP elastomer that holds the starch fraction in the cooked idli microstructure - it can be a dominant or a minor volume-filling domain in the idli composite microstructure without greatly altering the mechanical properties of the cooked product soon after cooking. It is probable that globulin proteins which contribute to the foaming capacity of the BBM fraction are also important for formation of the elastomeric protein-rich gel on structure setting. In wheat-flour doughs, the structure-forming gluten proteins are not reported as contributing the major surface-active proteins in wheat dough. However, SP formulations containing egg proteins may have protein components that contribute to both interface functionality and gel formation.

In studies of partial substitution of pulse flours into SP formulations made with cereal flours, the high protein content of the pulse flours affected both foam-forming activity and water relations (e.g. De la Hera, Ruiz-París, Oliete, & Gómez, 2012; Gomez et al., 2008 ; Marco & Rosell, 2008). In the idli system, soluble BG protein and NSP (and possibly BG saponins) first saturate the foam interface before surface-

active components from flours are added. Additionally, batter pH conditions favour the solubility of BG surface-active proteins. This initial saturation of the interface by BG components and the synergistic interaction between BG proteins and NSP may be the main factors which determine the flexibility and robustness of the idli formulation when substituted with markedly different flours.

5.10.2 Product architecture of the idli formulation under microwave cooking

The idli results identified several distinct physical design elements (ingredient chunks) which contribute to sub-elements of the three functional elements of foam formation, foam expansion and structure setting in SP design.

- The physical element 'wet-milled blackgram-buttermilk' is a multifunctional design chunk. It controls foam formation and foam stabilisation during expansion and heating (the functional design element 'foam control'). It also contributes a late-setting protein-NSP domain in the product microstructure that is compatible with a range of starch sources ('cooked elastomeric gel').
- The physical element 'flour' is a design chunk that introduces air entrained on particulates, adds soluble viscosifying agents to the batter to modify liquid phase viscosity, adds particulates to the gas-liquid-solid dispersion to modulate bubble size distribution, controls the timing of rapid batter viscosification, and contributes starch domains to the product microstructure (contributes to 'foam control', and determines 'structure setting').
- Salts, bicarbonate ions and organic acids in solution at specific concentration, plus the water content of idli batter, form a physical element that controls the rate of microwave heating, modulates timing of rapid viscosification by controlling water availability, and determines the degree of product expansion ('CO_2-H_2O heating rate and expansion control').

Note that wet-milling, an external, non-formulation structuring operation, is essential to provide the initial aeration necessary for successful product expansion. The robustness of the BG structuring system shows promise as a source for producing ingredient fraction for non-wheat formulations.

The novel observations in Chaps. 4 & 5 defined the contribution of non-wheat flour soluble components to SP bubble population dynamics during foam expansion and to cooked SP product microstructure, and identified roles for flour particulates in modulating SP structure. Chap. 6 evaluates the information from this SP system deconstruction (Chaps. 3, 4 & 5) together with the analysis of multiphase fluid flow requirements during extrusion-based AM (Chap. 2) within the context of the Food-Ink design process.

Chapter 6. Overall summary and conclusions

6.1 Study components

The overall aim of this study was to contribute to the design of Food-Ink formulations which produce an embedded image by voxel formation, colour-matching and deposition using the Food-Inks 3D printing system. The first prototype product target was for an unsweetened bread- or cake-like food (sponge product, SP) with post-deposition foam expansion and structure setting. Chap. 1 summarised Food Layered Manufacture, a new field in the manufacture of food solids, and applied product design tools to identify and prioritise the design sub-tasks. A summary was made of events during structure development in SP food foams. Prioritisation of design sub-tasks at the start of the study identified that control of SP foam expansion and setting would have the greatest impact on the fidelity of the 3D printed image (see Table 1.3). The primary research aims of the study were to define the requirements for control of structure formation in SPs within the context of Food-Ink formulation design, as well as the requirements for control of flow during piping, mixing and voxel deposition in the extrusion-based Food-Inks 3D printing application.

Chap. 2, the first experimental part of the study, examined Food-Ink flow behaviour in relation to the application requirements at different stages of printing and after deposition. As the design of printer pumping, mixing and deposition systems remained unfinalised, the section on structure formation in SPs formed the greater part of the study. To support the SP formulation experimentation, appropriate test systems were identified for the formulation and cooked product attributes most relevant to the key events on SP structure development (Chap. 3). These were supported by digital image analysis methods developed to quantify foam structure (Appendices D & E). Chaps. 4 & 5 deconstructed the development of foam structure in a non-wheat SP under microwave cooking. The non-flour blackgram-buttermilk fraction was the primary influence on foaming capacity and foam stability in uncooked batters, and determined the degree of product expansion. Flour type defined foam organisation in the cooked product, influencing bubble number density and size distribution in uncooked batters, and determining the timing of batter viscosification.

6.2 The design task

The design of printing materials is an integral part of the equipment design process for Additive Manufacturing and Food Layered Manufacture. The aim of the simplest 3D printing process is to form and set a 3D object from a digital file, with no positional variation in the deposited material. For the Food-Inks 3D printing application, the requirement for precise positioning of colour-matched voxels, at considerably higher resolution than most food structuring tasks, increases the complexity of the design task. Deposited voxels must maintain position after deposition until the printed object sets. The first prototype Food-Ink product target, a bread- or cake-like SP, increases the design complexity further. The Food-Ink must now produce an expanding foam structure that retains the fidelity of the embedded image until the structure is set in an additional heating step after deposition. Additionally, in SP production the foam expands during structure setting in a temperature- and time-dependent manner,

modifying not only the shape of the deposited form, but potentially also the initial position of voxels within the deposited material. With each level of complexity the number of design sub-tasks increases, and the sub-task priority changes within the overall design task.

The experimental work in this study was planned to support a SP Food-Ink prototype product. It also delivered more general conclusions about constraints for extrusion-based AM using structured fluids, and on ingredient components (design 'physical elements') which contribute structuring operations (design 'functional elements') that determine the final foam organisation of non-wheat SPs under rapid microwave cooking. The study conclusions therefore discuss the following topics in separate sections:

- Test systems for extrusion-based AM of food pastes and gels, and for SP formulation design.
- Flow behaviour of structured fluids on extrusion-based AM, identifying design considerations for 3D printing equipment and for formulations to produce a continuous or discrete stream of food material.
- Mixing and deposition of colour-matched voxels to produce a 3D edible image using the Food-Inks 3D printing application.
- Formulation design for manipulation of SP structure in a non-wheat SP produced by microwave cooking, and the relevance to the control of structure development in generic SP formulations.
- Summary of constraints in the prototype Food-Inks 3D design task, and suggestions for further design approaches based on the understanding developed in this study.

6.3 Test systems developed for this study

Chap. 1 listed quality factors determining the characteristics needed for the Food-Ink SP prototype formulation design (Table 1.1) and suggested possible tests to benchmark each quality factor. This section suggests appropriate functional tests for fluid flow behaviour and setting properties in a prototype Food-Inks formulation.

6.3.1 Modelling flow properties of structured fluids

The study examined general flow property requirements related to an extrusion-based AM technology which deposits a thread of structured fluid material; and also the flow properties of model structured fluids based on the prototype SP Food-Ink design target.

The following models were most relevant to the study aims:

- Rheological models for structured fluid flow behaviour at the initiation of flow at the start of pumping and rapid cessation of flow after deposition.
- Pipe flow models for structured fluids, including outlet flow.
- Models for the behaviour under flow of two-phase (liquid-particulate; gas-liquid) and three-phase (gas-liquid-particulate) structured fluids.

For extrusion-based AM the extrusion thread diameter, which determines print rate and print resolution, is the critical parameter that determines the choice of fluid flow model and defines the constraints on equipment design. Design specifications for the Food-Inks 3D printer place the scale for modelling between the scale for biofabrication and that for classic pipe flow models used in food manufacturing - the knowledge space is poorly filled at this scale. The time limits set by a point-of-sale

requirement also influence the solution space for flow models.

Looking at multiphase SP formulations, the question of interest ("how do particulates, bubbles and the liquid phase interact to modulate cooked product mesostructure?") is similar to that in volcanology, which seeks to predict 'batter' flow of lava from the 'cooked' lava rock structure. Suitable tools for modelling multiphase fluid flows are only just in development. Rheological tests for particulate-containing polymer dispersions were poorly represented in the scientific literature, and industry-oriented publications provided the most comprehensive information on suitable models for liquid-particulate dispersion flow behaviour. As open-source software solutions for modelling aspects of multiphase flows are now being developed and shared (e.g. OpenFOAM® and CFDEM®) computational 3D modelling of multiphase fluids may provide the best option for predictive modelling of flow behaviour in multiphase Food-Inks and materials for extrusion-based AM.

6.3.2 Analysis of structure development in sponge product formulations

The optimal testing regime to follow structure development during SP preparation is a combination of high-resolution imaging to observe real-time changes in mesostructure in batter and dough during preparation and cooking, coupled with sampling during cooking to monitor changes in mesostructure and microstructure attributes. In this study equipment constraints, together with the variability in product heating rate on microwave cooking, limited the study to observation of SP structures before and after cooking and to indirect tests of batter flow behaviour, foaming properties, and structure setting. The flours substituted into the formulation generated enough structure variation to allow interpretation of the behaviour of the idli system, and to deconstruct the influence of flour and non-flour components on the development of cooked product mesostructure and microstructure.

The methods developed for quantification of batter bubble population dynamics and of void organisation in the cooked product, combined with imaging of cooked product microstructure, provided critical insights into the influence of batter components on structure development. The preparation of SP light microscopy sections by cryo-sectioning with minimal fixing and staining, a method reported in only two publications, produced more detailed information of the microstructure than generally-reported images produced by electron microscopy or confocal scanning light microscopy. The methods used to characterise bubble and void populations, including bubble measurement by light microscopy, and x-ray microtomography imaging, are low-cost in comparison with electron microscopy and confocal scanning laser microscopy and are simple to perform, although post-acquisition image analysis is time-intensive and would benefit from automation.

Bulk property measurements, such the apparent viscosity of multiphase batters and flour pasting responses, could be interpreted correctly only within the context provided by observation of quantification of features in batters and cooked products.

Indirect test methods for SP attributes are well-characterised for Western-style baked wheat-flour SPs; many SP studies apply these tests to non-wheat systems without optimisation and without validating studies to link an indirect test on an isolated ingredient with the ingredient functionality under formulation conditions. A good example is the analysis of starch gelatinisation in flours using the

RVA pasting system, which few studies of non-wheat SP formulations optimise for flour content. Additionally, pasting in non-wheat systems should be carried out with the liquid phase conditions and flour handling approximating those experienced by flours in the SP formulation, as batter/dough components greatly affect local water availability during starch gelatinisation.

Optimally, testing approaches for analysis of poorly-characterised SP systems should have these features:

- To interpret the influence of formulation components on mesostructure development, a systems approach should be applied to examine each stage of foam formation, foam expansion and structure setting.
- Bulk property tests (e.g. flow behaviour, batter density) and indirect tests must be supported by visual observation of ingredient interactions.
- Unless a clear association is validated between an indirect test on an ingredient and the target cooked product quality factors, testing conditions should approximate those in dough/batter as closely as possible.

6.3.3 Comprehensive test system for structure development in sponge products

Based on the results of this study, a minimum list of tests on dough/batter and cooked product to enable a comprehensive analysis of SP structure development is proposed. For poorly-characterised systems, fractionation studies, such as those carried out by Susheelamma's group on the idli system, may be also need to be done. Items in [brackets] are preferable, but less critical.

A. Attributes of uncooked dough or batter, or appropriate fractions, under conditions as close as feasible to those on preparation:
    a. Volume fraction of solid, liquid and gas phases at all stages of preparation.
    b. Changes in formulation pH and dough/batter titratability at different stages of production.
    c. Bulk rheology under rotational and oscillating shear deformation.
    d. Foaming capacity and foam stability of liquid phase.
    e. Bubble population dynamics at all stages of preparation.
    f. [Individual flow behaviour analysis of fractionated liquid fraction, deaerated particulate-liquid phase].
B. Attributes of dough or batter (or appropriate fractions) during cooking, under conditions as close as feasible to those on preparation:
    a. Heating rate, water loss and expansion on cooking.
    b. Bulk rheology on heating (given limitations of sample reproducibility).
    c. Bubble interface formation from the liquid phase, and stability before and after heating.
    d. Timing of rapid batter thickening (preferably using standard rheological geometries).
C. Attributes of the cooked product:
    a. Water content, density.
    b. Macrostructure analysis (shape and volume).
    c. Mesostructure (visual appearance of crumb, void and wall organisation by μCT).
    d. Microstructure (light microscopy of microtome sections).
    e. [Mechanical response on destructive deformation].

6.4 Flow behaviour of structured fluids on extrusion-based Additive Manufacturing

6.4.1 Evaluation of quality factors related to the design of the Food-Inks 3D printer

The multiple stages of the Food-Inks 3D printing application each have distinct flow behaviour requirements. Some are generic to an extrusion-based AM process (and extrusion-based FLM); some are specific to the delivery and stable positioning of a colour-matched voxel within an embedded 3D image, and some specific to a point-of-sale short production time concept. Chap. 1 defined a preliminary set of end user/process needs and the quality factors associated with those needs. Table 6.1 lists experimental work, model calculations and test systems for flow behaviour reported in this thesis against the appropriate quality factor identified in Chap. 1. The quality factors are arranged in the table in order of importance, firstly for a generic AM technology using extrusion of a continuous or discontinuous thread of structured fluid; and secondly for the delivery of a voxel by the Food-Inks 3D printing application which sets in correct position after deposition. Structure development during setting of food fluids may be mediated by reversible temperature change (e.g. cooling of chocolate, gelatin), chemical bonding (e.g. calcium-mediated alginate gelation) or irreversible structure transformation (e.g. starch gelatinisation, protein denaturation and aggregation).

Latter parts of this section discuss the overall impact of flow behaviour in structured food fluids on equipment and formulation design for a Food-Inks 3D printer system.

6.4.2 Requirements and constraints for extrusion-based Additive Manufacturing

6.4.2.1 Flow behaviour of structured fluids

Most food fluids are non-Newtonian and do not respond linearly to an applied force. Many carry internal structures in the fluid phase (e.g. entangled polymers) that produce a viscoelastic response on experiencing a change in shear deformation, as when pipe flow velocity changes. Particles in the liquid phase (emulsions, bubbles, and particulates such as starch granules) influence flow behaviour markedly by providing barriers to localised liquid phase flow. The flow history of a structured food fluid also influences its immediate behaviour, as fluid structures may have only partly returned to a fully rested state by the start of the next deformation cycle.

The simplest model for flow behaviour of a structured food fluid is for a non-Newtonian fluid with yield stress behaviour. The yield stress is the initial resistance within the structured fluid to changes in flow until transient fluid structures have broken down. Non-Newtonian food structured fluids are generally shear-thinning, so that as shear deformation increases, the fluid flows more readily. The exception is any food fluid containing particles at a concentration high enough to enable particle-particle jamming. Soft-jamming in food particulate systems impedes bulk fluid flow, resulting in shear-thickening, as described in this study for xanthan-salt solutions at high rice flour concentrations.

Table 6.1 Evaluation of Food-Ink flow behaviour specifications in relation to design considerations for formulation (F) and equipment (E), aligned with the appropriate quality factors identified in Table 1.1. Quality factors are listed in order of importance to the 3D Food-Ink printing application.

Quality factor	Description	Section
Extrusion-based AM deposition of a structured fluid or paste		
Correct shape of thread on deposition	Shape of pipe outlet (E)	2.5.2 & 2.5.3
	Shear rate at pipe outlet for power law fluids (E & F)	2.10.3
	Flow rate of thread deposition (E)	2.5.3
	Stop-start-STOP flow to fix voxel post-deposition (F)	2.11.3
	Die swell and oscillation at outlet for structured fluids (E & F)	2.3.4
Structure reforms rapidly	Time to recovery of structure in fluid (F)	2.11.3
	Viscoelastic fluid expansion at outlet (F)	2.3.4
Structural strength for multiple layers	Use of moulds to prevent lateral spread of printed material (E)	1.2.2
	Outlet shape influence on voxel spread (E)	2.5.3
	Determination of self-supporting behaviour (F)	2.5.1
Acceptable print time	Printer flow rate requirements to produce A5 size (E)	2.1.3
	Pressure drop and relation to outlet size, power law parameters and flow rate (E & F)	2.10.2
	Overcoming yield stress to break fluid structure and initiate printing (E)	2.9.3.5
	Avoidance of soft-jammed behaviour under high-shear deformation (F)	2.11.3
	Management of yield stress and shear-thinning flow behaviour by continuous agitation during printing (E)	2.11.4
Food-Inks 3D printing of ordered voxels		
Correct voxel shape and position	Definition of voxel size for 3D image resolution (E & F)	2.1.3
Micro-metered mixing with colour and flavor	Modelling lamination mixing of two fluids of varying volume ratios and viscosities (F)	2.14.3
	Modelling pipe flow at power law values derived for a model flour-polysaccharide dispersion (E & F)	2.10.1
	Limitations of static mixers (E)	2.14.3
	Suitability of continuous thread to deliver unmixed voxel train	2.3.1

Non-Newtonian behaviour greatly influences the mass transfer of a structured fluid on pumping along a pipe, during any mixing steps and on deposition through the outlet. In extrusion-based AM, the structuring material must be transferred from reservoirs to the point of deposition at a rate capable of producing a consistent thread of extruded material of the required shape and diameter to deliver the extrusion-printed 3D shape. Once deposited, the thread must retain shape and position until the structuring material is set.

The scale of AM piping flow falls between that for food fluid dispersions and for (non-food) filled-polymer systems at one end of the scale, events in capillary blood flow at the other. There are few published models of piping flow at the scale of interest to the Food-Inks 3D printer application.

6.4.2.2 Power requirements for pumping and extrusion

In sections 2.9 & 2.10, power law parameters derived from experimental data for a SP model fluid under shear deformation flow, together with published flow parameters for various SP batters, were substituted into simple numerical models for fluid behaviour during pipe flow. Excluding the effect of pipe friction and hydrostatic pressure, which depend greatly on equipment design, the fluid power index n and the pipe and outlet diameters have the greatest influence on the pressure required to pump and extrude a thread of structured fluid under conditions of fully developed flow. Structured fluids with greater shear-thinning capacity require less system pressure for extrusion-based AM once flow is fully developed. The pipe diameter has the greatest influence on the pressure drop across the system, increasing with decreasing pipe diameter.

As an example of design requirements for extrusion-based AM, the Fab@Home extrusion-based AM system has up to eight air pressure-driven syringe pumps driven by an external high-pressure compressed-air source, with maximum pressure of 6.9 x 10^3 MPa, and is used with tapered nozzles ranging from 0.6 0-3.0 mm i.d. at the outlet (J. Lipton, pers. comm.). Assuming no die swell at the outlet, this represents a resolution range of 6-40 dpi. When the Fab@Home was used to print freeform shapes from food materials (Cohen et al., 2009; Lipton, Arnold, et al., 2010) the displacement pumps were able to pump pastes as thick as meat pastes, Cheese Whiz, and stiff cookie dough. Pressure and flow rate settings were determined experimentally for each fluid before printing; extrusion-based 3D printers for biofabrication also require an initial print calibration to ensure that material for 3D printing behaves predictably under piping, mixing and forming.

Displacement pumps suit the Food-inks 3D printer application better than peristaltic pumps at the limit of their pumping capacity. The calibration requirement to determine pump conditions for each batch of printing fluid is inconsistent with a point-of-sale food product that needs to be produced quickly, using cost-effective equipment run by unskilled operators. Standardisation of Food-Ink flow behaviour to remove the need for flow calibration before each build remains a significant challenge to Food-Ink formulation design, and to AM using plant- and animal-derived materials in general.

6.4.2.3 Disruption and reformation of structures in fluids for extrusion-based Additive Manufacturing

When transient structures (e.g. particle networks, physically-reversible polysaccharide chain associations) form in non-Newtonian structured fluids during rest, they must be disrupted (stop-START-stop behaviour) before the fluid responds fully to an applied flow. The static yield stress is an experimentally-determined value characterising the initial fluid resistance to applied flow from complete rest. Conversely, rapid reformation of fluid structure on deposition is a critical requirement for extrusion-based AM, and is defined by the dynamic yield stress (relaxation time for stop-start-STOP flow behaviour). Disruption and reformation of structure is not instantaneous and each yield stress has an associated fluid relaxation time. Yield stress responses are also sensitive to the flow history of the fluid.

6.4.2.4 Disruption of fluid structures to facilitate material transfer during printing

Both the static and dynamic yield stress of a structured fluid influence pipe flow behaviour, the first

at the start of pumping, and the second once flow has started. A flow velocity gradient is generated during pipe flow from the pipe centreline (maximum flow) to the wall (zero flow). The gradient of flow velocity increases across the pipe with increasing shear-thinning behaviour, and decreases with increasing pipe diameter. If the net flow rate through a pipe is low enough that the velocity in a significant radius of the pipe produces a shear deformation below that of the fluid yield stress, the flow pattern degenerates into flow near the pipe centreline, surrounded by no flow towards the wall.

This effect is important for food safety considerations, if material trapped near the wall harbours microbial growth; and under conditions of intermittent flow, when fluid structure may reform in the pipe and increase the resistance of the fluid to flow on restarting (fluctuating power requirement for flow). Potential strategies for the equipment design to alleviate the effect of structure reformation during intermittent flow include:

- Optimisation of pipe diameter along the flow pathway
- Limiting the number of stop-start-stop events during printing
- Applying continual shear in reservoirs and along the flow path to disrupt fluid structure
- Use of positive-displacement pumps that physically sweep fluid from the wall during the pump cycle.

Under some situations, unpredicted flow has been reported to develop on piping food fluids, so that a thin layer of fluid lubricates the transfer of the rest of the fluid as an intact plug. While potentially useful as a strategy to control pipe flow behaviour in the Food-Inks 3D printer, this is a challenging design target, and is primarily dependent on the formulation flow behaviour.

6.4.2.5 Post-deposition development of structure in the extruded thread

After deposition the extruded thread must stay in place until the structure is fully set. Thread distortion under gravity and under the load of subsequent layers must be minimal. This self-supporting capacity depends on the apparent viscosity of the fluid at deposition and on the formation of both reversible and irreversible structure after deposition. Highly viscous fluids and pastes have much greater self-supporting potential, but also have greater resistance to pumping and mixing. The material thread should have limited spread (extensional flow outwards) and slump (distortion of deposited shape).

Slump models set a value of 100 Pa as the threshold value in formed pastes for maximal resistance to slump. There are two slump/spread timeframes for consideration. Firstly, when the XY-robotics system lays down a continuous thread of material in one layer using a zigzag pattern (see Fig. 1.3), the material already deposited constrains one side of the thread from spreading, while the far side is free to flow until the next line is deposited. The critical time period determining a suitable fluid relaxation time on extrusion of a continuous thread for this mode of deposition is the time between the start of one line across the build and the finish of the next.

A second relaxation time of relevance in the period between deposition and structure setting is associated with the spread on a deposited layer of material as a result of the hydraulic pressure of subsequent layers. When the Food-Inks 3D printer prototype and a model Food-Ink, with 1.6% xanthan-salt mixture in the liquid phase and 40% rice flour content, was used to print a continuous thread in three layers, there was some spread in the overall build at the end of the 10 min build time, but

individual layers could still be discerned. This whole-build spread can be mitigated by printing into a mould, stopping lateral flow of completed layers.

Therefore, on printing a continuous thread, as long as the build is constrained within a mould the critical consideration to retain the position of individual lines in multiple layers depends on the degree of spread in the deposited thread between the start of one line and the end of the next. Unless a thread is deposited using a square outlet profile at the outlet, the deposited material of a circular thread must spread enough to fill in the space between consecutive lines, while not encroaching into the space for the next line before it is deposited.

Rigid polymer chains in xanthan polymer solution produce a shear-thinning fluid and have a short relaxation time for structure reformation: modulating this relaxation time could be a strategy to control post-deposition spread. Around half of the pre-shear structure in a 1% xanthan-salt solution was reformed within 5 s after a round of extensive shear deformation. The relaxation time for structure reformation in xanthan-rice flour dispersions was determined, within a range of flour content appropriate to a SP formulation (i.e. able to produce a set SP structure after cooking in the presence of chemical leavening agent). Adding flour particulates did not reduce the relaxation time for structure reformation, so this is not a suitable strategy to lower the relaxation time and increase structure reformation.

Other strategies to ensure that a deposited thread retains position during the print run include ensuring structure setting shortly after forming. This may be by cooling structured food fluids: solidification of chocolate melt on cooling was used to set structure in an extrusion-based AM application. Alternatively, the use of a point-heating source to solidify a food fluid by immediate cooking at the point of deposition has been suggested as a design feature of extrusion-based FLM by both Cornell and MIT equipment designers.

Irreversible or reversible chemical cross-linking of biopolymers (e.g. calcium-induced gel formation for alginate polymers) is another strategy to set structure and maintain the build integrity. The requirement for a mixing step close to the point of deposition in the Food-Inks 3D printing application would allow for cross-linker to be added as part of the mixing process. Cross-linking is also initiated by photo-curing in some non-food 3D printing applications, and was used to set liquid egg white. For a Food-Ink based on a SP formulation however, maintaining build integrity is a separate process dependent on Food-Ink flow behaviour, as structure setting (microwave cooking) is independent of the printing process that forms the 3D object.

6.5 Mixing and positioning colour-matched voxels during Food-Inks 3D printing

The production of colour-matched voxels positioned correctly to produce a high-fidelity printed image requires additional control of extrusion-based AM.

6.5.1 Voxel formation and deposition in a single-thread extrusion process

Pipe flow generates a shear deformation gradient from the centreline of the pipe to the wall, producing a bullet shape front in the flow profile. Transfer of a train of coloured voxels within a thread of continuous thread by piping or by extrusion through an outlet is therefore impossible without voxel distortion. Even under conditions of plug flow, in which the majority of the fluid travels without experiencing shear deformation, the retention of a thin lubricating layer at the wall could trap enough coloured material to affect the colour of later uncoloured (white) voxels. Additionally, a voxel train under plug flow will be stretched unevenly on traversing bends and constrictions along the pipeline and by any intermittent change in flow rate.

For the Food-Inks 3D printer equipment design, the mixing process must therefore deliver discrete voxels, not a voxel train, and also ensure that all coloured material is removed before the components of the next voxel enter the mixer. Each voxel needs to be deposited directly from the mixer, as the introduction of any post-mixer pipe flow only reintroduces the problem of flow front distortion and retention of colour at the pipe wall. Optimal design places the mixer, material reservoirs and associated pumps to meter components into the mixer directly above the site of deposition in a fixed unit, while XYZ-movement may be introduced into the system by using a fixed deposition head for XY-axis movement and a moving platen for Z-axis movement.

6.5.2 Image resolution constraints on the Food-Inks 3D printing application

The choice of print resolution is critical in designing both equipment and Food-Ink formulations for the Food-Inks 3D printer. Product specifications at the start of the Food-Inks 3D printer project (Appendix B) set voxel volume at 270 µL, built up in five to seven layers. The choice of voxel size was based on colour matching at a ratio of 1: 10 total dye volume to structuring fluid volume, so that the voxel size was determined from the minimum volume of an individual dye to be metered into the mixer (10^{-1}-10^{-2} mL). Later recalculation reduced the voxel volume to between 16-132 µL, equivalent to voxel width of 2.5-5.1 mm (10 and 5 dpi, respectively), requiring and outlet diameter between 1.0-3.0 mm to compensate for die swell of viscoelastic fluids (section 2.1.3).

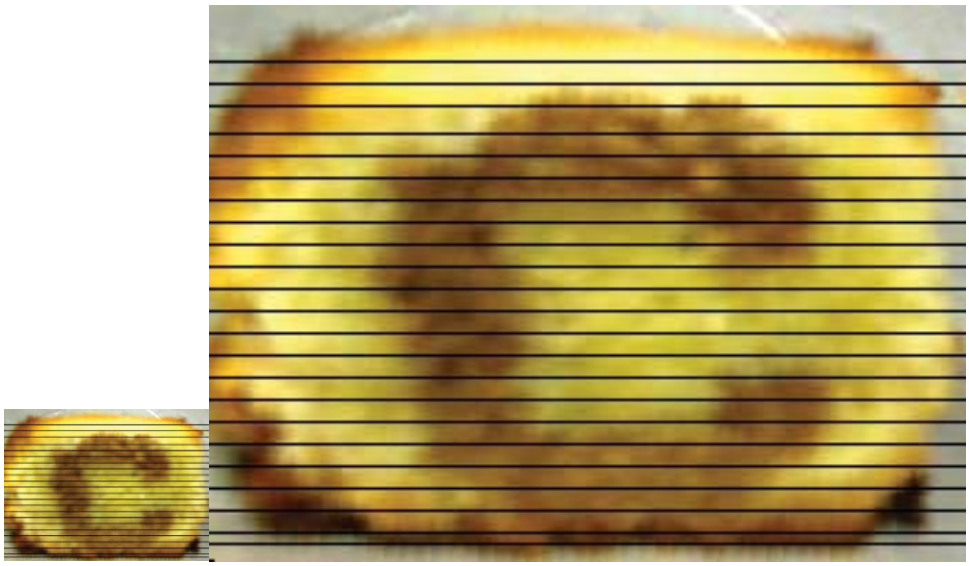

Figure 6.1 3D image of the letter 'C', extrusion-printed and cooked using egg- and butter-rich cookie dough,. Left: at true print size (lines represent print layers of 1 mm, ~20 dpi). Right: Enlarged from 20 mm height to 100 mm height (layers of 5 mm, ~5 dpi). Adapted with permission from Lipton et al. (2010), © 2010 Solid Freeform Fabrication Symposium.

Fig. 6.1 left shows a 3D-printed food image, made from cookie dough at actual size using the two-pump Fab@Home printer which produces continuous threads of different colour and/or composition, depositing one thread at a time (Lipton, Arnold, et al., 2010). The lines added to the image depict the probable number of layers needed to produce the curves in the embedded letter (20 layers of 1 mm), assuming that the cookie dough formulation develops little die swell. A thread of 1 mm width gives a print resolution of 20 dpi, one step finer than the resolution range set in for initial printer specification in Table 2.1. Limiting the die swell significantly improves image resolution, and should be considered as a general strategy to improve AM print quality.

As resolution decreases, image degradation increases. There is a direct conflict in the initial printer design specifications between image resolution and the design of metering equipment to colour-match a low-volume voxel.

The initial Food-Ink 3D printer application design outline suggested an object build with few layers (5-7 layers). Without developing an image along the XZ-plane, the design outline as initially specified essentially prints two 2D images stuck together. Commercial printing equipment already exists to reproduce a high-resolution colour image on the surface of a food, with pixel colour-matching based on mixing food-grade dyes (e.g. Russell, Candler, & Wright, 2009).

Adding enough information for a 3D image in the XZ-plane requires a minimum of 15-20 layers for a two colour image, as in Fig. 6.1, with at least 60 layers needed at 8 dpi resolution to match a full-colour image. 3D images with lower information content, such as the two-colour image of the letter 'C' in Fig. 6.1 left may be achievable as a point-of-sale, Food-Inks 3D printed product. If the product is not aimed at image reproduction then colour-matching of voxels is unnecessary. Existing 3D printers, such as the Fab@Home, and subsequent designs from the Cornell group, already produce this type of 3D printing

output using food materials.

To deliver a 3D object of A5 size with 20 layers and at 10 dpi resolution requires > 100,000 individual metering operations. To stay within print time limits, the size of the printed product must be considerably smaller than A5 size, so that the limited build time can be spent on printing at least 15-20 layers. Image reproduction in 3D with colour matching may be achievable if a large-enough shape is printed, but the trade-off is an increase in build time incompatible with point-of sale manufacture.

A 2D ink-jet printing process delivers very small volumes of colour-matched ink at high resolution. Nanolitre volumes are metered in a 4-dye process in which the white paper provides the white component of the colour. Inkjet printing is limited to low-viscosity fluids, but could provide a high-speed solution for low-volume colour-matching of voxels if printing was done by mixing and depositing an entire print line of discrete, colour-matched voxels in one step. Many voxels could be formed and deposited simultaneously, even if dye metering into multiple mixers was first carried out by a single high-speed inkjet print head before adding in Food-Ink base for mixing. This equipment design is no longer based on extrusion of a thread through a single outlet, but of many mixing and deposition events carried out simultaneously. Based on the number of possible metering operations to fabricate an image within a 3D object, a multi-voxel delivery strategy is the most sensible design choice for the Food-Inks 3D printer.

6.5.3 Voxel colour-matching

6.5.3.1 Sponge product structure and voxel resolution

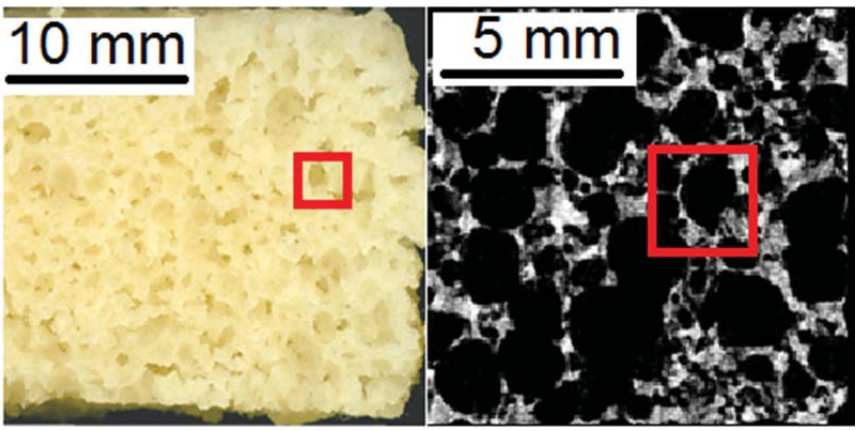

Figure 6.2 Typical mesostructure of rice1 idli cooked product in relation to a voxel with size 10 dpi. (red box). Left: digital image of cut image surface. Right: computed X-ray microtomography image.

In Fig. 6.2 the structure of a typical rice flour idli is marked with red boxes that represent a voxel at 10 dpi. The voxel size for image resolution overlaps with void size typically associated by consumers in SPs. It is clear from the relation of the desired image resolution to the expanded SP structure that 1) the initial 3D print resolution needs to be ~15-20 dpi (i.e. very small print voxel size) to compensate for later SP formulation expansion on cooking; and 2) the irregular structure of the expanded product introduces

distortion into voxel organisation. Image distortion and mixing between voxels will take place if large mobile bubbles travel through the batter or if there is extensive bubble coalescence/collapse. Bulk movement of batter due to convection flows generated on heating will also distort voxel positioning in SP batters, even under rapid microwave cooking. It is clear that SP foams are unsuited to the 3D Food Inks printing process. This does not exclude finer foams, such as ice cream foams, from being suited to voxel delivery.

6.5.3.2 Influence of flow behaviour on colour mixing

The process for colour-matching of voxels was assumed to be either 1) by mixing four or five pre-coloured streams of Food-Ink base with similar viscosity, or 2) by mixing concentrated low-viscosity dyes into an uncoloured Food-Ink base of greater viscosity. It was assumed that mixing between dyes and Food-Ink base is laminar in nature, i.e. occurs by stretching flow and lamination rather than by turbulent agitation. An evaluation of an inline static mixer system, as envisaged for the Food-Inks 3D printer prototype, concluded that the diluting out of material during residence time the mixer meant inline static mixing was unable to deliver a stream of discrete voxels in a continuous thread.

As mixing in a static mixer is laminar, information from published models for the influence of fluid stream properties (e.g. relative viscosity, mass ratio) on the effectiveness of static mixing gave a first approximation for prediction of mixing effectiveness for dye addition to Food-Ink base. The published computational models for laminar mixing suggest that option 1) 'mixing pre-coloured Food-Inks with similar viscosity' is more effective than mixing small volumes of liquid dye into a more viscous base.

6.6 Design of sponge product formulations

6.6.1 Doughs/batters as multiphase structured fluids

Microscopy observations of micro-rheological events in liquid-particulate-gas idli batters emphasised the role of localised interactions between batter phase components in the development of cooked idli mesostructure. Table 6.2 describes the distinct component phases in SP doughs and batters, their rheological characteristics, and the main chemical and physical transformation that each undergoes during heating. The lipid/solid fat content of idli formulations played a negligible role in idli structure development, but lipid- and fat-containing component phases are critical to bubble population dynamics and mesostructure development in fat-rich cake formulations, and need to be taken into account in any generic description of interactions in SP doughs and batters.

6.6.2 Formulation design elements for sponge products under microwave cooking

There are very few SP studies that quantify the dynamics of dough/batter bubble populations, and fewer still that correlate the uncooked mesostructure with that in the cooked product. Studies generally report foam structures within a size range associated by consumers with product quality, but interpretation of events in foam formation and expansion requires quantification of bubble population dynamics across a range of scales (Shea et al., 2010). Most SP studies reporting bubble data base their interpretations on assumptions derived from a few primary studies of wheat SP formulations

Table 6.2 Description of phase components in multiphase dough/batter dispersions, with the corresponding rheological properties and physico-chemical transformations on heating. The rheological behaviour of emulsions and fat dispersions is omitted as it was not discussed in this study.

Phase component	Liquid continuous phase	Gas-liquid foam	Liquid-solid dispersion (non-fat)	Liquid-lipid emulsion	Solid-solid-gas-(liquid) dispersion (fats)
Structural properties of uncooked dough/batter	Contains soluble protein, polysaccharide, sugars, salts and organic acids (pH-dependent composition)	Dynamic bubble population under gas transfer into bubble initiation sites, introduced by shear or on particulates	Starch, cell wall fragments from flour in liquid continuous phase	Liquid lipid droplets in a hydrophilic continuous phase	Soft deformable solid fat with solid sugar (& emulsifier) introduced by extensive shear (creaming, whisking)
Rheological properties in uncooked dough/batter	Non-Newtonian, shear-thinning fluid ↑ structures in solution (e.g. biopolymer networks) → ↑ viscoelasticity & yield stress	↑ gas phase volume → rapid ↑ viscoelasticity & yield stress Highly-aerated foam → soft-jammed foam	Non-Newtonian, yield stress, shear-thinning Particulate volume fraction & size distribution factors determine flow behaviour High particulate content → soft-jammed dispersion		
Transformation on heating	Spatiotemporal change in local viscosity due to: - Protein denaturation and aggregation - Conformational changes in NSPs - Temperature-dependent shifts in water availability due to water-active molecules e.g. sugars, proteins	Desolubilisation and expansion of CO_2 → rapid ↑ in gas phase volume ↑Water vapour pressure → ↑ in gas phase volume late in cooking Temperature-dependent changes to bubble interface	Uptake of water from liquid phase into starch granules Starch granule swelling → rapid ↑viscosity → Two-domain structure with setting of protein-NSP elastomer from the liquid phase	Emulsion interface destabilisation with heating may alter emulsion properties Liquid lipids may complex with hydrated starch polymers	Melting of fat produces a liquid-air phase later in heating, releasing gas bubbles for expansion Solubilised fats may complex with hydrated starch polymers

cooked by baking. In this study, the interpretation of structuring events in idli batters is supported by detailed observations of batter and product structures, by data from a holistic suite of test systems for batter and cooked product attributes, and by the serendipitous pairing of like/unlike idli mesostructure variants. Tools and models from non-food porous systems helped to interpret SP bubble population dynamics in multiphase batters.

Entrainment of air on flour addition is known as a mechanism, but is poorly characterised, with no definitive first-principles studies (R. Carl Hoseney, pers. comm.). In this study, substitution of different flours into the idli formulation generated clear differences in batter gas phase volume, bubble number and liquid phase behaviour in uncooked batter. Flour particulates, primarily starch granules and granule aggregates, significantly modified bubble population dynamics and altered the volume fraction of the liquid phase by water uptake during hydration, influencing mesostructure development. As the idli formulation contained a suitable 'elastic band' functional element able to support foam formation and foam expansion and produce a resilient, continuous domain of protein-NSP in the cooked microstructure, the contribution of the starch granule domain could be significantly reduced without losing typical SP structural cohesiveness and mechanical properties; while large cell wall fragments (e.g. BG bean fragments) were sometimes more important in defining and stabilising intersections in the solid foam structure than expanded starch granules. These are novel observations for structure development in SP formulations.

Chap. 1 listed three primary design functional elements (structuring operations) required in a SP formulation. Based on the deconstruction of the idli system, another two elements can be added to the design scheme. The five primary functional elements for control of mesostructure development under microwave cooking become 1) aerate formulation to produce a liquid-particulate-gas foam, 2) control bubble size distribution during formation, 3) expand the multiphase foam by heating, 4) control mesostructure development in foam expansion, and 5) transition closed-cell foam to continuous open-cell sponge. The synthesis of information from this study with existing knowledge of SP development is summarised as a system-level design scheme for the control of mesostructure development in generic SPs formulations (Table 6.3, over page). This represents the stage in the Ulrich & Eppinger design process which summarises the main design elements to support specific design decisions. Column 1 lists the five primary functional design elements. These are split into distinct sub-elements (Col .2). Listed in columns 3 & 4 are mechanisms to produce each functional sub-element, with examples of ingredients and ingredient combinations (physical elements) to deliver each mechanism. Included in the system-level design scheme are the necessary external structuring operations (foam formation by physical means, and heating) which represent non-formulation 'user-interactions' as defined in section 1.4.2.

This information can be applied in the design of non-wheat SP formulations, such as gluten-free bread and cake products; and to the interpretation of events in poorly-characterised SP systems. Because the idli blackgram-buttermilk fraction is such a robust system, and is able to produce a satisfactory set structure under a broad range of batter conditions, it may useful as a model SP system to evaluate flour function.

Table 6.3 System-level design elements in the development of sponge product mesostructure, listing primary functional design elements with associated sub-elements (structuring operations), mechanisms and examples of physical elements (ingredient components).*Indicates user-specific, not formulation-specific, structuring operations.

Primary functional element	Sub-element	Mechanisms	Examples of possible physical elements
Aerate formulation to produce a liquid-particulate-gas foam	Incorporate gas phase	*Do physical work to introduce gas phase	
		Add air entrained between and on rough particulates (sifting)	Flour particles, granulated BiC, inert particulates (e.g. crystalline microcellulose)
		Modulate desolubilisation of added BiC	BiC acidulating agents
	Insert bubble initiation sites	*Do physical work to break up introduced gas phase (e.g. whipping)	
		Add microbubble entrained on and inside rough particulates	Flours with many free granules, sifted flours, particulates that carry microbubbles internally
Control bubble size distribution before heating	Decrease mean bubble size	*Do physical work to break up introduced gas phase (e.g. whipping)	
		Increase content of interface-stabilising compounds	
	Modulate interface stability	Stabilise interface by particulate clustering (steric stabilisation)	Fat particles
		Modify interface stabilising or destabilising components	Polar lipids, surface-active proteins
	Add physical barriers to reduce between-bubble interactions	Increase viscosity and yield stress of the liquid phase	Develop protein networks (e.g. gluten), increase levels of soluble polysaccharide to form a gel in the liquid phase
		Add particulates to segregate bubbles	Add inert particulates, e.g. microcrystalline cellulose
		Add absorbent particulates to reduce liquid phase volume	Cell wall fragments, starches with liquid absorbing capacity (e.g. pregelatinised starch)

Expand the three-phase foam by heating	Control heating rate under microwave cooking	Increase dipolar molecule concentration to increase heating rate	Water and ionic compound content
		Decrease bulk density to increase microwave penetration depth	Increase leavening content
			*Increase initial gas phase incorporation
		Increase surface area at which CO_2 and water vapour can partition into bubbles	Increase emulsifier content
	Control heating rate under baking or steaming	Modify water content	
	Modulate batter bulk viscosity during heating	Increase liquid phase flow viscosity	Viscosifying agents with well-characterised heat response
		Decrease liquid phase flow viscosity	Altered water content
		Incorporate heat-responsive water release agents	Soluble protein, sugars
		Incorporate heat-responsive water uptake agents	Starch polymers, starch granules
	Control volume of leavening gas	Modulate batter titratability and BiC concentration	Double-acting baking powder, coated BiC
		Increase foam interface area	Emulsifiers, foam-forming proteins
Transition closed-cell foam to continuous open-cell sponge	Control cooked crumb product volume	Modulate viscoelastic properties of liquid phase after heat-denaturation	Continuous phase with suitable viscoelastic properties after heat-denaturation
		Guarantee starch granule structure setting	Flours or isolated granules that gelatinise before solidification of the protein-NSP domain
Control mesostructure development on cooking	Modulate foam stability with increasing temperature	Control interfacial stability	Viscosifying agents with well-characterised heat response
		Control granule viscosification rate	Interfacial components with well-characterised heat response
	Control timing of product setting	Modify surface tension and dilatational modulus	
	Modulate bubble shape	Modify liquid phase viscosity	Starch source
		Modify surface tension and dilatational modulus	e.g. Add lipids, lipases
	Control cooked crumb product volume	Modify liquid phase viscosity	Viscosifying agents

6.7 Concluding remarks

Chap. 1 described the primary research aims of the study: 'to define the requirements for control of flow during piping, mixing, and voxel deposition; and for control of structure formation in sponge products, within the context of Food-Ink formulation design for the Food-Inks 3D printer'. This study has four parts: 1) a review of Food Layered Manufacture as a new process for structuring solid foods (Wegrzyn et al., 2012, bound with the thesis text); 2) flow behaviour characterisation of structured and multiphase fluids under pumping and deposition, including an analysis of voxel deposition and colour-matching for the Food-Inks 3D printing application; 3) development of a suite of testing methods, including structure quantification, for structuring events in uncooked and cooked SP formulations; 4) an analysis of structure development in SPs based on deconstruction of the non-wheat idli system.

Materials sets for Food Layered Manufacture require much greater control of the structure-forming behaviour than when formulating for conventional solid foods, while the work- and time-dependent nature of gluten-based systems excludes wheat-flour formulations from consideration as FLM materials. The requirement to fill a knowledge gap for non-wheat SP formulations under microwave cooking produced novel observations in this study regarding the contribution of non-wheat flour components to structure development in SP formulations.

SP formulations proved unsuitable for use as a Food-Ink in the Food-Ink 3D printing project, because: 1) SP product mesostructure is incompatible with the voxel resolution required for image delivery; 2) SP structure development cannot be reduced to the FLM structuring operations of metering, mixing, deposition and setting; and 3) control of positional information during foam expansion on cooking is problematic. For an extrusion-based Food-Ink 3D printing process, the disruptive effect of fluid flow behaviour on a train of voxels travelling within a continuous thread, together with the high number of individual metering operations needed to deliver a 3D Food-Ink image, eliminate the first extrusion-based prototype Food-Inks 3D printer design from consideration. An analysis of rheological flow behaviour models relevant to the Food-Inks 3D printing technology, together with the observed behaviour of a model SP Food-Ink fluid during stop-start-stop flow, leads to the conclusion that mixer emptying and voxel deposition must be carried out by a single equipment design chunk; and that the design of this mixer-deposition component is fundamental to producing a successful Food-Inks 3D printing technology. Balancing the need for rapid structure reformation after deposition of a Food-Ink (stop-start-STOP behaviour) with mixability and pumpability is a difficult formulation design task.

From a design process perspective this study produced the following design components:

A. Concept generation for FLM technologies and consumer products.
B. Flow behaviour specifications for structured fluids which constrain equipment design decisions for extrusion-based FLM, and for voxel formation and deposition in the Food-Inks 3D printing application for colour-matching voxels to an image.
C. A system-level design scheme for sponge product formulations, incorporating novel design elements from the idli system deconstruction.
D. A holistic suite of test systems to quantify structure development in sponge products.

E. A list of relevant material properties to meet extrusion-based FLM technologies using structured fluids.

The emphasis in this study has been to support design decisions for the Food-Inks 3D printer project by focusing on structure formation and loss in multiphase fluids during piping and deposition, and on structuring events in sponge product formulations. A systems approach (as advocated by Hadiyanto) is necessary in order to address the constraints of the FLM process. While taking a systems approach on experimental analysis is highly intensive and requires examination and interpretation of many aspects of the system, taking this approach has delivered new insights into flow behaviour of structured food fluids on piping at the scale of Food-Inks 3D printer, structure development in SPs, and potential SP formulation design strategies.

Bibliography

Abramoff, M. D., Magalhaes, P. J., & Ram, S. J. (2004). Image processing with ImageJ. *Biophotonics International, 11*, 36-42.

Aguilera, J., & Lillford, P. (2008). Structure-property relationships in foods. In J. Aguilera & P. Lillford (Eds.), *Food materials science. Principles and Practice* (pp. 229-254). New York, US.: Springer.

Aguilera, J., & Stanley, D. (1999). Fundamentals of structuring. *Microstructural principles of food processing and engineering*. Gaithersburg, US.: Aspens Publishing.

Al-Muslimawi, A., Tamaddon-Jahromi, H. R., & Webster, M. F. (2013). Simulation of viscoelastic and viscoelastoplastic die-swell flows. *Journal of Non-Newtonian Fluid Mechanics, 191*, 45-56.

Alamri, M. S., Mohamed, A. A., & Hussain, S. (2012). Effect of okra gum on the pasting, thermal, and viscous properties of rice and sorghum starches. *Carbohydrate Polymers, 89*, 199-207.

Allais, I., Edoura-Gaena, R.-B., Gros, J.-B., & Trystram, G. (2006). Influence of egg type, pressure and mode of incorporation on density and bubble distribution of a lady finger batter. *Journal of Food Engineering, 74*, 198-210.

Allen, W. (2013). A summary of the principles of hierarchy theory. Retrieved 20 Jun 2013 from http://www.isss.org/hierarchy.htm

Andersson, H., Öhgren, C., Johansson, D., Kniola, M., & Stading, M. (2011). Extensional flow, viscoelasticity and baking performance of gluten-free zein-starch doughs supplemented with hydrocolloids. *Food Hydrocolloids, 25*, 1587-1595.

Angiolini, A., & Collar, C. (2008). Small and large deformation viscoelastic behaviour of selected fibre blends with gelling properties. *Food Hydrocolloids, 23*, 742-748

Angiolini, A., & Collar, C. (2009). Bread crumb quality assessment: a plural physical approach. *European Food Research and Technology, 229*, 21-30.

AOAC International. (1992). AOAC Offical method 991.36. *Journal of AOAC International, 75*, 289.

Araki, E., Ikeda, T., Ashida, K., Takata, K., Yanaka, M., & Ida, S. (2009). Effects of rice flour properties on specific loaf volume of one-loaf bread made from rice flour with wheat vital gluten. *Food Science and Technology Research, 15*, 439-448.

Arntfield, S., & Murray, E. (1981). The influence of food processing parameters on food protein functionality. I. Differential Scanning Caloirimetry as an indicator of protein denaturation. *Canadian Institute of Food Science and Technology, 14*, 289-294.

Arteaga, G. E., Li-Chan, E., Vazquez-Arteaga, M. C., & Nakai, S. (1994). Systematic experimental designs for product formula optimization. *Trends in Food Science and Technology, 5*, 243-254.

Ashwini, A., Jyotsna, R., & Indrani, D. (2008). Effect of hydrocolloids and emulsifiers on the rheological, microstructural and quality characteristics of eggless cake. *Food Hydrocolloids, 23*, 700-707.

ASTM International (2012) Standard terminology for Additive Manufacturing technologies ASTM F2792-10e1 Standard C.F.R..

Autio, K., & Salmenkallio-Marttila, M. (2001). Light microscopic investigations of cereal grains, doughs and breads. *Lebensmittel-Wissenschaft und-Technologie, 34*, 18-22.

Babin, P., Della Valle, G., Chiron, H., Cloetens, P., Hoszowska, J., Pernot, P., . . . Dendievel, R. (2006). Fast X-ray tomography analysis of bubble growth and foam setting during breadmaking. *Journal of Cereal Science, 43*, 393-397.

Baik, O., & Marcotte, M. (2003). Modeling the moisture diffusivity in a baking cake. *Journal of Food Engineering, 56*, 27-36.

Baixauli, R., Salvador, A., & Fiszman, S. M. (2007). Texture and colour changes during storage and sensory shelf life of muffins containing resistant starch. *European Food Research and Technology, 223*, 523-530.

Baixauli, R., Salvador, A., Martínez-Cervera, S., & Fiszman, S. M. (2008). Distinctive sensory features introduced by resistant starch in baked products. *LWT - Food Science and Technology, 41*, 1927-1933.

Baixauli, R., Sanz, T., Salvador, A., & Fiszman, S. M. (2007). Influence of the dosing process on the rheological and microstructural properties of a bakery product. *Food Hydrocolloids, 21*, 230-236.

Baixauli, R., Sanz, T., Salvador, A., & Fiszman, S. M. (2008). Muffins with resistant starch: Baking performance in relation to the rheological properties of the batter. *Journal of Cereal Science, 47*, 502-509.

Baker, B. A., Davis, E. A., & Gordon, J. (1990). The influence of sugar and emulsifier type during

microwave and conventional heating of a lean formula cake batter. *Cereal Chemistry, 67*, 451-457.

Batey, I. (2007). Interpretation of RVA curves. In G. Crosbie & A. Ross (Eds.), *The RVA Handbook* (pp. 19-30). St Paul, US.: AACC International.

Baxter, G., Zhao, J., & Blanchard, C. (2010). Albumin significantly affects pasting and textural characteristics of rice flour. *Cereal Chemistry, 87*, 250-255.

Bell, A., Berger, K., Russo, J., White, G., & Waether, T. (1975). A study of the microbaking of sponges and cakes using cine and television microscopy. *Journal of Food Technology, 10*, 147-156.

Bellido, G. G., Scanlon, M. G., & Page, J. H. (2009). Measurement of dough specific volume in chemically leavened dough systems *Journal of Cereal Science, 49*, 212-218.

Bellido, G. G., Scanlon, M. G., Page, J. H., & Hallgrimsson, B. (2006). The bubble size distribution in wheat flour dough. *Food Research International, 39*, 1058-1066.

BeMillar, J., Derby, R., & Trimbo, H. (1973). A pictorial representation for the increase in viscosity of a heated wheat starch-water suspension. *Cereal Chemistry, 50*, 271-280.

Bennion, E., & Bamford, G. (1997). Cake-making processes. *The technology of cake making* (6th ed., pp. 250-274). London, UK.: Blackie.

Bhattacharya, S., & Bhat, K. (1997). Steady state rheology of rice-black gram suspensions and suitability of rheological models. *Journal of Food Engineering, 32*, 241-250.

Bikard, J., Coupez, T., Della Valle, G., & Vergnes, B. (2008). Simulation of bread making process using a direct 3D numerical method at microscale: Analysis of foaming phase during proofing. *Journal of Food Engineering, 85*, 259-267.

Bikard, J., Coupez, T., della Valle, G., & Vergnes, B. (2012). Simulation of bread making process using a direct 3D numerical method at microscale: Analysis of baking step. *International Journal of Material Forming, 5*, 11-24.

Bkorkroff, J., & Holzapfel, W. (2006). Genera *Leuconostoc, Oenococcus* and *Wiessella*. In M. Dworkin, S. Falkow, E. Rozenberg, K. Schleifer, & E. Stackebrandt (Eds.), *The Prokaryotes. A handbook on the biology of bacteria* (Vol. 4, pp. 267-319): Springer.

Bloksma, A. (1980). Effect of heating rate on the viscosity of wheat flour doughs. *Journal of Texture Studies, 10*, 261-269.

Bloksma, A. (1990a). Dough structure, dough rheology, and baking quality. *Cereal Foods World, 35*, 237-244.

Bloksma, A. H. (1990b). Rheology of the breadmaking process. *Cereal Foods World, 35*, 228-236.

Blower, J. D., Keating, J. P., Mader, H. M., & Phillips, J. C. (2002). The evolution of bubble size distributions in volcanic eruptions. *Journal of Volcanology and Geothermal Research, 120*, 1-23.

Bogracheva , T. Y., Wang, Y. L., Wang, T. L., & Hedley, C. L. (2002). Structural studies of starches with different water contents. *Biopolymers, 64*, 268-281.

Bonn, D., & Den, M. (2009). Yield stress fluids slowly yield to analysis. *Science, 324*, 1401-1402.

Bonnoit, C., Darnige, T., Clement, E., & Lindner, A. (2010). Inclined plane rheometry of a dense granular suspension. *Journal of Rheology, 54*, 65-79.

Bourne, M. (1978). Texture Profile Analysis. *Food Technology, 32*, 62-66, 72.

Bourne, M. (1990). Basic principles of food texture measurement. In H. Faridi & J. Faubion (Eds.), *Dough Rheology and baked product texture* (pp. 331-341). New York, US.: AVI.

Brooker, B. E. (1996). The role of fat in the stabilisation of gas cells in bread dough. *Journal of Cereal Science, 24*, 187-198.

Buffler, C. (1992). *Microwave cooking and processing: Engineering fundamentals for the food technologist*. New York, US.: Van Nostrand Reinhold.

Campbell, G., Rielly, C., Fryer, P., & Sadd, P. (1998). Aeration of bread dough during mixing: Effect of mixing dough at reduced pressure. *Cereal Foods World, 43*, 163-167.

Campbell, G. M., & Martin, P. J. (2012). Bread aeration and dough rheology. In S. Cauvain (Ed.), *Breadmaking: Improving quality* (2nd ed., pp. 229-328). Cambridge, UK: Woodhead Publishing.

Campbell, G. M., & Mougeot, E. (1999). Creation and characterisation of aerated food products. *Trends in Food Science and Technology, 10*, 283-296.

Causer, C. (2009). They've got a golden ticket. *Potentials, IEEE, 28*, 42-44.

Cauvain, S. (2003). *Bread making: Improving quality*. Roca Baton, US.: CRC Press.

Cauvain, S., & Young, L. (2000a). *Baking problems solved*. Boca Raton, US: CRC Press.

Cauvain, S., & Young, L. (2000b). Cakes and sponges. *Baking problems solved* (pp. 148-194). Boca Raton, US: CRC Press.

Cauvain, S., & Young, L. (2006a). *Baked products: Science, technology and practise*. Oxford, UK: Blackwell

Publishing.
Cauvain, S., & Young, L. (2006b). Characterisation of bakery products by formulation and the key functional roles of the main ingredients used in baking. *Baked products: Science, technology and practice* (pp. 35-71). Oxford, U.K.: Blackwell Publishing.
Cauvain, S., & Young, L. (2006c). Current approaches to the classification of bakery products. *Baked products technology* (pp. 1-13). Oxford, UK.: Blackwell.
Cauvain, S., & Young, L. (2006d). Ingredients and their influences. *Baked products: Science, technology and practice* (pp. 72-98). Oxford, U.K.: Blackwell Publishing.
Cauvain, S., & Young, L. (2006e). Interactions between formulation and process technologies. *Baked products: Science, technology and practise* (pp. 120-147). Oxford, UK: Blackwell Publishing.
Cauvain, S., & Young, L. (2006f). The nature of baked product structure. *Baked products: Science, technology and practice*. Oxford, U.K.: Blackwell Publishing.
Cauvain, S., & Young, L. (2007a). *Bakery food manufacture and quality: Water control and effects* London: Wiley-Blackwell.
Cauvain, S., & Young, L. (2007b). *Technology of breadmaking* (2nd ed.). New York Springer.
Chandrashekar, A., & Kirleis, A. W. (1988). Influence of protein on starch gelatinization in sorghum. *Cereal Chemistry, 65*, 457-462.
Changala Reddy, G., Susheelamma, N. S., & Tharanathan, R. N. (1990). Composition and properties of mucilaginous polysaccharide from native and fermented black gram flour. *Carbohydrate Polymers, 12*, 189-202.
Chateau, X., Ovarlez, G., & Trung, K. L. (2008). Homogenization approach to the behavior of suspensions of noncolloidal particles in yield stress fluids. *Journal of Rheology, 52*, 489-506.
Chesterton, A. K. S., De Abreu, D. A. P., Moggridge, G. D., Sadd, P. A., & Wilson, D. I. (2013). Evolution of cake batter bubble structure and rheology during planetary mixing. *Food and Bioproducts Processing, 91*, 192-206.
Chesterton, A. K. S., Meza, B. E., Moggridge, G. D., Sadd, P. A., & Wilson, D. I. (2011). Rheological characterisation of cake batters generated by planetary mixing: Elastic versus viscous effects. *Journal of Food Engineering, 105*, 332-342.
Chin, N. L., Campbell, G. M., & Thompson, F. (2005). Characterisation of bread doughs with different densities, salt contents and water levels using microwave power transmission measurements. *Journal of Food Engineering, 70*, 211-217.
Chiotelli, E., Rolee, A., & Le Meste, M. (2000). Effect of sucrose on the thermomechanical behavior of concentrated wheat and waxy corn starch-water preparations. *Journal of Agricultural and Food Chemistry, 48*, 1327-1339.
Choi, M. S., Young, J. K., & Kwon, S. H. (2013). Prediction on pipe flow of pumped concrete based on shear-induced particle migration. *Cement and Concrete Research, 52*, 216-224.
Chung, J. H. Y., Naficy, S., Yue, Z., Kapsa, R., Quigley, A., Moulton, S. E., & Wallace, G. G. (2013). Bio-ink properties and printability for extrusion printing living cells. *Biomaterials Science, 1*, 763-773.
Cohen-Addad, S., Höhler, R., & Pitois, O. (2013). Flow in foams and flowing foams. *Annual Review of Fluid Mechanics, 45*, 241-267.
Cohen-Addad, S., Krzan, M., Höhler, R., & Herzhaft, B. (2007). Rigidity percolation in particle-laden foams. *Physical Review Letters, 99,* art. 168001..
Cohen, D., Lipton, J., Cutler, M., Coulter, D., Vesco, A., & Lipson, H. (2009, 3-5 Aug). *Hydrocolloid printing: A novel platform for customized food production.* Paper presented at the 20th Solid Freeform Fabrication Symposium (SFF'09), Austin, TX, US.
Cole Parmer. (2012). Masterflex Technical Library Article No 678.
Confroti, F. (2006). Cake manufacture. In Y. Hue (Ed.), *Bakery Products: Science and Technology* (pp. 393-410). Oxford, UK: Blackwell Publishing.
Coulson, J., Richardson, J., Backhurst, J., & Harker, J. (1999a). Flow of fluids in pipes and open channels. *Chemical Engineering* (Vol. 1, pp. 53-142). Oxford: Butterworth Heinmann.
Coulson, J., Richardson, J., Backhurst, J., & Harker, J. (1999b). Flow of multiphase mixtures. *Chemical Engineering* (Vol. 1, pp. 181-231). Oxford: Butterworth Heinmann.
Coulson, J., Richardson, J., Backhurst, J., & Harker, J. (1999c). Pumping of fluids. *Chemical Engineering* (Vol. 1, pp. 314-378). Oxford: Butterworth Heinmann.
Coussot, P. (2005a). Experimental procedures and problems in paste viscosity. *Rheometry of pastes, suspensions, and granular materials* (pp. 81-152). Hoboken, US.: Wiley-Interscience.
Coussot, P. (2005b). Material mechanics. *Rheometry of pastes, suspensions, and granular materials* (pp. 4-40). Hoboken, US.: Wiley-Interscience.

Coussot, P. (2005c). Non-viscometric flows of yield stress fluids. *Rheometry of pastes, suspensions, and granular materials* (pp. 41-80). Hoboken, US.: Wiley-Interscience.

Coussot, P. (2005d). Practical rheometrical techniques. *Rheometry of pastes, suspensions, and granular materials* (pp. 285-246). Hoboken, US.: Wiley-Interscience.

Coussot, P., & Gaulard, F. (2005). Gravity flow instability of viscoplastic materials: The ketchup drip. *Physical Review E - Statistical, Nonlinear, and Soft Matter Physics, 72*, art. no. 031409.

Datta, A. (2001). Fundamentals of heat and moisture transport for microwaveable food product and process development. In A. Datta & R. Anantheswaran (Eds.), Handbook of microwave technologies for food applications (pp. 115-172). New York, US: Marcel Dekker

Datta, A. K., Sahin, S., Şumnu, G., & Keskin, S. O. (2007). Porous media characterization of breads baked using novel heating modes. *Journal of Food Engineering, 79*, 106-116.

Dàvila, E., Toldrà, M., Saguer, E., Carretero, C., & Parés, D. (2007). Characterization of plasma protein gels by means of image analysis LWT - Food Science and Technology, 40 1321-1329.

Delcour, J. A., Bruneel, C., Derde, L. J., Gomand, S. V., Pareyt, B., Putseys, J. A., . . . Lamberts, L. (2010). Fate of starch in food processing: From raw materials to final food products. Annual Review of Food Science and Technology, 1, 87-111.

De la Hera, E., Ruiz-París, E., Oliete, B., & Gómez, M. (2012). Studies of the quality of cakes made with wheat-lentil composite flours. *LWT - Food Science and Technology, 49*, 48-54.

de Souza Mendes, P. R., Thompson, R.L. (2013). A unified approach to model elasto-viscoplastic thixotropic yield-stress materials and apparent yield-stress fluids. *Rheologica Acta, 52*, 673-694.

Debet, M. R., & Gidley, M. J. (2006). Three classes of starch granule swelling: Influence of surface proteins and lipids *Carbohydrate Polymers, 64*, 452-465.

Derby, R. I., Miller, B. S., Miller, B. F., & Trimbo, H. B. (1975). Visual observation of wheat-starch gelatinization in limited water systems. *Cereal Chemistry, 52*, 702 - 713.

Dobraszczyk, B. J., & Morgenstern, M. P. (2003). Rheology and the breadmaking process *Journal of Cereal Science, 38*, 229-245.

Dodson, C. (2001). *Basic principles for using a home microwave oven*. New York, US: Marcel Dekker.

Donald, A. (2001). Plasticization and self-assembly in the starch granule. *Cereal Chemistry, 78*, 307-314.

Donovan, J. W. (1977). A study of the baking process by differential scanning calorimetry. *Journal of the Science of Food and Agriculture, 28*, 571-578.

Döring, C., Nuber, C., Stukenborg, F., Jekle, M., & Becker, T. (2015). Impact of arabinoxylan addition on protein microstructure formation in wheat and rye dough. *Journal of Food Engineering, 154*, 10-16.

Doube, M., Kłosowski, M. M., Arganda-Carreras, I., Cordelières, F. P., Dougherty, R. P., Jackson, J. S., . . . Shefelbine, S. J. (2010). BoneJ: free and extensible bone image analysis in ImageJ. *Bone, 47*, 1076-1079.

Dougherty, R., & Kunzelmann, R. (2007a). Computing local thickness of 3D structures with ImageJ. *Microscopy and Microanalysis, 13*, 1678-1679.

Dougherty, R. P., & Kunzelmann, K.-H. (2007b, August 5-9, 2007). *Computing Local Thickness of 3D structures with ImageJ.* Paper presented at the Microscopy & Microanalysis Meeting, Ft. Lauderdale, US.

Earle, M. D., & Earle, R. L. (2009a). *Creating New Foods. The Product Developer's Guide, the Web Edition* Retrieved from http://www.nzifst.org.nz/creatingnewfoods/about.htm

Earle, M. D., & Earle, R. L. (2009b). *Creating New Foods. The Product Developer's Guide, the Web Edition: Product design and process development* M. D. Earle & R. L. Earle (Eds.), Retrieved from http://www.nzifst.org.nz/creatingnewfoods/about.htm

Edwards, W. (2007). Raw materials. *The science of bakery products* (pp. 56-134). Cambridge, UK.: The Royal Society of Chemistry.

Eliasson, A. (2003). Utilization of thermal properties for understanding baking and staling processes. In G. Kaletunc & K. Breslauer (Eds.), *Characterization of cereals and flours* (pp. 65-115). New York, US.: Marcel Dekker.

Eliasson, A., & Larsson, K. (1993). *Cereals in breadmaking: A molecular colloidal approach*. Boca Raton, US.: CRC Press.

Emady, H., Caggioni, M., & Spicer, P. (2013). Colloidal microstructure effects on particle sedimentation in yield stress fluids. *Journal of Rheology, 57*, 1761-1772.

Escudier, M. P., & Presti, F. (1996). Pipe flow of a thixotropic liquid. *Journal of Non-Newtonian Fluid Mechanics, 62*, 291-306.

Everitt, S. L., Harlen, O. G., & Wilson, H. J. (2006a). Bubble growth in a two-dimensional viscoelastic

foam. *Journal of Non-Newtonian Fluid Mechanics, 137*, 46-59.
Everitt, S. L., Harlen, O. G., & Wilson, H. J. (2006b). Competition and interaction of polydisperse bubbles in polymer foams. *Journal of Non-Newtonian Fluid Mechanics, 137*, 60-71.
Everitt, S. L., Harlen, O. G., & Wilson, H. J. (2006c). Competition and interaction of polydisperse bubbles in polymer foams *Journal of Non-Newtonian Fluid Mechanics, 137*, 60-71.
Faergemand, M., & Krog, N. (2006). Interactions of emulsifiers with other components in foods. In A. Gaonkar & A. McPherson (Eds.), *Ingredient interactions. Effects on food quality* (2nd ed., pp. 390-421). Boca Raton, US.: CRC Press.
Falcone, P. M., Baiano, A., Zanini, F., Mancini, L., Tromba, G., Dreossi, D., . . . Del Nobile, M. A. (2005). Three-dimensional quantitative analysis of bread crumb by X-ray microtomography. *Journal of Food Science, 70*, E265-E272.
Fall, A., Huang, N., Bertrand, F., Ovarlez, G., & Bonn, D. (2008). Shear thickening of cornstarch suspensions as a reentrant jamming transition. *Physical Review Letters, 100*, art. 018301.
Fan, J., Mitchell, J. R., & Blanshard, J. M. V. (1999). A model for the oven rise of dough during baking. *Journal of Food Engineering, 41*, 69-77.
Farrera-Rebollo, R. R., de la Salgado-Cruz, M. P., Chanona-Pérez, J., Gutiérrez-López, G. F., Alamilla-Beltrán, L., & Calderón-Domínguez, G. (2012). Evaluation of image analysis tools for characterization of sweet bread crumb structure. *Food and Bioprocess Technology, 5*, 474-484.
Farris, R. (1968). Prediction of the viscosity of multimodal suspensions from unimodal viscosity data. *Journal of Rheology, 12*, 281-301.
Favero, J. L., Secchi, A. R., Cardozo, N. S. M., & Jasak, H. (2010). Viscoelastic fluid analysis in internal and in free surface flows using the software OpenFOAM. *Computers & Chemical Engineering, 34*, 1984-1993.
Feng, J., & Bertolo, C. (2004). Prediction of bubble growth and size distribution in polymer foaming based on a new heterogeneous nucleation model. *Journal of Rheology, 48*, 439-462.
Fessas, D., & Schiraldi, A. (2000). Starch gelatinization kinetics in bread dough. DSC investigations on 'simulated' baking processes. *Journal of Thermal Analysis and Calorimetry, 61*, 411-423.
Fischer, P., Pollard, M., Erni, P., Marti, I., & Padar, S. (2009). Rheological approaches to food systems. *Comptes Rendus Physique, 10*, 740-750.
Fischer, P., & Windhab, E. J. (2011). Rheology of food materials. *Current Opinions in Colloid and Interface Science, 16*, 36-40.
Foegeding, E. A., Luck, P. J., & Davis, J. P. (2006). Factors determining the physical properties of protein foams *Food Hydrocolloids, 20*, 284-292
Fretzdorff, B., Bechtel, D. B., & Pomeranz, Y. (1982). Freeze-fracture ultrastructure of wheat flour ingredients, dough and bread. *Cereal Chemistry, 59*, 113 - 120.
Fruhner, H., Wantke, K.-D., & Lunkenheimer, K. (2000). Relationship between surface dilational properties and foam stability. *Colloids and Surfaces A: Physicochemical and Engineering Aspects, 162*, 193–202.
Gaines, C. S., & Donelson, J. R. (1982). Cake batter viscosity and expansion upon heating. *Cereal Chemistry, 59*, 237-240.
Gan, H., Karim, R., Muhammad, S., Bakar, J., DM., H., & Rahman, A. (2007). Optimization of the basic formulation of a traditional baked cassava cake using response surface methodology. *Lebensmittel-Wissenschaft und-Technologie, 40*, 611-618.
Gharsallaoui, A., Roudaut, G., Beney, L., Chambin, O., Voilley, A., & Saurel, R. (2012). Properties of spray-dried food flavours microencapsulated with two-layered membranes: Roles of interfacial interactions and water. *Food Chemistry, 132*, 1713–1720.
Ghiasi, K., Hoseney, R. C., & Varriano-Marston, E. (1983). Effects of flour components and dough ingredients on starch gelatinization. *Cereal Chemistry, 60*, 58-61.
Gibson, L., & Ashby, M. (1997a). *Cellular solids: Structure and properties* (2nd ed.). Cambridge, U.K.: Cambridge University Press.
Gibson, L., & Ashby, M. (1997b). The mechanics of foams: Basic results. *Cellular solids: Structure and properties* (2nd ed., pp. 175-234). Cambridge, U.K.: Cambridge University Press.
Gibson, L., & Ashby, M. (1997c). The structure of cellular solids. *Cellular solids: Structure and properties* (2nd ed., pp. 15-51). Cambridge, U.K.: Cambridge University Press.
Gomez, M., Oliete, B., Rosell, C., Pando, V., & Fernandez, E. (2008). Studies on cake quality made of wheat-chickpea flour blends. *LWT - Food Science and Technology, 41*, 1701-1709.
Gonera, A., & Cornillon, P. (2002). Gelatinization of starch/gum/sugar systems studied by using DSC, NMR, and CSLM. *Starch - Stärke, 54*, 508-516.

Gonzales-Barron, U., & Butler, F. (2008a). Prediction of panellists' perception of bread crumb appearance using fractal and visual textural features. *European Food Research and Technology, 226*, 779-785.

Gonzales Barron, U., & Buteler, F. (2008b). Crumb features quantification by cryo-scanning electron microscopy images. In G. Campbell, M. Scanlon, & D. Pyle (Eds.), Bubbles in Food 2 (pp. 89-97). St Paul, US.. Eagen Press.

Gonzalez-Barron, U., & Butler, F. (2006). A comparison of seven thresholding techniques with the k-means clustering algorithm for measurement of bread-crumb features by digital image analysis. Journal of Food Engineering, 74, 268-278.

Gray, N. (2010). Looking to the future: Creating novel foods using 3D printing. Food Navigator. Science-Nutrition, 1. http://www.foodnavigator.com/Science-Nutrition/Looking-to-the-future-Creating-novel-foods-using-3D-printing/

Grenier, D., Lucas, T., & Le Ray, D. (2010). Measurement of local pressure during proving of bread dough sticks: Contribution of surface tension and dough viscosity to gas pressure in bubbles. Journal of Cereal Science, 52, 373-377.

Griswold, R. (1962). Evaluating food by objective methods. Experimental study of foods (pp. 540-541). Boston, US.: Houghton MiZin Co.

Guillermic, R.-M., Volland, S., Faure, S., Imbert, B., & Drenckhan, W. (2013). Shaping complex fluids - How foams stand up for themselves. Journal of Rheology, 57, 333-348.

Guy, R. C. E., & Sahi, S. S. (2006). Application of a lipase in cake manufacture. Journal of the Science of Food and Agriculture, 86, 1679-1687.

Hadiyanto. (2007). Quality design driven food process design. (PhD thesis), Wageningen University, Wageningen, The Netherlands.

Hadiyanto, Asselman, A., van Straten, G., Boom, R., Esveld, D., & van Boxtel, A. (2007). Quality prediction of bakery products in the initial phase of process design. Innovative Food Science & Emerging Technologies, 8, 285-298.

Hadiyanto, Esveld, D., Boom, R., van Straten, G., & van Boxtel, A. (2008). Product quality driven design of bakery operations using dynamic optimization. Journal of Food Engineering, 86, 399-413.

Hamaker, B., & Bugusu, B. (2003, 2-4 April). Overview: sorghum proteins and food quality. Paper presented at Afripro. Workshop on the proteins of sorghum and millets: enhancing nutritional and functional properties for Africa, Pretoria, South Africa.

Handleman, A. R., Conn, J. F., & Lyons, J. W. (1961). Bubble mechanics in thick foams and their effects on cake quality. Cereal Chemistry, 38, 294-305.

Henningsson, M., Östergren, K., & Dejmek, P. (2006). Plug flow of yoghurt in piping as determined by cross-correlated dual-plane electrical resistance tomography. Journal of Food Engineering, 76, 163-168.

Herran, C. L., & Coutris, N. (2013). Drop-on-demand for aqueous solutions of sodium alginate. Experiments in Fluids, 54, art. no. 1548.

Herzhaft, B., Kakadjian, S., & Moan, M. (2005). Measurement and modeling of the flow behavior of aqueous foams using a recirculating pipe rheometer. Colloids and Surfaces A: Physicochemical and Engineering Aspects, 263 (1-3 SPEC. ISS.), 153-164.

Hessel, V., Löwe, H., & Schönfeld, F. (2005). Micromixers—a review on passive and active mixing principles. Chemical Engineering Science, 60, 2479–2501.

Hildebrand, T., & Rüegsegger, P. (1997). A new method for the model-independent assessment of thickness in three-dimensional images. Journal of Microscopy, 185, 67-75.

Hill, M. (2009). Chemical Product Engineering—The third paradigm. Computers and Chemical Engineering, 33, 947-953.

Hinch, E. (2013). Lecture 7: Stress relaxation. www.whoi.edu/fileserver.do?id=28331&pt=10&p=17274

Hoover, R., & Sosulski, F. (1991). Composition, structure, functionality, and chemical modification of legume starches: A review. Canadian Journal of Physiology and Pharmacology, 69, 79-92.

Hoseney, C. R., Miller, R. A., Bassi, S., & Maningat, C. C. (2001). Microwaveable bread products US6482454

Hoseney, R. (1984). Starch and other polysaccharides: Basic structure and function in food. In F. Meuser (Ed.), Carbohydrates, protein, lipids: Basic views and new approaches in food technology.

Hoseney, R. (1994). Yeast-leavened products. Principles of cereal science and technology (2nd ed.). St Paul, US.: American Association of Cereal Chemists.

Hoseney, R., Lineback, D., & Seib, P. (1978). Role of starch in baked foods. Baker's Digest, 52, 11.

Howard, C., & Reed, M. (2005a). Estimation of total surface area and surface density. Unbiased

stereology (2nd ed., pp. 103-118). Oxon, United Kingdom: BIOS Scientific Publishers.
Howard, C., & Reed, M. (2005b). Number estimation. Unbiased stereology (2nd ed., pp. 65-102). Oxon, United Kingdom: BIOS Scientific Publishers.
Howard, C., & Reed, M. (2005c). Random sampling and random geometry. Unbiased stereology (2nd ed., pp. 17-34). Oxon, United Kingdom: BIOS Scientific Publishers.
Howard, C., & Reed, M. (2005d). Unbiased stereology (2nd ed.). Oxon, United Kingdom: BIOS Scientific Publishers.
Howard, N., Hughes, D., & Strobel, R. (1968). Function of the starch granule in the formation of layer cake structure. Cereal Chemistry, 45, 329-338.
Huang, J., Schols, H. A., van Soest, J. J. G., Jin, Z., Sulmann, E., & Voragen, A. G. J. (2007). Physicochemical properties and amylopectin chain profiles of cowpea, chickpea and yellow pea starches. Food Chemistry, 101, 1338-1345.
Hug-Iten, S., Handschin, S., Conde-Petit, B., & Escher, F. (1999). Changes in starch microstructure on baking and staling of wheat bread. Lebensmittel-Wissenschaft und-Technologie, 32, 255-260.
Israkarn, K., Hongsprabhas, P., & Hongsprabhas, P. (2007). Influences of granule-associated proteins on physicochemical properties of mungbean and cassava starches. Carbohydrate Polymers, 68, 314-322.
Iwata, H., & Ukai, Y. (2002). SHAPE: A computer program package for quantitative evaluation of biological shapes based on elliptic Fourier descriptors. Journal of Heredity, 93, 384-385.
Jackson, G. M., & Roufs, J. G. (1989). Dry mix for microwave layer cake. US4857353.
Jood, S., Chauhan, B. M., & Kapoor, A. C. (2006). Saponin content of chickpea and black gram: Varietal differences and effects of processing and cooking methods. Journal of the Science of Food and Agriculture, 37, 1121-1124.
Joseph, E., Crites, S., & Swanson, B. (1993). Microstructure of idli. Food Microstructure, 12, 483-488.
Joshi, K., Lee, J.G., Shafi, M.A., Flumerfelt, R.W. (1998). Prediction of cellular structure in free expansion of viscoelastic media. Journal of Applied Polymer Science, 67, 1353-1368.
Joye, I. J., Lagrain, B., & Delcour, J. A. (2009). Endogenous redox agents and enzymes that affect protein network formation during breadmaking - A review. Journal of Cereal Science, 50, 1-10.
Juhász, R., & Salgó, A. (2008). Pasting behavior of amylose, amylopectin and their mixtures as determined by RVA curves and first derivatives. Starch - Stärke, 60, 70-78.
Kaletunc, G., & Breslauer, K. J. (2003). Calorimetry of pre- and postextruded cereal flours. In G. Kaletunc & K. J. Breslauer (Eds.), Characterization of cereals and flours. Properties, Analysis and Applications. New York, US.: Marcel Dekker.
Kalichevsky, M., & Ring, S. (1987). Incompatability of amylose and amylopectin in aqueous solution. Carbohydrate Research, 162, 323-328.
Kamble, S., Pandey, A., Rastogi, S., & Lele, A. (2013). Ascertaining universal features of yielding of soft materials. Rheologica Acta, 52, 859-865.
Kaplan, A. M., & Haenlein, M. (2006). Toward a parsimonious definition of traditional and electronic mass customization. The Journal of Product Innovation Management, 23, 168-182.
Karperian, A. (2007). User's Guide for FracLac, V. 2.5. 36. http://rsbweb.nih.gov/ij/plugins/fraclac/FLHelp/Introduction.htm
Kaur, M., Singh, N., & Sandhu, K. S. (2004). Relationships between selected properties of black gram seeds and their composition. International Journal of Food Properties, 7, 541 - 552
Keskin, S. O., Şumnu, G., & Sahin, S. (2004). Bread baking in halogen lamp-microwave combination oven. Food Research International, 37, 489-495.
Khalil, S., & Sun, W. (2007). Biopolymer deposition for freeform fabrication of hydrogel tissue constructs. Materials Science and Engineering C, 27, 469-478.
Kim, S. (2015). Rendering complex colour inside 3D printed foods. (PhD thesis), Massey University.
Kim, S., Golding, M., & Archer, R. H. (2012). The application of computer color matching techniques to the matching of target colors in a food substrate: A first step in the development of foods with customized appearance. Journal of Food Science, 77, S216-S225.
Kinno, A., & Miura, M. (2010). Certification of 'Multiple Binarization Imaging Method' using bread-crumb imitating boards and its application to digital image analysis of crumb grain of commercial white pan breads. Nippon Shokuhin Kagaku Kogaku Kaishi, 57, 517-524.
Kloek, W., Van Vliet, T., & Meinders, M. (2001). Effect of bulk and interfacial rheological properties on bubble dissolution. Journal of Colloid and Interface Science, 237, 158-166.
Kobylanski, J., Perez, O., & Pilosof, A. (2004). Thermal transitions of gluten-free doughs as affected by water, egg white and hydroxypropylmethylcellulose. Thermochimica Acta, 44, 81-89.

Kogan, M., Ducloué, L., Goyon, J., Chateau, X., Pitois, O., & Ovarlez, G. (2013). Mixtures of foam and paste: Suspensions of bubbles in yield stress fluids. Rheologica Acta, 52, 237-253.
Kokelaar, J. J., & Prins, A. (1995). Surface rheological properties of bread dough components in relation to gas bubble stability. Journal of Cereal Science, 22, 53-61.
Kosson, R., Czuchajowska, Z., & Pomeranz, Y. (1994). Smooth and wrinkled peas. 1. General physical and chemical characteristics. Journal of Agricultural and Food Chemistry, 42, 91-95.
Kroustrup, J. P., & Gundersen, H. J. G. (2001). Estimating the number of complex particles using the ConnEulor principle. Journal of Microscopy, 203, 314-320.
Kukukova, A., Aubin, J., & Kresta, S. M. (2009). A new definition of mixing and segregation: Three dimensions of a key process variable. Chemical Engineering Research and Design, 87, 633-647.
Kumagai, H., Lee, B.-H., Kumagai, H., & Yano, T. (1990). Critical radius and time course of expansion of an isolated bubble in wheat flour under a temperature rise. Agricultural and Biological Chemistry, 55, 1081-1087.
Kusunose, C., Fujii, T., & Matsumoto, H. (1999). Role of starch granules in controlling expansion of dough during baking. Cereal Chemistry, 76, 920-924.
Lai, K. P., Steffe, J. F., & Ng, P. K. W. (2000). Average shear rates in the Rapid Visco Analyser (RVA) mixing system. Cereal Chemistry, 77, 714-716.
Lambert, L. L. P., Gordon, J., & Davis, E. A. (1992). Water-loss and structure development in model cake systems heated by microwave and convection methods. Cereal Chemistry, 69, 303-309.
Langevin, D. (2014). Rheology of adsorbed surfactant monolayers at fluid surfaces. Annual Review of Fluid Mechanics, 46, 47-65.
Lareo, C., Fryer, P. J., & Barigou, M. (1997). The fluid mechanics of two-phase solid-liquid food flows: A review. Food and Bioproducts Processing: Transactions of the Institution of of Chemical Engineers, Part C, 75, 73-105.
Lassoued, N., Babin, P., Della Valle, G., Devaux, M.-F., & Réguerre, A.-L. (2007). Granulometry of bread crumb grain: Contributions of 2D and 3D image analysis at different scale Food Research International, 40, 1087-1097.
Lassoued, N., Delarue, J., Launay, B., & Michon, C. (2008). Baked product texture: Correlations between instrumental and sensory characterization using Flash Profile. Journal of Cereal Science, 48, 133-143.
Lee, S., Prosky, L., & DeVries, J. (1992). Determination of total, soluble and insoluble dietary fiber in foods - enzymatic-gravimetric method. MES-tris buffer: collaborative studty. Journal of AOAC International, 75, 395-416.
Leng, D., & Calabrese, R. (2004). Immiscible liquid-liquid systems. In E. Paul, V. Atiemo-Obeng, & S. Kresta (Eds.), Handbook of industrial mixing: science and practice (pp. 639-753). Hobken, US.: Wiley-Interscience.
León, A., Rosell, C. M., & Benedito de Barber, C. (2003). A differential scanning calorimetry study of wheat proteins. European Food Research and Technology, 217, 13-16.
Li, A., & Walker, C. (1996). Cake baking in conventional, impingement and hybrid ovens. Journal of Food Science, 61, 188-191.
Li, M. G., Tian, X., Schryer, D., & Chen, X. (2011). Effect of needle geometry on flow rate and cell damage in the dispensing-based biofabrication process. AIChE Journal, 27, 1777-1784.
Li, W., Shan, Y., Xiao, X., Luo, Q., Zheng, J., Ouyang, S., & Zhang, G. (2013). Physicochemical properties of A- and B-starch granules isolated from hard red and soft red winter wheat. Journal of Agricultural and Food Chemistry, 61, 6477-6484.
Liang, H.-N., & Tang, C.-H. (2013). pH-dependent emulsifying properties of pea [Pisum sativum (L.)] proteins. Food Hydrocolloids, 33, 309-319.
Lim, K. S., & Barigou, M. (2004). X-ray micro-computed tomography of cellular food products. Food Research International, 37, 1001-1012.
Lineback, D., & Wongsrikasem, E. (1980). Gelatinization of starch in food products. Journal of Food Science, 45, 71-74.
Lipton, J., Boban, M., Hiller, J., & Lipson, H. (2010). Freeform fabrication of stochastic and ordered cellular structures. Paper presented at the 21st Solid Freeform Fabrication Symposium (SFF'10).
Lipton, J. I., Arnold, D., Nigl, F., Lopez, N., Cohen, D. L., Noren, N., . . . Cohen, D. (2010, 13 Jan 2011). Multi-material food printing with complex internal structure suitable for conventional post-processing. Paper presented at the 21st Solid Freeform Fabrication Symposium (SFF'09), Austin, US.
Liu, L., Herald, T., Wang, D., Wilson, J., & Aramouni, F. (2012). Characterization of sorghum grain and

evaluation of sorghum flour in a Chinese egg noodle system. Journal of Cereal Science, 55, 31-36.
Liu, Z., & Scanlon, M. (2003). Predicting mechanical properties of bread crumb. AIChE Journal, 81C, 224-238.
Livescu, S. (2012). Mathematical modelling of thixotropic drilling mud and crude oil flow in wells and pipelines. Journal of Petroleum Science, 98-99, 174-184.
Lopez-Sanchez, P., & Farr, R. (2012). Power laws in the elasticity and yielding of plant particle suspensions. Food Biophysics, 7, 15-27.
Lostie, M., Peczalski, R., & Andrieu, J. (2004). Lumped model for sponge cake baking during the "crust and crumb" period. Journal of Food Engineering, 65, 281-286.
Mack, S., Hussein, M. A., & Becker, T. (2013). On the theoretical time-scale estimation of physical and chemical kinetics whilst wheat dough processing. Food Biophysics, 8, 69-79.
MacRitchie, F. (1985). Studies of the methodology for fractionation and reconstitution of wheat flours. Journal of Cereal Science, 3, 221-230.
Mader, H. M., Llewellin, E. W., & Mueller, S. P. (2013). The rheology of two-phase magmas: A review and analysis. Journal of Volcanology and Geothermal Research, 257, 135-158.
Majumder, S. R., & Mazumdar, S. (2007). Mechanical breakdown of trabecular bone: Dependence on microstructure Physica A: Statistical Mechanics and its Applications, 377, 559-564.
Malda, J., Visser, J., Melchels, F. P., Jüngst, T., Hennink, W. E., Dhert, W. J. A., . . . Hutmacher, D. W. (2013). 25th anniversary article: Engineering hydrogels for biofabrication. Advanced Materials, 25, 5011-5028.
Malkin, A. Y. (2012). Liquids. Rheology. Concepts, methods and applications (2nd ed., pp. 127-222). Toronto, Canada: ChemTec Publishing.
Malvern Instruments. (2012). Understanding yield stress measurements. Malvern Instruments technical paper.
Marco, C., & Rosell, C. (2008). Functional and rheological properties of protein enriched gluten free composite flours. Journal of Food Engineering, 88, 94-103.
Marcotte, M., Sablani, S., Kasapis, S., Baik, O., & Fustier, P. (2004). The thermal kinetics of starch gelatinization in the presence of other cake ingredients International Journal of Food Science and Technology, 39, 807-810.
Marcotte, M., Taherian, A., Trigui, M., & Ramaswamy, H. (2004). Evaluation of rheological properties of selected salt-enriched food hydrocolloids. Journal of Food Engineering, 48, 157-167.
Martin, D. J., & Tsen, C. C. (1981). Baking high-ratio white layer cakes with microwave energy. Journal of Food Science, 46, 1507-1513.
Martinie, L., Buggisch, H., Willenbacher, N. (2013). Apparent elongational yield stress of soft matter. Journal of Rheology, 57, 627-646.
Mascitelli, R. (2011). Mastering lean product development. Northridge, US.: Technology Perspectives.
Massey, A., Khare, A., & Niranjin, K. (2001). Air inclusion into a model cake batter using a pressure whisk: Development of gas hold-up and bubble size distribution. Journal of Food Science, 66, 1152-1157.
Matz, S. (1972). Baking technology and engineering (2nd ed.). Westport, US.: The Avi Publishing Co.
Meadows, F. (2002). Pasting process in rice flour using Rapid Visco Analyser curves and first derivatives. Cereal Chemistry, 79, 559-562.
Meares, C. A., Bogracheva, T. Y., Hill, S. E., & Hedley, C. L. (2004). Development and testing of methods to screen chickpea flour for starch characteristics. Starch - Stärke, 56, 215-224.
Megahey, E. K., McMinn, W., & Magee, T. (2005). Experimental study of microwave baking of Madeira cake batter. Food and Bioproducts Processing, 83, 277-287.
Metzger, T. (2002). The rheology handbook. Hannover: Vincentz Verlag.
Meza, B. E., Chesterton, A. K. S., Verdini, R. A., Rubiolo, A. C., Sadd, P. A., Moggridge, G. D., & Wilson, D. I. (2011). Rheological characterisation of cake batters generated by planetary mixing: Comparison between untreated and heat-treated wheat flours. Journal of Food Engineering, 104, 592-602.
Michaelides, E. (2006). Molecular and statistical modelling. Particles, bubbles & drops (pp. 325-342). Hakensack, US.: World Scientific.
Mills, E., Wilde, P., Salt, L., & Skeggs, P. (2003). Bubble formation and stabilization in bread dough. TransIChemE, 81 Part C, 189-193.
Mills, E. N. C., Salt, L. J., & Wilde, P. J. (2007). Bubble formation and stabilisation in bread dough. In D. J. McClements (Ed.), Understanding and controlling the microstructure of complex foods (pp.

691-705). Boca Raton, US.: CRC Press.
Mitschka, P. (1982). Simple conversion of Brookfield R.V.T. readings into viscosity functions. Rheologica Acta, 21, 207-209.
Mizukoshi, M. (1983). Model studies of cake baking. III. Effects of silcone on foam stability of cake batter. Cereal Chemistry, 57, 396-399.
Mizukoshi, M., Kawada, T., & Matsui, N. (1979). Model studies of cake baking. I. Continuous observations of starch gelatinization and protein coagulation. Cereal Chemistry, 56, 305-.
Mizukoshi, M., Maeda, H., & Amano, H. (1980). Model studies of cake baking. II. Expansion and heat set of cake batter during baking. Cereal Chemistry, 57, 352-355.
Mohamed, S., & Hamid, N. A. (1998). Effects of ingredients on the characteristics of rice cakes. Journal of the Science of Food and Agriculture, 76, 464-468.
Moiraghi, M., de la Hera, E., Pérez, G. T., & Gómez, M. (2013). Effect of wheat flour characteristics on sponge cake quality. Journal of the Science of Food and Agriculture, 93, 542-549.
Mondal, A., & Datta, A. K. (2008). Bread baking - A review. Journal of Food Engineering, 86, 465-474.
Moore, W., & Hoseney, R. C. (1985). The leavening of dough. Cereal Foods World, 30, 791-792.
Morgan, T., & Depp, M. (2008). The scale-up and commercialization of new food products. In A. Brody & J. Lord (Eds.), Developing new food products for a changing marketplace (2nd ed., pp. 407-438). Boca Raton, US.: CRC Press.
Morrison, F. (2013). Using the solver Add-in Microsoft ExcelR. Retrieved 4 Jan 2014 2014 from http://www.chem.mtu.edu/~fmorriso/cm4650/Using_Solver_in_Excel.pdf
Mudgett, R. E. (1986). Microwave properties and heating characteristics of foods. Food Technology, 40, 84-93.
Murphy, S., Skardal, A., & Atala, A. (2013). Evaluation of hydrogels for bio-printing applications. Journal of Biomedical Material research part A, 101A, 272-284.
Nagaraju, V. D., & Manohar, B. (2000). Rheology and particle size changes during Idli fermentation. Journal of Food Engineering, 43, 167-171.
Narsimhan, G. (2012). Model for growth of bubbles during proofing of viscoelastic dough. Bubble Science, Engineering and Technology, 4, 63-71.
Narsimhan, G., & Ruckenstein, E. (1996). Structure, drainage, and coalescence of foams and concentrated emulsions. In R. Prud'homme & S. Khan (Eds.), Foams (pp. 99-187). New York, US.: Marcel Dekker.
Nauman, E. B. (2004). Residence time distributions. In E. Paul, V. Atiemo-Obeng, & S. Kresta (Eds.), Handbook of industrial mixing : science and practice (pp. 1-18). Hoboken, US.: Wiley-Interscience.
Navickis, L. L., & Bagley, E. B. (1983). Yield stresses in concentrated dispersions of closely packed, deformable gel particles. Journal of Rheology, 27, 519-536.
Ndife, M. K., Şumnu, G., & Bayindirli, L. (1998). Dielectric properties of six different species of starch at 2450 MHz. Food Research International, 31, 43-52.
Newport Scientific, L. (1998). Applications manual for the Rapid ViscoTM Analyser. Warriwood, Australia.
Obanni, M., & BeMiller, J. (1996). Ghost microstructures of starch from different botanical sources Cereal Chemistry, 72-3, 333-337.
Ovarlez, G., Cohen-Addad, S., Krishan, K., Goyon, J., & Coussot, P. (2013). On the existence of a simple yield stress fluid behavior. Journal of Non-Newtonian Fluid Mechanics, 193 68-79.
Ovarlez, G., Tocquer, L., Bertrand, F., & Coussot, P. (2013). Rheopexy and tunable yield stress of carbon black suspensions. Soft Matter, 9, 5540-5549.
Ozmutlu, O., Şumnu, G., & Sahin, S. (2001). Effects of different formulations on the quality of microwave baked breads. European Food Research and Technology, 213, 38-42.
Padhye, V. W., & Salunke, D. (1979). Biochemical studies on black gram (Phaseolus mungo L.) seeds: Amino acid composition and subunit constitution of fractions of the proteins. Journal of Food Science, 44, 606-610, 614.
Papalamprou, E. M., Doxastakis, G. I., Biliaderis, C. G., & Kiosseoglou, V. (2009). Influence of preparation methods on physicochemical and gelation properties of chickpea protein isolates. Food Hydrocolloids, 23, 337-343.
Pareyt, B., Finnie, S. M., Putseys, J. A., & Delcour, J. A. (2011). Lipids in bread making: Sources, interactions, and impact on bread quality. Journal of Cereal Science, 54, 266-279.
Park, S. H., Wilson, J. D., Chung, O. K., & Seib, P. A. (2004). Size distribution and properties of wheat starch granules in relation to crumb grain score of pup-loaf bread. Cereal Chemistry, 81, 699-

704.
Parkkonen, T., Heinonen, R., & Autio, K. (1997). A new method for determining the area of cell walls in rye doughs based on fluorescence microscopy and computer-assisted image analysis. LWT - Food Science and Technology, 30, 743-747.
Perrot, A., Mélinge, Y., Estellé, P., Rangeard, D., & Lanos, C. (2011). The back extrusion test as a technique for determining the rheological and tribological behaviour of yield stress fluids at low shear rates. Applied Rheology, 21, art. no. 53642.
Phan-Thien, N., & Safari-Ardi, M. (1998). Linear viscoelastic properties of flour–water doughs at different water concentrations. Journal of Non-Newtonian Fluid Mechanics, 74, 137-150.
Pierre, A., Lanos, C., & Estellé, P. (2013). Extension of spread-slump formulae for yield stress evaluation. Applied Rheology, 23, art. no. 63849.
Pomeranz, Y., Meyer, D., & Seibel, W. (1984). Wheat, wheat-rye and rye dough and bread studied by electron scanning microscopy. Cereal Chemistry, 61, 51-53.
Pool Water Treatment Advisory Group.). Carbon dioxide in water equilibrium. Retrieved 16 May 2014 from ww.pwtag.org/researchdocs/Used%20Ref%20docs/52%20Carbondioxide%20in%20water 20equilibrium.pdf
Poortinga, A. T., Koman-boterblom, H., & Wijnen, M. E. (2005). EP1520484
Primo-Martin, C., Hamer, R., & de Jongh, H. H. J. (2006). Surface layer properties of dough liquour components: Are they key parameters in gas retention in bread doughs? Food Biophysics, 1, 83-93.
Primo-Martin, C., van Neuwenhuijzen, N., Hamer, R., & Van Vliet, T. (2007). Crystallinity changes in wheat starch during the bread-making process: Starch crystallinity in the bread crust. Journal of Cereal Science, 45, 219-226.
Puncha-arnon, S., Pathipanawat, W., Puttanlek, C., Rungsardthong, V., & Uttapap, D. (2008). Effects of relative granule size and gelatinization temperature on paste and gel properties of starch blends. Food Research International, 41, 552-561.
Raeker, M., & Johnson, L. (1995). Cake-baking (high-ratio white layer) properties of egg white and bovine blood plasma, and their protein fractions. Cereal Chemistry, 72, 299-303.
Rakkar, P. (2007). Development of a gluten-free commercial bread. (Masters Thesis), Auckland University of Technology, Auckland, New Zealand. Retrieved from http://aut.researchgateway.ac.nz/bitstream/handle/10292/438/RakkarP.pdf;jsessionid=B87A2 6609C76FB132E3A100A6A56186D?sequence=1
Ramachandran, A. (2013). A macrotransport equation for the particle distribution in the flow of a concentrated, non-colloidal suspension through a circular tube. Journal of Fluid Mechanics, 734, 219-252.
Rao, M. (2007a). Appendix 3-B. Analysis of steady laminar fully developed flow in a pipe. In M. Rao (Ed.), Rheology of fluid and semisolid foods (2nd ed., pp. 145-149). New York, US.: Springer.
Rao, M. (2007b). Application of rheology to fluid food handling. In M. Rao (Ed.), Rheology of fluid and semisolid foods (2nd ed., pp. 427-470). New York, US.: Springer.
Rao, M. (2007c). Flow and functional models for rheological properties of fluid foods. In M. Rao (Ed.), Rheology of fluid and semisolid foods (2nd ed., pp. 27-58). New York, US.: Springer.
Rao, M. (2007d). Measurement of flow and viscoelastic properties. In M. Rao (Ed.), Rheology of fluid and semisolid foods (2nd ed., pp. 59-151). New York, US.: Springer.
Rao, M. (2007e). Rheological behavior of processed fluid and semisolid foods. In M. Rao (Ed.), Rheology of fluid and semisolid foods, 2nd edition (2nd ed., pp. 223-260). New York, US.: Springer.
Rao, M. (2007f). Rheology of food gum and starch dispersions. In M. Rao (Ed.), Rheology of fluid and semisolid foods (2nd ed., pp. 153-222). New York, US.: Springer.
Raphaelides, S. N., & Georgiadis, N. (2007). Effect of fatty acids on the rheological behaviour of pea starch dispersions during heating. Food Hydrocolloids, 21, 1188-1200.
Rasband, W. (2005). ImageJ (Vol. Avaliable at http//:rsb.info.nih.gov/ij/). Bestheda, US.: US National Institutes for Health.
Rasper, V. F., & deMan, J. M. (1980). Effect of granule size of substituted starches on the rheological character of composite doughs. Cereal Chemistry, 57, 331 - 340.
Ratnayake, W. S., Hoover, R., & Warkentin, T. (2002). Pea starch: composition, structure and properties - A Review. Starch - Stärke, 54, 217-234.
Rayment, P., Ross-Murphy, S. B., & Ellis, P. R. (1995). Rheological properties of guar galactomannan and rice starch mixtures. I. Steady shear measurements. Carbohydrate Polymers, 28, 121-130.
Rayment, P., Ross-Murphy, S. B., & Ellis, P. R. (1998). Rheological properties of guar galactomannan and

rice starch mixtures. II. Creep measurements. Carbohydrate Polymers, 35, 55-63.
Rayment, P., Ross-Murphy, S. B., & Ellis, P. R. (2000). Effect of size and shape of particulate inclusions on the rheology of guar galactomannan solutions. 43Carbohydrate Polymers, 1-9.
Reddy, N., Sathe, S., Pierson, M., & Salunkhe, D. K. (1982). Idli, an Indian fermented food: A review. Journal of Food Quality, 5, 89-101.
Regner, M., Östergren, K., & Trägårdh, C. (2008). Influence of viscosity ratio on the mixing process in a static mixer: Numerical study. Industrial and Engineering Chemistry Research, 47 3030-3036.
Renzetti, S., Dal Bello, F., & Arendt, E. K. (2008). Microstructure, fundamental rheology and baking characteristics of batters and breads from different gluten-free flours treated with a microbial transglutaminase. Journal of Cereal Science, 48, 33-45.
Rielly, C. (1997). Mixing in food processing. In P. Fryer, D. Pyle, & C. Rielly (Eds.), Chemical engineering for the food industry (1st ed., pp. 383-433). London, UK.: Blackie Academic and Professional.
Rojas, J. A., Rosell, C. M., Benedito de Barber, C., Pérez-Munuera, I., & Lluch, M. (2000). The baking process of wheat rolls followed by cryo scanning electron microscopy. European Food Research and Technology, 212, 57-63.
Romero, A., Beaumal, V., David-Briand, E., Cordobes, F., Guerrero, A., & Anton, M. (2012). Interfacial and emulsifying behaviour of rice protein concentrate. Food Hydrocolloids, 29, 1-8.
Rouille´, J., Della Valle, G., Lefebvre, L., Sliwinski, E., & van Vliet, T. (2005). Shear and extensional properties of bread doughs affected by their minor components Journal of Cereal Science, 42, 45-57.
Rouyer, F., Haffner, B., Louvet, N., Khidas, Y., & Pitois, O. (2014). Foam clogging. Soft Matter.
Russ, J. (1999). Statistical interpretation of data. Practical Stereology. New York, US.: Plenum Press.
Russ, J. (2005a). Measuring features. Image analysis of food structure. Boca Raton, US.: CRC Press.
Russ, J. (2005b). Stereology. Image analysis of food structure (pp. 1-49). Boca Raton: CRC Press.
Russ, J. (2007a). The image processing handbook. (5th ed., pp. 817). Boca Raton, US.: CRC Press
Russ, J. (2007b). Segmentation and thresholding. The image processing handbook (5th ed., pp. 397-441). Boca Raton, US.: CRC Press
Russell, J. R., Candler, A. M., & Wright, A. (2009). US.
Rust, A. C., & Manga, M. (2002). Effects of bubble deformation on the viscosity of dilute suspensions. Journal of Non-Newtonian Fluid Mechanics, 104, 53-63.
Ryynänen, S. (1995). The electromagentic properties of food materials: a review of basic principles. Journal of Food Engineering, 29, 409-429.
Sablani, S., Marcotte, M., Baik, O., & Castaigne, F. (1998). Modeling of simultaneous heat and water transport in the baking process. Lebensmittel-Wissenschaft und-Technologie, 31, 201-209.
Sagis, L. M. C., & Scholten, E. (2014). Complex interfaces in food: Structure and mechanical properties. Trends in Food Science and Technology, 37, 59-71.
Sahi, S. S., & Alava, J. M. (2003). Functionality of emulsifiers in sponge cake production. Journal of the Science of Food and Agriculture, 83, 1419-1429.
Sahni, J. (1990). Moghul microwave: William Morrow.
Sahu, J., & Niranjan, K. (2009). Gas-liquid mixing. In P. Cullen (Ed.), Food Mixing: Principles and applications (pp. 231-252). Oxford, U.K.: Blackwell Publishing.
Sakiyan, O., Şumnu, G., Sahin, S., & Meda, V. (2007). Investigation of dielectric properties of different cake formulations during microwave and infrared-microwave combination baking. Journal of Food Science, 72, E205-E213.
Sakonidou, E. P., Karapantsios, T. D., & Raphaelides, S. N. (2003). Mass transfer limitations during starch gelatinization. Carbohydrate Polymers, 53, 53-61.
Salmon, P. (2004). A short guide to analysis of bone by micro-CT. Atseelar, Belgium: Skyscan NV.
Samustri, W., & Suphantharika, M. (2012). Effect of salts on pasting, thermal, and rheological properties of rice starch in the presence of non-ionic and ionic hydrocolloids. Carbohydrate Polymers, 87, 1559-1568.
Sánchez-Pardo, M. E., Ortiz-Moreno, A., Mora-Escobedo, R., Bello-Pérez, A., Yee-Madeira, H., & Ramos-López, G. (2008). Effect of baking method on some characteristics of starch in pound cake crumbs. Journal of the Science of Food & Agriculture, 88, 207-213.
Sánchez-Pardo, M. E., Ortiz-Moreno, A., Mora-Escobedo, R., Chanona-Pérez, J. J., & Necoechea-Mondragón, H. (2008). Comparison of crumb microstructure from pound cakes baked in a microwave or conventional oven. LWT - Food Science and Technology, 41, 620-627.
Sánchez-Vioque, R., Clemente, A., Vioque, J., Bautista, J., & Millán, F. (1999). Protein isolates from chickpea (Cicer arietinum L.): chemical composition, functional properties and protein

characterization. Food Chemistry, 64, 237-243.
Sandstedt, R., Schaumberg, L., & Fleming, J. (1954). The microscopy of the structure of bread and dough. Cereal Chemistry, 31, 43-45.
Sankar, D. (2011). Two-phase non-linear model for blood flow in asymmetric and axisymmetric stenosed arteries. International Journal of Non-Linear Mechanics, 46, 296-305.
Sanz, T., Salvador, A., Biaixauli, R., & Fiszman, S. (2009). Evaluation of four types of resistant starch in muffins. II. Effects in texture, colour and consumer response. European Food Research and Technology, 229, 197-204.
Sapirstein, H. D., Roller, R., & Bushuk, W. (1994). Instrumental measurement of bread crumb grain by Digital Image Analysis. Cereal Chemistry, 71, 383-391.
Scanlon, M. G., & Zghal, M. C. (2001). Bread properties and crumb structure. Food Research International, 34, 841-864.
Schiffmann, R. (2005). Packaging for microwave foods. Woodhead Publishing, Cambridge, England.
Schindelin, J. (2008, 6-7 Nov 2008). Fiji is just ImageJ- with batteries. Paper presented at the ImageJ User and Developer Conference, Luxembourg.
Schober, T., Bean, S., & Boyle, D. (2007). Gluten-free sorghum bread improved by sourdough fermentation: biochemical, rheological, and microstructural background. Journal of Agricultural and Food Chemistry, 55, 5137-5146.
Schober, T., Bean, S., Boyle, D., & Park, S.-H. (2008). Improved viscoelastic zein–starch doughs for leavened gluten-free breads: Their rheology and microstructure. Journal of Cereal Science, 48, 755-767.
Shea, T., Houghton, B. F., Gurioli, L., Cashman, K. V., Hammer, J. E., & Hobden, B. J. (2010). Textural studies of vesicles in volcanic rocks: An integrated methodology. Journal of Volcanology and Geothermal Research, 190, 271-289.
Shehzad, A., Chiron, H., Della Valle, G., Kansou, K., Ndiaye, A., & Réguerre, A. L. (2010). Porosity and stability of bread dough during proofing determined by video image analysis for different compositions and mixing conditions. Food Research International, 43, 1999-2005.
Shenoy. (1999a). Introduction. Rheology of filled polymer systems. (pp. 1-43). Dordrecht, Nld: Kluwer Academic.
Shenoy, A. (1999b). Basic rheological concepts. Rheology of filled polymer systems (pp. 54-111). Dordrecht, Nld: Kluwer Academic.
Shenoy, A. (1999c). Constitutive theories and equations for suspensions. Rheology of filled polymer systems (pp. 136-174). Dordrecht, Nld: Kluwer Academic.
Shenoy, A. (1999d). Extensional flow properties. Rheology of filled polymer systems (pp. 395-415). Dordrecht, Nld: Kluwer Academic.
Shenoy, A. (1999e). Steady shear elastic properties. Rheology of filled polymer systems (pp. 312-337). Dordrecht, Nld: Kluwer Academic.
Shenoy, A. (1999f). Steady shear viscous properties. Rheology of filled polymer systems (pp. 203-311). Dordrecht, Nld: Kluwer Academic.
Shimiya, Y., & Nakamura, K. (1997). Changes in size of gas cells in dough and bread during breadmaking and calculation of critical size of gas cells that expand. Journal of Texture Studies, 28, 273-288.
Shimiya, Y., & Yano, T. (1987). Measurements of accompanying air, specific surface area and micropore volumes of some flour particles. Agricultural and Biological Chemistry, 51, 25-30.
Shukla, T., & Anantheswaran, R. (2001). Ingredient interactions and product development for microwave heating. In A. Datta & R. Anantheswaran (Eds.), Handbook of microwave technologies for food applications (pp. 355-395). New York, US: Marcel Dekker.
Singh, A., & Bhattacharya, M. (2005). Development of dynamic modulus and cell opening of dough during baking. Journal of Texture Studies, 36, 44-67.
Singh, N., Kaur, L., Sodhi, N. S., & Sekhon, K. S. (2005). Physicochemical, cooking and textural properties of milled rice from different Indian rice cultivars. Food Chemistry, 89, 253-259.
Skyscan. (2009). Structural parameters measured by Skyscan™ CT-analyzer software. Kontich, Belgium: Skyscan NV.
Sliwinski, E. L., Kolster, P., & Van Vliet, T. (2004). On the relationship between large-deformation properties of wheat flour dough and baking quality. Journal of Cereal Science, 39, 231-245.
Smith, M. (2014). Viscosities of common liquids. In http://www.michael-smith-engineers.co.uk/pdfs/ViscositiesofCommonLiquids2.pdf (Ed.).
Soares, S., Kupfer, P., Nicholls, B., Spears, K., Walters, P., & Southerland, D. (2011). Insects Au Gratin. Retrieved 3 Mar 2012 from http://www.susanasoares.com/index.php?id=82

Song, J., & Shin, M. (2007). Effects of soaking and particle sizes on the properties of rice flour and gluten-free rice bread Food Science and Biotechnology, 16, 759-764.
Sroan, B. S., Bean, S. R., & MacRitchie, F. (2009). Mechanism of gas cell stabilization in bread making. I. The primary gluten–starch matrix. Journal of Cereal Science, 49, 32-40.
Sroan, B. S., & MacRitchie, F. (2009). Mechanism of gas cell stabilization in breadmaking. II. The secondary liquid lamellae. Journal of Cereal Science, 49, 41-46.
Stading, M., Franzoni, G., & Johansson, D. (2012). What determines foaming ability of a melt - rheology or surface tension? Annual Transactions of the Nordic Rheology Society, 20, 141-144.
Stauffer, C. (1998). Principles of dough formation. In S. Cauvain & L. Young (Eds.), Technology of breadmaking. London, UK.: Chapman and Hall.
Steeneken, P. (1989). Rheological properties of aqueous suspensions of swollen starch granules. Carbohydrate Polymers, 11, 23-42.
Steffe, J. F., & Daubert, C. R. (2006a). Bioprocessing pipelines: Rheology and analysis. East Lansing, US.: Freeman Press.
Steffe, J. F., & Daubert, C. R. (2006b). Fanning friction factors. Bioprocessing pipelines: Rheology and analysis (pp. 63-74). East Lansing, US.: Freeman Press.
Steffe, J. F., & Daubert, C. R. (2006c). Pipeline rheology. Bioprocessing pipelines: Rheology and analysis (pp. 15-34). East Lansing, US.: Freeman Press.
Steffe, J. F., & Daubert, C. R. (2006d). Rheological properties of biological fluids. Bioprocessing pipelines: Rheology and analysis (pp. 1-14). East Lansing, US.: Freeman Press.
Stoll, H. W. (1999). Product design methods and practices. New York, US.: Marcel Dekker.
Şumnu, G. (2001). A review on microwave baking of foods. International Journal of Food Science and Technology, 36, 117-127.
Şumnu, G., & Sahin, S. (2005). Baking using microwave processing. In H. Schubert & M. Regier (Eds.), The microwave processing of foods (pp. 119-141). Cambridge, England: Woodhead Publishing.
Susheelamma, N., & Rao, M. (1974). Surface-active principle in black gram (Phaseolus mungo) and its role in the texture of leavened foods containing the legume. Journal of the Science of Food and Agriculture, 25, 665-673.
Susheelamma, N., & Rao, M. (1978). Isolation and characterization of arabinogalactan from black gram (Phaseolus mungo). Journal of Agricultural and Food Chemistry, 26, 1434-1437.
Susheelamma, N., & Rao, M. (1979). Functional role of the arabinogalactan of black gram (Phaesolus mungo) in the texture of leavened foods (steamed puddings). Journal of Food Science, 49, 1309-1316.
Swain, M. J., James, S. J., & Swain, M. V. L. (2008). Effect of power output reduction of domestic microwave ovens after continuous (intermittent) use on food temperature after reheating. Journal of Food Engineering, 87, 11-15.
Swain, M. J., Spinassou, A., & Swain, M. V. L. (2008). A test procedure to characterise the heating performance of domestic microwave ovens. International Journal of Food Science and Technology, 43, 15-23.
Sympatec. (2011a). Model distribution Sympatec Scientific Forum. Retrieved 25 Jun 2013 from http://www.sympatec.com/Science/Characterisation/03_ModelDistribution.html
Sympatec. (2011b). Particle-Size distribution Sympatec Scientific Forum. Retrieved 25 Jun 2013 from http://www.sympatec.com/Science/Characterisation/02_ParticelSizeDistribution.html
Szczezniak, A. (1987). Correlating sensory withn instrumental texture measurements- an overview of recent developments. Journal of Texture Studies, 18, 1-15.
TA_Instruments. (2012). Rheology applications note. Rheology software models (flow). TA Instruments Research Note, (RN-9), 5. www.tainstruments.com/library_download.aspx?file=RN9.PDF
TA Instruments. (2013). Understanding rheology of structured fluids. www.tainstruments.com/pdf/literature/AAN016_V1_U_StructFluids.pdf
TA Instruments. (2014). Exponent software for TA-texture Analyser, verison 6, 1, 5, 0. Application guide
Tadmor, Z., & Gogos, C. (2002). Mixing. Principles of polymer processing (2nd ed., pp. 322-408). Hobokken, US.A: Wiley-Interscience.
Tang, Y., Bian, X., Du, Z., & Wang, C. (2015). Measurement and prediction model of carbon dioxide solubility in aqueous solutions containing bicarbonate anion. Fluid Phase Equilibria, 386, 56-64.
Tanner, F. X., Al-Habahbeh, A. A., Feigl, K. A., Nahar, S., Jeelani, S. A. K., Case, W. R., & Windhab, E. J. (2012). Numerical and experimental investigation of a non-newtonian flow in a collapsed elastic tube. Applied Rheology, 22, 639101-639108.
Taylor, R. A., Penney, W. R., & Vo, H. X. (2005). Scale-up methods for fast competitive chemical reactions

in pipeline mixers. Industrial and Engineering Chemistry Research, 44, 6095-6102.
Tessmar, J., Brandl, F., & Gopferich, A. (2009). Hydrogels for tissue engineering. In U. Meyer, T. Meyer, J. Handschel, & H. Wiesmann (Eds.), Fundamentals of tissue engineering and regenerative medicine (pp. 495-517). Berlin, F.R.G.: Springer.
Tester, R., & Morrison, W. R. (1990). Swelling and gelatinization of cereal starches. 1. Effects of amylopectin, amylose, and lipids. Cereal Chemistry, 67, 551-557.
Texture-Technologies. (2008). Texture Profile Analysis http://www.texturetechnologies.com/texture_profile_ analysis.html
Thakur, R. K., Vial, C., Nigam, K. D. P., Nauman, E. B., & Djelveh, G. (2003). Static mixers in the process industries - a review. Chemical Engineering Research and Design, 81, 787-826.
Tharanathan, R. N., Reddy, G. C., Muralikrishna, G., Susheelamma, N. S., & Bhat, U. R. (1994). Structure of a galactoarabinan-rich pectic polysaccharide of native and fermented blackgram (Phaseolus mungo). Carbohydrate Polymers, 23, 121-127.
The CandyFab Project. (2008). Welcome to candyfab.org and The CandyFab Project! http://wiki.candyfab.org/
the imagine machine. (2013). Image 3D printer specifications. Retrieved 27 Dec 2013 from http://www.theimaginemachine.com/en/specifications
The Sugar Lab. (2013). 3D printed sugar. Retrieved 8 Aug. 2013 from The-Sugar-Lab.com
Thomas, D., & Atwell, W. (1999). Starches. St Paul, Minnesota, US.: Eagan Press.
Toews, R., & Wang, N. (2013). Physicochemical and functional properties of protein concentrates from pulses. Food Research International, 52, 445-451.
Tolstoguzov, V. (2003). Some thermodynamic considerations in food formulation. Food Hydrocolloids, 17, 1-23.
Tolstoguzov, V. (2006). Texturising by phase separation. Biotechnology Advances, 24, 626-628.
Trinh, K. T., & Trinh, B. (2009a). Solid rheology and textural analysis. 141.292/280.297. Food and packaging engineering 1/ Industrial material technology. Study notes (pp. 72). Palmerston North: Massey University.
Trinh, K. T., & Trinh, B. (2009b). Viscoelasticity. 141.292/280.297. Food and packaging engineering 1/ Industrial material technology. Study notes (pp. 30). Palmerston North: Massey University.
Tsamopoulos, J., Makopoulos, D., Chatzidai, N., Karapetas, G., & Pavlidis, M. (2008). Steady bubble rise and deformation in Newtonian and viscoplastic fluids and conditions for bubble entrapment. Journal of Fluid Mechanics, 601, 123-164.
Ubbink, J., Burbidge, A., & Mezzenga, R. (2008). Food structure and functionality. Soft Matter, 4, 1569-1581.
Ulrich, K., & Eppinger, S. (2008). Product design and development (5th ed.). Boston, US.: McGraw-Hill Higher Education.
Ulrich, K., & Eppinger, S. (2011a). Product architecture. Product design and development (5th ed., pp. 183-206). Boston, US.: McGraw-Hill Higher Education.
Ulrich, K., & Eppinger, S. (2011b). Product design and development (5th ed.). Boston, US.A.: McGraw-Hill Higher Education.
Ulrich, K., & Eppinger, S. (2011c). Product specifications. Product design and development (5th ed., pp. 91-116). Boston, US.A.: McGraw-Hill Higher Education.
Umbach, S., Davis, E., & Gordon, J. (1990). Effects of heat and water transport on the bagel-making process: Conventional and microwave baking. Cereal Chemistry, 67, 355-360.
Van Der Vaart, K., Rahmani, Y., Zargar, R., Hu, Z., Bonn, D., & Schall, P. (2013). Rheology of concentrated soft and hard-sphere suspensions. Journal of Rheology, 57, 1195-1209.
van Vliet, T., Janssen, A. M., Bloksma, A., & Walstra, P. (1992). Strain hardening of dough as a requirement for gas retention. Journal of Texture Studies, 23, 439-460.
Vargaftik, N., Volkov, B., & Voljak, L. (1983). International tables of the surface tension of water. Journal of Physical & Chemical Reference Data, 12, 817-820.
Viebke, C. (2004). Order–disorder conformational transition of xanthan gum. In S. Dumitriu (Ed.), Polysaccharides: CRC Press Retrieved from DOI: 10.1201/9781420030822.ch17
Viturawong, Y., Achayuthakan, P., & Suphantharika, M. (2008). Gelatinization and rheological properties of rice starch/xanthan mixtures: Effects of molecular weight of xanthan and different salts. Food Chemistry, 111, 106-114.
Voortman, L. (2006). Network representation of a connected cellular matrix. (Bachelor of Applied Physics Student project), Delft University of Technology, Delft.
Wagner, M., Quellec, S., & Trystram, G. L., T. (2008). MRI evaluation of local expansion in bread crumb

during baking. Journal of Cereal Science, 48, 213-223
Waigh, T. A., Gidley, M. J., Komanshek, B. U., & Donald, A. M. (2000). The phase transformations in starch during gelatinisation: a liquid crystalline approach. Carbohydrate Research, 328, 165-176.
Walstra, P. (2003a). Formation of emulsions and foams. Physical chemistry of foods (pp. 355-390). New York, US.: Marcel Dekker.
Walstra, P. (2003b). Surface phenomena. Physical chemistry of foods (pp. 279-354). New York, US.: Marcel Dekker.
Wang, S., Karrech, A., Regenauer-Lieb, K., & Chakrabati-Bell, S. (2013). Digital bread crumb: Creation and application. Journal of Food Engineering, 116, 852-861.
Weaire, D., & Hutzler, S. (1999). Making foams. The physics of foams (pp. 246). Oxford: Clarendon Press.
Wegrzyn, T. F., Golding, M., & Archer, R. H. (2012). Food Layered Manufacture: A new process for constructing solid foods. Trends in Food Science and Technology, 27, 66-72.
Wein, O. (2005). Viscometric flow under apparent wall slip in parallel-plate geometry Journal of Non-Newtonian Fluid Mechanics, 126, 1005-1114.
Whitworth, M. (2008). X-ray tomography of structure formation in bread and cakes during baking. In G. Campbell, M. Scanlon, & D. Pyle (Eds.), Bubbles in Food 2 (pp. 273-286). St Paul, US.: Eagen Press.
Wibowo, C., & Ng Ka, M. (2001). Product Oriented Process Synthesis and development: cream and pastes. Process System Engineering, 47, 2746-2767.
Wikipedia. (2014). Hemorheology. Retrieved 2 Jan 2014 from http://en.wikipedia.org/wiki/Hemorheology #cite_note-29
Wikipedia. (2015). Nucleation. Retrieved 21 April 2015 from http://en.wikipedia.org/wiki/Nucleation
Wilderjans, E., Luyts, A., Brijs, K., & Delcour, J. A. (2013). Ingredient functionality in batter type cake making. Trends in Food Science & Technology, 30, 6-15.
Wilderjans, E., Luyts, A., Goesaert, H., Brijs, K., & Delcour, J. A. (2010). A model approach to starch and protein functionality in a pound cake system Food Chemistry, 120, 44-51.
Willhoft, E. (1973). Mechanism and theory of staling of bread and baked goods, and associated changes in textural properties. Journal of Texture Studies, 4, 292-322.
Wilson, D. I., & Rough, S. L. (2012). Paste engineering: Multi-phase materials and multi-phase flows. Canadian Journal of Chemical Engineering, 90, 277-289.
Wyatt, N. B., Gunther, C. M., & Liberatore, M. W. (2011). Increasing viscosity in entangled polyelectrolyte solutions by the addition of salt. Polymer, 52 2437-2444.
Wyatt, N. B., & Liberatore, M. W. (2009). Rheology and viscosity scaling of the polyelectrolyte xanthan gum. Journal of Applied Polymer Science, 114, 4076-4084.
Xu, Y., Howes, T., Adhikari, B., & Bhandari, B. (2012). Investigation of relationship between surface tension of feed solution containing various proteins and surface composition and morphology of powder particles. Drying Technology, 13.
Xue, J., & Ngadi, M. (2007). Thermal properties of batter systems formulated by combinations of different flours. LWT - Food Science and Technology, 40, 1459-1465.
Yang, X., & Foegeding, E. A. (2011). The stability and physical properties of egg white and whey protein foams explained based on microstructure and interfacial properties. Food Hydrocolloids, 25, 1687-1701.
Yano, T., & Shimiya, Y. (1987). Expansion of a spherical hole in elastic food materials with surface tension. Agricultural and Biological Chemistry, 52, 3113-3117.
Yeow, Y., Leong, L., & Khan, A. (2006). Non-Newtonian flow in parallel-disk viscometers in the presence of wall slip. Journal of Non-Newtonian Fluid Mechanics, 139, 85-92.
Young, L., Davies, P., & Cauvain, S. (1999, December 1999). Cakes: getting the right balance. Paper presented at the Proceedings of ES98, the Eighteenth Annual International Conference of the British Computer Society Specialist Group on Expert Systems, Cambridge, England.
Yue, P., Feng, J. J., Bertelo, C. A., & Hu, H. H. (2007). An arbitrary Lagrangian-Eulerian method for simulating bubble growth in polymer foaming. Journal of Computational Physics, 226, 2229-2249.
Zanoni, B., Smaldone, D., & Schiraldi, A. (1991). Starch gelatinization in chemically leavened bread. Journal of Food Science, 56, 702-706.
Zghal, M. C., Scanlon, M. G., & Sapirstein, H. D. (2002). Cellular structure of bread crumb and its influence on mechanical properties. Journal of Cereal Science, 36, 167-176.
Zhang, J., & Datta, A. (2006). Mathematical modeling of bread baking process. Journal of Food

Engineering, 75, 78-89.
Zhang, G., & Hamaker, B. (2003). A three component interaction among starch, protein, and free fatty acids revealed by pasting profiles. Journal of Agricultural and Food Chemistry, 51, 2797-2800.

Appendix A Terms and abbreviations

A.1 General terms and abbreviations

TERM	DEFINITION
Additive Manufacturing	Joining materials layer by layer to make objects from a 3D digital model
AM	Additive Manufacturing
BF	Bean fragments
BG	Blackgram
BiC	Sodium bicarbonate
Bin	A sorting category in digital image analysis
Binarisation	Sorting digital image pixels into one of two bins
BBM	Bean-buttermilk base in idli formulations
BBM_{Liq}	Particulate-free bean-buttermilk fraction
BM	Buttermilk
BM_{Liq}	Particulate-free buttermilk fraction
Biopolymer domain	Discrete biopolymer-rich region within the sponge product solid phase, a level in hierarchy of structure for sponge products
CP	Chickpea
CSLM	Confocal scanning laser microscopy
CoV	Coefficient of variance
Crumb	Interior of a baked sponge product
Crust	Dry surface of a baked product
CT	Computed x-ray tomography
D_B	Fractal box dimension
Degree of anisotropy	Unevenness in porosity distribution with a porous solid
Die swell	Expansion of fluid on exiting an outlet due to fluid elastic effects
dpi	Dots per inch
DSC	Differential scanning calorimetry
dwb	Dry weight basis
EM	Electron microscopy
First-principle relationships	Events at the molecular level and fundamental properties of the system
FV	Final Viscosity value on pasting using the Rapid ViscoAnalyser™
Food Layered Manufacture	Forming solid or gelled food items using the Additive Manufacturing process
FLM	Food Layered Manufacture
FoV	Field of view
GF	Gluten-free
HD	Hadiyanto thesis “Quality design driven food process design”
Hierarchy of structure	Ordering of structural features into distinct levels defined by the observer
h	Hour

TERM	DEFINITION
i.d.	Internal diameter
Image pre-processing	Optimisation of digital image features before analysis, by filtering, etc.
LDS	Laser diffraction particle sizing
Loss modulus	Viscous component of material response to oscillating shear
LT	Local Thickness
Mesostructure	Organisation of the liquid closed-cell foam and solid open-celled foam, a level in hierarchy of structure for sponge products
MCC	Micro-crystalline methyl cellulose
Microbubbles	Small bubbles of gas trapped on and in particulates
Microstructure	Composite structure in the sponge product solid phase formed of distinct biopolymer domains, a level in hierarchy of structure for sponge products
µCT	Computed x-ray micro-tomography
min	Minute
NSP	Non-starch polysaccharide
Object	The whole item to be examined by sectioning on digital image analysis
Particle	In digital image analysis, a discrete item identified in sections of a whole object
Particle	In material characterisation, drops, bubbles, or solid particles
Particulate	In this study, a solid (material) particle
PE	Pea
Process-intensive product design	Design requiring product and process to be developed together
PV	Peak Viscosity on pasting using the Rapid ViscoAnalyser™
Retrogradation	Increasing crystallinity of starch polymer organisation in sponge products microstructure over time
Rheology	Study of material behaviour under deformation
R1	Rice1
R2	Rice2
RVA	Rapid ViscoAnalyser™
SD	Standard deviation
s	Second
SE	Standard error
Segmentation	Partitioning of digital image pixels into categories for analysis
SG	Sorghum
Storage modulus	Elastic component of material response to oscillating deformation
Strain hardening	Stiffening of viscoelastic materials under bi-extensional flow
Sub-structure	Structures within biopolymer domains, a level in hierarchy of structure for sponge products
Technology-push	Design for a product for which no market exists as yet
Tortuosity	Interconnectivity of voids in a porous solid
Transformation	Phase change (e.g. from liquid to solid) or a change in chemical composition

TERM	DEFINITION
U&E	Ulrich and Eppinger text “Product design and development”
Unbiased count	Unbiased particle counting in images by use of a count box
Viscoelastic	Having properties of both viscous fluid flow and elastic solid
Void	Open-cell bubble in cooked sponge product
Voxel	Volumetric unit corresponding to an image pixel
vs.	versus
Wall slip	Lubricating layer formed on pipe flow in structured fluids due to friction at the boundary surface
wwb	Wet weight basis

A.2 Engineering and chemical terms

TERM	DEFINITION	UNIT
a	Exponent for Carreau-Yasuda equation	
B	Consistency coefficient for Herschel-Bulkley equation	Pa s^n
c	Exponent for Carreau-Yasuda equation	
Ca	Capillary number, ratio of external fluid viscous forces and interfacial surface tension acting on a bubble	dimensionless
d	Diameter	m
E_f	Energy loss in a pipe system due to friction	J/ kg
$\boldsymbol{g}$	Gravitational force	m/ s^2
G'	Storage modulus, elastic component of material response to oscillating deformation	Pa
G''	Loss modulus, viscous component of material response to oscillating deformation	Pa
GRe	Generalised Reynolds number for power law fluids	dimensionless
K	Consistency coefficient for power law fluid equation	Pa s^n
L	Length	m
n	Power index exponent for power law fluid equation	dimensionless
P	Pressure	Pa, N/m^2
p	Exponent for Herschel-Bulkley fluid equation	
Q	Flow rate	m^3 /s
RE	Reynolds number for Newtonian fluids	dimensionless
v_z	Average velocity of fluid flow in a pipe at point z	m/ s
s	second	
W	Work	J/ kg
X	Mass fraction	kg

GREEK SYMBOLS

TERM	DEFINITION	UNIT
ρ	Fluid density	
σ	Shear stress force occurring perpendicular to fluid flow	Pa
σ_{YS}	Yield stress, minimal stress value at which a structured fluid flows	Pa
γ	Shear strain, change in length, width and height relative to pre-deformation values	Unit/unit
$\dot{\gamma}$	Shear rate	/s
$\dot{\gamma}_{\mathrm{Wall}}$	Shear rate at pipe wall	/s
η_{A}	Apparent viscosity of non-Newtonian fluid	Pa s
η_{YS}	Apparent viscosity at yield stress	Pa s
η_{∞}	Infinite shear viscosity	Pa s
η'	Normalised viscosity	dimensionless
λ	Relaxation time, typical time-period for a system to adjust to a change in deformation	s
ϕ	Phase volume fraction	dimensionless
Λ	Lacunarity, fractal measure of void organisation	dimensionless
Γ	Interfacial surface tension	N/ area

Appendix B F-Inks Food design Outline, April 2008

B.1 Problem

Develop a shelf-stable *coloured and flavoured* printable food ink paste (F-ink) that retains integrity of printed form during rapid baking to give a novel edible food product. The target is at least one ingredient form suitable for patenting of proof of concept of F-ink products by Oct 2008.

B.1.1 Objective

Formulate a storable *coloured and flavoured* ingredient paste that is pipeable at low pressure and can maintain a complex printed form without slumping. The paste must cook rapidly into an edible leavened product that retains the character of the printed form.

B.2 Output variables

Ingredient variables	**Consumer product**
Retains form on printing	Retains printed form on cooking (appearance and colour)
Cooks evenly within time constraints	Expands to appropriate product volume
Shelf-stable	Acceptable taste
Pipeable	Acceptable texture (mouth-feel)

B.3 Product concept

An ingredient paste with minimal microbial growth stored over 60 days at 20 ºC in an F-ink printer cartridge. The ingredient paste can be coloured and flavoured into different F-inks either during production or as part of the printing process.

The F-ink paste can be pumped from the nozzle of an F-ink X-Y printer at low pressures (1 kPa) and a flow rate 200-300 cm^3/min into discrete layers 3-5 mm thick) onto a pre-prepared flatbread. The final printed form may be 15-30 mm in height. Ingredient layers will retain their printed outline without slumping for at least 5 min standing time and though cooking.

Cooking should occur within 5 min by microwave or microwave-combination heating. Through the use of leavening agents or introduced gas the printed form may expand to 30-50 mm in height on cooking. The final product will have an acceptable flavour and pleasant mouth-feel to consumers and retain the printed format.

B.4 Development constraints

Initial ingredient development will focus on pre-gelatinised starch-based pastes, presumably in a cake or bread-like form leavened by non-yeast agents. Cooking will use a domestic tabletop combination microwave-convection oven. The final texture of the product will be limited by the successful F-ink ingredient paste composition(s). These may be crisp cookie, soft cake or savoury rice paste forms or some combination).

B.5 Input variables

Ingredient variables	Processing variables
Starch content	Degree of starch pre-gelatinisation (partial to complete)
Water content	(Drying of gelatinised starch)
Fats	Order of ingredient addition
Polysaccharides	Holding period after gelatinisation and mixing (days)
Protein	Printing rate (min-max)
Sugar	Microwave power (20-100% power, 2450 MHz)
Emulsifier	Non-microwave power in combination with microwave cooking?
Humifactant	Position in oven (bottom, middle, top)
Salt	Cook time (3-5 min)
Leavening agent	
Preservative	
(Flavour)	

B.6 Experimental approach

B.6.1 Product output: measurement methodologies

1. Retains form on printing (digital record of printed form)
2. Cooks evenly within time constraints (evaluation of starch gelatinisation through segments of product, light microscopy; iodine staining)
3. Shelf-stable (storage trial, followed by microbial testing, colour evaluation and printing/cooking evaluation)
4. Pipeable (RVA analysis of ingredient texture; print trial or emulation trial)
5. Retains printed form on cooking (digital record of product)
6. Expands to appropriate product volume (measurements of dimensions; volume by rapeseed method; volume after compression at 24 kg).
7. Acceptable texture (informal sensory evaluation; Instron spike test; Instron deformation test)
8. Acceptable taste (informal sensory evaluation).

Appendix C Food-Inks 3D Printer: Delivering controlled colour into a voxel

C.1 Background

The process target for 3D printing requires the controlled high-resolution addition of colour into a line of continuous batter flow. The aim is to produce many colour shades within a small volume of the continuous flow on rapid mixing (target voxel of 0.3 mL; flow rate 200-300mL/min). A second mixing task is the addition of a gas phase to aerate the batter before deposition. The two tasks may be separate processes, or a combination mixing process.

The batter (a dispersion including flour particles) is required to be pipeable and to have a rapid set-up after deposition. Xanthan addition to the formulation may be one way of managing stop-start-stop flow characteristics. The viscosity range limits the mixing options to in-line static mixers or combination mixing-aeration system such as the Mondomix. The equipment design also needs to be easy-to-clean, using CIP or disposable mixer elements which are compatible with fast-food or domestic usage.

C.1.1 Research sections

1. Colour
    a. Carrier type
        - Synthetic water soluble dyes
        - Lakes (water-soluble dyes on insoluble base)
        - Pastes
        - Powders
    b. Dye addition process order options
        - Pre-coloured batters (4- or 5-colour)
        - Binary (Dyes premixed + batter)
        - Multiple dyes + substrate
            i. One insertion site or many insertion sites
        - Multistage addition
2. Mixing geometry
    a. Minus or plus aeration
    b. In-line continuous flow or separate chamber
3. Batter properties
    a. Define viscosity constraints within equipment and mixer option constraints.

C.2 Aims of study

To support the equipment and formulation design for the controlled delivery of colour in prototype equipment. The study will a) Define the flow properties of the mixing process when colour and flavour are mixed into the base formulation, b) Test different mixer design geometries, and c) Identify the best agents to deliver colour into the food materials. The material constraints identified in this study will contribute directly to the design of the equipment and formulation decisions.

Appendix D Structure analysis of sponge products

D.1 Terms and methods

In this study the term *technique* refers to the general analysis process and *method* refers to the specific application developed for a technique. In image analysis the term *particle* refers to discrete elements detectable in the whole *object* (e.g. a muffin) and is also used as a structural term to describe the general group comprising drops, bubbles and solid particulates. Details of digital image analysis methods developed for the study are given in Appendix E. Recommendations on randomised uniform sampling strategies to sub-sample images within a sectioned object were applied as described in section 1.5.5, as well as strategies to minimise operator bias.

Curve fitting was carried out using SigmaPlot (versions 11 or 12) (Systat Software, San Jose, US), unless otherwise stated.

D.2 Digital image analysis

To assess the potential for a SP structure to be compatible with voxel forming and Food-Ink structure setting requires some way to quantify the SP structure. Chap. 1 introduced methods for quantification and analysis of the SP solid-gas foam (see section 1.5.5). While the analysis of structural features in microscopy sections and in 2D images of the SP surface can be carried out by manual measurement, digital image analysis (IA) is generally carried out by semi-automated and automated methods. Table D.1 (over page) defines IA terms as used in this study. The raw data for images and structures are composed of *pixels* (for 2D images) or *voxels* (for 3D structures). The resolution depends on the size and number density of pixels/voxels (Russ, 1999).

A 2D digital image can be described mathematically by a number matrix carrying position and intensity information for each pixel. Pixels are individually assigned a brightness intensity value along a non-linear brightness scale partitioned into separate *bins*. Image data may be stored as tones of black and white (*greyscale*) or as colour. The RGB system described in Table D.1 is one approach to storing colour information. The source image data generally undergoes transformation to enhance features (*pre-processing*) before IA. Many transformations are matrix operations to modify the intensity value of an individual pixel based on the properties of neighbouring pixels.

Feature detection tasks that appear simple to human vision, particularly edge detection, are much more difficult for machine vision, while machine vision is more sensitive to intensity detection and size range discrimination (Russ, 2005a). The main task for IA quantification of structural features is to partition the image into count/non-count sections (*segmentation*). For the cut surface of a sponge product (SP), the task is more complex when the three-dimensional surface is captured as a two dimensional image (as in a scan), so that void edges must be identified from the demarcation between lit surface and shadowed voids (Sapirstein, Roller, & Bushuk, 1994).

Some IA techniques to characterise structural features in the SP are directly applicable to greyscale images of the cut SP surface with little or no pre-processing. These include: *granulometric filtering*, the use of structuring elements of increasing size to act as digital sieves to quantify regions with similar brightness intensities; *fractal analysis* of the shape of solid and void fractions, and interfacial boundaries; and *image texture analysis* (note this term refers to pixel texture, not sensory texture).

Image pre-processing to optimise the count/non-count assignment simplifies further analysis, but may also reduce the information content of raw data. Many IA techniques require *thresholding* of image pixels to define the pixels of interest. Thresholding an image into two regions only, count/non-count, is *binarisation*. Pixel intensities of binarised images are assigned to two bins, either pure black or white. *Denoising* (and other related methods of outlier removal) identify and remove islands of non-conforming pixels from an image. To minimise operator bias, pre-processing and IA must be carried out in a methodical way that limits operator decision-making. Pre-processing settings are first optimised manually, before semi-automated or automated processing is applied for the actual comparisons (Russ, 1999).

D.3 Structure analysis software for digital image analysis

Reproduction of structure analysis methods reported in many published studies is difficult without expert knowledge of IA. IA methods are often abbreviated, while many studies use commercial and in-house software inaccessible to most researchers. A number of software packages developed for porous media applications were evaluated for suitability in structure characterisation of SPs (Table D.2, over page).

The main software for IA used in this study was ImageJ freeware, an open-source, Java-based project for processing and analysis of scientific images (Abramoff et al., 2004). ImageJ works through a GUI interface, basic commands can be linked without programming knowledge and source code can be tailored by the user. Many plugins are downloadable for specific IA tasks. ImageJ *distributions* assemble a range of ImageJ functions in specialist packages, and are generally open-access if not open-source. Examples of ImageJ distributions used in this study are Fiji (Schindelin, 2008) for 3D and time-series images; and BoneJ for cancellous bone analysis (Doube et al., 2010). Open-source and open-access freeware, such as these examples, enables IA methods to be readily shared between studies if well-reported.

Table D.1 Definitions for general digital image analysis terms as applied in this study.

Term	Description
Greyscale image	A digital image in which brightness intensity is graduated along a non-linear scale from pure black to pure white. In an 8-bit image, the scale ranges from black (0) to white (255), representing 256 possible intensity values (bins).
RGB colour image	A colour digital image in which data is carried in three colour channels (red, green, and blue; R, G, B) to produce a gamut of colours in the composite image. Each channel has brightness intensity graduated along a non-linear scale from most to least intensity. For example, pure red is assigned RGB value (255, 0, 0) in an 8-bit colour image.
Pixel	The smallest 2D unit is square or rectangular in shape and is assigned to a single bin value.
Voxel	The smallest 3D unit in an image of a 3D structure is cubic or box-shaped and is assigned to a single bin value.
Object	In this study, the whole sample under examination.
Particle	In this study, individual objects within the image for analysis.
Pre-processing	Enhancement of image features before further IA or manual analysis.
Segmentation	Portioning an image into what is and what is not the phase of interest.
Thresholding	Simplification of image information by reduction or compression of bins in an image.
Binarisation	Reduction of a greyscale image into two bins (white or black) to simplify further analysis.
Denoising	Removal of pixel noise and small groups of outlier pixels to simplify the image for analysis.
Image texture	Regularity in the pattern of pixel intensity in specific parts of an image that differentiates portions of the sample.

Table D.2 Structure analysis software evaluated for sponge product structure characterisation. Software with an asterisk was used in further analyses of sponge product structure.

Software	Description	Features	Evaluation
3DMA-Rock	3D analysis of pore structure in µCT images of rock (http://www.ams.sunysb.edu/~lindquis/3dma/3dma_rock/3dma_rock.html), available as open-access for academic use. Accessed 17 Mar 2013.	Includes indicator kriging to improve segmentation by interpolating pixel intensity values. Determines connectivity in pore system. Pore throat determination.	A large manual component in pore identification. Many parameters not relevant to SPs. High computational requirements.
FOAMS*	2D characterisation of vesicle textures in volcanic rock. (http://www2.hawaii.edu/~tshea/foams/) Matlab^{R}-based, available as open-access. Accessed 17 Mar 2013.	No programming required, full GUI interface. Supporting literature outlines effective sampling strategy (Shea et al., 2010) across five orders of magnitude.	Some manual manipulation of watershedded images required. Generates a distribution of particle sizes in section without correction to produce unbiased count.
Avizo Fire	Commercial software for 3D porous rock analysis (FEI, Burlington, US). (http://www.vsg3d.com/avizo/fire), Accessed 17 Mar 2013.	Powerful, validated, hi-quality visualisation graphics. Includes interconnectivity analysis.	Short-term trial version too truncated to evaluate SP samples. Full version is costly.
3D model from µCT images	Student project for 3D modelling of a porous food (cracker) (Voortman, 2006), Matlab^{R} based program.	Builds a watershedded image, identifies cell walls, separating voids and numbers voids correspondingly.	Post-processing manual checking of watershedded images required. In-house coding, not open-access.

Skyscan™ CT-analyzer*	Skyscan™ µCT software for bone density analysis, version 2009 (Skyscan, 2009). Accessible by users of Skyscan™ instruments.	Porosity, surface area, bone thickness and other bone-specific structural features, assuming an underpinning geometric model.	This version generates 'black-box' values and numbers impossible to relate to image features. Depends on a geometric model of trabecular bone.
BoneJ*	ImageJ-based open-access distribution (http://bonej.org/). Accessed 17Mar 2013. (Doube et al., 2010).	Porosity, surface area, bone thickness and other bone-specific structural features, produced without need for geometric models.	Packages a number of porous structure parameters, no underlying geometric model. Not all features applicable to SPs.
FracLac ImageJ plugin*	ImageJ plugin authored by Karperian (2007). Accessed 17Mar 2013.	Calculates fractal box-count dimension D_B and lacunarity Λ by box counting of a 2D binarised image.	Supported by literature (Dàvila et al., 2007).
Fiji, 3D object counter	ImageJ Fiji 3D distribution http://fiji.sc/Fiji Accessed 17Mar 2013.	Separates and counts objects in 3D. Appears to follow a process similar to Voortman (2006).	Not effective for complex SP structures, with too few separated particles counted.
Fiji, 3D Skeletonise	ImageJ Fiji 3D distribution http://fiji.sc/Fiji Accessed 17 Mar 2013.	Creates a continuous backbone in 3D.	Not able to handle complex 3D interconnected structures of SP µCT images.
Fiji TrackEM2*	ImageJ Fiji 3D distribution plug-in (http://www.ini.uzh.ch/~acardona/trakem2_manual.html#dissectors). Accessed 17 Mar 2013.	'Disector' tool for estimating number density of particles in a section.	Manual feature identification required. Only a few features in each section series can be analysed.
SHAPE*	Open-access shape recognition software. (Iwata & Ukai, 2002), http://lbm.ab.a.u-tokyo.ac.jp/~iwata/shape/. Accessed June 2010.	Fourier analysis maps object outlines in binarised images	Provides statistically valid output as Principle Component Analysis, in graphical and numerical form. Easy to use.

D.4 Analysis of sponge product macrostructure

The baking industry carries out extensive quantitative measurement of product physical attributes during flour evaluation for standardisation of baking quality. SP shape is the result of events during cooking and cooling, and can be diagnostic for specific deficiencies in flour quality or in product manufacture. Parameters of macrostructure (for both uncooked formulations and cooked products) include:

- Shape
- Volume
- Interfacial surface area
- Bulk porosity.

In this study, cooked products volumes were determined by displacement measurement (see section 3.6.1). Interfacial surface area and bulk porosity were estimated using IA methods on images of cooked product structure generated by computed tomography (see sections D.8).

D.5 Analysis of sponge product mesostructure

D.5.1 Presentation of bubble/void distribution data

As described in Shea et al. (2010) the distribution data for bubbles/voids carries information about events during foam development (see Fig. 1.13). The convention for plotting size distribution of a particle population is to have bar graph format (with X-axis value set at the mid-point of the class) for non-cumulative distributions, with line-and-symbol format (X-axis value at the end-point of the class) for cumulative distributions and bin size increasing exponentially (Sympatec, 2011b). However, bubble/void distributions are not composed of discretely sized items, but form a continuous distribution with arbitrary size binning; therefore plotting with line-and-symbol format is not incorrect, and is used in some studies. To simplify comparisons between multiple data sets, non-cumulative bubble/void distribution data were generally plotted in line-and-symbol format, with X-axis value set at the end-point of the bin size range.

The choice of bin number and distribution had a marked influence on the information content of data (Fig. D.1). In some cases, a linear increment in bin size produced too many bins to expose distribution trends, while an exponential increment partitioned the data too finely at small particle size and too coarsely at large size. Generally, incrementing bin size by a multiplicative coefficient produced the most informative plots. Some data were plotted on a logarithmic axis, or with exponentially increasing bins. Distributions with differing bin sizes were compared as the cumulative distributions. During data processing, pixel intensity values assigned a decimal value did not always partition evenly into bins incrementing by whole numbers.

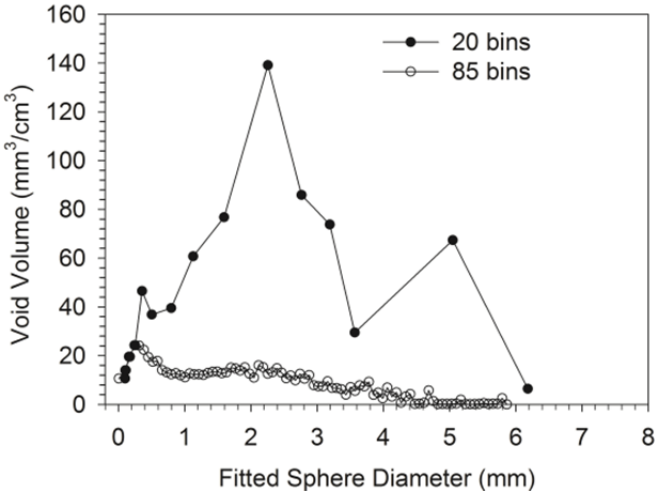

Figure D.1 Influence of bin size on the appearance of size distributions. Rice2 cooked idli void size data determined using Local Thickness were binned into 20 bins of increasing size (multiplicative scaling) or 85 bins of equal size (linear scaling).

Particle and drop distributions with normal or lognormal distribution may also be reported as probability density functions (Leng & Calabrese, 2004; Sympatec, 2011a). The degree of variation from the normal/lognormal distribution (e.g. skewedness, peak tailing) is described by moments of the density function (Leng & Calabrese, 2004). Quantile values may also be used as distribution descriptors. For example, Q_{10} describes the value below which 10% of particles are found.

D.6 Feature measurement of mesostructure

This section describes and evaluates feature measurement techniques for mesostructure in dough/batter and in cooked products. Idli made with rice2 or pea flour in the formulation are used as examples of cooked products. Rice2 batters produced idli with large voids having a regular ellipsoidal shape, while pea batter voids were generally smaller and more irregular in shape (Fig. D.2).

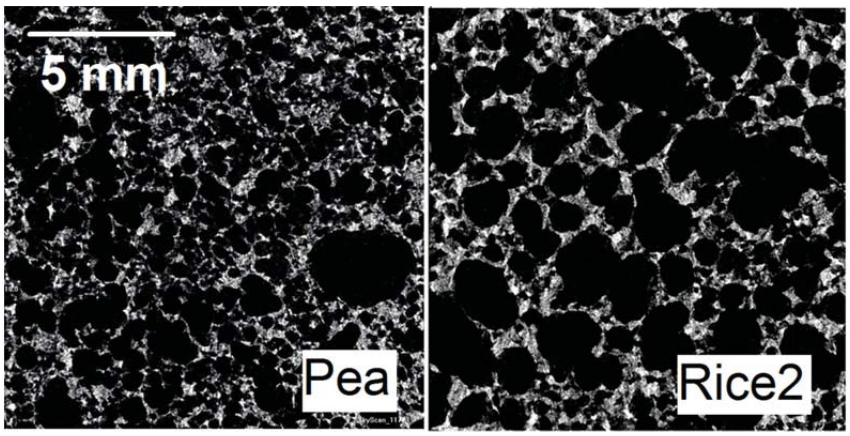

Figure D.2 Mesostructure of idli made with pea flour or rice2 flour, visualised in source x-ray microtomography output images.

Light microscopy was used to determine bubble size distribution and number density in batter fractions before flour addition (BBM), after flour hydration (-BiC batter) and 5 min after sodium bicarbonate addition to initiate bubble expansion (+BiC batter). Allais, Edoura-Gaena, Gros, & Trystram (2006) suggest a minimum bubble count of 250 for adequate characterisation of batter foam populations. In this study, 200-1500 bubbles were counted in each replicate at multiple randomly-placed views per slide. The idli batters in this study were less opaque than wheat-flour batters, and bubble populations could be observed in relatively thick sections. A video file of time series images for +BiC samples was collated in ImageJ.

D.6.1 Methods for light microscopy

- *Bright-field images were captured digitally using an Axiophot microscope, DFC320 camera and LAC 3.3 software (Carl Zeiss, Auckland, New Zealand), to give a 2.67 x 3.60 mm field of view (FoV). For –BiC slides four randomly-placed views were captured, one in each quadrant. For +BiC slides a single view was captured at 20 s intervals to produce a time series. At T = 5 min post-BiC addition one additional view was captured from the other quadrants.*
- *Micrograph images were imported into Fiji (Schindelin, 2008), a distribution of the open-source, scientific image analysis freeware ImageJ (Abramoff et al., 2004). Image contrast was enhanced using the ImageJ CLAHE function ('blocksize' 127, 'histogram bin' 256, 'max slope' 3.0, 'fast option' unticked).*
- *The same imaging system was used to capture images of particulates.*

D.6.2 Methods for processing micrographs and feature measurement

- *Particle sizes in images were measured manually as the diameter of spherical particles or as the major axis d_1 and minor axis d_2 of non-spherical particles.*
- *For quantification of bubbles in batters, those that fell more than 50% outside the image frame were excluded. Small bubbles at the surface of larger bubbles and circular objects embedded within the samples were classed as independent measurements.*
- *For each batter sample, data from the four quadrant FoVs was pooled, and the volume of uncompressed spherical bubbles was calculated (as $V = \pi d^3/6$). The volume of non-spherical bubbles was estimated as $V = \left(\frac{\pi d_1^3}{6} + \frac{\pi d_2^3}{6}\right)/2$. To compensate for bubble compression, the diameter (h) was recorded for bubbles in each FoV that showed the smallest cleared spots (i.e. those just touching both slide and coverslip). Mean sample thickness h_{Mean} was calculated as the mean of combined h values from the four quadrant FOVs, and ranged between 0.150-0.205 mm. The volume of bubbles with diameter > h_{Mean} was approximated as the volume of a cylinder ($V = \pi r^2 h_{Mean}$). The mean total volume of a sample in all four FoVs, calculated as [4 x (2.67 x 3.60 x h_{Mean})/1000] cm^3, was used to estimate bubble number density as Count/cm^3 and bubble gas phase volume as mm^3/cm^3. The calculated bubble volumes were used to sort bubbles into 24 diameter size classes increasing by a multiplicative coefficient.*

- *To compensate for the varying gas phase volume fraction in samples (Shea et al., 2010) the values for Total bubble count and Total bubble gas phase volume were calculated as Count/g sample and mm^3/g sample by dividing by the specific volume of the corresponding sample in cm^3/g.*
- *Video files of the +BiC time series were collated in Fiji from image stacks after CLAHE processing at default settings, fast option 'off'.*
- *For data on the rate of change in bubble size with time, bubbles in one quarter of the field of view were outlined manually in each frame by an ellipse, and areas measured in ImageJ. If the bubble disappeared during the analysis, the last observation was subtracted from zero, and divided by the time the bubble remained visible.*

D.7 Mesostructure of cooked sponge products

Structural features relevant to mesostructure include

- Void size distribution
- Void shape (irregularity)
- Solid phase thickness distribution
- Unevenness in void distribution across the structure (*degree of anisotropy*)
- Interconnectivity between voids (*tortuosity*).

Several factors contribute to positional differences in porosity (the degree of anisotropy). These include flattening of cells close to the crust due to pressure of expanding crumb against the set crust during the later stages of baking; and the increasing gradient of hydrostatic pressure that exists from the top to the bottom of uncooked dough/batter.

D.7.1 3D structure imaging by computed tomography

Quantitative analysis of highly interconnected structures such as SPs requires a 3D model of the structure (Kroustrup & Gundersen, 2001) and is complicated by difficulty in segmenting the structure into discrete, countable particles. The 3D structure of SPs in this study was recorded using x-ray computed microtomography (Skyscan™ µCT system and software, Skyscan NV, Kontich, Belgium), which can differentiate between gas phase and solid phase in doughs and cooked SPs. The process records multiple autoradiography images of a rotating sample and deconvolutes the data into a Z-axis stack of XY-plane sections after acquisition. Each section (slice) is one pixel thick, where the µCT resolution setting determines pixel size.

D.7.2 Method for computed tomography analysis of idli samples

- *A vertically-orientated 20 x 20 x 30 mm cube was cut between the centre and the edge of a single idli. µCT visualisation was carried out on the covered sample with a Skyscan1172 x-ray computed micro-tomography system (Skyscan NV, Kontich, Belgium). Scan settings were voxel size of 13.3 µm, source voltage 59 kV, Misalignment compensation on, Ring artefacts on, Beam-hardening condition 5%, and analysis time 20 min. Skyscan CT Analyser (Vers. 1.11 4.2+) was used to produce bitmap images cropped to a 15 x 15 mm sequential XY-axis stack of 700 images, with pixel density of 57.7 pixels/mm, and voxel size of 13.3 x 13.3 x 13.3 µm. Images were imported into ImageJ for further*

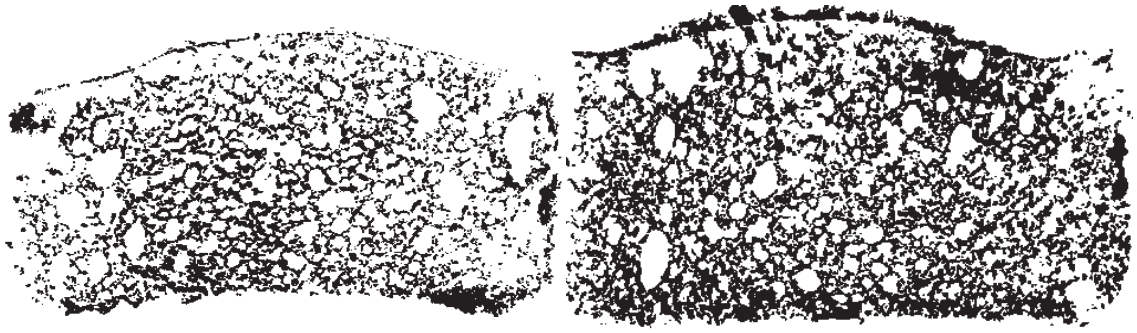

Figure D.3 Ink prints of cut surfaces for idli made with rice2 flour (left) and pea flour (right) showing the vertical section through the centre of the idli at true size.

processing. Details of digital image pre-processing methods developed for the study are given in Appendix E.1.

D.7.3 Imaging the cut surface of cooked products

The simplest technique to record mesostructure is to print the inked surface of a cut SP onto paper to capture a cross-sectional outline of voids. A second method is to scan or photograph the cut surfaces under conditions that shadow the voids. In ink prints of SP surfaces, differences in crumb organisation are discernible by eye, as seen for idli made with different flours (Fig. D.3). One way to quantify the differences is by manual demarcation and measurement of void areas, but this is time-intensive and prone to user bias.

D.7.3.1 Methods for recording idli cut surface by digital scanning and ink printing

- *Idli were cut in half vertically, the cut surface scanned at 600 dpi with a ScanMaker 1900 scanner (Microtek, Hsinchu, Taiwan), and the image contrast enhanced in Fiji, (version 1.47) (Schindelin, 2008), an open source, open-access distribution of ImageJ (Rasband, 2005) with ImageJ CLAHE function.*
- *After a digital scan of the cut idli, idli surfaces were inked on an inkpad and printed onto paper, and ink prints recorded digitally as scanned digital images.*

In scanned images and photographs, void edges are identified from differences in pixel intensity. Examples of studies to optimise estimation of void size distribution from scanned images of SP cut surfaces include Kinno & Miura (2010) and Gonzales-Barron & Butler (2008a, 2008b). Cut-off values of threshold settings to transform greyscale scans and photographic images into binarised images are generally chosen to suit the purpose of the analysis. To show the sensitivity of thresholding to the source image, a scan of rice2 idli cut surface (Fig. D.4 top left) was thresholded with ImageJ Otsu threshold function (Fig. D.4 bottom left), as recommended by Gonzales-Barron & Butler (2006) for breads. The same Otsu thresholding was applied to the source image after contrast enhancement with ImageJ CLAHE function (Fig. D.4 top right). On thresholding the scanned image, the output after contrast-enhancement (Fig. D.4 bottom right) is closer to consumer perception of crumb structure at the cut surface, while the scan without enhancement is a more accurate depiction of the void interface at the cut surface.

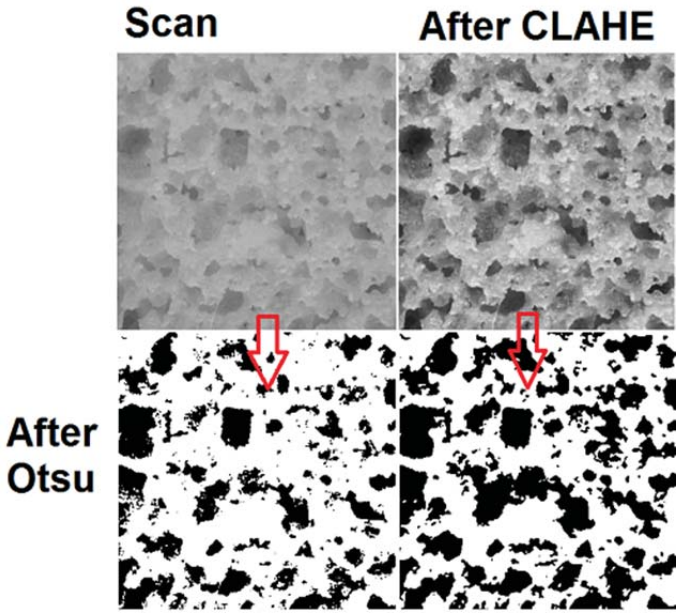

Figure D.4 Influence of source image on Otsu thresholding for binarisation. Top: scan of rice2 idli cut surface (10 x 10 mm) scan before and after ImageJ CLAHE contrast enhancement. Bottom: output after Otsu thresholding at the same settings using ImageJ Otsu threshold.

D.8 Quantification of particle size in 2D images

D.8.1 Fractal measures of sponge product structure

Fractal analysis to characterise the roughness of the boundary between two phases (fractal dimension, *D*) has been carried out on both greyscale and binarised images of SP cut surfaces. The technique applies a series of grids of increasing size (decreasing resolution) over the image to count pixel intensity in each grid box. *D* is based on the variation of pixel intensity at the boundary between differing pixel intensities. Fractal values generated for SPs have been linked to attributes of product quality, such as sensory score and mechanical response.

While the fractal dimension *D* is a fractal measure of the shape and roughness of object boundaries, lacunarity (Λ) is a fractal measure of particle void organisation. According to Majumder & Mazumdar (2007), lacunarity is a topological attribute that gives "a measure of the largeness and spatial organisation of gaps in a structure…and degree of homogeneity": cellular foams with the same bulk porosity value can differ markedly in internal organisation. D fractal values were generated by fractal analysis of grey-scale photographs from three types of bread (Farrera-Rebollo et al., 2012), but had no direct relation to structure as perceived by eye. Information in the greyscale image additional to boundary roughness, such as transparency/opacity of the solid phase, confounded the calculation, i.e. the fractal value was related to the image texture, not to void size.

Lacunarity values were used as quantitative descriptors of voids observed in photomicrographs of protein gels (Dàvila et al., 2007). According to Karperian (2007, p.13) lacunarity using ImageJ FracLac plugin is "calculated as the variation in pixel density at different resolution using the CoV [coefficient of variance] for pixel distribution". Lacunarity is determined by a *sliding box* technique. Data variance is determined by recording pixel intensities in a count box slid incrementally across the entire image.

Pixels partition into the count box less randomly when box sizes are close to the size of a particular structural feature. As the CoV value of the count population decreases, so does the value of Λ. A sliding box count method is also used to generate the equivalent *fractal box dimension* (D_B) for the corresponding measurement of the non-void phase.

D.8.2 Methods for fractal analysis

FracLac method details are given in Appendix E.1.2.

- *Lacunarity was determined by sliding box count using ImageJ FracLac_2.5 plugin (release. 1e) as described in Appendix E.1.2, on a random, uniform series of µCT sections after binarisation as described in Appendix E.1. Analysis settings were: geometric boxes/15 samples/white background.*
- *FracLac Box Count and FracLac Sliding Box Count functions were also used to characterise fractal distributions in digital images.*

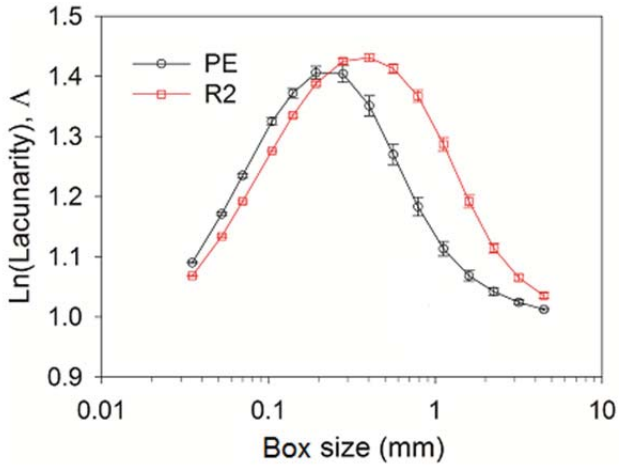

Figure D.5 Lacunarity values generated from sliding fractal box count applied to binarised µCT sections of idli made with rice2 flour (R2) or pea flour (PE), *n* = 10 ± SE. Determined with ImageJ FracLac_2.5 plugin (Karperian, 2007).

ImageJ FracLac plugin was applied to pre-processed µCT sections of the rice2 and pea idli shown in in Fig. D.1. In a plot of ln(Lacunarity value) against box size (i.e. feature size) the peak for rice2 idli occurred at a greater Λ value than that for pea idli (Fig. D.5; Table D.3). It was positioned at a larger box size (0.40 vs. 0.19 mm) and had a broader size range, as calculated from 80% of the total area under the peak. Void size and position distribution in rice2 idli was therefore broader and more homogeneous than in pea idli. Note that Λ peak values fall below sizes most evident when the images are evaluated by eye i.e. they are biased to the smaller population. Table D.3 summarises fractal analysis values of rice2 and pea idli. Values generated on fractal analysis seem to be product-specific, with no phenomenological correlation to product mesostructure, limiting the usefulness of this type of fractal analysis as a comparative tool across studies.

Table D.3 Summary of values for quantification techniques. [1]Source images were binarised denoised image of µCT data. [2] Source images were greyscale scans of cut surface.

	Sample size	Rice2	Pea	Method
Fractal DB Boundary value	$n = 10 \pm SD^1$	1.746 ± 0.018	1.825 ± 0.023	FracLac Box Count
ImageJ plugin MapFractalCount	$n = 12 \pm SD^2$	2.745 ± 0.001	2.759 ± 0.035	(Farrera-Rebollo et al., 2012)
Lacunarity (Λ) *Ln(Peak height) *Peak value (mm)	$n = 10 \pm SD^1$	 1.431 ± 0.019 0.19	 1.401 ± 0.011 0.40	FracLac Sliding Box Count, Lacunarity

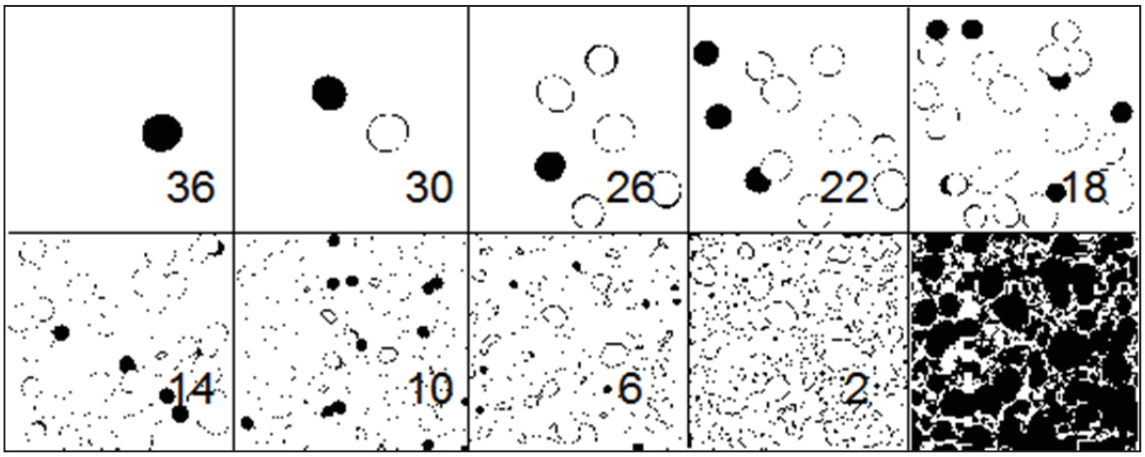

Figure D.6 Example output produced after ImageJ Gran Filter sizing of a binarised denoised µCT source image (at bottom right), using a circular structuring element at 1 pixel increment, and with a post-processing operation to delete voids of larger size classes. Numbers refer to discrete pixel size classes.

D.8.3 Granulometric Filtering

Another method to quantify voids in an image without segmentation into discrete particles is *Granulometric filtering* (GFil) which sieves image features digitally by the use of *morphometric structuring elements* (mathematical operator matrices). A circular structuring element matrix, for example, produces output images with rounded particles which look as if a ball of the chosen size had rolled around inside the features under analysis. As an example, voids in a cooked idli sample were analysed using ImageJ plugin Granulometry Filter (Fig. D.6). A circular structuring element of increasing pixel size was applied, followed by a set of subtractive image operations to produce discrete size categories from the initial output (see Appendix E.2 for IA details). GFil only approximates the object size. When output images were recombined, the count region was lower by 5-10% than the source image, while the use of a square element over-assigned non-count pixels to the count region (data not shown).

D.8.4 Watershedding

IA is also poor at identification of particles with incomplete walls. For example, in an ink print of the idli cut surface (e.g. Fig. D.3) evaluation by eye can recognize differences in void size and shape between idli made with different flours. Quantitation of void size from these source images using an IA particle analysis function cannot be done directly, as IA is unable to interpolate void shapes in the same way as human vision. As an example, ImageJ 'Analyse Particle' function applied to the pea idli ink print (Fig. D.7 left) identified only a single interconnected particle (Fig. D.7 right).

One approach to extract void size information from such a highly-interconnected structure is to transform void spaces into discrete particles. Application of the *watershed* function partitions the pea ink print image into a series of peaks and valleys (Fig. D.8 A), where the peaks represent darker cell wall pixels and the valleys represent the brighter void pixels. Method details for Watershedding in ImageJ are given in Appendix E.3.

Based on this topographical analysis, the function makes a best estimate of missing ridge lines (Russ, 2007b). Interconnected valleys are closed off into discrete watershed regions (Fig. D.8 B). Denoising must be first optimised in the source image, as outlier pixels result in over-partitioned watershed outputs. Watershedded voids may also have a more jagged shape than the corresponding void shape as interpolated by eye. In ImageJ, watershedding was carried out in two dimensions with Binary/Watershed function. A 3D watershed plugin for ImageJ was not effective in separating voids in SP µCT images due to the complexity of the interconnected mesostructure.

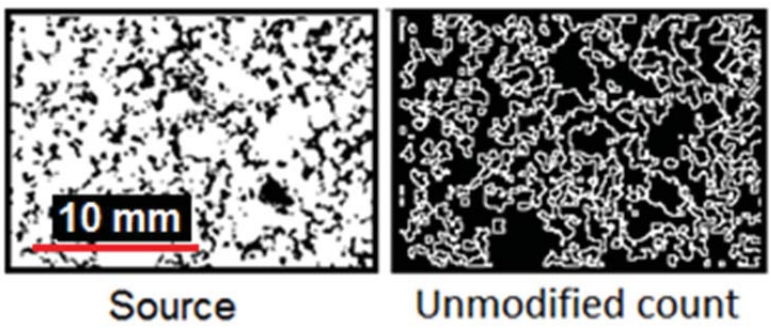

Figure D.7 Left: greyscale scan of pea idli ink print. Right: outlines of detected particles after binarisation of the scan and ImageJ Analyse Particles function.

D.8.5 Unbiased count

Estimation of 3D measures for specific particles, as opposed to object bulk properties, is not straightforward for microscopy sections. For example, sectioning a set of same-size spheres embedded in a medium generates sections with a population of circles of different sizes. Using various algorithms, measurements of circle populations in a section can be used to infer the sphere diameter. A measurement procedure based on this approach was proposed for foamed confectionery products by Lim & Barigou (2004). However, the relationship between section area and true particle volume is too complex to be precisely deconvoluted for more complex systems (Russ, 2005b).

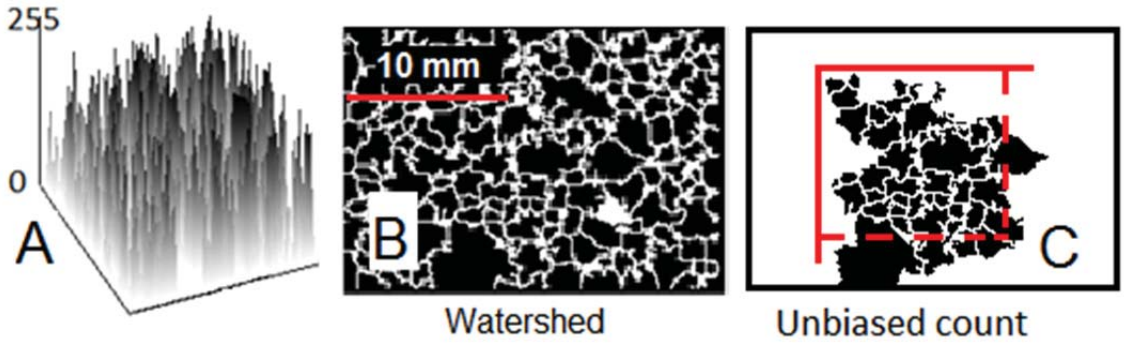

Figure D.8 Image transformation for particle counting of the pea ink print in Fig. D.7 left. A) ImageJ Surface Plot is used to plot greyscale intensity (0-255 bins) across a source image in greyscale format. B) Binary/Watershed function is used to partition source image A) after binarisation into voids. An unbiased count is made of the watershedded image B), applying a guard frame with two permitted sides (dashed) and two non-permitted sides (solid) for counting. C) The resultant measurement output image identifies the objects permitted by the guard frame.

A statistically-valid quantification of particle size and number requires the use of a compensatory counting technique. Fig. D.8 C illustrates the particle output after an unbiased count of watershedded voids in Fig. D.8 B. Use of a guard frame (in red) removes bias from the particle measurement population (Howard & Reed, 2005c). Particles touching the two non-permitted sides of the guard frame are not included, while the entirety of any particle touching a permitted side is measured. The count is unbiased as long as the guard frame is large and the field of view is three times that of the largest particle (Russ, 2005a). For example, the field of view of image size in Fig. C8 B is too small to remove bias for large particles, as one counted particle is truncated at the image edge. Methods for creating watershedded images from a stack of µCT images, and counting the discretised voids with an unbiased guard frame were developed in ImageJ (Appendix E.4).

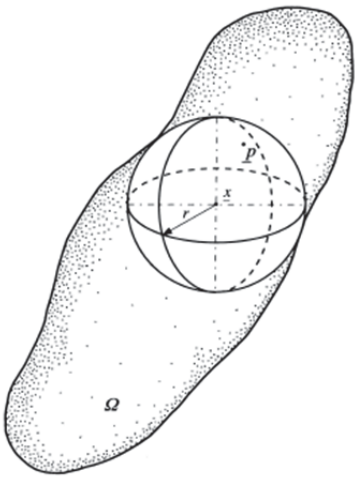

Figure D.9 **The Local Thickness value for voxel p in a 3D object composed of voxel set Q is determined by fitting the largest sphere containing p, with centre x positioned at the farthest distance from the object boundary. The measure of Local Thickness is the sphere diameter $2r$. Reproduced with permission from Hildebrand & Rüegsegger (1997), © The Royal Microscopical Society.**

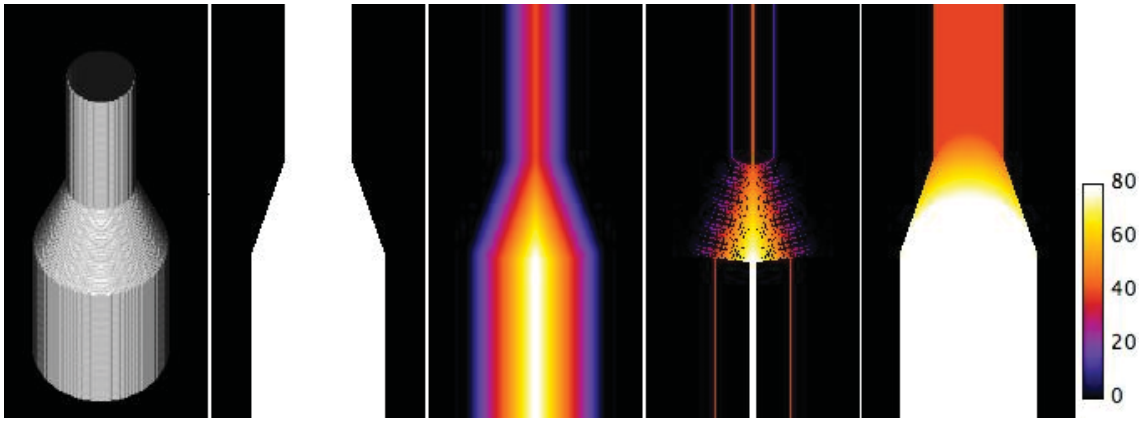

Figure D.10 **Stages in Local Thickness analysis. From left: 3D rendition of the source object; section through object centre; distance map showing distance of points from the object surface; distance ridge with medial line and key surface points produced by deletion of unneeded distance map points; size assignment after sphere fitting to the distance ridge. The thickness scale is shown on the far right. Adapted with permission from Dougherty & Kunzelmann (2007b), © 2007 R.Dougherty.**

D.8.6 Local Thickness

An alternative method to quantify the size of features (applicable to both 2D and 3D structures) is Local Thickness determination (LT) (Hildebrand & Rüegsegger, 1997). The method was adapted by Dougherty & Kunzelmann (2007a) for ImageJ in the form of the Local Thickness plugin, and used as the main measurement method for bone strut thickness in BoneJ. LT assigns a size value to each voxel in a binarised image based on the diameter of the largest sphere able to fit the 3D void around the target voxel (shown for a 3D structure in Fig. D.9). LT is responsive to 3D constrictions in structure. The technique first calculates the centre line and edges of the object to be measured before the spheres are fitted. The stages in LT analysis are shown in Fig. D.10.

Fig. D.11 B shows the output after LT analysis of a 2D greyscale scan derived from the pea ink print in Fig. D.7. For the method developed for this study, LT output image needed to be corrected by overlaying the original, non-void pixels (compare Fig. D.11 B & C) before size measurements were captured from the output image as pixel intensity (method details in Appendix E.5). Note that LT cell size determination is influenced by void shape, as regular spheres and ellipsoids can fit larger spheres than irregular voids with equivalent volume.

LT analysis is also sensitive to outlier pixels unless the image is pre-processed to remove outliers which result in false assignment of object edges. Note that, compared with particle sizing in a watershedded image (e.g. Fig. D.8 C), the sizes assigned to voids at the image boundary do not appear truncated as sphere fitting is not constrained by the image edge. Fitting an unbiased guard frame is not possible in LT analysis as the void space is not partitioned into discrete particles. Edge effects in LT analyses were therefore disregarded in this study, and the void size distribution calculated as the sum of all individual voxel LT measures.

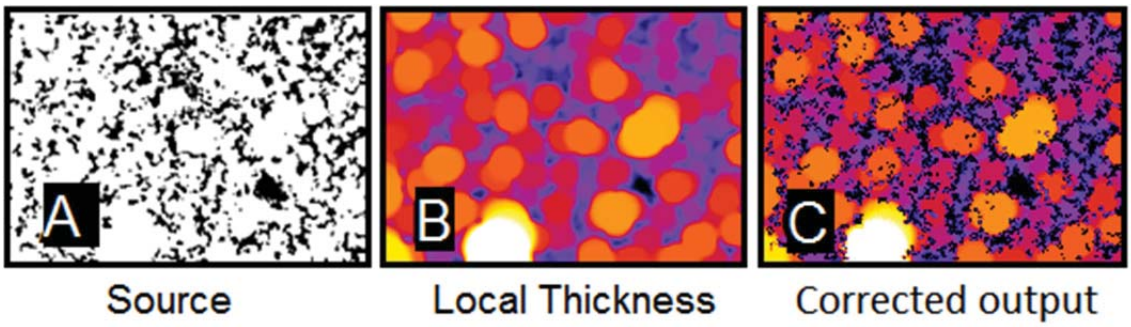

Figure D.11 Outputs at stages in Local Thickness image analysis for voids. A) Pea ink print source image; B) false colour output after ImageJ Local Thickness analysis of denoised image with hotter colours representing larger voids; C) sum of A) and B) to generate an image trimmed of overhang pixels, before size quantification derived from Local Thickness pixel intensity.

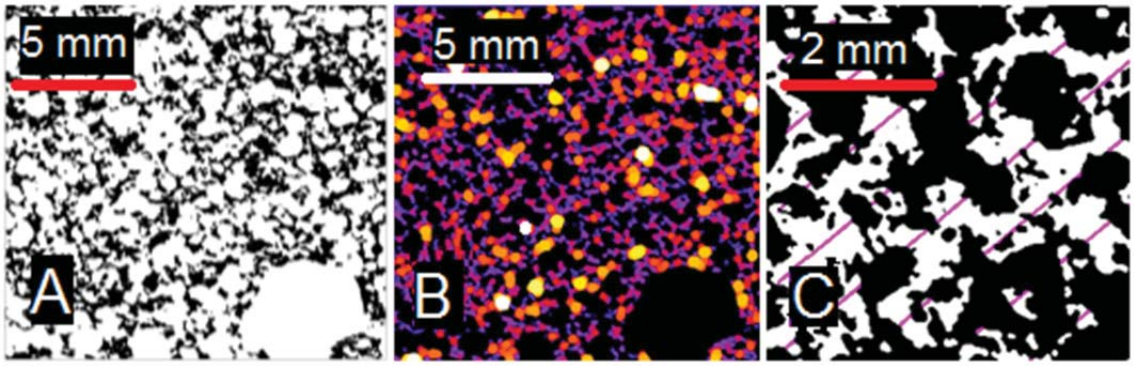

Figure D.12 Size determination of pea idli solid phase using different techniques. A) Source binarised denoised µCT image from pea idli. B) Output after Local Thickness analysis of the solid phase. C) 3x magnification of A) after inversion to denote solid phase in white, with a grid of 1 pixel parallel lines overlaid for Line Intercept analysis. Line grid intercepts with the solid phase are in magenta.

Fig. D.12 B shows the application of LT to analysis to a pre-processed µCT image of pea idli (Fig. D.12 A). As LT generates a false colour range for each output based on the pixel intensity range within each image, the intensity range must be first normalised to a standard scale to be able to make between-sample comparisons.

D.8.7 Grid counting using Line Intercept

Russ (2005a) described a stereological method to estimate the wall thickness of a sample having cell walls of similar width. Observational bias on sectioning is due to oblique cuts that produce a population of walls thicker or thinner than the actual width. The actual wall width when all the cell walls are of similar width can be estimated from the value at two-thirds of the maximal value along a frequency plot of inverse intercept lengths. Intercepts from lines at one angle were overlaid onto the pre-processed µCT image of pea idli in Fig. D.12 A (enlarged in Fig. D.12 C image to show intercept lines). Data were measured at many angles of line interception (ImageJ macro details in Appendix E.7). Although the walls had varying thickness, after transformation the majority of wall values occurred as a lognormal distribution.

D.9 Methods to estimate 3D structure of sponge product structure

What seems to be a simple task on first glance is not simple at all and involves the translation of two dimensional information into three dimensions.

D.9.1 Particle number density using disector analysis

Estimation of particle number density in a 3D object from consecutive microscopy sections (essentially 2D slices) can be done using the *disector* method (Howard & Reed, 2005b; Russ, 2005b). Individual features/particles within a section are marked, and subsequent sections at a uniform distance (look-up sections) are examined to identify the distance at which they are no longer visible. The disector analysis may need to be repeated at two or more different look-up distances to evaluate particles of different size. ImageJ TRAKEM plugin has a semi-automated disector function. Disector methods require high manual input and easy identification of large particles between the look-up sections, and are not

effective for continuous size classes or interconnected void structures.

D.9.2 3D Granulometric Filtering

Lassoued, Babin, Della Valle, Devaux, & Réguerre (2007) described quantification of void and wall size distributions in high resolution µCT images of bread by in-house 3D GFil software. A 3D octahedral structuring element of increasing size was used to measure and then remove voids. Wall thickness and void size was measured using different combinations of IA *erosion* and *dilation* steps as the structuring element size was increased incrementally. At each increment an erosion step removed wall material thinner than the structuring element and a dilation step removed voids smaller than the structuring element. However, programming for this type of analysis is not generally available as open-source or freeware, and requires significant processing resource and specialist programming knowledge to reproduce.

D.9.3 Skyscan™software analysis

Software supporting Skyscan™ µCT equipment calculates a number of parameters associated with cancellous bone density (Salmon, 2004), which has a porous mesostructure similar to that of SPs. Skyscan™ software calculations for bone density parameters depend on underpinning geometric models (Salmon, 2004). Data analysed by this version of the software generated nonsense values for many bone density parameters when applied to SP samples.

Note that the Skyscan™ software is undergoing updating in partnership with Avizo (FEI, Burlington, US), developers of powerful analysis software for porous systems, and should overcome the limitations of the software versions used in this study.

D.9.4 3D Local Thickness

BoneJ (Doube et al., 2010) is an open-access distribution of ImageJ that avoids the need for geometric models in analysis by applying Local Thickness on µCT images. Although BoneJ was able to produce output images from µCT images of cooked idli to derive void size distribution, ImageJ LT analysis was preferentially carried out using the Fiji distribution of ImageJ. BoneJ functions were then used to analyse the ImageJ LT output instead to the BoneJ LT analysis, in order to have closer control of pre-processing and analysis settings (image pre-processing method details in Appendix E.1). The processing hardware limited the maximum sample size for LT analysis to 100 µCT sections at standard resolution. LT output was similar in perpendicular sections taken along the XZ-axis to that for the XY-axis plane sections (data not shown).

Other BoneJ functions, including Degree of anisotropy, Connectivity and Surface Area, were applied in this study to quantify variation in SP void organisation (details in Appendix E.7). Not all functions were applicable to SPs due to the more detailed structure of SPs compared with bone and to the emphasis of BoneJ on solid phase attributes.

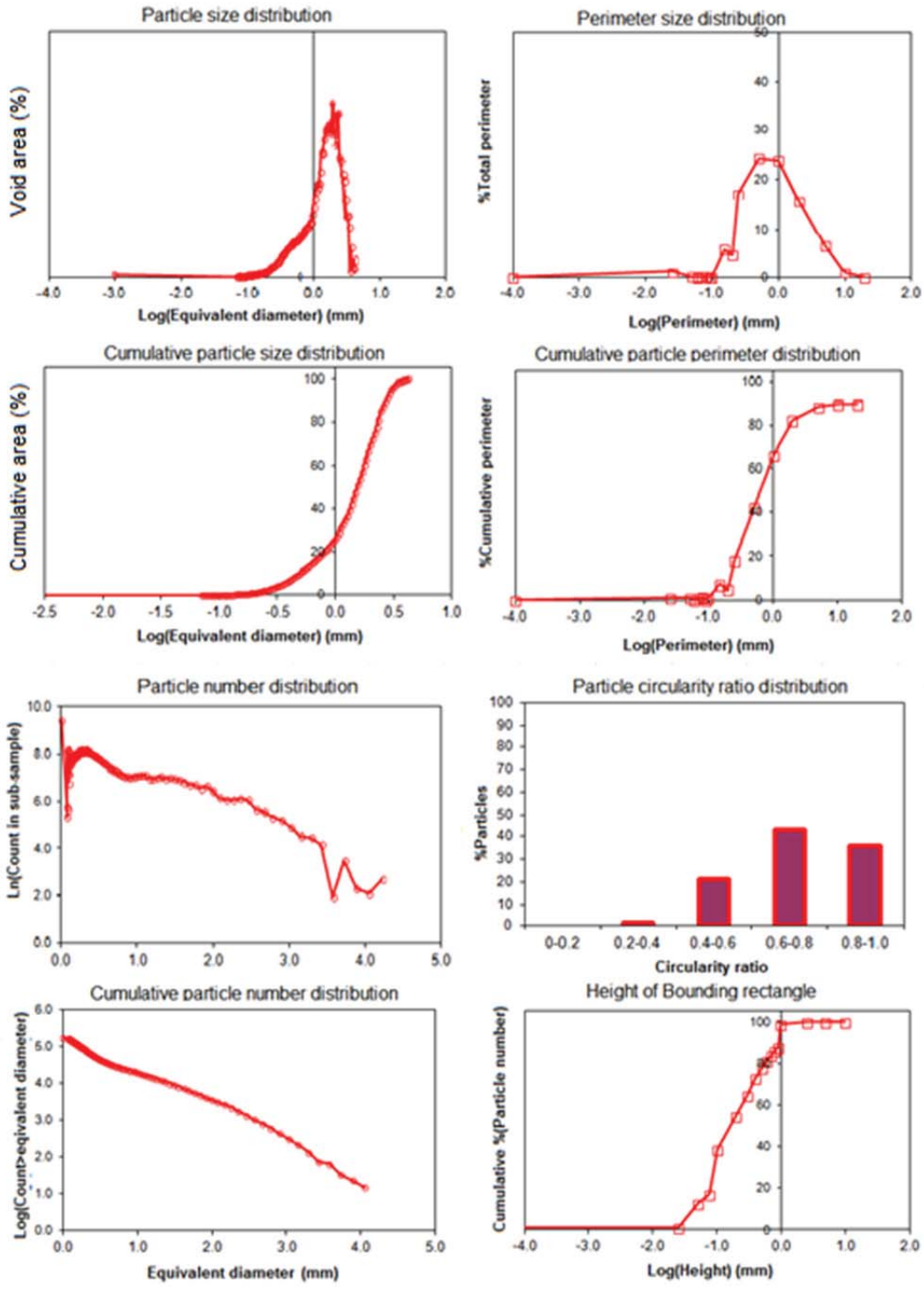

Figure D.13 Typical Excel 2007 evaluation plots after Unbiased Count analysis on binarised denoised µCT images of rice2 idli. Left: void size and number distributions. Data normalised to area. Right: attribute options in Analyse Particle function (particle perimeter, circularity and height of bounding rectangle). Circularity ratio 1 describes a perfect circle. An arbitrary X-axis value was assigned to give the Y-axis intercept point in logarithmic plots, *n* = 700 images.

D.9.5 2D Particle analysis of µCT data after Watershedding: Unbiased count

Idli µCT image slices were individually analysed for particle size distribution, after watershed partitioning into countable particles using Unbiased Count (method details in Appendix E.4). Data evaluation plots for particle size and number distribution (e.g. Fig. D.13 left) were laid out in a similar way to those described for model bubble populations by Shea et al. (2010), but on the basis of unit area and not volume.

The plots in Fig. D.13 corresponded to those in Shea (see Fig. 1.13) as follows:

- Particle size distribution to Shea Volume Fraction,
- Cumulative particle distribution to Shea Cumulative Volume Fraction,
- Particle number distribution to Shea Number Density, and
- Cumulative particle number distribution to Shea Cumulative Number Density.

Particle size distributions (determined as in Fig. D.13) were compared in µCT images and ink prints after binarisation and watershedded using ImageJ. Ink prints have a loss of detail at lower range and require watershedding with manual input, but increase sampling of larger voids, which is limited by the small volume of the µCT sample (2400 mm^3).

Fig. D.14 shows the differences in void assignment for pea and rice2 idli samples between µCT images after binarisation, ink prints of the cut surface, and images of scans of the cut surface after each had been independently thresholded.

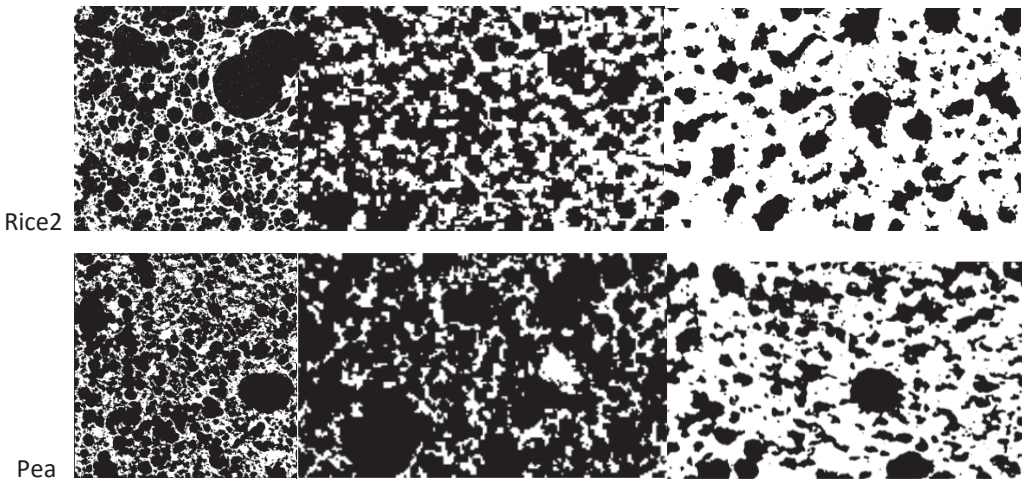

Figure D.14 Idli mesostructure visualised by µCT (left), inverted ink print image (centre) or thresholding of scanned images made of the cut surface (right). Height = 15 mm, solid phase in white.

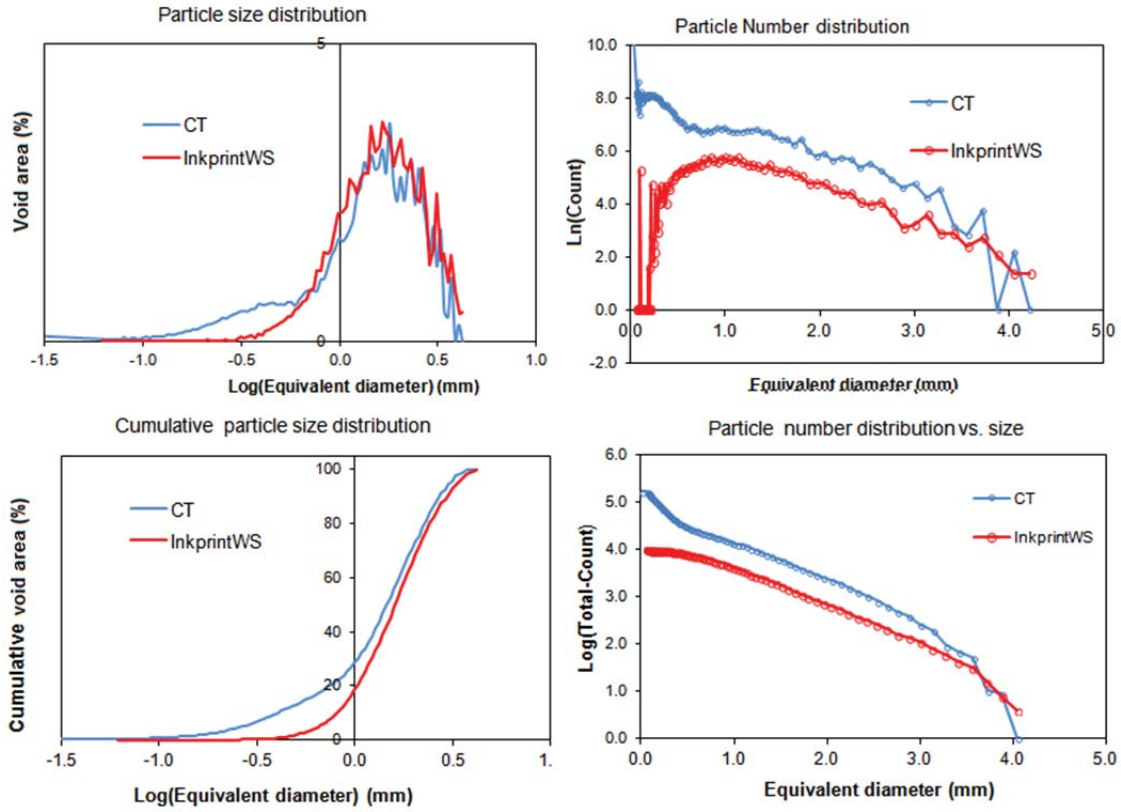

Figure D.15 Evaluation plots on Unbiased Count for particle size and unnormalised number distributions in binarised denoised µCT images of rice2 idli (*n* = 70) or in ink print scans at 300% resolution after binarisation and watershedding (*n* =10). Plotted in Excel 2007.

There was good correspondence for void diameters > 0.8 mm between Unbiased Count data from µCT images and ink print void distribution analysis for rice2 idli samples (Fig. D.15), while scan data of the cut surface was poorly correlated (data not shown). Void area was greatly underestimated in thresholded scans: for example, the %void area in rice2 idli images was 76% in µCT samples, 62% in ink prints, but only 40% in scans after Otsu thresholding.

Ink prints provided more accurate source images for larger voids than scans made on a standard digital scanner, but also had marked information loss or distortion. Comparison of size distributions for pea idli ink prints with µCT images (after binarisation and watershedding) clearly provided additional data at larger void size in ink prints (Fig. D.16). However, the overlap between ink print and µCT data was less continuous that that for rice2 idli, with detail at small size completely lost. Ink print images may provide void distribution information at the largest void size, dependent on the type of product, but are not necessarily accurate records of the cut surface. However, the preferable approach in place of ink prints is to acquire µCT images of the same sample at both low and high image resolution, to increase the frequency of large void data.

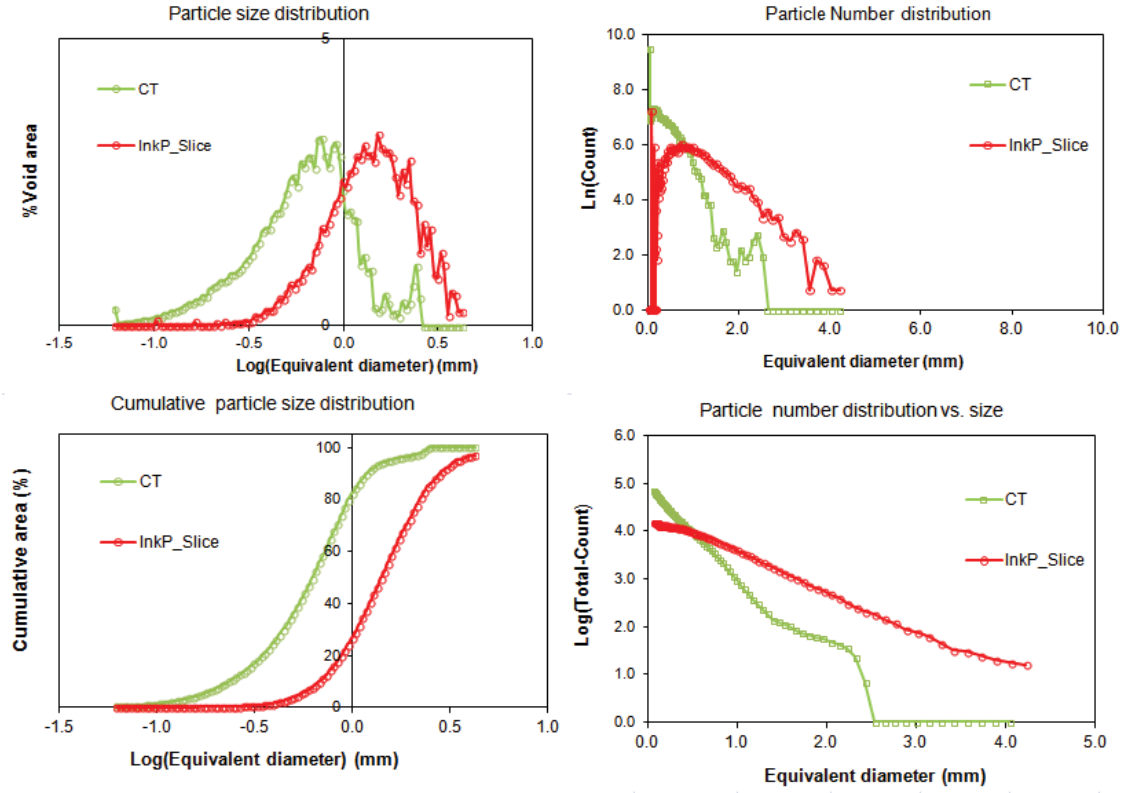

Figure D.16 Evaluation plots on Unbiased Count for particle size and unnormalised number density in binarised denoised µCT images of pea idli (*n* = 70) or in ink print scans at 200% resolution after binarisation and watershedding (*n* = 7). Plotted in Excel 2007.

D.9.6 2D Particle analysis of µCT data after Watershedding: FOAMS analysis

FOAMS is an open-access MATLAB^{R}-based software developed by Shea et al. to quantify bubble size distribution data in microscopy sections of lava rocks (Shea et al., 2010). Graphical output from FOAMS is in the form of size distributions for bubble volume fraction, cumulative volume fraction, number density and cumulative number density, as shown for model bubble populations in Fig. 1.12. A nested image magnification strategy (with up to 20 source images) ensures coverage of the full bubble size range. Missing bubble walls are completed manually before analysis. All particles not touching the edges are counted. FOAMS assigns a diameter to an individual particle derived from the circle of equivalent area. FOAMS bins the size data into fixed size classes with exponentially increasing diameter. It corrects for biased count in three dimensions due to over-representation of large voids on sectioning, by applying a statistical correction that assumes the measured particles are sections through a population of spheres with a self-scaling size distribution.

D.10 Comparison of structure quantification techniques

D.10.1 Image analysis techniques used to quantify idli meso- and microstructure

Table D.4 summarises the IA techniques applied to size voids and walls in µCT images.

Table D.4 Image analysis methods applied to µCT images to quantify sponge product mesostructure.

	Approach	**Function**
Pre-processing	Background removal, denoising, binarisation, filter application	Image clean up before further analysis
Manual particle detection in sections	Draw in equivalent ellipses by eye (voids) or measure width of bubbles and particulates	Count and size distribution of observed particles
Granulometric Filtering on pre-processed sections	Apply circular and square structuring elements on uniform random sample of sections, assembled as a montage	Sieving into size classes by Granulometric Filtering
Unbiased Count particle analysis of pre-processed sections	Pre-process: Watershed to create discrete particles for counting from interconnected voids	Count and size distribution of observed 2D particles using a count box to correct for counting bias
Local Thickness on pre-processed µCT sections	Sphere-fitting to voids after distance mapping of whole structure. Pre-process: Binarisation, outlier removal, watershed	Size distribution of all void spaces with additional 3D information
FOAMS lava void analysis on pre-processed µCT sections, scans and ink prints	Pre-process: Resizing, binarisation and outlier removal before watershed. Uniform random sample.	Calculates diagnostic void attributes (Volume fraction, Cumulative volume fraction, Number density, Cumulative number density)
Line Intercept on pre-processed sections	Pre-process: Binarisation, analysis on uniform random sample of sections	Grid counting to estimate wall thickness, with rotating grid to remove anisotropic bias

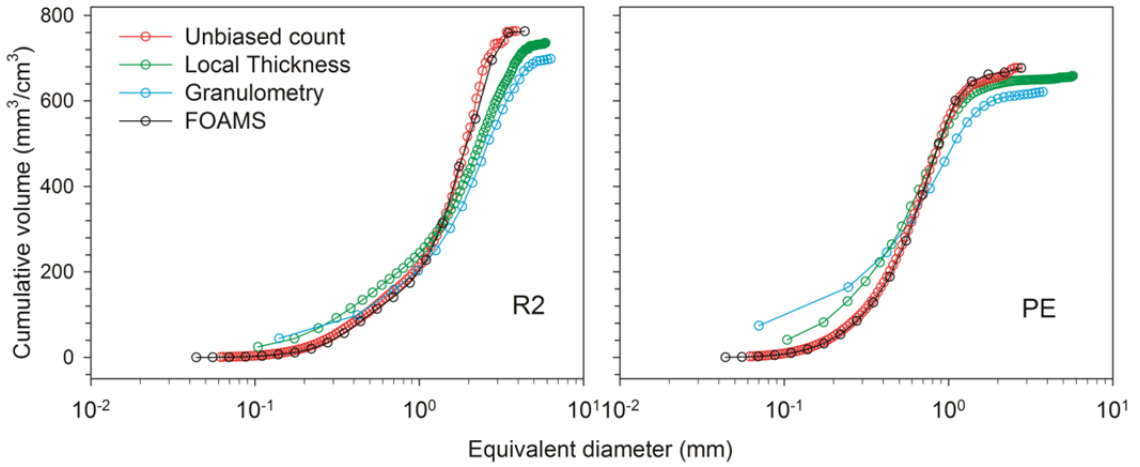

Figure D.17 Evaluation of void size determination techniques using the same test sets of binarised denoised µCT image stacks (15 x 15 x 1.33 mm) from rice2 (R2) or pea (PE) idli. Techniques: Unbiased count was carried out with ImageJ Analyse Particles, as described in Fig. D.8, (n = 100 watershedded images, 114 pix/mm); ImageJ Local Thickness plugin (n = 100 images, 57 pix/mm); ImageJ Granulometry Filter function with post-analysis image subtraction (n = 20 images, 114 pix/mm); FOAMS (n = 20 watershedded images, 114 pix/mm).

D.10.2 Quantification of gas phase voids in sponge products

FOAMS, Unbiased Count, LT and GFil were evaluated for effectiveness of counting using sets of test images (Fig. D.17, details in legend). FOAMS and Unbiased Count cumulative volume distributions mapped closely onto one another, even though each method applied a different strategy to correct for count bias. The S-shaped distribution curves in Fig. D.17 fitted best to a 4-parameter Chapman sigmoidal growth curve (Table D.5). The parameters a and Y_0, describing upper and lower limits for Y-axis values, were larger in LT and GFil distributions. An increase in the values of b and c correlated with an increase in slope. Sizing of voids by GFil and LT produced a smaller total void volume (a parameter) than on FOAMS and Unbiased Count (UC) analysis, with GFil producing the lowest values. GFil and LT were able to size voids of larger diameter than UC and FOAMS and also estimated a greater volume fraction for small voids.

Table D.5 Curve parameters calculated by SigmaPlot 11 on fitting a 4-parameter sigmoidal Chapman function to void size distribution data in Fig. D.17, ± SE of the fit as calculated by SigmaPlot.

Chapman curve parameter	Unbiased Count	FOAMS	Local Thickness	Granulometric Filtering
a	665.92 ± 3.37	675.17 ± 8.14	610.71 ± 4.80	600.98 ± 11.91
b	2.85 ± 0.05	2.90 ± 0.13	2.65 ± 0.04	1.78 ± 0.12
c	3.61 ± 0.11	3.89 ± 0.32	2.76 ± 0.10	1.51 ± 0.15
Y_0	8.75 ± 1.84	6.67 ± 4.32	41.22 ± 4.68	24.18 ± 10.30
R2	0.9991	0.9986	0.9990	0.9959

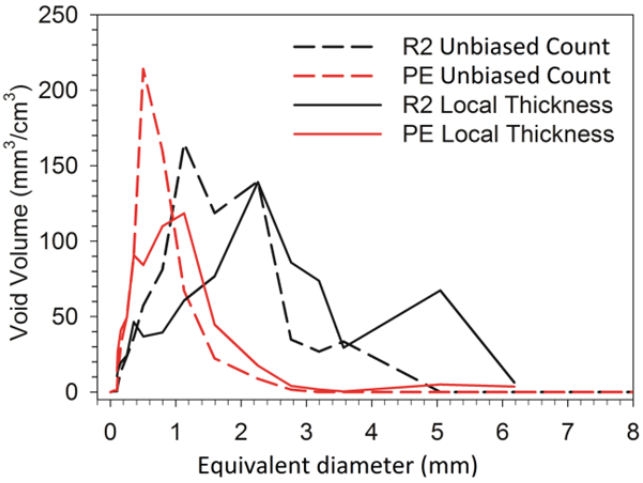

Figure D.18 Comparison of 10-bin sampling for Unbiased Count and Local Thickness analysis of processed µCT images. R2, rice 2; PE, pea.

Both LT and GFil increase sizing elements in pixel increments of radius, so that the lowest measurements are made at the limit of detection, on an image with resolution loss associated with denoising and binarisation. Measurement accuracy decreases significantly for these methods as the measured particle approaches the resolution limit of the image. Measurement data at small bubble size in LT and GFil is therefore less correct than for FOAMS and Unbiased Count, which measure particle area. The sigmoidal growth curve describes the summed effect of growth in void size during idli batter production and cooking, and also of measurement bias introduced by a specific 2D measurement technique (e.g. infilling of irregular void pockets with smaller void size spheres).

A comparison of a 10-bin count distribution for UC and LT on the same set of images (plotted on a linear axis in Fig. D.18) highlights differences between LT and FOAMS measurement techniques. Based on the low overall volume estimation for GFil compared with other sizing techniques and the underrepresentation of larger voids in Unbiased Count and FOAMS, Local Thickness is the best technique to approximate 3D void size distributions.

D.11 Quantification of solid phase structure

D.11.1 Local Thickness analysis

When wall thickness was measured in µCT images of cooked idli using LT, part of the distribution showed an exponential relationship between size and frequency at wall thickness above 0.5-1.0 mm (Fig. D.19). At this size range, the exponential relationship applies to the largest wall sizes at bubble intersection points (nodes) and may represent a self-scaling size increment (J. Russ, pers. comm.). Both rice2 and pea distributions were inflected around 0.5-0.6 mm. The probable cause was the presence of larger bean fragments (with modal size 523 µm on laser diffraction sizing that were caught within the thinning liquid phase of idli batter during rapid batter expansion on cooking.

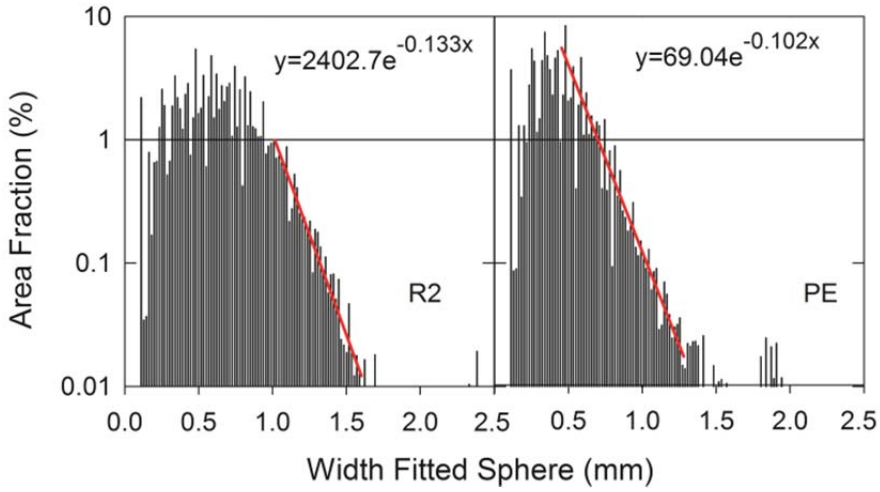

Figure D.19 Local Thickness determination of wall thickness in binarised denoised µCT images of pea and rice2 idli. An exponential function was fitted to logarithmically decreasing values using curve fitting in SigmaPlot 11 (red lines).

D.11.2 Line Intercept analysis

A Line Intercept analysis (see section D.7.6) was carried out to determine the thickness distribution of the solid phase in µCT sections. Plotting the intercept size frequency against intercept length on lin-log axes produced a straight line plot of line frequency for wall thickness > 1.0 mm (rice2 sample) or > 0.5 mm (pea sample) (data not shown). An exponential slope fitted approximately to the log-linear portion of the data, indicating the frequency of wall width size decreased more rapidly in rice2 idli than in pea idli.

When the intercept frequency was plotted as the cumulative distribution, a 2-parameter exponential decay function could be fitted to Line Intercept data, $f = a.\exp^{(-bx)}$, where parameters a and b define the slope of the curve (Fig. D.20 left).

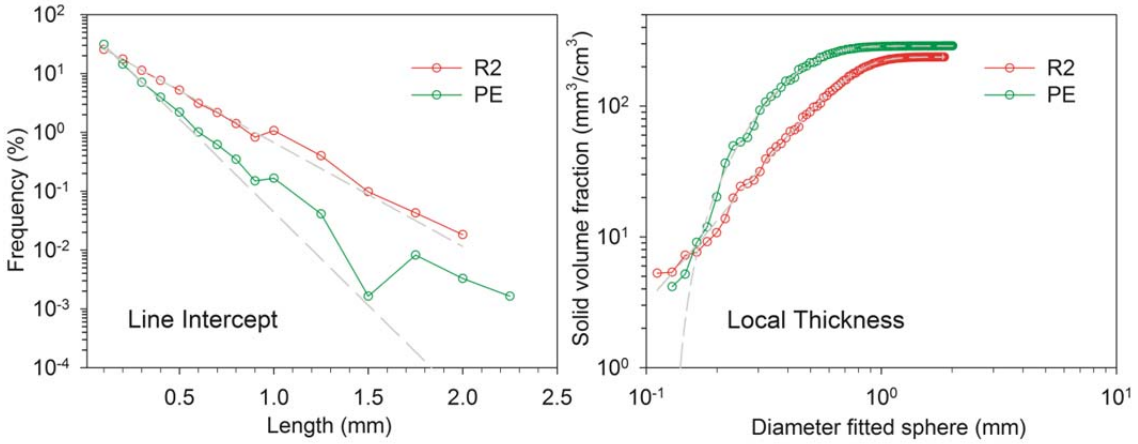

Figure D.20 Solid phase wall width in rice2 (R2) and pea (PE) idli determined in binarised µCT slices by Line intercept analysis (20 size bins) or by Local Thickness (100 size bins). An exponential decay function could be fitted using SigmaPlot 11 to Line Intercept data at values < 0.1 mm diam.; and a sigmoidal Weibull function to Local Thickness data. Fitted curves are shown as dashed lines.

Table D.6 Parameter values calculated by SigmaPlot 11 on fitting an exponential decay function to Line Intercept data for solid phase thickness; and a Weibull function to the corresponding Local Thickness data (values ± SigmaPlot, SE of Fit).

	Line Intercept (exponential decay)		Local Thickness (5-parameter Weibull)	
	Rice2 idli	**Pea idli**	**Rice2 idli**	**Pea idli**
a	64.270 ± 1.133	38.6893 ± 0.4093	282.5935 ± 1.6012	237.4132 ± 1.6796
b	7.2871 ± 0.1218	4.0629 ± 0.0491	0.3003 ± 0.0062	0.7152 ± 0.0284
c	-	-	1.6091 ± 0.03600	2.5991 ± 0.0966
x_0	-	-	0.3845 ± 0.015	0.5772 ± 0.0025
y_0	-		4.9198 ± 1.5945	-0.8190 ± 1.7207
R^2	0.9998	0.9994	0.9993	0.9998

D.11.3 Curve fitting using SigmaPlot 11 Dynamic Fit

On Local Thickness analysis of the wall fraction, the volume fraction of each size class (as mm^3/cm^3) was plotted against diameter of the fitted sphere (Fig. D.20 right). A sigmoidal 5-parameter Weibull function could be fitted to LT data:

$$f = if\ (x \leq\ x_0 - bln(2)^{\frac{1}{c}}, y_0, y_0 + a(1 - exp\left(-\left|\frac{x-x_0+bln(2)^{\frac{1}{c}}}{b}\right|\right)^c).$$

Weibull parameters a, x_0 and $y_0$defined upper and lower limits for Y-axis values, while b and c defined the curve slope (Table D.6). The term at the function start excludes values difficult to fit at the curve beginning and end.

LT analysis of wall thickness provided more detailed information about wall thickness distribution than the Line Intercept method. The use of LT as a single preferred analysis method for both wall and void analysis simplifies data handling during SP structure analysis.

D.12 Particle shape analysis in 2D

A simple shape factor for 2D particles and images of 3D objects is the Shape Factor derived from perimeter (P) and Area (A) as $Shape\ Factor\ = 4\pi A/P^2$, (Shea et al., 2010). While this is adequate to extract aspect ratio data important for volcanology applications, Shape Factor is a poor predictor of particle shape. SHAPE freeware (Iwata & Ukai, 2002) provides a statistical analysis of shape outlines. After semi-automated binarisation, watershedding and erosion-dilation to generate closed structures (an example analysis of a pea idli µCT image shown in Fig. D.21 left A & B), SHAPE applies a Fourier analysis to map outlines of target shapes selected by the user. Details of the SHAPE method are given in Appendix E.9

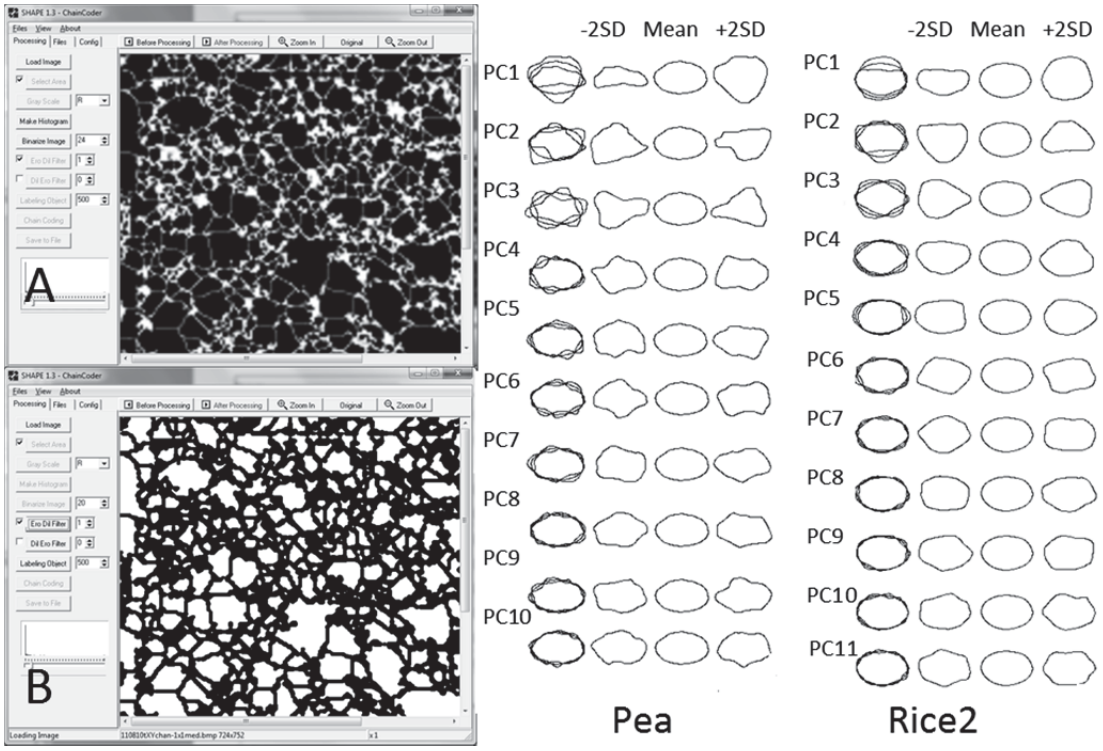

Figure D.21 Output from SHAPE freeware program (Iwata & Ukai, 2002) during void shape quantification. A: For pea idli, source µCT image after initial binarisation and watershedding by SHAPE. B: Erosion-dilation step on the image to thicken lines before SHAPE Fourier analysis. Right: Principle Component Analysis factors (PC_x) and standard deviations generated by SHAPE for pea and rice2 idli samples (n > 300).

The output of the SHAPE statistical analysis is a Principle Component Analysis reported as PCA factors, in graphic or tabular form. The SHAPE graphic output for more irregular pea idli voids is compared with that of more regular rice2 idli voids (Fig. D.21 right). The PCA factors describe the statistical divergence of void shape firstly, from an ellipse (PC1), then downwards to more complex polygons. Looking at the 2SD forms provided by the PC1 value, for example, we can guess that the PC1 factor refers to length-to-width ratio of the shape. The analysis was carried out for all idli but, unless presented in graphical form, the interpretation of the Principle Component Analysis data generated by SHAPE requires further work. Nevertheless, SHAPE may be a powerful tool for void shape quantification.

D.13 Analysis of cooked product microstructure

The cryo-sectioning method of Hug-Iten et al. (1999) proved fast and effective after minor modification. In this study, the minimal disruption of the solid phase microstructure on microwave cooking compared with standard baking (as reported in Sánchez-Pardo et al. ((2008), see Fig. 1.16), contributed to the retention of detail in micrographs of cooked idli microstructure.

D.13.1 Method for imaging stained cryo-sections of sponge product microstructure

- *Pieces of freshly prepared idli were cut and fixed minimally as described in Hug-Iten et al. (1999), except that the ratio of 20% sucrose to fixing solution was changed from 4:1 to 1:4, and sections were cryo-sectioned into 5 µm instead of 10 µm sections. Mounted sections were stained with 1% Light Green SF in 0.1% acetic acid for 3 min, rinsed by dipping into multiple changes of water and blotted dry. They were stained in iodine solution (1.4 mM I_2, 4.4 mM KI) for ~10 s, rinsed minimally, and blotted dry before immediate examination. Bright-field images were captured digitally using an Axiophot microscope, DFC320 camera and LAC 3.3 software (Carl Zeiss, Auckland, New Zealand). Post-processing, ImageJ CLAHE function was applied to improve image sharpness.*

D.14 Summary of quantification techniques for sponge product structure

In this chapter a number of digital image analysis methods were evaluated for describing SP structure.

- The best source images for structure quantification of SPs were µCT sections, followed by ink prints of the cut surface. Scanned images of the cut surfaces were not effective, as true void edges were difficult to determine from binarised images of the 3D surface, and were highly dependent on the choice of threshold setting. A specialist visualisation system for the surface of SPs, such as the C-Cell with optimised surface lighting and tailored software, overcomes some limitations of cut-surface analysis, but does not capture small void size.
- Most IA techniques required pre-processing to binarise images into count/non-count regions before analysis. Techniques that fit (mathematical) structuring elements to count regions (Local Thickness, GFil) can be applied directly to binarised images. Techniques that counted the areas of discrete particles (Unbiased Count, FOAMS) require watershedding to separate interconnected areas into discrete particles which approximate bubbles just before structure setting.
- Fractal image analysis, which can evaluate the regularity of the boundary between gas and solid phases (fractal dimension) and of void organisation (lacunarity), is sensitive to image acquisition methods. There is no standardised method for between-study comparison. The single number values generated on boundary analysis did not produce a ranking system with a direct relationship to observable features. Lacunarity plots had a complex relationship to structural features, generating size distributions with much smaller peak values than determined by other void quantification techniques.

- Consistent with the self-scaling nature of SP mesostructure, lognormal size distributions and sigmoidal cumulative distributions described the data for voids and wall distributions for part or all of the data range.
- Although Local Thickness over-represented voids at smaller size, it was chosen as the best technique to quantify mesostructure organisation in SPs, based on the capacity of the technique to capture data at the larger end of the scale and to produce a suitable analysis for wall thickness distribution.
- To quantify the wall thickness, a 5-parameter Weibull function described the exponential portion of the distribution while including non-logarithmic data. Sigmoidal cumulative void fraction distributions could be fitted by a 4-parameter Chapman function.

With careful image pre-processing, digital image analysis methods on 2D images can provide a quantitative description of void size and wall thickness distributions in the cooked SP mesostructure.

Appendix E Methods for digital image analysis

Fiji (Schindelin, 2008) is an open source, open-access distribution of ImageJ (IJ) (Rasband, 2005). ImageJ has a macro record function which can be edited to tailor macros for image processing tasks. Tasks can also be batch processed from a target folder. Mthods in this section refer primarily to ImageJ macros developed for this study.

E.1 Pre-processing in ImageJ

Output stacks were imported into ImageJ (version 1.47) for further processing. Unless otherwise stated, image transformations followed the same protocol for all samples, as recommended by Russ (2007a) to minimise operator bias.

E.1.1 Method for image pre-processing in ImageJ

- *A uniform, random stack of images was sub-sample, resized to 2x image size, converted to 8-bit image and, binarised with 'Image/Threshold/Moment', "Invert'. Before watershedding with 'Process/Binary/Watershed', images were denoised with two or more rounds of 'Light' setting, and one or more rounds of 'Dark', in 'Process/Noise/Remove outliers' ('Pixel'=1, Threshold'=1 setting unless otherwise required). Operator judgment was first used set the optimum denoising settings for each set of images to be used in automated image preprocessing. The source µCT .bmp images and watershedded images acted as references for manual pre- optimisation of threshold and denoising settings.*

E.1.2 Methods for FracLac_2.5 Lacunarity and fractal value D_B (Boxcount)

- *Use binarised images.*
- *Settings FracLac sliding box analysis for Lacunarity: 'Binary or grey-scale' Use binary, 'Background color' white, 'Type of series' geometric, 'Sizes per series' 15, 'Minimum size' 5 pixels, 'Max box size' 100%.*
- *Settings FracLac sliding box analysis for fractal value D_B: Binary or grey-scale' Autothreshold to binary, 'Background color' black, 'Block' ticked', Type of series' Use Default boxes, 'Sizes per series' 10, 'Minimum size' 5 pixels, 'Max box size' 50%.*

E.2 ImageJ Macro set: Granulometry Rolling Ball

E.2.1 µCT output pre-processing before granulometry

The denoised 700 image stack used for Local Thickness analysis was split into 100 image stacks and converted into a 10 x 10 image montage at 0.5 scale with borders of 5 pixels. The resultant image of 4128 x 4128 pixels was thresholded using ImageJ/Threshold/Huang option.

E.2.2 ImageJ Macro: granulometry-_arith_100.txt

A circular granulometry filter is applied with increasing pixel size.

1. Select Window ("Mont.tif");
2. run ("Gran Filter""type=circle radius=1 step- 1 euclidian"); For a 2 pixel diameter shape, output in image form.
3. Select Window ("Mont.tif");

4. run (“Gran Filter”“type=circle radius=1 step- 2 euclidian”); ….Repeat with increasing structuring element size.

The lines in green are repeated for pixel size of 1, 2, 3, 4, 5, 7, 8, 11, 13, 17, 22, 27, 35, 44, 56, 71, 89, 113, 144. This covers a granulometry size range from 89 µm to 8.0 mm, in 20 bins increasing arithmetically by a factor of 1.414 between bins. Image sizing was stopped at the largest size image able to generate shapes.

E.2.3 IJ Macro:/Fiji/macro/Teresa/Gran_Count_2pix.ijm

The macro ensures Granulometry output files are binary for later image addition steps, before creating a difference image for particle analysis, by sequential removal of larger size from the next granulometric image of smaller count size. Produces images as a stack with granulometric output partitioned according to size.

1. setAutoThreshold("Huang dark");
2. //run("Threshold...");
3. setThreshold(1, 255);
4. run("Convert to Mask");
5. run("Granulometry ", "minimal=1 maximal=50 step=2 plot=radius show=yes");
6. close();
7. run("Tile");
8. selectWindow("Image 1.0");
9. setAutoThreshold("Huang dark");
10. setThreshold(50, 255);
11. run("Convert to Mask");
12. selectWindow("Image 3.0");……
13. selectWindow("Image 45.0");
14. run("Analyze Particles...", "size=1.62-Infinity circularity=0.00-1.00 show=Masks display summarize record"); Size minimums calculated as area of circle if granulometric element rolled in place.
15. selectWindow("Mask of Image 45.0");
16. rename("Mask Sum");
17. imageCalculator("Subtract", "Image 43.0","Mask Sum"); Remove all pixels already counted.
18. run("Analyze Particles...", "size=1.62-Infinity circularity=0.00-1.00 show=Masks display summarize record");…..

The output calculates area fraction automatically as the summary output when chosen in ImageJ Set Measurements window.

The output is packaged into an image stack before particle counting. In this case, the output of the entire section is counted sequentially, but smaller images can be cropped to count individual frames if required.

E.2.4 ImageJ Macro: 100_cut.ijm

Quantifies particle size in the montage stack produced for Granulometry Filtering

1. run("Set Scale...", "distance=428 known=15 pixel=1 unit=mm global");
2. run("Set Measurements...", "area perimeter skewness area_fraction display redirect=None decimal=3");
3. saveAs("Tiff", "C:\\Users\\Desktop\\Gran_count.tif");
4. makeRectangle(0, 0, 428, 428);
5. run("Crop");
6. run("Analyze Particles...", "size=10-Infinity pixel circularity=0.00-1.00 show=Nothing display summarize stack");
7. run("Close"); open("C:\\Users\\Desktop\\Gran_count.tif");

The section in green can be used to analyse individual images in the montage stack, by working through the entire set of vertex co-ordinates at the top left hand of each slice start within the montage.

E.3 ImageJ Macro: Watershed partitioning for Unbiased Count and FOAMS

The output is an image stack showing particles as detected and measured in the unbiased box, a data set of measurements for each particle, and a summary of measurements in each section. In ImageJ Set Measurements choose Area, Slice label and XY co-ordinates.

Source images: denoised binary image stack of µCT sections

1. run("Collect Garbage");
2. run("Set Measurements...", "area perimeter bounding feret's area_fraction display redirect=None decimal=4");
3. run("Set Scale...", "distance=856 known=15 pixel=1 unit=mm global");
4. saveAs("Tiff", "C:\\Documents and Settings\\Desktop\\StackO.tif");
5. run("Watershed", "stack");
6. saveAs("Tiff", "C:\\Documents and Settings\\Desktop\\Stack.tif");
7. run("Collect Garbage");
8. *CREATE L-SHAPED COUNT MASKS TO PRODUCE AN UNBIASED COUNT BOX*
9. //setTool(0);
10. makeRectangle(0, 0, 570, 570); *start vertex of box should be randomly chosen*
11. run("Analyze Particles...", "size=0-Infinity circularity=0.00-1.00 show=Masks stack");
12. saveAs("Tiff", "C:\\Documents and Settings\\Desktop\\Mask2.tif");
13. close();
14. selectWindow("Stack.tif");
15. //setTool(2);
16. makePolygon(854,0,570,0,570,570,0,570,0,854,854,854); *start vertex of box should be randomly chosen*
17. run("Analyze Particles...", "size=0-Infinity circularity=0.00-1.00 show=Masks stack");
18. run("Collect Garbage");

```
19. saveAs("Tiff", "C:\\Documents and Settings\\Desktop\\Mask3.tif");
20. selectWindow("Stack.tif");
21. run("Analyze Particles...", "size=0-Infinity circularity=0.00-1.00 show=Masks exclude stack");
22. selectWindow("Mask3.tif");
23. imageCalculator("Subtract stack", "Mask3.tif","Mask of Stack.tif");
24. run("Collect Garbage");
25. //run("Image Calculator...", "image1=Mask3.tif operation=Subtract image2=[Mask of Stack.tif] stack");
26. run("Save", "save=[C:\\Documents and Settings\\Desktop\\Mask3.tif]");
27. selectWindow("Stack.tif");
28. close();
29. open("C:\\Documents and Settings\\Desktop\\Mask2.tif");
30. imageCalculator("Add stack", "Mask2.tif","Mask3.tif");
31. //run("Image Calculator...", "image1=Mask2.tif operation=Add image2=Mask3.tif stack");
32. run("Save", "save=[C:\\Documents and Settings\\Desktop\\Mask2.tif]");
33. imageCalculator("Add stack", "Mask2.tif","frame.tif");
34. //run("Image Calculator...", "image1=Mask2.tif operation=Add image2=frame.tif stack");
35. run("Collect Garbage");
36. run("Save", "save=[C:\\Documents and Settings\\Desktop\\Mask2.tif]");
37. selectWindow("Mask3.tif");
38. close();
39. selectWindow("Mask2.tif");
40. run("Collect Garbage");
41. run("Analyze Particles...", "size=0-Infinity circularity=0.003-1.00 show=Masks display exclude clear summarize stack");
42. selectWindow("Mask of Stack.tif");
43. close();
44. selectWindow("Mask2.tif");
45. close();
```

E.4 ImageJ Unbiased Count

For unbiased counting, particles that intersect two adjacent sides of a randomly-positioned count box are counted, and those touching the non-permitted sides are not. A count box with length > 2x the largest particle diameter (ideally, > 3x) is created as a frame and pasted onto a binarised image stack. The left-top vertex is placed at a randomly-determined position within the left-hand top quarter of the image. To satisfy the statistical requirements of an unbiased count a random number generator and a spreadsheet are used to calculate a random XY co-ordinate position for the vertex.

A particle count is made with ImageJ 'Analyse particles, include on edge, Show Masks'. The output is captured as the mask output (showing solid images for all the particles counted), and saved as 'Mask2'. The portion of counting particles overhanging the frame on the non-permitted sides is blanked in 'Mask 2' by adding an L-shape overlay. 'Analyse Particles, exclude On Edges, Show Masks' is run on the blanked image, and the output stack saved as 'Mask3'. Mask 3 is subtracted from Mask2 using 'Image Calculator' to produce only those particles that fall completely or partly inside the count box, removing any particles that touch non-permitted side of the count box and retaining the entirety of any particles touching permitted sides. This output image is added to back to the frame image, before particle counting using the resultant image.

Large stacks are analysed more effectively when source image stacks are saved onto the Desktop, intermediate output stacks are saved for the next process (hence the number of saveAs steps in the macro), and "Create New Window" options are chosen only when necessary.

1. selectWindow("stack.tif");
2. //setTool(0);
3. makeRectangle(0,0,854,0,854,854,0,854); *make frame*
4. run("Analyze Particles...", "size=0-Infinity circularity=0.00-1.00 show=Masks exclude stack");
5. selectWindow("Mask of stack.tif"); *capture the stack with frame overlaid*
6. saveAs("Tiff", "C:\\Documents and Settings\\Desktop\\Mask1.tif");
7. //setTool(2);
8. makePolygon(854,0,570,0,570,570,0,570,0,854,854,854); *L-SHAPE OVERLAY WITH RANDOM START*
9. run("Analyze Particles...", "size=0-Infinity circularity=0.00-1.00 show=Masks stack");
10. saveAs("Tiff", "C:\\Documents and Settings\\Desktop\\Mask2.tif");
11. selectWindow("stack.tif");
12. run("Analyze Particles...", "size=0-Infinity circularity=0.00-1.00 show=Masks exclude stack");
13. selectWindow("Mask2.tif");
14. imageCalculator("Subtract stack", "Mask2.tif","Mask of stack.tif");
15. //run("Image Calculator...", "image1=Mask2.tif operation=Subtract image2=[Mask of stack.tif] stack");
16. run("Save", "save=[C:\\Documents and Settings\\Desktop\\Mask2.tif]");
17. imageCalculator("Add stack", "Mask1.tif","Mask2.tif");
18. //run("Image Calculator...", "image1=Mask1.tif operation=Add image2=Mask2.tif stack");
19. run("Save", "save=[C:\\Documents and Settings\\Desktop\\Mask3.tif]");
20. \\"Set Measurements...", "area perimeter bounding feret's area_fraction display redirect=None decimal=4");

21. run("Analyze Particles...", "size=0-Infinity circularity=0.00-1.00 show=Masks display exclude summarize stack"); *Analyse the output image for particle size.*

E.4.1 ImageJ Countholes_InkP_WS.ijm macro

Scans of ink prints were combined into image stacks in RGB form (unscaled) and resized to three times origin pixel size before running the macro.

1. run("8-bit");
2. setAutoThreshold("Moments");
3. //run("Threshold...");
4. setOption("BlackBackground", false);
5. run("Convert to Mask", "method=Moments background=Light calculate");
6. run("Close");
7. saveAs("Tiff", "C:\\Users\\Desktop\\StackScan.tif");
8. run("Collect Garbage");
9. run("Invert", "stack");
10. run("Watershed", "stack");
11. run("Set Measurements...", "area perimeter shape area_fraction display redirect=None decimal=4");
12. run("Set Scale...", "distance=1544 known=70 pixel=1 unit=mm global");
13. run("Analyze Particles...", "size=0-Infinity circularity=0.00-1.00 show=Masks display exclude stack"); *the mask output was trimmed manually to exclude false watersheds at edges before rerunning Analyze Particles*
14. run("Analyze Particles...", "size=0-Infinity circularity=0.00-1.00 show=Masks display exclude summarise stack");
15. close();

E.5 ImageJ plugin LocalThickness (LT) analysis

When LT analysis was carried out on a sub-sample of the object, sections were taken from the µCT Z-axis stack at a regular interval, starting with a randomly-chosen initial section (Howard & Reed, 2005c). Data variability within the sample was calculated from LT outputs of consecutive 100-section sub-stacks.

E.5.1 ImageJ Macro: New Void.ijm

This runs Local Thickness (LT) on the void fraction of a 700 image 3D stack. The stack is split sequentially into 100 image stacks to manage the data flow. After cleaning noise from images, the LT output image stack is compared by eye against the binarised source image stack. If the LT output had assigned too many small pores due to image noise additional iterations of 'bright stack' and 'dark stack' outlier removal are added until LT output and source become congruent. Once the number of denoising iterations has been optimised for a specific sample, further denoising is carried out automatically on each sample. The output of each analysis cycle is a 32-bit false-colour image stack, in which Fitted Sphere diameter is reported as pixel intensity. The macro runs a Histogram analysis

binning pixel intensity of each 100 section stack into a bin size range suitable for further data display.

1. saveAs("Tiff", "C: \\Desktop\\stack.tif");
2. run("Make Substack...", "slices=1-100");
3. selectWindow("stack.tif");
4. close();
5. selectWindow("Substack (1-100)");
6. run("Remove Outliers...", "radius=1.6 threshold=10 which=Bright stack");
7. run("Remove Outliers...", "radius=1.6 threshold=10 which=Bright stack");
8. run("Remove Outliers...", "radius=1.6 threshold=10 which=Dark stack");
9. run("Local Thickness (complete process)", "threshold=1 inverse");
10. run("32-bit");
11. imageCalculator("AND create stack", "Substack (1-100)","Substack (1-100)_LocThk"); *overlays the original binary image in 32-bit to trim off pixel overhangs produced by LT*
12. selectWindow("Substack (1-100)");
13. close();
14. run("Collect Garbage"); *DUMPS DATA FROM BUFFER*
15. run("Histogram", "bins=255 x_min=0.05 x_max=280.1 y_max=Auto stack"); *the choice of values can be chosen to normalise histogram bin settings in order to compare output stacks with differing maximum and minimum values*
16. selectWindow("Substack (1-100)_LocThk");
17. close();
18. open("C:\\Users\\Desktop\\stack.tif");
19. run("Make Substack...", "slices=101-200");

Repeat cycle from steps 3-19 for consecutive stacks of 1-100,…601-700.

E.5.2 ImageJ Macro: New Mat.ijm

As for NewVoid.ijm, but for analysis of the solid fraction. The lines in green are replaced with

9. run("Local Thickness (complete process)", "threshold=1"); and

15. run("Histogram", "bins=62 x_min=0.05 x_max=60.2 y_max=Auto stack");.

E.5.3 ImageJ Macro: SET3D_LUT_minmax.ijm

This sets the LT false-colour output stack (which LT automatically fits to a range with maximum and minimum values determined by each individual output stack) so that different images carry the same false-colour assignment. Look Up Table (LUT) colour assignments between different LT image output stacks can be normalised to the same min-max values.

1. var min, max; // global variables
2. macro "Set Display Range...";
3. min = getNumber("Min:", min);
4. max = getNumber("Max:", max);

5. setMinAndMax(0.05,62);. Insert values chosen as appropriate Min and Max values for between-image comparison.

E.6 BoneJ

The ImageJ BoneJ distribution for analysis of bone density applies ImageJ Local Thickness to grey-scale μCT images. As the BoneJ binarisation and denoising (Purify) option was less effective at pre-processing images produced in this study than the pre-processing applied in Appendix E.1, pre-processed stacks of 100 slices were imported into BoneJ for size void size determination (BoneJ Local Thickness analysis). Default BoneJ settings were chosen for BoneJ analysis options, such as Degree of anisotropy, Isosurface (calculates surface area by constructing a triangular surface mesh by marching cubes and summing the areas of the mesh triangle.

E.7 ImageJ Line intercept

A grid made of parallel lines 1 pixel thick, 20 pixels apart is rotated through 180° to generate a series of grid images with incremental rotation. A twenty-slice montage is made, AND is calculated for each grid image and the montage. Intersecting regions in the output image are measured with Analyse particles in each slice of the montage, including 'Bounding rectangle'. X- and y-results in pixels for the Bounding rectangle are used to derive a true value for line segment lengths during post-processing rather than rely on the area function of ImageJ.

E.7.1 ImageJ Macro: Grid-Count.txt

Makes a montage from binarised denoised 700 slice stack, with 'Row', 5 x 'Column', 4; 'First slice' a random start between 1-34, 'Slice period' 35, 'Border' 2 pixel, and saves as Mont.tif

1. open("D: \\Templates\\Grid_XYMont_0.tif");
2. imageCalculator("AND create", "Grid_XYMont_0.tif","Mont.tif");
3. selectWindow("Result of Grid_XYMont_0.tif");
4. run("Run...", "run=[D:\\ImageJ\\macros\\Teresa\\Count_Grid_Y.txt]");
5. selectWindow("Result of Grid_XYMont_0.tif"); = grid 0°, incrementing to 170° at 20° intervals
6. close();
7. selectWindow("Grid_XYMont_0.tif");
8. close(); *The macro continues in steps in which the filename in bold increments in 20° intervals to 170°.*
9. Macro: Count_Grid_Y.txt
10. Counts intercept length distribution.
11. run("Set Measurements...", "area perimeter bounding area_fraction display redirect=None decimal=4");
12. //setTool("rectangle");
13. makeRectangle(0, 0, 856, 856);
14. run("Analyze Particles...", "size=0-Infinity circularity=0.00-1.00 show=Nothing display summarize");

15. makeRectangle(0, 856, 856, 856);
16. run("Analyze Particles...", "size=0-Infinity circularity=0.00-1.00 show=Nothing display summarize");…Continues to capture data in each slice.

E.8 FOAMS analysis

The % Void value was taken as that determined from all 700 of the µCT images for each idli sample. Preliminary analyses determined a suitable bin size allocation to standardise output X-axes across samples. In some cases, a mix of µCT images and ink prints were analysed together.

E.8.1 Method for FOAMS analysis

- *Individual pre-processed images were imported into FOAMS (version 1.0.4) (http://www2.hawaii.edu/~tshea/foams/downloads.html) run within MATLABR 7.11.0 (2010b) student toolbox The MathWorks, Ltd 2004-2010). 'Size threshold' was set at 5 pixels, and 'Sample parameter/normalisation by known' chosen.*

E.9 SHAPE analysis

SHAPE was downloaded from http://lbm.ab.a.u-tokyo.ac.jp/~iwata/shape/.

E.9.1 Method for SHAPE analysis

- *Five µCT slices were chosen with random-start and uniform interval from the 700 XY-axis stack, and each cropped to a 10 x 10 mm .bmp image at 45.6 pixel/mm resolution. The images were imported into SHAPE Chain Coder and binarised with no erosion, cutoff 200. In CHCNef conversion of the binarised output, each shape was screened manually to exclude extremes. Around 500 shapes were screened for each sample.*